Downloaded from orbit.dtu.dk on: May 22, 2019

DTU Library

Multi-scale design methods for Topology Optimization

Groen, Jeroen Peter

Publication date:
2018

Document Version
Publisher's PDF, also known as Version of record

Link back to DTU Orbit

Citation (APA):
Groen, J. P. (2018). Multi-scale design methods for Topology Optimization. Kgs. Lyngby: Technical University of Denmark (DTU). DCAMM Special Report, No. S254

General rights
Copyright and moral rights for the publications made accessible in the public portal are retained by the authors and/or other copyright owners and it is a condition of accessing publications that users recognise and abide by the legal requirements associated with these rights.

- Users may download and print one copy of any publication from the public portal for the purpose of private study or research.
- You may not further distribute the material or use it for any profit-making activity or commercial gain
- You may freely distribute the URL identifying the publication in the public portal

If you believe that this document breaches copyright please contact us providing details, and we will remove access to the work immediately and investigate your claim.

Multi-scale design methods for Topology Optimization

Jeroen Peter Groen

Kgs. Lyngby 2018
DCAMM Special Report No. S254

Multi-scale design methods for Topology Optimization
December2018

Author:
Jeroen Peter Groen

Main supervisor:
Professor Ole Sigmund
Technical University of Denmark

Co-supervisors:
Associate Professor Niels Aage
Technical University of Denmark

Senior Researcher Boyan S. Lazarov
Technical University of Denmark

© 2018 Jeroen Peter Groen

Technical University of Denmark
Department of Mechanical Engineering
Building 404, DK-2800 Kgs. Lyngby, Denmark
Phone: +45 45 25 25 25, Fax: +45 45 25 19 61
E-mail: info@mek.dtu.dk, URL: www.mek.dtu.dk

MEK-PHD: ISSN 0903-1685, ISBN 978-87-7475-549-4

Preface

This thesis is the outcome of the Ph.D. project titled *multi-scale design methods for topology optimization*, performed at the department mechanical engineering at the Technical University of Denmark (DTU). The Ph.D. project has been funded by the Department of Mechanical Engineering, DTU. Secondary funding has been provided by the Villum Foundation through the *NextTop* project. The work has been carried out at the Department of Mechanical Engineering, Section of Solid Mechanics, at DTU during the period from the first of January 2016 and the 31th of December 2018. The main supervisor has been Professor Dr.techn. Ole Sigmund and the co-supervisors have been Associate Professor Ph.D. Niels Aage and Senior Researcher Ph.D. Boyan S. Lazarov.

First of all, I would like to thank Ole Sigmund for his great and inspiring support and for granting me a lot of freedom during the Ph.D. project. I benefited from the generous help of Niels Aage and Boyan Lazarov who always had time to help me understand numerical methods and teach me about high performance computing. I would like to thank Andreas Bærentzen for introducing me to the field of computational geometry processing. Furthermore, I would like to thank Jun Wu, with whom I shared an office at the start of my Ph.D. studies, and who later hosted me at TU Delft during the external part of my Ph.D. project. It was a pleasure being in Delft and being back in the Netherlands.

I want to thank all of my present and former colleagues in the TopOpt Group and in the Section of Solid Mechanics at DTU. The working environment is fantastic and I am grateful for the nice discussions and good company, both on scientific and personal level. A special thanks to Yiqiang Wang and Federico Ferrari for proofreading parts of this thesis.

On a personal level I would like to thank my family and girlfriend who have always supported me throughout the Ph.D. project. I am sorry that you had to endure me during the Christmas holidays when I was very busy finishing this thesis. Finally, I would like to thank my friends and roommates for the great times I had in the last three years.

Abstract

In this thesis multi-scale design methods for topology optimizations are presented. The goal of these methods is to find manufacturable designs, with a close to optimal stiffness at a reduced computational cost compared to well-established topology optimization methods.

First, the theory of homogenization-based topology optimization is discussed. The modeling of microscopic details is considered, as well as optimal microstructures that have extremal stiffness. This theory is well-developed and can be used to find an overall optimal material distribution at low computational cost. A downside of these optimal multi-scale designs is that they cannot be manufactured on a single length-scale. The main contribution of the research in this thesis is to develop and extend on new methods, such that these optimal designs can be interpreted on a single scale, while still being close to what is theoretically possible.

Simple and close to optimal single-scale microstructures are presented that are optimized for multiple anisotropic loading conditions. A method to approximate optimal microstructures on a single-scale is proposed, which are close (*e.g.* 10-15%) to the theoretical bounds. When used as starting guess for topology optimization these proposed microstructures can be further improved, outperforming topology optimized designs using classical starting guesses both in performance and simplicity. Furthermore, a class of simple periodic truss lattice structures is presented that exhibit near-optimal performance in the high porosity limit, while still being well-connected. The performance difference between closed and open-walled microstructures is presented for anisotropic loading situations, where it is demonstrated that the maximum difference occurs when isotropic microstructures are considered.

Furthermore, a method to interpret spatially varying microstructures on a single-scale is presented. Using this method high-resolution and near optimal designs can be achieved on a standard PC in less than 10 minutes. An extension of this method to enforce a minimum feature size and a method to locally adapt the microstructure spacing are shown. The promise and drawbacks of this multi-scale design method are discussed with emphasis on the full-scale performance. Furthermore, the overall solution procedure is shown as well as an extension of the method to obtain coated designs, *i.e.* a solid shell surrounding porous infill material. In a similar work, the link between Michell's theory of least-weight trusses and optimal laminates is exploited to extract a discrete frame structure from a continuum design. Subsequent frame optimization results in convergence towards known optimal solutions at low computational cost.

Publications

The following journal publications are submitted as part of this Thesis:

[P1] J.P. Groen and O. Sigmund. Homogenization-based topology optimization for high-resolution manufacturable micro-structures. *International Journal for Numerical Methods in Engineering*, 113(8):1148–1163, 2018 (online, 2017). doi:10.1002/nme.5575

[P2] S.D. Larsen, O. Sigmund and J.P. Groen. Optimal truss and frame design from projected homogenization-based topology optimization. *Structural and Multidisciplinary Optimization*, 57(4):1461–1474, 2018. doi:10.1007/s00158-018-1948-9

[P3] E. Träff, O. Sigmund and J.P. Groen. Simple single-scale microstructures based on optimal rank-3 laminates. *Structural and Multidisciplinary Optimization*, 1-11, 2019. doi:10.1007/s00158-018-2180-3

[P4] J.P. Groen, J. Wu and O. Sigmund. Homogenization-based stiffness optimization and projection of 2D coated structures with orthotropic infill. *Computer Methods in Applied Mechanics and Engineering*, 349(1):772–742, 2019. doi:10.1016/j.cma.2019.02.031

[P5] Y. Wang, J.P. Groen and O. Sigmund. Simple optimal lattice structures for arbitrary loadings. *Extreme Mechanics Letters*, (accepted), 2019.

The following journal publication was published during the Ph.D. studies; however is not considered part of this thesis:

[P6] J.P. Groen, M. Langelaar, O. Sigmund and M. Ruess. Higher-order multi-resolution topology optimization using the finite cell method. *International Journal for Numerical Methods in Engineering*, 110(10):903–920, 2017. doi:10.1002/nme.5432

Contents

1 Introduction

1.1 Motivation and goal

Topology optimization is a mature design method, with various applications in industry. Recently, Aage et al. [2017] optimized the material distribution in an airplane wing using more than 1 billion design variables. This giga-scale design gives engineers new insights in how wing design can be performed; however, at a very large computational cost (a high-performance computer with 8000 cores was needed). Hence, to fully exploit topology optimization as a design tool, a large reduction in computational cost is needed.

This reduction in cost can be achieved by considering multi-scale modeling techniques. To be more specific, it is well-known that the optimal shape for a compliance minimization problem consists of periodic composites on a microscopic length-scale. Homogenization-based topology optimization is a well-established design method to find an optimal material distribution of these composite microstructures at low computational cost. However, a downside of these optimal multi-scale designs is that they cannot be manufactured on a single length-scale. This might be the reason why the interest in this method has faded in favor of the popular density-based design methods.

The main goal of this Ph.D. project is to develop and extend existing methods to interpret optimal homogenization-based designs on a single scale. The corresponding single-scale designs have to be:

- Close in performance to what is theoretically possible.
- Simple to manufacture.
- Obtained in a short time.

In this thesis I will discuss several steps that have to be taken to satisfy these requirements. Emphasis is put on the numerical implementation details, potential pitfalls and on the performance of the obtained single-scale designs.

It has to be noted that the study is restricted to mechanical problems in the context of linear elasticity. However, parts of the theory can be applied to problems considering different physics or non-linear behavior. Furthermore, overlaps between the presented work and different research fields, *e.g.* geometry modeling, are discussed.

1.2 Structure of the thesis

The goal of this thesis, is to present all methods, required to interpret homogenization-based design on a single-scale and the practical issues involved in doing so. A broad overview of the considered topics is given, to present the reader a clear picture on how multi-scale design can be performed. I have tried to describe all methods such that an interested reader can implement them and can understand why certain design choices are made. For clarity I have repeated some parts of the attached papers in

this thesis; however, it should be noted that for consistency a different notation for some variables is used.

Since a lot of topics are considered, it is not possible to discuss all the details. Therefore, I assume that the readers are familiar with linear algebra, the finite element method (FEM) [Cook et al., 2001; Szabó and Babuska, 1991], numerical algorithms for constrained optimization [Nocedal and wright, 2006], and density-based topology optimization [Bendsøe and Sigmund, 2004]. A good overview on recent developments in the field of topology optimization is given in the review papers by Deaton and Grandhi [2013]; Sigmund and Maute [2013].

This thesis is structured as follows. A discussion on homogenization-based topology optimization is given in Chapter 2. In Chapter 3 different methods are presented to create simple, near-optimal single-scale microstructures, optimized for multiple anisotropic loading cases. A method to approximate a spatially varying multi-scale design on a single-scale is given in Chapter 4. An overview of the entire multi-scale design procedure is given in Chapter 5. Here I discuss practical issues, as well as the problem of getting a good parameterization for 3D and multiple load case designs. Finally, this thesis is concluded with Chapter 6, where the most important results are discussed, and recommendations are given for future work.

2 Homogenization-based topology optimization

In this chapter I will introduce the concept and definitions of homogenization-based topology optimization. The method is a multi-scale design method in the sense that the design consists of composite materials, which are assumed to be periodic on a microscopic length-scale. Only on a much larger length-scale (the macroscopic length-scale) are the properties of these composites, e.g. directions of lamination and corresponding layer widths allowed to vary. Hence, the required computational cost to evaluate the response of a design consisting of these microscopic details would be astronomical. To overcome this problem one can use the theory of homogenization to calculate the effective macroscopic properties of a complex but periodic composite. A macroscopic description of these 'homogenized' properties allows one to model the response of such a multi-scale design at a reasonable computational cost.

In homogenization-based topology optimization the goal is to find the macroscopic material description of these composite materials that minimizes a desired objective $\mathcal{J}$, subject to a number of constraints. In this thesis I focus on a classical type of optimization problem in the setting of linear elasticity, *i.e.* compliance minimization (maximizing stiffness) of a design consisting of two-phase composite materials, with an upper bound on the usage of one material phase.

This chapter starts with a short description of the need for a design description by composite materials. Afterwards, the homogenization method is introduced, including its applications for the derivation of optimal composite materials and other types of material design. Subsequently, homogenization-based topology is introduced, where different problem formulations are considered. This chapter is concluded with a literature overview of the field of multi-scale topology optimization approaches.

2.1 Brief introduction to the relaxed design space

Structural optimization has been applied in many fields, one of the most classical being truss optimization, where Michell [1904] used a continuum description to represent an optimal truss design. As is discussed by many authors, amongst others Prager and Rozvany [1977], this continuum description is a limit case. Only by allowing for an infinite number of truss members, the solution of Michell [1904] can be approached. In other words, when one tries to represent the truss like continua using N discrete bars, a better solution can be found with $N + 1$ members.

Similarly, Cheng and Olhoff [1981] found that for the case of optimizing the reinforcement of a circular plate under pressure, more stiffener-like thickness variation could be found if they allowed for more. Hence, the solution is dependent on the mesh. They concluded that in the limit of an infinitely fine mesh there would be an infinite number of stiffening members [Cheng, 1981; Olhoff et al., 1981]. Only by restricting the variation in the shape as is done by Niordson [1983] existence of a solution can be shown.

Similarly it can be shown that a material distribution problem in 2 or 3 dimensions has no solution when a continuous material description is used, *i.e.* a point-wise material or void description. The lack of being able to determine whether there exists a solution using only a finite number of *e.g.* thickness variations can be problematic. However, by restricting the freedom using either: slope constraints [Petersson and Sigmund, 1998], perimeter control [Ambrosio and Buttazzo, 1993], or length-scale enforcement through filter methods [Bourdin, 2001] existence of a solution can be shown. Nevertheless, these solutions are not optimal, since a smaller length-scale will result in a better performance.

Kohn and Strang [1986] discuss that the optimal solution of a material distribution problem can be solved by relaxing the solution space. In this case the problem becomes well-posed such that an optimal solution can be found. Relaxing the design space means the use of a continuous composite description, allowing for more freedom than a point-wise material or void description. Performing topology optimization using a continuous composite description will be the topic of the remainder of this chapter.

2.2 Homogenization and optimal microstructures

In this section I will discuss the equations that can be used to determine the effective properties of a periodic composite unit-cell. The discussion is brief, and meant as a simple indication to the reader where some of the results come from. For a rigorous discussion on the well-developed theory of homogenization the reader is referred to the books of Allaire [2002]; Bensoussan et al. [1978]. The work by Guedes and Kikuchi [1990] is recommended for a reader interested in the practical aspects of numerical homogenization using the finite element method (FEM). Finally, a publicly available MATLAB code to estimate the effective properties of a composite material in 2D is introduced by Andreassen and Andreasen [2014].

2.2.1 Review of homogenization equations

Consider domain $\Omega \in \mathbb{R}^N$ for $N = 2, 3$, shown in Figure 2.1(a), for which we want to model the displacement field $\boldsymbol{u}$ for a given set of applied body forces $\boldsymbol{b}$ and tractions $\boldsymbol{t}$ that are applied at Neumann boundary Γ_N. Using the assumption of linear elasticity the governing equations are written as,

$$\begin{aligned}
&\boldsymbol{\nabla} \cdot \boldsymbol{\sigma} + \boldsymbol{b} = \boldsymbol{0} && \forall \boldsymbol{x} \in \Omega, \\
&\boldsymbol{\sigma} \cdot \boldsymbol{n} = \boldsymbol{t} && \forall \boldsymbol{x} \in \Gamma_N, \\
&\boldsymbol{u} = \boldsymbol{u}_D && \forall \boldsymbol{x} \in \Gamma_D, \\
&\boldsymbol{\sigma} = \boldsymbol{E} : \boldsymbol{\varepsilon} && \forall \boldsymbol{x} \in \Omega, \\
&\boldsymbol{\varepsilon} = \frac{1}{2}\left(\nabla \boldsymbol{u} + \nabla \boldsymbol{u}^T\right) && \forall \boldsymbol{x} \in \Omega.
\end{aligned} \tag{2.1}$$

Here the first equation describes the balance of momentum, with $\boldsymbol{\sigma}$ the stress tensor. $\boldsymbol{n}$ represents the vector normal to the domain boundary $\Gamma = \Gamma_N \cup \Gamma_D$, with $\Gamma_N \cap \Gamma_D = \emptyset$. At the Dirichlet boundary Γ_D prescribed displacements $\boldsymbol{u}_D$ are applied.

Furthermore, the fourth-order elasticity tensor $\boldsymbol{E}$ is used to link the strains $\boldsymbol{\varepsilon}$ to the stresses.

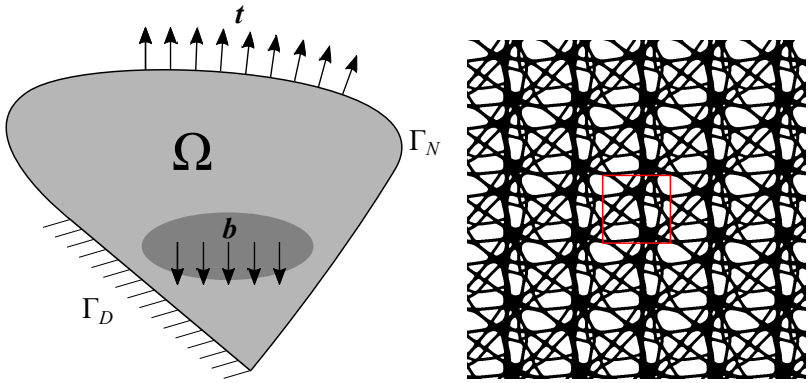

(a) Domain Ω. (b) Periodic composite in Ω.

Figure 2.1: Modeling domain Ω and a microscopic periodic composite in Ω.

Now let Ω consists of composite microstructures, hence if one zooms in with a microscope at a point $\boldsymbol{x}$ one can see a periodic sequence of base-cells as shown in Figure 2.1(b), which are of order ϵ, which is a very small positive number. $\boldsymbol{Y}$ is used to describe the periodic unit-cell (base-cell), which is a parallelogram in $\mathbb{R}^2$ or a parallelepiped in $\mathbb{R}^3$.

The composite properties are allowed to vary smoothly on macroscopic level $\boldsymbol{x}$; however on the microscopic level $\boldsymbol{y} = \boldsymbol{x}/\epsilon$ the composite is assumed to be periodic. This means that all quantities (*e.g.* elastic constants and displacements) have dependencies on these two scales $\boldsymbol{x}$ and $\boldsymbol{y}$. In the limit of $\epsilon \to 0$, there are a large number of periodic unit-cells at a point $\boldsymbol{x}$. This means that the dependence of properties on $\boldsymbol{y}$ can be considered periodic, which is called $\boldsymbol{Y}$-periodic. Due to the dependence on $\boldsymbol{x}$ and $\boldsymbol{y}$ it is assumed that the displacement field $\boldsymbol{u}$ can be expressed as an asymptotic expansion.

$$\boldsymbol{u}(\boldsymbol{x},\boldsymbol{y}) = \epsilon^0\boldsymbol{u}^0(\boldsymbol{x},\boldsymbol{y}) + \epsilon^1\boldsymbol{u}^1(\boldsymbol{x},\boldsymbol{y}) + \epsilon^2\boldsymbol{u}^2(\boldsymbol{x},\boldsymbol{y}) + ... \tag{2.2}$$

This expression for $\boldsymbol{u}$ can be substituted into the governing equations. The corresponding formulation can be sorted in powers of ϵ and after various calculations it can be shown that the displacement coefficient $\boldsymbol{u}^0$ only depends on the macroscopic length-scale $\boldsymbol{x}$. Furthermore, a description of the effective, or so-called homogenized properties of the elasticity tensor $\boldsymbol{E}^H$ can be found, such that the macroscopic displacement behavior in Ω can be modeled. To do this, consider the equilibrium in a unit-cell for an applied macroscopic unit-strain $\boldsymbol{\varepsilon}^0$,

$$\frac{1}{2}\int_{\boldsymbol{Y}} E_{ijpq}\Big(\frac{\partial v_i}{\partial y_j} + \frac{\partial v_j}{\partial y_i}\Big)\Big(\frac{\partial \chi_p}{\partial y_q} + \frac{\partial \chi_p}{\partial y_q}\Big)\mathrm{d}\boldsymbol{Y} = \int_{\boldsymbol{Y}} E_{ijpq}\Big(\frac{\partial v_i}{\partial y_j} + \frac{\partial v_j}{\partial y_i}\Big)\varepsilon^0_{pq}\mathrm{d}\boldsymbol{Y}. \tag{2.3}$$

Here $\boldsymbol{\chi}$ is the microscopic displacement field corresponding to the macroscopic applied strain $\boldsymbol{\varepsilon}^0$, and $\boldsymbol{v}$ is a virtual displacement in the space of kinematically admissible

displacement fields. The microscopic displacement field can be used to identify the locally varying strain ε_{pq},

$$\varepsilon_{pq}(\boldsymbol{\chi}) = \frac{1}{2}\Big(\frac{\partial \chi_p}{\partial y_q} + \frac{\partial \chi_p}{\partial y_q}\Big). \tag{2.4}$$

Using the locally varying strain the homogenized elasticity tensor can be derived as,

$$E^H_{ijkl} = \frac{1}{|\boldsymbol{Y}|}\int_{\boldsymbol{Y}} \left(E_{ijkl} - E_{ijpq}\frac{1}{2}\Big(\frac{\partial \chi^{kl}_p}{\partial y_q} + \frac{\partial \chi^{kl}_p}{\partial y_q}\Big)\right) \mathrm{d}\boldsymbol{Y}. \tag{2.5}$$

Here $\boldsymbol{\chi}^{kl}$ are the microscopic displacement fields corresponding to three unit-strains in 2D, and six unit-strains in 3D. Furthermore, $|\boldsymbol{Y}|$ indicates the volume occupied by the unit-cell. In different notation the effective properties can be calculated as,

$$E^H_{ijkl} = \frac{1}{|\boldsymbol{Y}|}\int_{\boldsymbol{Y}} E_{pqrs}\Big(\varepsilon^{0(ij)}_{pq} - \varepsilon^{ij}_{pq}\Big)\Big(\varepsilon^{0(kl)}_{rs} - \varepsilon^{kl}_{rs}\Big)\mathrm{d}\boldsymbol{Y}. \tag{2.6}$$

The effective properties E^H_{ijkl} can be used into Equations 2.1 to model the macroscopic responses in Ω by taking into account the composite material at a reasonable computational cost.

2.2.2 Optimal microstructures for compliance minimization

The homogenization equations can be used to determine bounds on the properties that can be achieved by using several material phases. This study is restricted to two-phase composites, where it has to be noted that void, *i.e.* the lack of material can also be seen as a material phase. In general, these two-phase composites consist of a better performing phase, which is more expensive, such that the goal is to find the optimal composite arrangement subject to an upper bound in volume of the best phase.

There is a vast amount of literature in which researchers try to find bounds on the properties that composite materials can achieve. Classical bounds by Reuss [1929] and Voigt [1966] have been used by Paul [1960] in the context of elasticity, these bounds later have been improved by Hashin and Shtrikman [1963]. The bounds were improved in a sense that the set of possible properties composite materials can exhibit is tightened. Similar to studies on finding the bounds, a large amount of works deal with finding composite materials that are able to achieve these bounds or parts of them. In other words, the goal is to find material descriptions that allows the composite to perform at the limit of what is possible. *E.g.* Sigmund [2000] contains an extensive study on isotropic microstructures achieving maximum bulk moduli bounds. Good starting points for the reader interested to know more about material bounds and composite materials that can reach these bounds are the books by Allaire [2002]; Cherkaev [2000]; Milton [2002] and reference therein.

Several research groups independently and more or less simultaneously realized that sequential laminates using a finite number of layers are a class of two-phase composites that can achieve the theoretical upper bounds for maximum strain

energy [Francfort and Murat, 1986; Lurie and Cherkaev, 1984; Milton, 1986; Norris, 1985]. These so-called rank-N laminates have the nice feature that the corresponding effective elastic properties can be derived analytically. Using this property the minimum number of layers N required for different classes of problems has been identified in subsequent studies [Avellaneda, 1987; Francfort et al., 1995]:

- Rank-2 laminates with orthogonal layers, for plane problems s.t. a single strain.
- Rank-3 laminates, for plane problems s.t. multiple strains.
- Rank-3 laminates with orthogonal layers, for problems in 3D s.t. a single strain.
- Rank-6 laminates for problems in 3D s.t. multiple strains.

A periodic laminate of rank-1 in the context of planar elasticity can be seen in its local frame of reference (y_1, y_2) in Figure 2.2 (a). The layered material with period $[0, 1] \times \mathbb{R}$ consists of two different orthotropic materials with elasticity tensors $\boldsymbol{E}^+$ and $\boldsymbol{E}^-$ representing the expensive/stiff (+) and compliant material (-). The orientation of the laminate in the global frame of reference (x_1, x_2) can be described by the layer normal $\boldsymbol{n}^1$ and layer tangent $\boldsymbol{t}^1$. Furthermore, the relative layer width of the stiff material is described by parameter $\mu_1 \in [0, 1]$, hence the layer width of the compliant material is $(1 - \mu_1)$.

In a similar fashion, a parameterization of a rank-2 laminate can be realized, where the compliant material is replaced by a rank-1 microstructure . Please note that the rank-1 laminate is periodic at an infinitely finer length-scale compared to the length-scale of the second rank, such that the properties of the rank-1 laminate can be assumed uniform on the length-scale of the second rank. This process can be repeated N times to create a rank-N laminate.

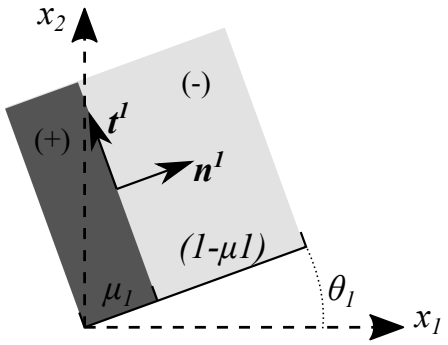

Figure 2.2: A rank-1 laminate, of which one period is shown, the stiff material (+) has width μ_1, while the compliant material (-) has width $(1 - \mu_1)$.

Using the homogenization equations and by assuming perfect bonding between the two materials one can directly derive the elasticity tensor $\boldsymbol{E}^{R1}$ of this rank-1 laminate. An excellent explanation of this process is given by Hassani and Hinton [1998a,b,c]. However, a different and probably more intuitive way to understand the derivation of the constitutive properties is to use the smear-out technique discussed by Olhoff et al. [1981], which is in detail described in [Bendsøe and Sigmund, 2004; Krog and Olhoff, 1997]. Below I will give a brief summary of the approach.

The homogenization equations described above can be used to describe a macroscopic stress field σ_{ij}^0 as,

$$\sigma_{ij}^0 = E_{ijkl}^H \varepsilon_{kl}^0 = \frac{1}{|\boldsymbol{Y}|} \int_{\boldsymbol{Y}} E_{ijkl} \left(\varepsilon_{kl}^0 - \varepsilon_{kl}(\chi) \right) \mathrm{d}\boldsymbol{Y}. \tag{2.7}$$

The locally varying elasticity tensor E_{ijkl} can be written as,

$$E_{ijkl} = \begin{cases} E_{ijkl}^+, & \text{in material (+)}, \\ E_{ijkl}^-, & \text{in material (-)}. \end{cases} \tag{2.8}$$

Furthermore, there is constant strain in each of the materials,

$$\left(\varepsilon_{kl}^0 - \varepsilon_{kl}(\chi) \right) = \begin{cases} \varepsilon_{ij}^+, & \text{in material (+)}, \\ \varepsilon_{ij}^-, & \text{in material (-)}. \end{cases} \tag{2.9}$$

Hence, ε_{ij}^+ and ε_{ij}^- are constant fields. Equations 2.8 and 2.9 can be combined to find the constant stress fields in each of the materials.

$$E_{ijkl} \left(\varepsilon_{kl}^0 - \varepsilon_{kl}(\chi) \right) = \begin{cases} \sigma_{ij}^+, & \text{in material (+)}, \\ \sigma_{ij}^-, & \text{in material (-)}. \end{cases} \tag{2.10}$$

A definition for the macroscopic strain ε_{ij}^0 can be obtained if Equation 2.9 is integrated over period $\boldsymbol{Y}$,

$$\varepsilon_{ij}^0 = \frac{1}{|\boldsymbol{Y}|} \int_{\boldsymbol{Y}} \left(\varepsilon_{kl}^0 - \varepsilon_{kl}(\chi) \right) \mathrm{d}\boldsymbol{Y} = \mu_1 \varepsilon_{ij}^+ + (1 - \mu_1) \varepsilon_{ij}^-. \tag{2.11}$$

Similarly, an expression for the macroscopic stress tensor σ_{ij}^0 can be obtained, if Equations 2.8-2.10 are combined,

$$\sigma_{ij}^0 = \frac{1}{|\boldsymbol{Y}|} \int_{\boldsymbol{Y}} E_{ijkl} \left(\varepsilon_{kl}^0 - \varepsilon_{kl}(\chi) \right) \mathrm{d}\boldsymbol{Y} = \mu_1 E_{ijkl}^+ \varepsilon_{kl}^+ + (1 - \mu_1) E_{ijkl}^- \varepsilon_{kl}^-. \tag{2.12}$$

Using Equations 2.7-2.11, and 2.12, it is possible to describe the homogenized elasticity tensor of a rank-1 laminate E_{ijkl}^{R1} in terms of local strains and known quantities,

$$(E_{ijkl}^+ - E_{ijkl}^{R1}) \mu_1 \varepsilon_{kl}^+ = (1 - \mu_1)(E_{ijkl}^{R1} - E_{ijkl}^-) \varepsilon_{kl}^-. \tag{2.13}$$

Hence, the goal is to find a description of ε_{ij}^+ and ε_{ij}^- to allow for an analytical description of E_{ijkl}^{R1}. To do so, we make use of the continuity conditions at the interface between material (-) and (+):

1. The normal component of the stress along the interface is continuous.
2. The shear components of the stress is continuous along the interface.
3. The tangential component of the strain has to be continuous along the interface.

These three conditions can be written as,

$$\begin{aligned} \sigma_{ij}^{+} n_i^1 n_j^1 = \sigma_{ij}^{-}(-n_i^1)(-n_j^1) \quad \text{or} \quad E_{ijkl}^{+}\varepsilon_{kl}^{+} n_i^1 n_j^1 = E_{ijkl}^{-}\varepsilon_{kl}^{-} n_i^1 n_j^1, \\ \sigma_{ij}^{+} n_i^1 t_j^1 = \sigma_{ij}^{-}(-n_i^1)(-t_j^1) \quad \text{or} \quad E_{ijkl}^{+}\varepsilon_{kl}^{+} n_i^1 t_j^1 = E_{ijkl}^{-}\varepsilon_{kl}^{-} n_i^1 t_j^1, \\ \varepsilon_{ij}^{+} t_i^1 t_j^1 = \varepsilon_{ij}^{-}(-t_i^1)(-t_j^1). \end{aligned} \tag{2.14}$$

Furthermore, the following description for the difference between ε_{ij}^{+} and ε_{ij}^{-} is used,

$$\varepsilon_{ij}^{+} - \varepsilon_{ij}^{-} = c_1 n_i^1 n_j^1 + \frac{c_2}{2}[n_i^1 t_j^1 + t_i^1 n_j^1] + c_3 t_i^1 t_j^1, \tag{2.15}$$

with c_i constants. These constants can be found by subsituting Equation 2.15 into the interface conditions and assuming that the strong material (+) is isotropic with Young's modulus E_0 and Poisson's ratio ν_0. Hence, after some manipulations one can write,

$$\varepsilon_{ij}^{+} = \varepsilon_{ij}^{-} - \frac{(1-\nu_0^2)}{E_0}\Lambda_{ijkl}^{1}(E_{klmn}^{+} - E_{klmn}^{-})\varepsilon_{mn}^{-}. \tag{2.16}$$

With,

$$\Lambda_{ijkl}^{1} = n_i^1 n_j^1 n_k^1 n_l^1 + \frac{t_i^1 n_j^1 t_k^1 n_l^1 + n_i^1 t_j^1 t_k^1 n_l^1 + t_i^1 n_j^1 n_k^1 t_l^1 + n_i^1 t_j^1 n_k^1 t_l^1}{2(1-\nu_0)}. \tag{2.17}$$

One can substitute Equation 2.16 into Equation 2.13 and after extensive but not necessarily difficult derivations the elasticity tensor of the rank-1 laminate can be obtained,

$$E_{ijkl}^{R1} = E_{ijkl}^{+} - (1-\mu_1)\Big((E_{ijkl}^{+} - E_{ijkl}^{-})^{-1} - \frac{\mu_1(1-\nu_0^2)}{E_0}\Lambda_{ijkl}^{1}\Big)^{-1}. \tag{2.18}$$

Similarly, one can derive the compliance tensor $\boldsymbol{C}^{R1}$ using this method, as well as the expressions in 3D. It has to be mentioned that if a rank-N laminate is considered, there exists an alternative method to write the properties without directly using relative layer widths μ_i. Instead a volume fraction ρ is used for material (+) and relative layer contributions p_n are used s.t. $\sum_{n=1}^{N} p_n = 1$. In this way the properties for a rank-N laminate can be described as,

$$E_{ijkl}^{RN} = E_{ijkl}^{+} - (1-\rho)\Big((E_{ijkl}^{+} - E_{ijkl}^{-})^{-1} - \frac{\rho(1-\nu_0^2)}{E_0}\sum_{n=1}^{N} p_n \Lambda_{ijkl}^{n}\Big)^{-1}. \tag{2.19}$$

Furthermore, in 2D the entire space of possible rank-N laminate properties for a fixed volume fraction can be uniquely described by using only 4 trigonometric moments [Avellaneda and Milton, 1988].

$$\begin{aligned} m_1 = \sum_{n=1}^{N} p_n \cos(2\theta_n), \quad m_2 = \sum_{n=1}^{N} p_n \sin(2\theta_n), \\ m_3 = \sum_{n=1}^{N} p_n \cos(4\theta_n), \quad m_4 = \sum_{n=1}^{N} p_n \sin(4\theta_n), \end{aligned} \tag{2.20}$$

where these four moments can be substituted in Equation 2.19. The feasible set of moments $\mathcal{M}$ is described using the result of Krein and Nudelman [1977].

$$\mathcal{M} = \boldsymbol{m} \in \mathbb{R}^4, \quad s.t. \begin{cases} m_1^2 + m_2^2 \leq 1, \\ -1 \leq m_3 \leq 1, \\ \frac{2m_1^2}{1+m_3} + \frac{2m_2^2}{1-m_3} + \frac{m_4^2}{1-m_3^2} - \frac{4m_1 m_2 m_4}{1-m_3^2} \leq 1. \end{cases} \tag{2.21}$$

The description in terms of moments has been used to prove many properties of rank-N laminates. Furthermore, Lipton [1994a] has introduced a method to link these moments to a rank-3 laminate description, finding relative layer contributions p_n and angles θ_n, which describe vectors $\boldsymbol{n}^n$ and $\boldsymbol{t}^n$. For 3D problems Díaz and Lipton [2000] showed that 15 moments are needed to describe the space of possible rank-6 laminates for a given volume fraction ρ.

Finally, it has to be mentioned that an important property of finite rank laminates is that for any set of applied strains and a fixed volume fraction ρ, the sum of strain energies is concave, w.r.t. the description of the elasticity tensor $\boldsymbol{E}^{RN}$. The proof is given by Lipton [1994b] and it has several important implications. Naturally, this property also implies that for a set of applied stresses the sum of complementary energies is convex w.r.t. compliance tensor $\boldsymbol{C}^H$. Furthermore, for a given microstructure density distribution in domain Ω it is possible to find the optimal composite design to achieve maximum stiffness.

2.2.3 Inverse homogenization for microstructural design

The theory of numerical homogenization, can also be turned around to find a microstructure with some desired effective properties. This process of designing a material with desired homogenized properties was introduced by Sigmund [1994] and is generally referred to as the inverse homogenization method. In the context of elasticity, this design method has led to materials with negative Poisson's ratio [Andreassen et al., 2014; Clausen et al., 2015b; Larsen et al., 1997; Sigmund, 1994], materials with maximum shear and bulk moduli [Sigmund, 1999, 2000], or materials with increased buckling strength [Neves et al., 2002; Thomsen et al., 2018].

Besides elasticity problems, Sigmund and Torquato [1996, 1997] considered thermal expansion problems, while Torquato et al. [2002] included thermal and electrical conductivity. Microstructures optimized for both bulk modulus and fluid permeability have been proposed by Guest and Prévost [2007]. Furthermore, topology optimization of photonic and phononic materials have been considered by Bonnecaze et al. [2003]; Jensen and Sigmund [2011]. It should be mentioned that a more detailed discussion of the field of material design using topology optimization for various types of physics is given in the recent review papers by Cadman et al. [2013]; Osanov and Guest [2016] and the Ph.D. thesis by Andreassen et al. [2015].

Finally, inverse homogenization is extensively used to design microstructures that maximize the stiffness with respect to a certain set of strains or stresses acting on it. As is discussed in Chapter 3 and in [P3] it is possible to approximate a rank-3 laminate by a single-scale design, to identify how much one loses in performance if one goes

from multi-scale to single-scale composites. The design of these microstructures with extremal stiffness is used extensively in multi-scale topology optimization methods. This is amongst others, is the topic of the next section.

2.3 Topology optimization using the relaxed space

Consider the total potential energy Π_{tot} in domain Ω, which depends on the internal Π_{int} and external Π_{ext} work. Note that Ω consists of composite materials and the effective properties $\boldsymbol{E}^H$ are known.

$$\Pi_{tot} = \Pi_{int} - \Pi_{ext} = \frac{1}{2}\int_\Omega \boldsymbol{\varepsilon}(\boldsymbol{u}) : \boldsymbol{E}^H : \boldsymbol{\varepsilon}(\boldsymbol{u})\mathrm{d}\Omega - \int_\Omega \boldsymbol{b}\cdot\boldsymbol{u}\mathrm{d}\Omega - \int_{\Gamma_n} \boldsymbol{t}_N\cdot\boldsymbol{u}\mathrm{d}\Gamma_n. \quad (2.22)$$

The corresponding stationary point that minimizes the total potential energy can be found by solving the following variational problem,

$$\int_\Omega \boldsymbol{\varepsilon}(\boldsymbol{u}) : \boldsymbol{E}^H : \boldsymbol{\varepsilon}(\boldsymbol{v})\mathrm{d}\Omega = \int_\Omega \boldsymbol{b}\cdot\boldsymbol{v}\mathrm{d}\Omega - \int_{\Gamma_n} \boldsymbol{t}_N\cdot\boldsymbol{v}\mathrm{d}\Gamma_n. \quad (2.23)$$

with $\boldsymbol{v}$ the test field. Both $\boldsymbol{u}$ and $\boldsymbol{v}$ are in the space of kinematically admissible displacement fields $\boldsymbol{U}$. The compliance of a structure is the applied external work Π_{ext}, which we want to minimize. Hence, the goal is to find a structure that maximizes the potential energy Π_{tot}, while equilibrium is satisfied in case of a single load. In case of n_F independent load-cases it possible to find objective $\mathcal{J}$, which is the sum of the weighted compliances for each load case, *i.e.*

$$\mathcal{J} = \sum_{k=1}^{n_F} w^k \Big(\int_\Omega \boldsymbol{b}^k\cdot\boldsymbol{u}^k\mathrm{d}\Omega + \int_{\Gamma_n} \boldsymbol{t}_N^k\cdot\boldsymbol{u}^k\mathrm{d}\Gamma_n\Big) = -2\sum_{k=1}^{n_F} w^k\Pi_{tot}^k. \quad (2.24)$$

Here w^k corresponds to the weighting factor of the k^{th} load case. It should be noted that different objectives than the weighted sum of compliances can be considered, *e.g* to minimize the largest compliance of the n_F load-cases [Krog and Olhoff, 1997]. Besides an equilibrium for each load case, an upper bound on the volume fraction of the expensive material phase (+) is posed, referred to as V_{max}.

$$\int_\Omega \rho\mathrm{d}\Omega \le V_{max}\int_\Omega \mathrm{d}\Omega. \quad (2.25)$$

A compliance minimization problem using the relaxed design space with multiple load cases can thus be written as,

$$\max_{\int_\Omega \rho\mathrm{d}\Omega\le V_{max}} \max_{\boldsymbol{E}^H(\rho)\in\boldsymbol{E}_{ad}} \min_{\boldsymbol{u}^k\in\boldsymbol{U}} \left\{ \sum_{k=1}^{n_F} w^k\Pi_{tot}^k \right\}, \quad (2.26)$$

where $\boldsymbol{E}_{ad}$ indicates the admissible set of elasticity tensors considered. This can for example be the set of rank-3 microstructures. For a plane problem $\boldsymbol{E}^H$ of a

rank-3 laminate can be described using three different parameterizations. First, one can use a density ρ and four trigonometric moments m_1, m_2, m_3, m_4, using these moments requires two point-wise inequality constraints to bound the feasible set of moments (see Equation 2.21). Second, the rank-3 laminate can be parameterized using a density ρ, relative layer contributions p_1, p_2, p_3 and layer orientations $\theta_1, \theta_2, \theta_3$. This requires a single point-wise equality constraint, since $\sum_{i=1}^{3} p_i = 1$. Finally, a rank-3 laminate can be parameterized using relative layer widths μ_1, μ_2, μ_3 and layer orientations $\theta_1, \theta_2, \theta_3$. In this way, ρ is a function of the relative layer widths. Hence, such a problem can be written as,

$$\max_{\substack{\boldsymbol{\mu},\boldsymbol{\theta} \\ \int_\Omega \rho(\boldsymbol{\mu})\mathrm{d}\Omega \leq V_{max}}} \min_{\boldsymbol{u}^k \in \boldsymbol{U}} \left\{ \sum_{k=1}^{n_F} w^k \Pi_{tot}^k \right\}. \tag{2.27}$$

There are many different ways to solve the optimization problems written in Equations 2.26 and 2.27. One can derive the optimality conditions and solve the problem as a large system using a Newton method, *e.g.* [Hoppe et al., 2006; Kočvara and Mohammed, 2016]. This is the so-called simultaneous analysis and design (SAND) approach. However, by far the most conventional approach is to solve Problem 2.26 in a sequence of separable convex approximations, see *e.g* [Fleury, 1993]. For a given design and applied load cases the equilibrium Equation 2.23 is solved, and subsequently using the fixed displacements field a convex sub-problem is created to update the parameters describing the elasticity tensor based on their gradients and possibly second-order derivatives. This process can then be repeated until convergence, and is called the nested analysis and design (NAND) approach. The most widely used method to update the design variables is the method of moving asymptotes (MMA) introduced by Svanberg [1987]. However, besides this first-order method, several other optimization algorithms can be used, see *e.g* the recent review paper by Rojas-Labanda and Stolpe [2015].

In this thesis and papers [P1],[P2] and [P4] I will consider the NAND approach, in combination with the MMA for the update of the design variables. Consider Equation 2.27, then for fixed displacement fields $\boldsymbol{u}^k$ the gradients of objective $\mathcal{J}$ can be derived with respect to the parameters describing the design. This is in general done by solving for adjoint states $\boldsymbol{\lambda^k}$; however, a compliance minimization problem has the nice property of being self-adjoint. Hence, $\boldsymbol{\lambda^k} = -\boldsymbol{u}^k$.

2.3.1 Hierarchical problem form

In some cases it can be beneficial to interchange the maximization w.r.t $\boldsymbol{E}^H$ and the minimization w.r.t. $\boldsymbol{u}$ in Equation 2.26. The reason for that is that maximization w.r.t $\boldsymbol{E}^H$ can be solved as a local problem. Solving it locally, would mean that one can parallelize these local subproblems, but also that the KKT-matrix used in the optimization step can be split up in smaller matrices. This is especially beneficial considering the large amount of point-wise constraints inherent to a rank-3 parameterization using trigonometric moments $\boldsymbol{m}$.

For a function ϕ depending on two parameters x, y we have the following classical result,

$$\max_x \min_y \phi(x,y) \leq \min_y \max_x \phi(x,y), \tag{2.28}$$

where the equality holds if ϕ is concave in x and convex in y. As is shown by Lipton [1994b] the strain energy density $\mathcal{E}$ for any set of applied strains is concave, w.r.t. the elasticity tensor of a rank-N laminate for a fixed composite density ρ. The strain energy density can be written as,

$$\mathcal{E} = \frac{1}{2}\sum_{k=1}^{n_F} w^k \Big(\int_\Omega \boldsymbol{\varepsilon}(\boldsymbol{u}^k) : \boldsymbol{E}^H : \boldsymbol{\varepsilon}(\boldsymbol{u}^k) \mathrm{d}\Omega = \sum_{k=1}^{n_F} w^k \Pi_{int}^k. \tag{2.29}$$

Using the concavity of the strain energy density, Lipton [1994b] showed that there exists a saddle point, which allows the interchange the min- and max-operators in Equation 2.26 without loss in optimality. Hence, Equation 2.26 can be rewritten as,

$$\max_{\substack{\rho \\ \int_\Omega \rho \mathrm{d}\Omega \leq V_{max}}} \min_{\boldsymbol{u}^k \in \boldsymbol{U}} \left\{ \max_{\boldsymbol{E}^H(\rho) \in \boldsymbol{E}_{ad}} \left\{ \mathcal{E}(\boldsymbol{\varepsilon}^k, \rho) \right\} - \sum_{k=1}^{n_F} w^k \Pi_{ext}^k \right\}. \tag{2.30}$$

Such a problem can be solved efficiently using a parameterization of a rank-3 laminate with four trigonometric moments and the following three-step algorithm for a design update in a NAND approach [Díaz et al., 1995]:

1. For a fixed design ρ, m_1, m_2, m_3, m_4 solve displacement fields $\boldsymbol{u}^k$.
2. For fixed ρ and $\boldsymbol{u}^k$ maximize the local strain energy density $\mathcal{E}$.
3. Update the density s.t. the global volume constraint based on the gradients.

The local problems to maximize the strain energy density can be solved for each point independently. This allows for a parallel computation of the update of moments $\boldsymbol{m}$.

In general, one can have a microstructure description which is not concave in strain energy, *e.g.* if microstructure design using an inverse homogenization method is considered. Nevertheless, a procedure using Equation 2.30 still makes sense. A hierarchical solution method as proposed by Rodrigues et al. [2002] is in general the only way to make the massive amount of computations manageable.

2.3.2 Relation to SIMP

The solid isotropic microstructure with penalty (SIMP) method is the best-known topology optimization method. Introduced by Bendsøe [1989] and in slightly modified form by Zhou and Rozvany [1991], the method assumes an isotropic elasticity tensor defined by a density variable $\rho \in [0,1]$, Poisson's ratio ν_0 and a Young's modulus E_0, which are the material properties of the fully solid isotropic material. The effective Young's modulus E^* can be interpolated for intermediate values of density ρ using,

$$E^*(\rho) = 10^{-9} E_0 + (1 - 10^{-9}) E_0 \rho^p. \tag{2.31}$$

Here the penalization parameter $p > 1$ makes it non-economical to have material with intermediate density. Hence, the density distribution converges towards binary values, meaning the design can easily be interpreted by an engineer. Please note that the interpolation introduced by Sigmund [2007] is considerer here, which allows the density to be exactly zero, while still having a small ($10^{-9}E_0$) stiffness, such that the displacement can be modeled on a fixed finite element mesh.

Although initially considered as an artificial material model, Bendsøe and Sigmund [1999] have shown that intermediate values of density can be considered to be isotropic microstructures. However, to not violate the Hashin-Shtrikman bounds [Hashin and Shtrikman, 1963] the penalization parameter p needs to be bounded from below, where this bound depends on ν_0 and the dimension of the design domain. Since the elasticity tensor $\boldsymbol{E}^H$ completely depends on the density distribution ρ, the minimization problem 2.26 using the SIMP method can be written as,

$$\max_{\substack{\rho \\ \int_\Omega \rho \mathrm{d}\Omega \leq V_{max}}} \min_{\boldsymbol{u}^k \in \boldsymbol{U}} \left\{ \sum_{k=1}^{n_F} w^k \Pi_{tot}^k \right\}. \tag{2.32}$$

Several codes are publicly available to perform compliance minimization using the SIMP method. Sigmund [2001] introduced a MATLAB program to do topology optimization in 2D, which was later improved for efficiency by Andreassen et al. [2010]. For topology optimization in 3D there is the MATLAB code by Liu and Tovar [2014], while Aage et al. [2014] introduced a code for efficient large scale topology optimization in the PETSc framework.

As a final note, it is known that setting $p = 1$ for 2D problems corresponds to the variable thickness sheet design problem as introduced by Rossow and Taylor [1973], where ρ can be interpreted as a thickness in the third dimension. A problem of this type ($p = 1$) is convex and existence of a solution is known (a detailed discussion is given in Bendsøe and Sigmund [2004]). Since this is not the case for a problem using $p > 1$, it is generally recommended to start the optimization iterations using $p = 1$ and then increase the value of p using a continuation approach (see *e.g.* [Sigmund et al., 2016]).

2.4 Literature review of multi-scale design methods

There is a vast amount of research on different methods to perform multi-scale topology optimization for compliance minimization problems. These methods can be broadly classified into two categories: 1) multi-scale methods using optimal microstructures, 2) multi-scale methods using single-scale microstructures optimized using inverse homogenization, possibly with severe restrictions on the microstructure shape.

2.4.1 Topology optimization using optimal multi-scale microstructures

After the landmark contribution on topology optimization by Bendsøe and Kikuchi [1988], Bendsøe [1989] was the first to consider the use of optimal rank-2 laminates for the solution of a topology optimization problem in 2D s.t a single load case. Similarly, this class of microstructures was considered by Allaire and Francfort [1993]; Allaire and Kohn [1993], where the dual problem of 2.26 is solved, which is in terms of stresses rather than displacements. By doing so, it was shown that the optimal complementary energy can be written only in terms of the stress tensor $\boldsymbol{\sigma}$, where the relative layer widths and orientations follow from $\boldsymbol{\sigma}$. A similar problem reduction for in terms of strain tensor $\boldsymbol{\varepsilon}$ is provided by Jog et al. [1994]; however, in this case the microstructure density ρ remains a design variable.

Besides single load case problems, multiple load case problems have been considered for 2D problems. This problem has been solved for both plane problems [Allaire et al., 1996; Cherkaev et al., 1998] and plate optimization problems [Díaz et al., 1995; Hammer et al., 1997; Krog and Olhoff, 1997]. In the case of plate problems, several parameterizations can be considered, *e.g.* a reinforced plate consisting of compliant core material.

A generalization to 3D structures has been made by Allaire et al. [1997]; Cherkaev and Palais [1996]; Díaz and Lipton [1997]; Olhoff et al. [1998] where orthogonal rank-3 laminates are considered, which are optimal for single load cases. Furthermore, Díaz and Lipton [2000] considered the 3D design problem with multiple independent load cases. To solve such a problem, they parameterized the rank-6 laminate using 15 trigonometric moments $\boldsymbol{m}$ and a local volume fraction ρ.

An important benefit of using optimal microstructures is that complex designs can be represented on a relatively coarse mesh. The reason is that a point-wise composite material description holds much more information than a point-wise material or void description, as is the case using the SIMP method. This allows for an overall efficient solution procedure. Hence, performing multi-scale topology optimization with optimal microstructures can give an engineer valuable insights about the optimal design (*e.g.* material use and layer directions) in a relatively short time. Furthermore, a lower bound on the compliance $\mathcal{J}$ can be found, which cannot be beaten by a single-scale design method.

Finally, it has to be mentioned that if one is purely interested in having an efficient reference objective value $\mathcal{J}$, there is the possibility to solve the optimization problem using a free material optimization (FMO) formulation. This method, introduced by Ringertz [1993] and Bendsoe et al. [1994], considers the symmetric positive definite elasticity tensor $\boldsymbol{E}^H$ itself as the design variable. A relation between a local density distribution can be made by considering either the trace norm or the Frobenius norm of $\boldsymbol{E}^H$. For an overview of FMO methods, as well as efficient interior-point algorithms to solve large-scale optimization problems, I refer the interested reader to the Ph.D. thesis of Weldeyesus et al. [2014] and references therein.

2.4.2 Topology optimization using single-scale microstructures

The seminal paper on topology optimization by Bendsøe and Kikuchi [1988] is the first work to consider multi-scale topology optimization with single-scale microstructures. The considered class of single-scale microstructures are square unit-cells, with a rectangular hole. The parameters describing elasticity tensor $\boldsymbol{E}^H$ are the height a_1 and width a_2 of the hole, as well as the unit-cell orientation θ. The corresponding unit-cell parameterization can be seen in Figure 2.3

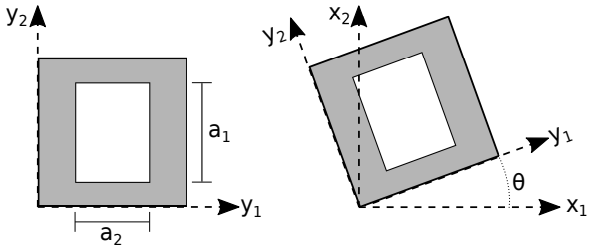

Figure 2.3: Layout of the unit-cell with a rectangular hole, in local (y_1,y_2), and global (x_1,x_2) coordinate system.

The 2D optimization problem s.t. a single load is solved in a very similar manner as when optimal rank-2 laminates are used. Furthermore, the designs using the square unit-cell with rectangular hole perform very close to optimal rank-2 designs.

A more general multi-scale optimization method using single-scale microstructures is the hierarchical optimization method introduced by Rodrigues et al. [2002]. Here the optimization from Equation 2.30 is considered, where the local problems are optimized using an inverse homogenization approach. Compared to the use of rank-N laminates, a very large number of design variables is involved. For a result in a relatively short time the method has to be parallelized [Coelho et al., 2011], which can easily be done since the local sub-problems are independent of each other. It should be mentioned that in the context of shape optimization the method has been extended by Barbarosie and Toader [2012], and for non-linear elasticity by Xia and Breitkopf [2017].

An often hear critique of the above-mentioned method is that the involved computational cost is very large, and that the microstructures are not connected. To reduce the computational cost, one can restrict the number of allowable microstructures [Sivapuram et al., 2016]; however, this does not say anything about connectivity. To circumvent this Liu et al. [2008] use only one type of microstructure. Hence, the macroscopic density distribution can either have the prescribed microstructure density or is void, while the microstructure is optimized to achieve the overall best performance. The use of graded structures, *e.g.* [Cramer et al., 2015; Wang et al., 2017] allows for slightly more freedom. In these approaches, there is a base geometry described by a level-set, which can be thresholded at several levels for varying density. Hence, this base shape ensures connectivity between the microstructures. However, it should be noted that none of these works using a restricted number of microstructures,

describe a comparison in performance with designs optimized using the unrestricted hierarchical approach by Rodrigues et al. [2002].

Besides using heavily restricted microstructures, one can also enforce continuity through constraints. Zhou and Li [2008b] proposed a method to connect different microstructures using an interface zone. Unfortunately, this connection method does not contain any information about the load transfer and therefore should be used with care. Another method to ensure well-connected microstructures, with less restriction is the sequential approach introduced by Schury et al. [2012]. Here the optimal density and elasticity distribution is first found using FMO. Afterwards, the microstructures are approximated on a single scale using inverse homogenization, while continuity is enforced.

Interestingly, all above-mentioned methods with restricted and or connected microstructures lack a full-scale analysis of the optimized shape. This raises the question if the connectivity between the microstructure is only cosmetic, or if it actually allows for efficient load transfer. The work by Zhang and Sun [2006] is one of the few, that does compare the difference in performance of a full-scale analysis with a homogenization-based analysis. More details on the scale effect of structures designed by the inverse homogenization method, and analysis on the full domain can be found in the work by Coelho et al. [2016].

Finally, it should be mentioned that Lazarov [2014] and Alexandersen and Lazarov [2015] employ the multi-scale finite element method (MsFEM) for the design of large scale high-resolution designs. There is no separation of scales assumed for the design description, instead the equilibrium equations are solved in a multi-scale manner. Furthermore, the design description can be specified as periodic, allowing for an even more efficient solution method. In this case, large scale well-connected periodic designs can be obtained with an excellent performance on the full scale. Nevertheless, the involved computational cost is still high compared to homogenization-based topology optimization using optimal microstructures.

2.4.3 Concluding remarks

Over the recent decades a variety of different methods have been proposed to do multi-scale topology optimization. A large part has focused on optimal or near-optimal microstructures; however, partially due to mature AM methods a great deal of attention has been given to methods to get well-connected designs as well.

For many of the latter approaches the performance is still modeled by assuming separation of scales. This raises the question on how well these designs actually perform, and if the connectivity is only ensured for visualization. Furthermore, there seems to be a lack of knowledge about the classical and well-established multi-scale optimization methods, since no comparisons are made on how much is lost in performance, compared to truly optimal microstructures.

In general, it is my opinion that explicitly enforcing single-scale microstructures optimized using inverse homogenization to be connected throughout domain Ω poses a too large restriction on the performance of the design. I believe that it is better to find a close to optimal microstructure description, which is globally smoothly varying such that it can be interpreted by geometrical means as is proposed by Pantz

and Trabelsi [2008]. Finding such a parameterization, which should be close to the optimal multi-scale microstructures will be discussed in more detail in Chapters 4 and 5.

3 Interpretations of optimal microstructures on a single scale

Although multi-scale microstructures can reach the optimal energy, there are no means to practically manufacture them. Therefore, it is important to identify the reduction in performance when optimal microstructures are interpreted on a single scale. Two-phase composites with an isotropic stiff phase defined by E_0 and ν_0 and a void phase are considered. The most classical case, compliance minimization of a plane stress problem with a single load case is considered first. For this type of problem there actually exists a class of single-scale microstructures, which can reach the optimal energy for certain loading conditions.

Furthermore, it is well-known that in the low volume fraction limit a multi-scale microstructure reduces to one on a single scale. This theory can be used for the design of truss lattice structures (TLS) in 3D. Here a simple and periodic class of lattice structures is considered, that remains close to the optimal energy bound for anisotropic loading situations. Furthermore, the difference between optimal closed-wall microstructures, *i.e.* plate lattice structures (PLS) and truss lattice structure will be shown.

This chapter is concluded by a discussion on optimal microstructures for plane stress problems, *i.e.* rank-3 laminates. The non-uniqueness of these laminates will be discussed, and I will discuss how these optimal microstructures can be interpreted on a single scale, with a relatively small loss in optimality.

3.1 Topology optimization in 2D using a single loading case

It is well-known that a rank-2 laminate with orthogonal layers can reach the optimal energy bound for a single load case. For a fixed microstructure volume fraction ρ, and a microstructure oriented along the principal stress directions, the relative layer widths μ_1 and μ_2 can be written in terms of, the principal stresses (σ_I and σ_{II}) [Allaire and Kohn, 1993]. Hence, the optimal energy, which can be reached by a rank-2 laminate can be written as a ratio of the principal stresses $\eta_\sigma = \sigma_I/\sigma_{II}$.

Interestingly, when this ratio is positive, *i.e.* when $\eta_\sigma \geq 0$, there exists a class of single-scale microstructures, the so-called Vigdergauz structures that can reach the optimal energy bound [Grabovsky and Kohn, 1995; Vigdergauz, 1994]. These microstructures have an inclusion that can be described by a geometrical relation. An example of such a Vigdergauz microstructure obtained inverse homogenization for $\rho = 0.5$, $E_0 = 1$, $\nu_0 = 1/3$, and $\eta_\sigma = 0.25$ can be seen in Figure 3.1(a), while an optimized structure for $\eta_\sigma = 0.5$ is shown in Figure 3.1(b). Unfortunately, as discussed by Allaire and Aubry [1999], there is no single-scale microstructure that can achieve the optimal energy for $\eta_\sigma < 0$.

A comparison between the energy that can be obtained for different optimally oriented microstructures using $\rho = 0.5$ and different values of η_σ can be seen in Figure 3.2 [Bendsøe and Sigmund, 1999]. For $\eta_\sigma \geq 0$ the rank-2 and Vigdergauz

(a) $\eta_\sigma = 0.25$. (b) $\eta_\sigma = 0.5$.

Figure 3.1: Vigdergauz microstructures, obtained using inverse homogenization for two different principal stress ratios, with $\rho = 0.5$ and $\nu_0 = 1/3$.

microstructures reach the same optimal energy. For $\eta_\sigma < 0$ it can be seen that the obtained energy using Vigdergauz microstructures is very close to the energy that can be obtained using the sub-optimal square unit-cells with a rectangular hole, introduced by Bendsøe and Kikuchi [1988].

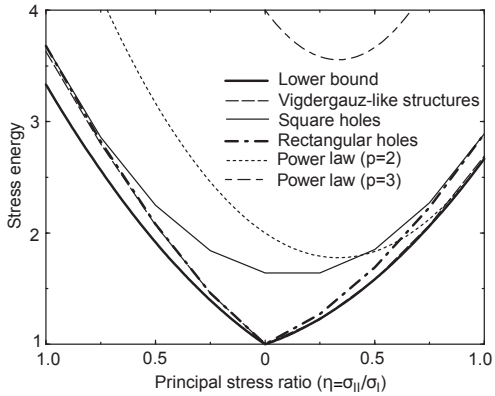

Figure 3.2: Comparison of complementary energies as a function of principal stress ratio for $\rho = 0.5$ and various microstructures, picture from [Bendsøe and Sigmund, 1999] included with permission from Ole Sigmund.

To identify the performance loss of using single-scale microstructures, consider the cantilever beam example shown in Figure 3.3(a), which is optimized using both rank-2 laminates and the square unit-cell with a rectangular hole. The compliance minimization problem is solved in a nested analysis and design approach. The domain is discretized in $n_x \times n_y$ bi-linear finite elements, which each have a unique microstructure, *e.g.* for a rank-2 laminate described by θ_e, $\mu_{e,1}$ and $\mu_{e,2}$ for element e. As shown by Pedersen [1989, 1990], the optimal orientation of an orthotropic composite coincides with the principal stress directions. Hence, the design vector containing the unit-cell orientations $\boldsymbol{\theta}$ is updated in each minimization step, using the displacement and corresponding stress calculation. Subsequently, design vectors

$\boldsymbol{\mu}_1$ and $\boldsymbol{\mu}_2$ are updated based on their gradients using the updated microstructure orientation. The discretized optimization problem can thus be written as,

$$\begin{aligned} \min_{\boldsymbol{\mu}_1,\boldsymbol{\mu}_2,\boldsymbol{\theta}} &: \mathcal{J}(\boldsymbol{\mu}_1,\boldsymbol{\mu}_2,\boldsymbol{\theta},\mathbf{U}), \\ \text{s.t.} &: \mathbf{K}(\boldsymbol{\mu}_1,\boldsymbol{\mu}_2,\boldsymbol{\theta})\mathbf{U} = \mathbf{F}, \\ &: \mathbf{v}^T\boldsymbol{\rho}(\boldsymbol{\mu}_1,\boldsymbol{\mu}_2) - V_{max}A \leq 0, \\ &: \mathbf{0} \leq \boldsymbol{\mu}_1,\boldsymbol{\mu}_2 \leq \mathbf{1}. \end{aligned} \tag{3.1}$$

where $\mathbf{v}$ is the vector containing the element volumes, V_{max} is the maximum allowed fraction of the material in Ω, with A is the area of Ω. Stiffness matrix $\mathbf{K}$ is a function of $\boldsymbol{\mu}_1$,$\boldsymbol{\mu}_2$ and $\boldsymbol{\theta}$. $\mathbf{F}$ describes the loads acting on the domain, and $\mathbf{U}$ describes the solution of the equilibrium equation. For the design update of $\boldsymbol{\mu}_1$,$\boldsymbol{\mu}_2$ the MATLAB implementation of the Method of Moving Asymptotes (MMA) introduced by Svanberg [1987] is used.

Two issues remain. First, it has been shown by Díaz and Sigmund [1995] that a checkerboard-like pattern analyzed using bi-linear finite elements possesses higher stiffness than an optimal rank-2 laminate with same average density. To avoid these artificially stiff patterns, a classical density filter [Bourdin, 2001; Bruns and Tortorelli, 2001] with a radius R slightly larger than element length h is used, *i.e.* $R = 1.5\ h$. The second issue is that the compliance tensor for a rank-2 laminate using a stiff material and void is singular. Many different methods have been suggested to overcome this issue, see *e.g.* [Allaire, 2002]. In this numerical example, an isotropic weak material using $E_{min} = 10^{-4}E_0$ is simply added to the effective properties.

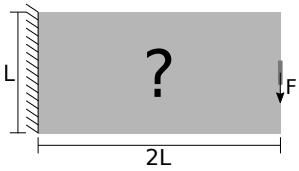

(a) Design domain and BC's.

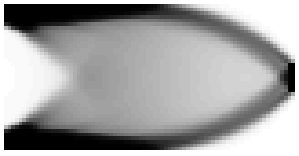

(b) Rank-2, 80×40 elements.

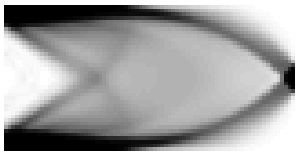

(c) Rectangular hole, 80×40 elements.

(d) sign$\{\eta_\sigma\}$ for (c).

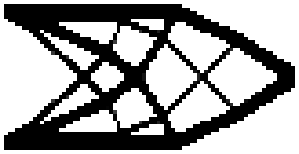

(e) SIMP, 80×40 elements.

(f) SIMP, 200×100 elements.

Figure 3.3: The Michell cantilever, optimized using different microstructure representations for different mesh sizes, with $V_{max} = 0.4$, $E_0 = 1$, and $\nu_0 = 0.3$.

The resulting compliance values $\mathcal{J}$ for the rank-2 design and for the microstructure with the rectangular hole can be seen in Table 3.1. The corresponding optimized density distributions using a discretization of 80×40 elements are shown in Figures 3.3(b)

and (c). The difference in compliance between the single-scale and multi-scale microstructure is small. Furthermore, the increase in performance using Vigdergauz microstructures instead of the unit-cell with rectangular hole would be negligible, since η_σ is negative in almost the entire domain, as can be seen in Figure 3.3(d). Here the blue color indicates $\eta_\sigma < 0$, while yellow means $\eta_\sigma \geq 0$. Please note that the yellow regions close to the Dirichlet boundary correspond to regions where one layer direction vanishes, *i.e.* $\eta_\sigma = 0$.

Table 3.1: Compliance values $\mathcal{J}$ for the Michell cantilever, optimized using different discretizations and microstructures, for $V_{max} = 0.4$, $E_0 = 1$ and $\nu_0 = 0.3$.

Microstructure	40×20	80×40	120×60	160×80	200×100
Rank-2	69.28	69.21	69.48	69.78	70.13
Rectangular hole	71.92	71.00	70.67	70.69	71.04
SIMP	79.86	75.72	73.66	73.06	72.58

Finally, the homogenization-based designs are compared with standard density-based designs. To do so, the SIMP methods is used with a continuation scheme that starts with penalization factor $p = 1$, every 50 iterations p increases by 0.25 until $p = 4$, in the final iterations no filtering is applied to ensure convergence to binary values. Two different designs are shown in Figure 3.3(e) and (f), while the compliance values for different mesh sizes are shown in Table 3.1. It can be seen that, as expected, the compliance values are improved when more design freedom is allowed. Nevertheless, the homogenization-based designs perform better, especially for coarse design descriptions. A method to interpret these coarse-scale designs on a very fine scale is presented in [P1] and Chapter 4.

3.2 Optimal microstructures in the low density limit

In the previous section, the result of Allaire and Aubry [1999] was discussed, which states that some extremal elasticity tensors $\boldsymbol{E}^H$ are only realizable by multi-scale composites, *i.e.* laminates of rank more than one. This statement can actually be relaxed in the low density limit. As is shown by Bourdin and Kohn [2008] a rank-N laminate can be approximated by summing the contributions of individual rank-1 laminates. Hence, for the compliance tensor of a rank-3 laminate described using relative layer widths $\boldsymbol{\mu}$ and layer orientations $\boldsymbol{\theta}$ we have the following relation,

$$\boldsymbol{E}^{R3}(\mu_1, \mu_2, \mu_3, \theta_1, \theta_2, \theta_3) \approx \sum_{i=1}^{3} \boldsymbol{E}^{R1}(\mu_i, \theta_i) - \mathcal{O}(\rho^2). \tag{3.2}$$

Here the error is thus in the order of the microstructure volume fraction ρ squared, if $\rho \to 0$ the error thus becomes negligible. Furthermore, in the low density limit,

$$\rho = \sum_{i=1}^{N} \mu_i. \tag{3.3}$$

3.2.1 The Michell-problem in the low density limit

Actually, it was shown by Allaire and Kohn [1993] and Bendsøe and Haber [1993] that a single load case problem in 2D using rank-2 laminates in the low-density limit corresponds to the lay-out theory of Michell trusses Michell [1904]. This is a continuum description of two orthogonal fields of tension/compression, with members that are directed along the principal stress/strain, and no interaction between these two members. Hence the corresponding elasticity tensor can be written in Voigt notation as,

$$\boldsymbol{E}^H = \boldsymbol{R}^T(\theta) \begin{bmatrix} E_0\mu_1 & 0 & 0 \\ 0 & E_0\mu_2 & 0 \\ 0 & 0 & 0 \end{bmatrix} \boldsymbol{R}(\theta), \tag{3.4}$$

where relative widths μ_1 and μ_2 are scaling parameters proportional to the size of the principal stresses/strains and θ describes the orientation of the principal directions. To circumvent a singular elasticity tensor, a background isotropic stiffness tensor is added, with a Young's modulus E_{min}, several orders of magnitude lower than E_0. The topology optimization problem is almost identical to Equation 3.1; however, there is no upper bound on layer widths μ_1 and μ_2, and the volume constraint can be seen as a scaling parameter.

More details on solving this type of topology optimization problems can be found in [P2]. Furthermore, a similar approach using truss-like continua has been applied for the case of multiple loads by Zhou and Li [2008a, 2010].

3.2.2 Finding optimal lattice structures in the low density limit

The approach of Bourdin and Kohn [2008] can be applied to represent rank-N laminates on a single scale. In 2D, this corresponds to truss lattice structures (TLS), and in 3D to plate lattice structures (PLS). In a similar fashion, truss lattice structures can be assembled in 3D. The elasticity tensor $\boldsymbol{E}^T$ of a TLS using n_t number of trusses can be defined as,

$$\boldsymbol{E}^T = \sum_{i=1}^{n_t} \mu_i \boldsymbol{R}^T(\boldsymbol{n}^i)\boldsymbol{E}^0\boldsymbol{R}(\boldsymbol{n}^i). \tag{3.5}$$

With $\boldsymbol{E}^0$ is the elasticity of a single truss member with unit-area in its own frame of reference, *i.e.* $E^0_{1111} = E_0$, while all other terms in $\boldsymbol{E}^0$ are zero. Furthermore, $\boldsymbol{R}$ is the classical rotation matrix which depends on $\boldsymbol{n}^i$, the pointing direction of bar i.

The above lattice description has been used by Christensen and Waals [1972] to determine the analytical properties of an isotropic TLS. By integrating over the entire space of possible orientations and assuming equal thickness μ for each member, they derived the effective Young's modulus E^*_T and Poisson's ratio ν^*_T of an isotropic TLS.

$$E^*_T = \frac{\rho}{6}E_0, \quad \nu^*_T = \frac{1}{4}. \tag{3.6}$$

Much more recently, Gurtner and Durand [2014]; Latture et al. [2018]; Messner [2016] found simple periodic isotropic TLS parameterizations.

In [P5] we were interested in finding TLS with maximum strain energy beyond isotropy. To this end, the space of possible lattice orientations can be discretized using a large number of equispaced members. Subsequently, the corresponding areas can be optimized, as proposed by Bourdin and Kohn [2008]. However, the number of possible lattice members needs to be very large in 3D, *e.g.* ($> 10^4$) to get close to a true optimal energy. A much more simple approach is to discretize a low number of truss members *e.g.* (6-10), using pointing direction $\boldsymbol{n}^i$ and member area μ_i per truss i as design variable. This discretization can be used to find the minimum complementary energy $\mathcal{C}^T$ for n_σ stress cases,

$$\begin{aligned} \min_{\boldsymbol{n},\boldsymbol{\mu}} : \mathcal{C}^T &= \sum_{k=1}^{n_\sigma} \frac{1}{n_\sigma} \boldsymbol{\sigma}^k : \Big(\sum_{i=1}^{n_t} \mu_i \boldsymbol{R}^T(\boldsymbol{n}^i) \boldsymbol{E}^0 \boldsymbol{R}(\boldsymbol{n}^i) \Big)^{-1} : \boldsymbol{\sigma}^k - \gamma_\mu \|\boldsymbol{\mu}\|, \\ \text{s.t.} : & \sum_{i=1}^{n_t} \mu_i \leq \bar{\rho}, \\ & : \mathbf{0} \leq \boldsymbol{\mu} \leq \bar{\boldsymbol{\rho}}. \end{aligned} \tag{3.7}$$

Here, $\bar{\rho}$ is a volume constraint. The regularization term $\gamma_\mu \|\boldsymbol{\mu}\|$ penalizes truss members with the same orientation, with $\gamma_\mu \geq 0$ the regularization factor and $\|\cdot\|$ the Euclidean norm. This approach is tested for a large number of different stress cases, *i.e.* we considered n_σ ranging from 2 to 7, where for each value n_σ 500 loading conditions have been randomly generated. More details on how these random stresses are created can be found in [P5].

Interestingly, the optimization method using Equation 3.7 outperforms the method of Bourdin and Kohn [2008] both in computational cost and performance. The performance difference is due to the fact that tiny changes in truss orientation can have a significant effect on the energy. The fact that the method continuously outperforms the convex optimization method by Bourdin and Kohn [2008], means that the obtained complementary energy can be considered as an optimal reference bound for practical comparison purposes. Furthermore, it has to be mentioned that using the developed reference approach an isotropic TLS with only 6 periodic members has been found. Unfortunately however, the TLS itself cannot be constructed as a stable lattice since the members cannot be connected.

3.2.3 Periodic lattice structures

Besides an optimal lattice description, we are looking for one which can be periodically tessellated in space. To do so, inspiration can be drawn from the field of geometry and crystallography, *e.g.* by looking at the well-known Bravais lattice structures and possible combinations of them Zok et al. [2016]. In [P5] we consider the parallelepiped 13 bar TLS, shown in Figure 3.4(b), which is composed of 3 periodic edge bars, 6 periodic face bars and 4 periodic body bars.

The orientation of all bars in this periodic TLS can be described by 6 Euler angles $\boldsymbol{\theta}$ (describing the orientation of the 3 periodic edge bars), and two length variables $\boldsymbol{s}$ describing the lengths of two of the edge bars, the third one is always kept at unit-length. Using these 8 variables, the orientation of all face and body bars can be

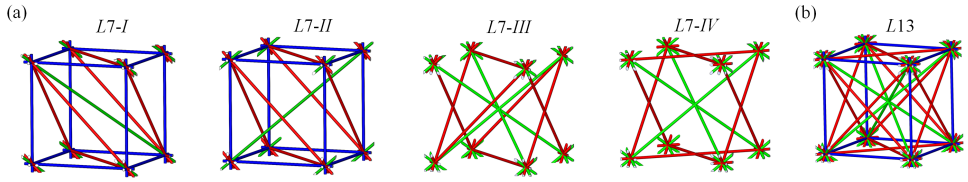

Figure 3.4: Proposed truss lattice structures (TLS) in cubic cells, including (a) four TLS with 7 periodic sets of members, and (b) a TLS with 13 periodic sets of bars. Blue, red and green bars indicate edge, face and body bars respectively.

described. Furthermore, a member area variable is required for each unique periodic member, which means a total of 21 variables is required to parameterize the 13 bar TLS.

The most important result of [P5] is that 4 different 7 bar TLS can be identified, which are all subsets of the 13 bar TLS; however, independent of each other as is shown in Figure 3.4(a). The first two TLS, $L7-I$ and $L7-II$ exhibit rigid behavior in most directions, while $L7-III$ and $L7-IV$ are able to behave rigidly in certain directions and compliant in the other. We proposed that for any type of anisotropic loading, one of these four simple 7 bar lattice structures will perform very close to the optimal energy bound, allowing an engineer to use this simple periodic microstructure in a design.

To test this hypothesis, the 5 periodic structures of Figure 3.4 are all optimized for the 3000 random load cases, using optimization Problem 3.7. For each load case we find the best performing 7-bar TLS with lowest complementary energy $\mathcal{C}^7$, which is compare to the postulated bound $\mathcal{C}^T$ using a non-periodic microstructure description to obtain relative difference d^7,

$$d^7 = \frac{\mathcal{C}^7 - \mathcal{C}^T}{\mathcal{C}^T}. \tag{3.8}$$

A similar difference can be found for the 13-bar TLS. For each number of stresses n_σ, the maximum relative differences (*i.e.* worst performance) out of the 500 possibilities are shown in Table 3.2.

Table 3.2: Maximum relative difference among 500 random loading situations in each group of n_σ stress cases.

n_σ	2	3	4	5	6	7
$\max\{d^7\}$	2.51E-06	3.99E-07	1.09E-03	6.7E-04	2.34E-14	2.54E-14
$\max\{d^{13}\}$	1.82E-06	4.80E-07	1.09E-03	6.71E-04	3.45E-14	5.04E-14

From these experiments very important conclusions can be drawn. First, the difference between the best 7 bar TLS and the 13 bar TLS is negligible. Second, the largest error difference occurs when 4 or 5 stresses are considered. The reason is that in this case the optimal elasticity tensor has one eigenvalue close to zero, when one

applies eigen decomposition of this tensor. The optimizer struggles to reach such a solution. A third conclusion is that for the lower number of stresses $n_\sigma \leq 5$ the elasticity tensor in general exhibits one or more zero eigenvalues, *e.g.* a single bar has only one non-zero eigenvalue.

When there is one eigenvalues close to zero, the best lattice design is either obtained using $L7-III$ or $L7-IV$, which can behave compliant in certain directions. When more stresses are applied, the best designs are either from the $L7-I$ or the $L7-II$ parameterization. In this case, the error with the optimal solutions is negligible. However, even the worst energy difference is only 0.1% from the postulated energy bound. Such a deviation is completely acceptable for engineering practice, hence the class of proposed 7 bar TLS is not only simple and manufacturable, but also highly optimal.

3.2.4 The difference between plate and truss lattice structures

It is well-known that plate lattice structures (PLS) are more optimal than TLS. Using a similar method as for the TLS, Christensen [1986] found that effective Young's modulus E_P^* and Poisson's ratio ν_P^* of an isotropic PLS.

$$E_P^* = \frac{2\rho E(7-5\nu_0)}{3(1-\nu_0)(9+5\nu_0)}, \quad \nu_P^* = \frac{1+5\nu_0}{9+5\nu_0}. \tag{3.9}$$

Hence, for an isotropic microstructure PLS with a material Poisson's ratio of $\nu_0 = 1/3$, the effective stiffness energy ratio between a PLS and TLS becomes $R = \mathcal{C}^T/\mathcal{C}^P = 3$. This ratio can also be found for the anisotropic loading conditions, discussed before. To do so, the TLS model with the postulated optimal energy bound (Equation 3.7) is compared with the energy obtained using a rank-6 parameterization in the low volume fraction limit. The comparison is done for all tested random stress situations, and ratio R is plotted against measure of anisotropy M. Where,

$$M = \frac{|\boldsymbol{e}|}{\|\boldsymbol{e}\|} - 1, \tag{3.10}$$

with $\boldsymbol{e}$ the eigenvalue vector of the elasticity tensor of the optimized TLS. Hence, for a single bar we have only one non-zero eigenvalue and $M = 0$. Furthermore, it can be shown that for an isotropic TLS $M = 1$. The corresponding $M - R$ chart is shown in Figure 3.5.

It can be seen that R is bounded between $R = 1$ for a single uni-axial stress and $R = 3$ for pure isotropy. Hence, for anisotropic loading conditions the stiffness inferiority of TLS compared to PLS is not more than a factor of 3. Furthermore, it can be seen that increasing the number of random stresses results in a more isotropic design. It can also be shown that there exists an explicit relation for the bounds on stiffness inferiority for a single random stress tensor, these are indicated by the gray areas shown in the Figure. For more details, the reader is referred to [P5].

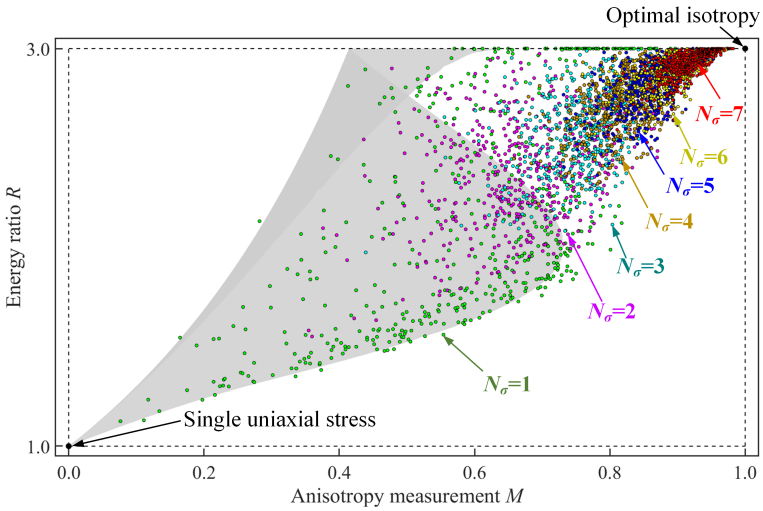

Figure 3.5: Energy ratios between optimal TLS and PLS, the gray region indicates the bounds for single stress cases with 3 orthogonal bar or plate sets, the colored dots indicate various groups of stress case numbers.

3.3 Simple microstructures based on optimal rank-3 laminates

As is discussed before, the extremal properties of rank-N microstructures using a finite volume fraction cannot be achieved on a single length-scale. To identify this optimality gap, Guedes et al. [2003] compared the performance of single-scale microstructures, optimized using inverse homogenization, with the energy bounds for optimal rank-3 laminates. In [P3] we went one step further, to find out if it possible to exploit information of the optimal rank-3 laminates, for the design of single-scale microstructures. However, to begin the non-uniqueness of optimal rank-3 laminates will be discussed.

3.3.1 On the non-uniqueness of rank-3 laminates

The goal is to minimize the complementary energy $\mathcal{C}$ on a periodic microstructure subjected to n_σ stress cases,

$$\mathcal{C} = \frac{1}{2}\sum_{j=1}^{n_\sigma} w_j \boldsymbol{\sigma}^j : \boldsymbol{C}^{RN} : \boldsymbol{\sigma}^j \tag{3.11}$$

With w_j the relative weighting of the j-th stress, such that $\sum_{j=1}^{n_\sigma} w_j = 1$. As is discussed in Section 2.2.2, different methods exist to parameterize a rank-N laminate for a fixed volume fraction ρ of the stiff material. $E.g.$ similar to Equation 2.19, we

can write the compliance tensor $\boldsymbol{C}^{RN}$ as,

$$C_{ijkl}^{RN} = C_{ijkl}^{+} - (1-\rho)\Big((C_{ijkl}^{+} - C_{ijkl}^{-})^{-1} - \rho E_0 \sum_{n=1}^{N} p_n t_i^n t_j^n t_k^n t_l^n\Big)^{-1}. \tag{3.12}$$

Where $\boldsymbol{t}^n$ corresponds to the vector tangent to layer n. Furthermore, $\boldsymbol{C}^{RN}$ can be written in terms of the 4 trigonometric moments $\boldsymbol{m}$. The benefit of such an approach is that the optimal energy is uniquely defined by these moments. However, the two constraints on the set of feasible moments $\mathcal{M}$ (Equation 2.21) have to be added to the minimization problem.

Consider the four stresses applied to a periodic unit-cell, which are weighted using parameter $\chi \in [0,1]$ as proposed by Guedes et al. [2003]. The four cases, with their respective weights are shown in Figure 3.6, and can be written out as,

$$\begin{aligned} w_1\sigma_1 &= \frac{\chi}{2}\begin{bmatrix}-1 & 0\\ 0 & 1\end{bmatrix}, & w_2\sigma_2 &= \frac{\chi}{2}\begin{bmatrix}0 & 1\\ 1 & 0\end{bmatrix}, \\ w_3\sigma_3 &= \frac{1-\chi}{2}\begin{bmatrix}1 & 0\\ 0 & 0\end{bmatrix}, & w_4\sigma_4 &= \frac{1-\chi}{2}\begin{bmatrix}0 & 0\\ 0 & 1\end{bmatrix}. \end{aligned} \tag{3.13}$$

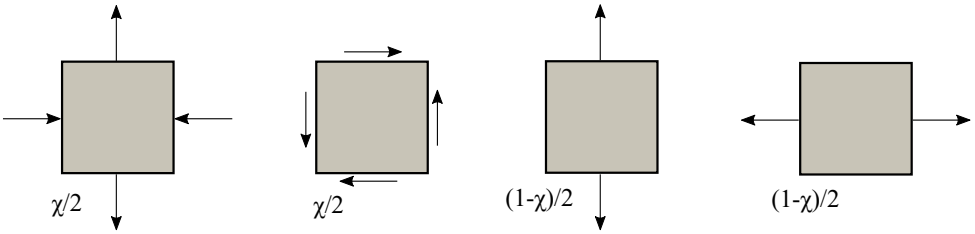

Figure 3.6: Illustration of the four stress cases and their respective weights.

For given $\rho = 0.5$ and $\chi = 0.7$, the optimal complementary energy $\mathcal{C}$ and compliance tensor $\boldsymbol{C}^{RN}$ can be obtained in terms of moments. Subsequently, the method by Lipton [1994a], can be used to obtain a rank-3 parameterization in terms of p_n and θ_n based on the set of optimal moments. A detailed description on the implementation of this method is given in the Appendix of [P3]. Using this method at least 4 non-unique rank-3 parameterizations can be retrieved. To indicate this non-uniqueness, the 4 parameterizations are represented in Figures 3.7(a)-(d). It can be observed that the layer orientations for each of the 4 rank-3 parameterizations are different; furthermore, the hierarchy of the rank-3 laminate is indicated using different layer spacings.

If the parameterization of $\boldsymbol{C}^{RN}$ from Equation 3.12 is used, another optimal rank-3 parameterization can be obtained as is shown in Figure 3.7(e). Here optimal means that the difference in $\mathcal{C}$ with a moment parameterization is negligible *i.e.* 10^{-12}.

To find out how many non-unique rank-3 laminate parameterizations exist, an extra constraint is added to the optimization problem using the compliance tensor

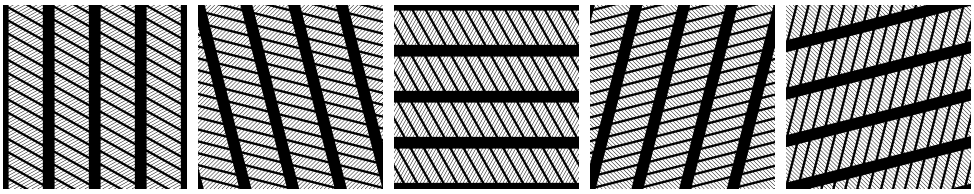

(a) From $\boldsymbol{m}$ (1). (b) From $\boldsymbol{m}$ (2). (c) From $\boldsymbol{m}$ (3). (d) From $\boldsymbol{m}$ (4). (e) From $\boldsymbol{\theta}$ and $\boldsymbol{p}$.

Figure 3.7: Visualizations of optimal rank-3 laminates with indicated hierarchy, optimized for the 4 stress cases using $\rho = 0.5$ and $\chi = 0.7$, a parameterization in moments $\boldsymbol{m}$ and using Equation 3.12 is used.

description form Equation 3.12. This constraint restricts the first layer orientation θ_1 to be a constant value c_θ. Using a large number of numerical tests, it can be shown that for any constant $c_\theta \in [0, \pi]$ the same optimal complementary energy $\mathcal{C}$ and compliance tensor $\boldsymbol{C}^{RN}$ can be retrieved. Hence, there exist an infinite number of rank-3 laminates that reach optimal energy for $\rho = 0.5$ and $\chi = 0.7$. A large number of numerical tests have been performed for other values of ρ and χ. For all cases it was found that restricting θ_1 to be constant did not affect the optimality of the solution.

It has to be noted that more challenging loading conditions might exist, for which only a finite number of optimal layer directions can be used. Nevertheless, the above result indicates that if one optimizes a rank-3 laminate for ultimate stiffness, it might be possible to optimize for something extra, besides finding the optimal energy.

3.3.2 An approximation of rank-3 laminates on a single scale

As proposed in [P3] it is possible to approximate a rank-3 laminate as a single scale periodic microstructure. To do so, assume that all layer spacings $\lambda_1, \lambda_2, \lambda_3$ have a similar order of magnitude, subsequently these spacings can be adapted to describe the unit-cell as a periodic parallelogram as indicated in Figure 3.8.

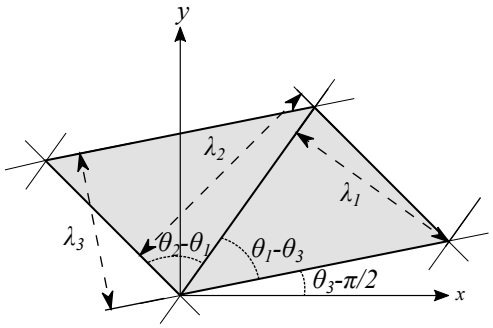

Figure 3.8: Parallelogram used as unit-cell and corresponding dimensions.

Since the layer spacings are relative to each other, it is possible to set $\lambda_3 = \epsilon$, with ϵ indicating the microscopic length-scale, and calculate the other two spacings using standard geometric relations.

$$\begin{aligned}\lambda_1 &= \left|\sin(\theta_1 - \theta_3)\right| \left| \frac{\epsilon}{\tan(\theta_2 - \theta_3)} - \frac{\epsilon}{\tan(\theta_1 - \theta_3)} \right|, \\ \lambda_2 &= \left|\sin(\theta_2 - \theta_3)\right| \left| \frac{\epsilon}{\tan(\theta_2 - \theta_3)} - \frac{\epsilon}{\tan(\theta_1 - \theta_3)} \right|.\end{aligned} \tag{3.14}$$

In case the optimal laminate is only a rank-2 laminate, the corresponding layer spacings are set equal. The area $|\boldsymbol{Y}|$ of the parallelogram is described as,

$$|\boldsymbol{Y}| = \left| \frac{\epsilon^2}{\tan(\theta_2 - \theta_3)} - \frac{\epsilon^2}{\tan(\theta_1 - \theta_3)} \right|. \tag{3.15}$$

The layer widths can be approximated on the single scale using the relative contribution of each layer, *i.e.* p_n for $n = 1, 2, 3$. The width of each layer used on the single scale w_n, is then obtained as,

$$w_n = \psi p_n, \quad n = 1, 2, 3. \tag{3.16}$$

Here ψ is a scaling parameter found using a bi-section algorithm, such that the projected microstructure has the same volume fraction ρ as the stiff material in the rank-3 laminate.

With the layer widths and relative spacings known, it is possible to describe the periodic microstructure as an implicit geometry description $\tilde{\rho}$. Each of the periodic layers i can be described by a periodic function $\tilde{\rho}_i$,

$$\tilde{\rho}_i(\boldsymbol{x}) = H\left((\frac{1}{2} + \frac{1}{2}\mathcal{S}\left\{ \frac{2\pi(\boldsymbol{n}^i \cdot \boldsymbol{x})}{\lambda_i} \right\}) - w_i(\boldsymbol{x}) \right). \tag{3.17}$$

Here $\mathcal{S} \in [-1, 1]$ corresponds to the `sawtooth` function in MATLAB, which is used in [P4] rather than in [P1] and [P3] . Furthermore H is the Heaviside function making sure that the exact layer width is obtained. The microstructure description $\tilde{\rho}$ can be recovered as,

$$\tilde{\rho}(\boldsymbol{x}) = \min\left\{ 1, \sum_{i=1}^{3} \tilde{\rho}_i(\boldsymbol{x}) \right\}. \tag{3.18}$$

Figure 3.9 shows an example of a single-scale microstructure, approximated as a parallelogram shape.

3.3.3 Inverse homogenization for ultimate stiffness

The effective properties of a rank-3 laminate approximated on a single scale, hereafter referred to as *Mapped Rank-3*, can be calculated using numerical homogenization. However, it is even more interesting to find out if the performance can be improved

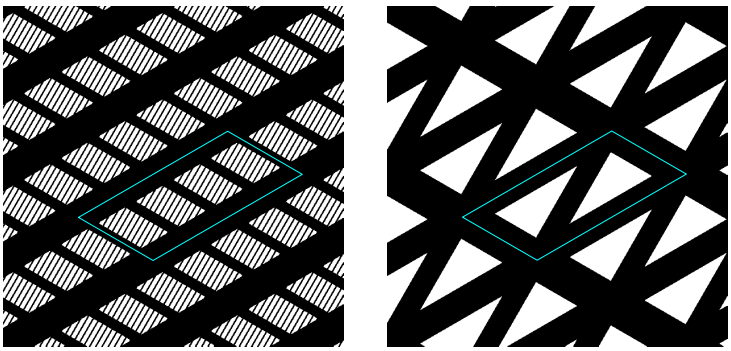

Figure 3.9: Left: rank-3 microstructure with indicated hierarchy, Right: approximated single-scale microstructure. Illustrations are based on a rank-3 laminate with, $\rho = 0.7$, $\theta_1 = \pi/3$, $p_1 = 2/7$, $\theta_2 = -\pi/6$, $p_2 = 2/7$, $\theta_3 = \pi/6$ and $p_3 = 3/7$.

using inverse homogenization. This is done in [P3], where a design from a starting guess based on the rank-3 laminate (*Mapped SG*), is compared to designs obtained using classical starting guesses in the context of inverse homogenization for material design (*e.g.* [Guedes et al., 2003]). These classical starting guesses are a random density field (*Random SG*), and a homogeneous density field (*Homog. SG*), which is slightly perturbed to avoid constant sensitivities throughout the domain.

An explicit length-scale f_{min} is enforced on the solid features of the microstructure using the smoothed Heaviside projection scheme introduced by Guest et al. [2004]. To allow for a fair comparison in the enforced length-scale, all unit-cell areas $|\boldsymbol{Y}|$ are scaled to unit-area. More details on the numerical implementation of the inverse homogenization algorithm, and on how the *Random SG* and *Homog. SG* are obtained can be found in [P3] and references therein.

The four stress cases from above, are used to obtain optimal rank-3 designs, and perform the inverse homogenization for the various starting guesses. The resulting complementary energies $\mathcal{C}$ normalized using the energy bound from the rank-3 designs are shown in Figure 3.10, for 11 equally spaced values of χ and two different minimum feature sizes f_{min} for the solid material.

It can be seen that the *Mapped Rank-3* always performs within 10-15% of the optimal energy bound. Using inverse homogenization this can be improved to 5-8% of the energy bound. This performance is very constant for all values of χ, while relatively simple and manufacturable microstructures can be obtained, as indicated in Figures 3.11(a) and (b). For a small feature size, better (but also worse) performing designs can be obtained using *Homog. SG* and *Random SG*. This is due to non-convex nature of the inverse homogenization problem that prevents the design from *Mapped SG* to deviate far from the shape corresponding to *Mapped Rank-3*. The designs of the *Homog. SG* and *Random SG* consist of more complex members as can be seen in Figures 3.11(c) and (d); however, this might be more problematic in terms of manufacturability.

Please note that the design obtained using *Homog. SG* consists of parallel

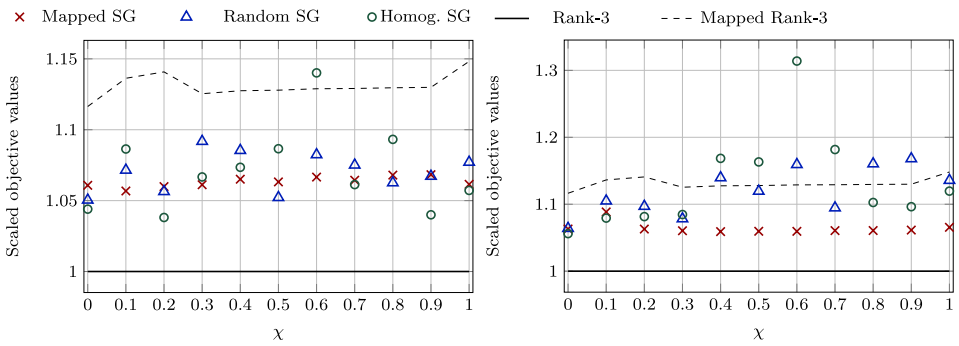

Figure 3.10: Normalized complimentary energy for different values of χ, $\rho = 0.5$. Left: $f_{min} = 0.05$, right: $f_{min} = 0.15$.

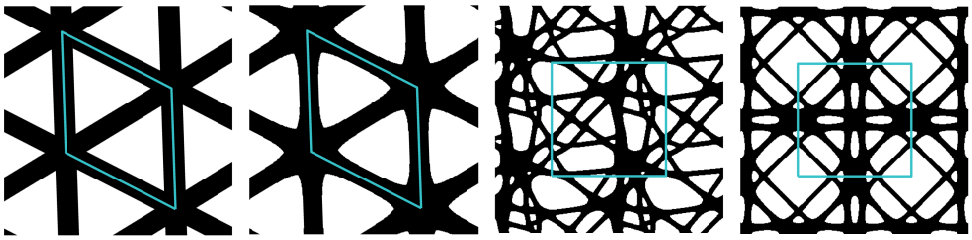

(a) *Mapped Rank-3.* (b) *Mapped SG.* (c) *Random SG.* (d) *Homog. SG.*

Figure 3.11: Resulting structures shown in a domain of size 2×2 with the unit-cell highlighted, for $\chi = 0.7$, $\rho = 0.5$, and a length-scale of $f_{min} = 0.05$.

members in the same direction, mimicking the class of extremal composites proposed by Sigmund [2000]. As is discussed in [P3] the approximation of a rank-3 on a single scale can be modified to allow for such designs as well. Finally, it is interesting to note that for a larger feature-size $f_{min} = 0.15$ both the *Mapped Rank-3* and *Mapped SG* exhibit a constant performance for different values of χ. Even more important is that designs using *Mapped SG* now significantly outperform the designs obtained with the classical starting guesses. Similar results have been obtained for different volume fractions and loadings as is shown in [P3].

4 Interpreting multi-scale designs on a single scale

In this chapter I will present a method to interpret homogenization-based designs on a single scale. The approach is inspired by the work of Pantz and Trabelsi [2008], which showed that the composite shape of an optimized rank-2 design could be projected/enlarged to a solid-void design on a fine but realizable scale.

I start this Chapter by presenting a method to interpret the topology optimized designs that use the microstructure of Bendsøe and Kikuchi [1988], an approach presented in [P1]. However, extensions that can be envisioned for different types of microstructures, and 3 dimensions will be discussed as well.

A key requirement for the presented method is that the input data has to be smooth, *i.e.* the angle field describing the microstructure orientation should be smoothly varying through domain Ω. The presentation in this chapter is based on the assumption that the considered fields are smooth. Methods to obtain smooth input fields will be the topic of Section 5.3.

4.1 Projecting a spatially variant microstructure

As is discussed in Section 3.3, an implicit geometry description $\tilde{\rho}(\boldsymbol{x})$ can be used to describe a periodic sequence of uniform rank-3 laminates, based on the layer normals $\boldsymbol{n}^i$, and layer widths w_i. A similar description can be made for the square unit-cell with rectangular hole shown in Figure 2.3. Instead of interpreting this periodic microstructure as a solid from which a periodic arrangement of holes is subtracted, it is possible to think of it as two periodic layers superimposed on each other [Pantz and Trabelsi, 2008]. The first layer, which is used to describe the height of the hole, can be described by normal direction $\boldsymbol{n}^1$, and layer tangent $\boldsymbol{t}^1$,

$$\boldsymbol{n}^1(\boldsymbol{x}) = \boldsymbol{t}^2(\boldsymbol{x}) = \begin{bmatrix} -\sin(\theta(\boldsymbol{x})) \\ \cos(\theta(\boldsymbol{x})) \end{bmatrix}, \quad \boldsymbol{n}^2(\boldsymbol{x}) = \boldsymbol{t}^1(\boldsymbol{x}) = \begin{bmatrix} \cos(\theta(\boldsymbol{x})) \\ \sin(\theta(\boldsymbol{x})) \end{bmatrix}. \tag{4.1}$$

Here, $\boldsymbol{n}^2$ and $\boldsymbol{t}^2$, are normal and tangent of the layer describing the width of the hole. The corresponding layer widths can be defined as, $w_i(\boldsymbol{x}) = (1 - a_i(\boldsymbol{x}))$.

4.1.1 Creating a map of the composite shape

Unfortunately, Equation 3.17 cannot be used to describe layer i if $\boldsymbol{n}^i(\boldsymbol{x})$ is spatially varying. Instead, the composite shape needs to be approximated using a mapping function ϕ_i, which maps the domain Ω to a periodic set in $\mathbb{R}^2$. This mapping can then be used to obtain,

$$\tilde{\rho}_i(\boldsymbol{x}) = H\left(\left(\frac{1}{2} + \frac{1}{2}\mathcal{S}\left\{P_i\phi_i(\boldsymbol{x})\right\}\right) - w_i(\boldsymbol{x}) \right). \tag{4.2}$$

Here P_i is a periodicity scaling, which as will be discussed later depends on mapping function ϕ_i. Ideally mapping ϕ_i should preserve the orientation θ and shape of the microstructures. Hence, a conformal (angle preserving) map should be considered.

Geometry modeling using conformal mapping is a research field in itself, with a large number of applications in fields such as cartography *e.g.* the Mercator projection, texture mapping [Lévy et al., 2002] and mesh generation [Kälberer et al., 2007]. Allaire et al. [2018] showed that a homogenization-based topology can be projected on a single scale using a conformal mapping approach. Moreover, they required their mapping to remain not only angle preserving, but also proportionality preserving, *i.e.* the mapped square unit-cell is ensured to have equal spacing between both orthogonal contour lines such that it does not become a rectangle. As a requirement for the mapping, the field describing the unit-cell orientation should be harmonic, *i.e.* $\Delta\theta = 0 \in \Omega$. Although the approach by Allaire et al. [2018] is promising and works well, we propose a slightly different approach, for the following reasons:

- The optimal orientation of the microstructures is not necessarily harmonic.
- In large parts of the domain one of the layer widths vanishes *i.e.* $w_i(\boldsymbol{x}) = 0$; hence, it does not matter if the mapped shape is square or rectangular. More specific, the requirements for mapping functions ϕ_i can be relaxed when the layer width vanishes or when the structure is solid, *i.e.* $\rho(\boldsymbol{x}) = 1$.
- The shape of the unit-cell is not necessarily square or cubic. If a spatially varying rank-3 laminate is projected to a single-scale, there is no need to pose a restriction on the shape.

As proposed in [P1] we only require the parameterization ϕ_i to be accurate in $\tilde{\Omega}_i$, where,

$$\boldsymbol{x} \in \tilde{\Omega}_i \quad \text{if} \quad w_i(\boldsymbol{x}) > 0 \text{ and } \rho(\boldsymbol{x}) < 1. \tag{4.3}$$

Furthermore, the angle field θ is not required to be harmonic, instead the angle field from the topology optimization algorithm is directly used to calculate ϕ_i. To obtain this mapping function ϕ_i the following two requirements have to be satisfied in $\tilde{\Omega}_i$:

- ϕ_i should be constant in the direction perpendicular to $\boldsymbol{n}^i$.
- The spacing between the contour lines of ϕ_i should be as regular as possible without violating the first requirement.

To solve for ϕ_i, the following spatially weighted constrained least-squares minimization problem is introduced,

$$\begin{aligned} \min_{\phi_i(\boldsymbol{x})} &: \mathcal{I}(\phi_i(\boldsymbol{x})) = \frac{1}{2}\int_\Omega \alpha_1^i(\boldsymbol{x}) \left\| \nabla\phi_i(\boldsymbol{x}) - \boldsymbol{n}^i(\boldsymbol{x}) \right\|^2 \mathrm{d}\Omega, \\ \text{s.t.} &: \alpha_2^i(\boldsymbol{x}) \nabla\phi_i(\boldsymbol{x}) \cdot \boldsymbol{t}^i(\boldsymbol{x}) = 0. \end{aligned} \tag{4.4}$$

The domain is split up into three parts, which dictate the weights on the objective α_1^i and the weights on the constraints α_2^i,

$$\alpha_1^i(\boldsymbol{x}) = \begin{cases} 0.01 & \text{if} \quad w_i(\boldsymbol{x}) = 0, \\ 0.1 & \text{if} \quad \rho(\boldsymbol{x}) = 1, \\ 1 & \text{if} \quad \boldsymbol{x} \in \tilde{\Omega}_i. \end{cases}, \quad \alpha_2^i(\boldsymbol{x}) = \begin{cases} 0 & \text{if} \quad w_i(\boldsymbol{x}) = 0, \\ 0 & \text{if} \quad \rho(\boldsymbol{x}) = 1, \\ 1 & \text{if} \quad \boldsymbol{x} \in \tilde{\Omega}_i. \end{cases} \tag{4.5}$$

The term α_1^i is introduced to relax the requirements for ϕ_i in regions that are either solid or void, where the low values still ensure some regularization to the lattice spacing. Furthermore, the term α_2^i is used to turn off exact angular enforcement in these regions. Please note that it is possible to ignore the calculation of ϕ_i completely in regions where $w_i = 0$, such an approach is used in [P4].

In 3D there is one more constraint, since $\nabla\phi_i$, should be orthogonal to a plane spanned by $\boldsymbol{t}^{i,1}$ and $\boldsymbol{t}^{i,2}$,

$$\begin{aligned} \min_{\phi_i(\boldsymbol{x})} &: \mathcal{I}(\phi_i(\boldsymbol{x})) = \frac{1}{2}\int_\Omega \alpha_1^i(\boldsymbol{x}) \left\| \nabla\phi_i(\boldsymbol{x}) - \boldsymbol{n}^i(\boldsymbol{x}) \right\|^2 \mathrm{d}\Omega, \\ \text{s.t.} &: \alpha_2^i(\boldsymbol{x})\nabla\phi_i(\boldsymbol{x}) \cdot \boldsymbol{t}^{i,1}(\boldsymbol{x}) = 0, \\ \text{s.t.} &: \alpha_2^i(\boldsymbol{x})\nabla\phi_i(\boldsymbol{x}) \cdot \boldsymbol{t}^{i,2}(\boldsymbol{x}) = 0. \end{aligned} \tag{4.6}$$

The constraint in the calculation of the mapping functions ϕ_i ensures that the microstructure is oriented with the material frame of reference, at the cost of relaxed periodicity. The local spacing can be identified by making use of the Euclidean norm of the derivatives of ϕ_i, *i.e.* $\|\nabla\phi_i\|$. If $\|\nabla\phi_i\| > 1$, then the corresponding layer distance is locally compressed, similarly if $\|\nabla\phi_i\| < 1$ the corresponding layer distance is locally stretched. In general, one would like to impose an average layer distance ϵ, which can be interpreted as the unit-cell size. To do so, it is possible define periodicity scaling parameter P_i based on the average lattice spacing in the domain of interest $\tilde{\Omega}_i$,

$$P_i = \frac{2\pi}{\epsilon} \frac{\int_{\tilde{\Omega}_i} \mathrm{d}\tilde{\Omega}_i}{\int_{\tilde{\Omega}_i} ||\nabla\phi_i(\boldsymbol{x})|| \mathrm{d}\tilde{\Omega}_i}. \tag{4.7}$$

4.1.2 Practical implementation

There are many ways to solve the minimization problem $\mathcal{I}$ in Equations 4.4 and 4.6. For example, the constraint for the angle enforcement can be either applied using Lagrange multiplier $\lambda(\boldsymbol{x})$ as proposed in [P1], or using a penalty approach with penalty parameter γ_ϕ as proposed in [P4]. Numerical experiments have shown that both methods give similar results; however, using Lagrange multipliers the discretized system is a saddle point problem, with more unknowns. Hence, for computational efficiency a penalty approach is pursued.

Furthermore, the problem can either be discretized using a finite difference method as proposed in [P1] or a finite element method as done in [P4]. Numerical experiments have shown that the finite difference scheme could lead to spurious oscillations, see *e.g.* Figure 8 in [P1]. These oscillations have not been observed when a finite element method is used to solve for ϕ_i. Hence, this is the preferred method.

Finally, it has to be mentioned that the the complete sequence of topology optimization, creating mapping fields, and creating an implicit geometry description can be solved in a multi-scale manner. It is known that homogenization-based topology optimization can be performed on a relatively coarse mesh $\mathcal{T}^c$, while it can still contain a lot of details. The implicit geometry function $\tilde{\rho}$ is a continuous description of the projected shape as long as the mapping functions ϕ_i and widths w_i

have a continuous description. For practical purposes $\tilde{\rho}$ is evaluated using a discrete number of points; however, at fine mesh $\mathcal{T}^f$, such that $h^f \leq h^c/20$. Furthermore, numerical experiments the best results are obtained if ϕ_i are calculated on an intermediate mesh $\mathcal{T}^i$, with $h^i \leq h^c/4$. An overview of this multi-scale approach can be seen in Figure 4.1, where it has to be noted that the interpolation of the layer widths w_i and orientation vectors $\boldsymbol{n}^i$ between the meshes is done using linear interpolation.

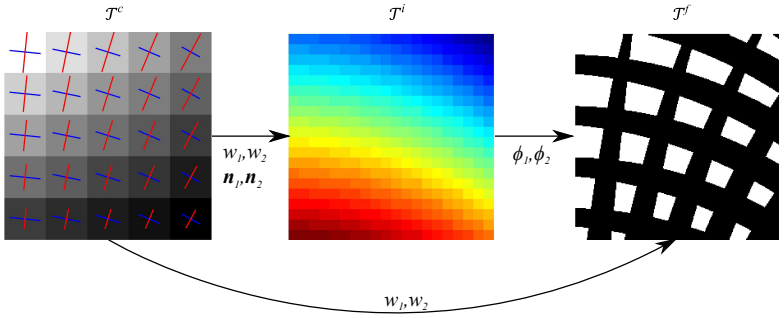

Figure 4.1: The different types of meshes and how they are linked.

4.1.3 Numerical examples

To demonstrate the approach consider domain 2D domain $\Omega = [0, 5] \times [0, 5]$, with the normal vectors, shown in Figure 4.2(a). The boundary of the domain has a solid coating with a width of 0.1. The corresponding projected shape using $\epsilon = 0.5$, and $\gamma_\phi = 10^3$ can be seen in Figure 4.2(b). Similarly, a 3D type of example is made that is shown in Figure 4.2(c).

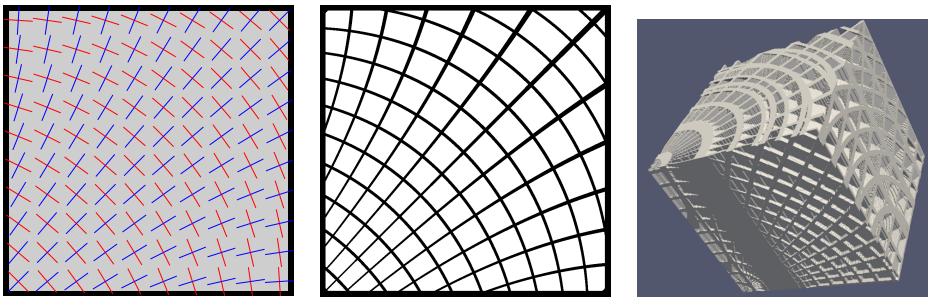

(a) ρ, $\boldsymbol{n}^1$ and $\boldsymbol{n}^2$. (b) 2D projection, $\epsilon = 0.5$. (c) 3D projection, $\epsilon = 0.5$.

Figure 4.2: Examples to demonstrate the projection of spatially variant design in 2- and 3D.

Finally, the optimized design for the Michell cantilever, using the square unit-cell with the rectangular hole, shown in Figure 3.3(c) is projected on a fine mesh $\mathcal{T}^f$ of 1600×800 elements as can be seen in Figures 4.3(a) and (b). For both Figures, $\gamma_\phi = 10^3$, for the first figure, an average unit-cell spacing of $\epsilon = 40\ h^f$ is used, while for the latter $\epsilon = 60\ h^f$.

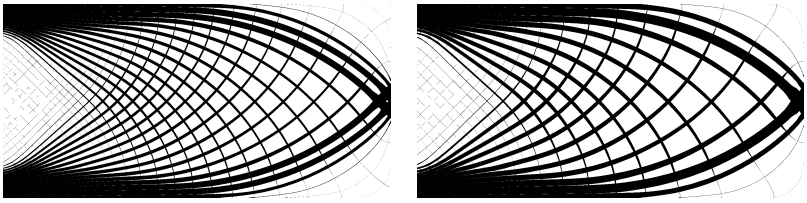

(a) $\epsilon = 40\ h^f$. (b) $\epsilon = 60\ h^f$.

Figure 4.3: Projection of topology optimized Michell cantilever shown in Figure 3.3(c). The designs are projected on a fine mesh of 1600×800 elements.

4.1.4 Projecting complex microstructures

Consider the periodic microstructure shown in Figure 3.11(d), such that $\boldsymbol{Y} = [0, 1[\times[0, 1[$. The material distribution in $\boldsymbol{Y}$ is known and described by $\psi^I(\boldsymbol{y})$. Assume that the microstructures are locally periodic; but with a macroscopically varying orientation θ. Similar as above, one can use Equation 4.4 to create ϕ_1 and ϕ_2, which can subsequently be used to get a geometry description $\tilde{\rho}$ of the sequence of spatially oriented microstructures,

$$\tilde{\rho}(\boldsymbol{x}) = \psi^I(\text{modulo}\left\{P_1\phi_1(\boldsymbol{x}), 2\pi\right\}, \text{modulo}\left\{P_2\phi_2(\boldsymbol{x}), 2\pi\right\}). \tag{4.8}$$

The corresponding projection of this sequence of microstructures is shown in Figure 4.4(a). Furthermore, it should be noted that the presented approach, also works for microstructures described as a parallelogram or parallelepiped. *E.g.* consider the microstructure shown in Figure 3.11(a), which can be mapped in a similar manner, as shown in Figure 4.4(b).

The approach described here is very similar to texture mapping. Actually, for this type of mapping, it will be better when a shape preserving conformal map is used, *e.g.* [Allaire et al., 2018]. Investigating such an approach for projecting uniform microstructures with spatially varying orientation, will be the topic of future studies.

Finally, I should mention another possibility of projecting a microstructure, which is by representing it as a complex exponential Fourier series as proposed by Rumpf and Pazos [2012]. A similar Equation as 4.4 is used, to calculate mapping function ϕ_i, which corresponds to the direction vector field of the i-th spatial harmonic. Hence, a downside of this approach is that a large number of mapping functions needs to be calculated, making it more cumbersome.

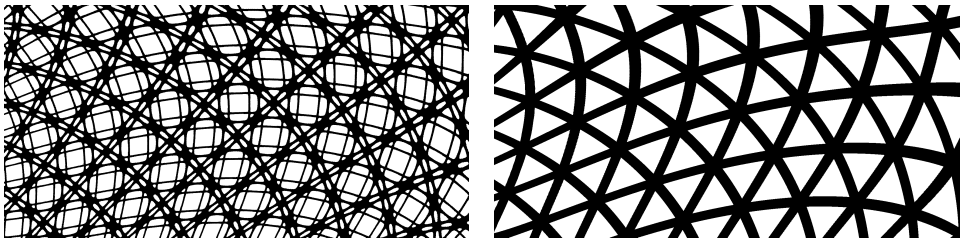

(a) Sequence of unit-cells from Figure 3.11(d). (b) Sequence of unit-cells from Figure 3.11(a).

Figure 4.4: Sequence of spatially oriented unit-cells for two types of microstructures.

4.2 Practical considerations for the projection approach

The optimization problem solved in Equation 4.4 works well for a smoothly varying normal vector $\boldsymbol{n}^i$. Unfortunately, the vector describing the microstructure orientation is rotationally symmetric. Rotating the microstructure 180 degrees has no influence on its shape or constitutive properties. However, it means that Equation 4.4 cannot be directly used. Furthermore, the orientation fields can point towards a single point, which is a so-called singularity. If this happens, the gradients of the corresponding mapping field become very large, resulting in a highly distorted projection in other parts of the domain.

4.2.1 Rotational symmetry

To demonstrate the problem of rotational symmetry on the projected shape, consider the projected design shown in Figure 4.3(a). If orientation vectors $\boldsymbol{n}^i$ are rotated 180 degrees in a part of the domain, the shape shown in Figure 4.5 is obtained. Here, the red-shaded areas indicate where the orientation vectors are rotated.

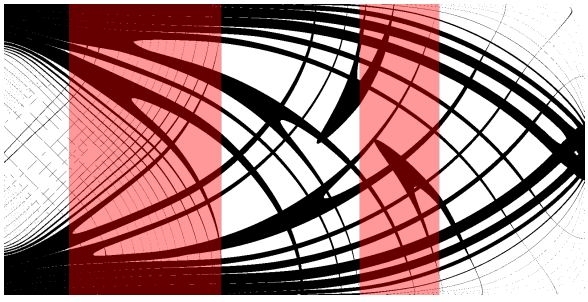

Figure 4.5: Projected shape obtained with similar settings as the Michell cantilever from Figure 4.3(a); however, the shaded areas indicate that the orientation vectors are rotated 180 degrees.

For a 2D single load case problem, the orientation can be smoothly defined with a rotational symmetry of 180 degrees. This π ambiguity means that one cannot

directly use the obtained angles to calculate ϕ_i. Several methods can be envisioned to overcome this problem, one of them using a well-known image analysis technique called connected component labeling [Shapiro and Stockman, 2001], as proposed in [P1].

The main idea of this method is to divide the image into separate components, such that the elements in each of the components have uniform or near-uniform properties. Using this technique it is possible to find the components in $\tilde{\Omega}_i$ where the vectors are rotated with π. To identify if neighboring elements k and adjacent elements l are in the same component, the following two conditions should be satisfied.

1. $\boldsymbol{n}^i(\boldsymbol{x}^k) \cdot \boldsymbol{n}^i(\boldsymbol{x}^l) > 0$.
2. Elements k and l should both be in $\tilde{\Omega}_i$.

The first condition assumes that the orientation field is smooth and should not rotate more than $\pi/2$ between two adjacent elements. The second condition is used to find the boundaries of regions in which there is no material in layer i, or when the shape is solid. Furthermore, it has to be noted that the technique works equally well on irregular meshes, provided that the adjacent elements are known.

To demonstrate the procedure, consider the vector field $\boldsymbol{n}^i$ shown in Figure 4.6(a). It is assumed that condition 2 is always satisfied. A component label is assigned to each of the elements as is shown in Figure 4.6 (b). The different components can then be oriented consistently by making sure that the difference in orientation of $\boldsymbol{n}^i$ at these boundaries is close to $k2\pi$, where k is an integer. This aligns the angle field in a consistent fashion, and subsequently the mapping field ϕ_i can be obtained by Equation 4.4.

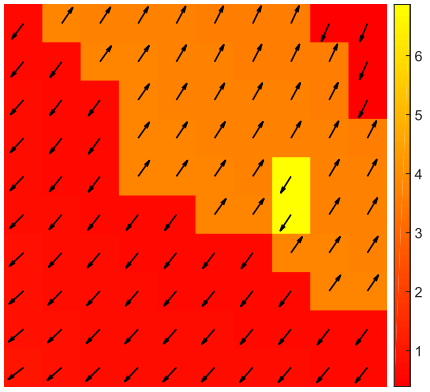

(a) $\boldsymbol{n}^i$ plotted on top of θ_i.

1	2	2	2	2	2	2	2	4	4
1	1	2	2	2	2	2	2	2	4
1	1	1	2	2	2	2	2	2	4
1	1	1	2	2	2	2	2	2	2
1	1	1	2	2	2	2	3	2	2
1	1	1	1	1	2	2	3	2	2
1	1	1	1	1	1	1	2	2	2
1	1	1	1	1	1	1	1	2	2
1	1	1	1	1	1	1	1	1	1
1	1	1	1	1	1	1	1	1	1

(b) Component labels.

Figure 4.6: Vector field $\boldsymbol{n}^i$, which exhibits rotational symmetry, and the corresponding connected component labeling.

The approach described above only works when the vector field is smoothly defined up to 180 degrees. There are cases where the angle field changes rapidly, *e.g.* at the introduction of a point load. However, at these points the volume fraction in

the microstructure ρ is solid, which means such a point is not in $\tilde{\Omega}_i$, and the mapping is calculated correct.

Besides the approach described above, different methods exist to treat the problem of rotational symmetry. Pantz and Trabelsi [2008] reformulated the problem and solved for vector fields $\boldsymbol{v}^i$ instead of the scalar fields ϕ_i. By doubling the amount of unknowns the issue of rotational symmetry can be overcome. However, the implementation of this approach is not necessarily straightforward. Another promising method has been proposed by Allaire et al. [2018]. A discontinuous Galerkin finite element approach is used to calculate mappings ϕ_i. The orientations are described at each element node and are only required to be continuous within each discontinuous finite element, hence a globally smooth vector field with continuity up to 2π is not required.

4.2.2 Treatment of singularities

A singularity in the orientation field means that the orientation vectors locally converge towards a single point, such that $\nabla\theta_i \to \infty$. Classical examples of singularities in the context of structural optimization can be found by using the Michell layout theory applied to the MBB-beam, Michell cantilever or L-shaped beam examples [Lewiński and Rozvany, 2008; Lewiński et al., 1994a,b; Rozvany, 1998]. In these works a singularity is referred to as a fan-like shape. An example of a singularity can be found if the L-shaped beam example shown in Figure 4.7(a) is considered. Here a singularity occurs at the corner of the design domain. In general, these singularities occur at the boundary of the domain Ω where a load or displacement condition is applied. In such cases the density field $\rho = 1$, which means that the mapping fields ϕ_i are relaxed, and the shape can be projected correctly using Equation 4.4 as is shown in Figure 4.7(b).

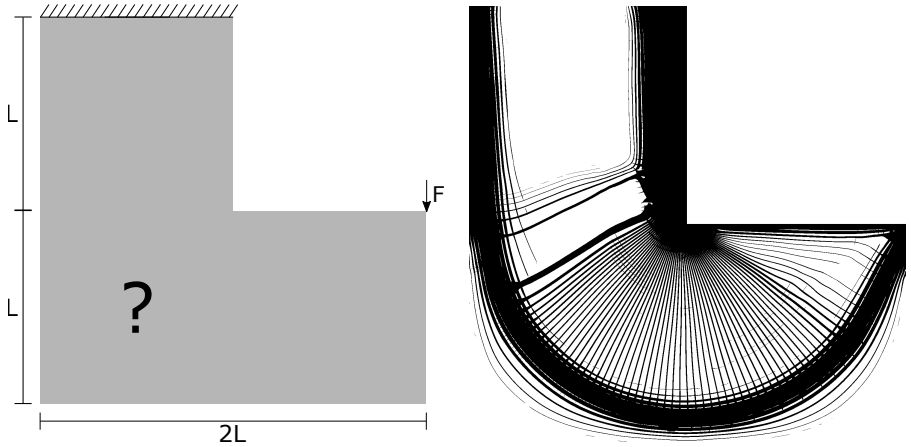

(a) Design domain and boundary conditions. (b) Projected shape on 1600×1600 elements.

Figure 4.7: The L-shaped beam example, optimized using $V_{max} = 0.3$, where member directions point to the corner, which has a singularity in the angle field.

It should be mentioned that in [P2] the calculation of ϕ_i is relaxed in regions where the angle field is quickly changing. The reason being that Michell's problem of least-weight trussed is considered, which means that no upper bound on the layer widths is used. In other words, the calculation of the mapping is relaxed when the angle field changes quickly instead of when $\rho = 1$. Another possibility to avoid singularities at the boundary of the domain is to restrict the gradient of the orientation, *i.e.* use a curvature restriction on the vector fields $\boldsymbol{n}^i$, in such a case the singularity will be pushed out of the domain [Allaire et al., 2018].

In the examples considered in [P1], [P2] and [P4] an internal singularity does not occur in $\tilde{\Omega}_i$. However, it should be mentioned that optimization examples with internal singularities can be envisioned. If this is the case, the singularity can result in a highly distorted mapping. In the context of projecting homogenization-based designs, an approach to modify mapping functions ϕ_i at singularities has been proposed by Pantz and Trabelsi [2010].

Although the treatment of singularities has not been investigated in detail during this work, it should be considered to further advance the topic of projecting homogenization-based designs. In this context, it can be beneficial to look at the research field of computer graphics, where a large portion of works consider the treatment of singularities. For example Polthier and Preuß [2003] propose an algorithm to automatically detect singularities. In [Kälberer et al., 2007] this approach is used to cut up the domain on which th mapping functions are calculated, later on these cuts are tied together without a loss in performance. Other approaches for the treatment of singularities can be found in [Bommes et al., 2009; Jiang et al., 2014; Nieser et al., 2011] and references therein.

4.3 Control of the projected shape

As is discussed, the Euclidean norm of the gradient of the mapping fields $\|\nabla\phi_i\|$, holds information about the local spacing of the projected shape. This information is valuable, and can be exploited to further improve the performance of the projected homogenization-based design.

4.3.1 Enforcing minimum length-scale

The local spacing corresponding to layer i in the projected shape λ_i can be calculated as,

$$\lambda_i(\boldsymbol{x}) = \frac{2\pi}{P_i\|\nabla\phi_i(\boldsymbol{x})\|}. \tag{4.9}$$

This local spacing can be used to get a description of the actual feature size on the solid f_i for layer i.

$$f_i(\boldsymbol{x}) = w_i(\boldsymbol{x})\lambda_i(\boldsymbol{x}). \tag{4.10}$$

In [P1] we proposed a method to add a minimum feature size f_{min} to the solid at places where this feature size was violated. This was done to avoid having members with a thickness of only 1 element, which cannot be correctly modeled using bi-linear finite elements. Furthermore, small feature sizes cannot be manufactured, and are

not robust against manufacturing errors [Wang et al., 2010]. To ensure a minimum feature size on the solid it is possible to obtain a modified local width w_i^* in cases where the feature size on the solid is violated, such that

$$w_i^*(\boldsymbol{x}) = \begin{cases} w_i(\boldsymbol{x}), & \text{if} \quad f_i(\boldsymbol{x}) \geq f_{min}, \\ \frac{f_{min}}{\lambda_i(\boldsymbol{x})}, & \text{if} \quad f_i(\boldsymbol{x}) < f_{min}. \end{cases} \tag{4.11}$$

This new width w_i^* is then used in Equation 4.2. However, this means that the volume of the projected shape is slightly increased. As is discussed in [P1] and in the next chapter, it is possible to slightly restrict the solution space and avoid very small and large values in w_i, hence this increase in volume can be considered acceptable. Another possibility is to perform once more homogenization-based topology optimization for fixed orientations, and by restricting bounds on w_i such that the minimum feature size f_{min} is always satisfied.

4.3.2 Adaptive periodicity projection

Solving for mapping fields ϕ_i using Equation 4.4, or as a conformal map means that the layer spacing is relaxed to allow for exact angle enforcement. This can lead to some significant differences in the size of the projected unit-cells as can be seen in Figures 4.3 (a) and (b). To overcome this issue, it is possible to locally adapt the layer widths as proposed in [P4]. Inspiration for adapting the periodicity came from coated structures which have been topology optimized using a density-based approach [Wu et al., 2017]. In these optimized structures it could be seen that structural members close to an applied boundary condition where branching out to enhance load transfer and to avoid large spacings between these members.

The methodology of adapting the layer spacing is explained in detail in [P4] and will not be repeated here. However, the core concept will be introduced using Figure 4.8. Consider the projected design shown in Figure 4.8(a), where it can be seen that the local unit-cell spacing significantly changes throughout the domain. It is possible to locally adapt the periodicity of the projected shape by using $\bar{\tilde{\rho}}_i$ instead of Equation 4.2,

$$\bar{\tilde{\rho}}_i(\boldsymbol{x}) = H\left(\big(\frac{1}{2} + \frac{1}{2}\mathcal{S}(2^{(\omega_i(\boldsymbol{x})+1)}\pi\phi_i(\boldsymbol{x}) + \omega_i(\boldsymbol{x})\pi)\big) - w_i(\boldsymbol{x}) \right). \tag{4.12}$$

In this formulation ω_i is a discrete periodicity scaling parameter. When $\omega_i = 0$, the function is identical to Equation 4.2, provided that $\epsilon = 1$ and $P_i = 1$. However, when $\omega_i = 1$, the function becomes similar for $\epsilon = 0.5$. Hence, the periodicity is doubled when ω_i is increased by one. The effective lattice spacing can be bounded to the interval $[\epsilon 2^{-1/2}, \epsilon 2^{1/2}]$ using,

$$\omega_i(\boldsymbol{x}) = \text{round}\Big(\log\big(\frac{1}{\epsilon||\nabla\phi_i(\boldsymbol{x})||}\big)\frac{1}{\log(2)}\Big). \tag{4.13}$$

The projected shape in Figure 4.8(b) corresponds to the one in Figure 4.8(a); however, using Equations 4.12 and 4.13 instead of Equation 4.2. From the figure it can be

seen that the average spacing between the members is more uniform; but as expected, there are discontinuities when ω_i changes. Several methods can be envisioned to reconnect the disconnected members. The projected shape shown in Figure 4.8(c) is obtained using the method proposed in [P4].

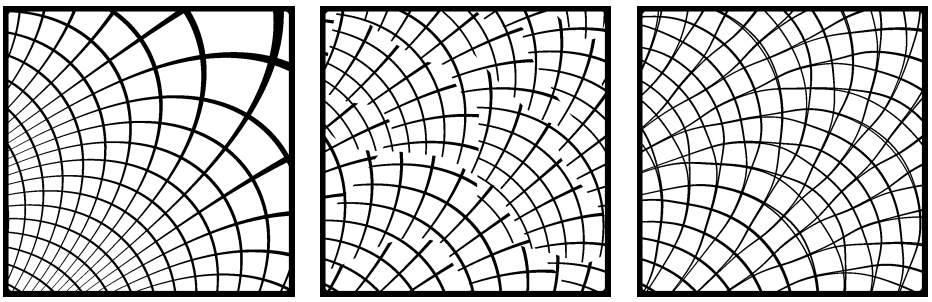

(a) $\tilde{\rho}$, original approach. (b) $\bar{\tilde{\rho}}$, using 4.12 (c) $\bar{\tilde{\rho}}$, connected.

Figure 4.8: Projection on a fine mesh $\mathcal{T}^f$ of 1000×1000 elements using $\epsilon = 80\ h^f$, to illustrate the adaptive periodicity projection approach.

It can be seen that smoothly splitting members are obtained. Numerical experiments have indicated that these splits have an almost negligible effect on the performance. Furthermore, it has to be mentioned that in the zone where a member splits, the unit-cell spacing is restricted to $[\epsilon^{-3/2}, \epsilon^{1/2}]$. The corresponding feature size f_i of a member is thus bounded by $[w_i\epsilon^{-3/2}, w_i\epsilon^{1/2}]$. Finally, the projected shape of the Michell cantilever from Figure 4.3(a) using the adaptive periodicity approach is shown in Figure 4.9

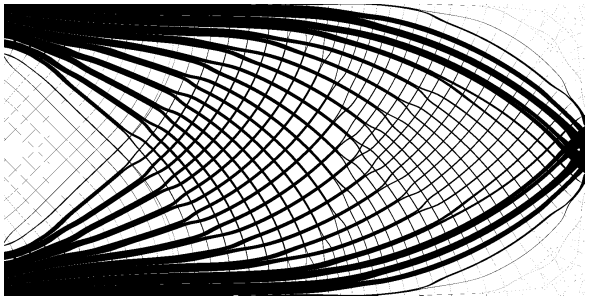

Figure 4.9: Projection of topology optimized Michell cantilever shown in Figure 3.3(c), on a fine mesh of 1600×800 elements. The adaptive periodicity projection approach is used using $\epsilon = 40\ h^f$.

4.3.3 Extracting a discrete truss or frame structure

Besides adapting the layer spacing, or a strict length-scale enforcement, mapping fields ϕ_i can also be used to extract a discrete truss or frame structure. Such an

approach is proposed in [P2], where Michell's problem of least-weight trusses is considered for a single load case problem in 2D. Below a brief summary of the developed approach will be given; however, for more details the reader is referred to [P2].

The lack of an upper bound on the layer widths μ_i of the single-scale microstructure allows for the use of point loads and point supports for the design domain. However, as discussed above, these supports are prone to singularities in orientation field θ. To avoid a distorted mapping at these supports, the calculation of ϕ_i is relaxed at points where the angle field is rapidly changing. An example of both mapping fields ϕ_1 and ϕ_2 for a Michell cantilever problem with point load and supports can be seen in Figure 4.10(a).

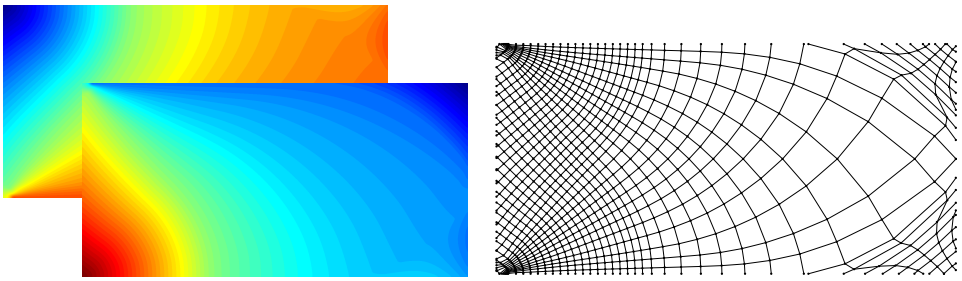

(a) Mapping functions ϕ_1 and ϕ_2.

(b) Elements and nodes for $\epsilon = 50\ h^f$.

Figure 4.10: The nodes and element-connectivity extracted from the mapping functions for the Michell cantilever problem.

Instead of using Equation 4.2, we can draw a contour line for every discrete value of ϕ_i, scaled to an average spacing using Equation 4.7. This can be done using standard MATLAB functions (*e.g.* `contour`), such that the coordinates of these lines can be extracted. Using this information it is possible to derive the nodal positions and element connectivity of the frame structure, an example nodes and connectivity corresponding to the mapping fields from Figure 4.10(a) is shown in Figure 4.10(b).

Besides the geometry information of the frame structure, it is also possible to obtain element areas based on the homogenization-based design. By making use of the local spacing information λ_i of the scaled mapping fields (*i.e.* scaled using P_i), a polygon can be drawn around an element, as can be seen in Figure 4.11(a). The layer width μ_i corresponding to the considered element can be integrated within the polygon and divided by the element length to obtain element area A. Finally, it is possible to remove all elements with an area that is smaller than threshold area A_η, to get the element area distribution shown in Figure 4.11(b).

The next step is to assign boundary conditions (BC's) to the appropriate nodes. At locations where the angle field is rapidly changing, the mapping is relaxed such that not all elements are exactly pointing towards the correct location of where the BC is applied. These points correspond to so-called fan-like BC's in the analytical solutions for Michell's problem of least-weight trusses (see *e.g.* [Lewiński et al., 1994b]). Hence, if the angle field is rapidly changing, all nodes within radius R_{BC},

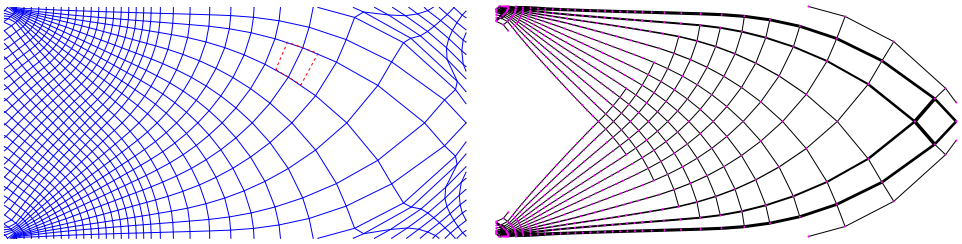

(a) Polygon around element. (b) Material mapped to elements.

Figure 4.11: Procedure for mapping material from the continuum solution of homogenization-based topology optimization to discrete frame elements.

are pulled and merged exactly into one node at the BC, as can be seen in Figure 4.12. For all other boundary conditions, at which the angle field is not rapidly changing, the closest node is put to the exact location of where the BC is applied.

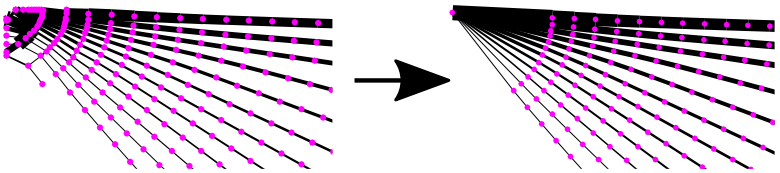

Figure 4.12: Operation that pulls in all nodes and elements within R_{BC} to generate a fan-like BC.

In a final step, all non-BC nodes, connected to only one or two elements are removed. Nodes connected to a single element are removed together with the corresponding elements. Nodes connected to only two elements are unstable and are therefore removed. The corresponding two elements are subsequently merged into a single element in a volume preserving manner. If due this merging operation two elements are crossing, then the largest of the two is removed. The frame structures for the Michell cantilever and L-shaped beam can be seen in Figures 4.13(a) and (b), respectively.

As is proposed in [P2], these frame structures can be post-optimized in a subsequent geometry and topology optimization step. A benefit of the approach above is that the initial frame structures from Figure 4.13 can be obtained in a relatively short time (both are obtained in less than 5 minutes including homogenization-based topology optimization). Furthermore, by changing ϵ the number of elements in the frame design can be changed. Although this results in an increasing computational cost, it does not scale as bad as a growth method [Martínez et al., 2007], where the required time to insert a new member scales exponentially.

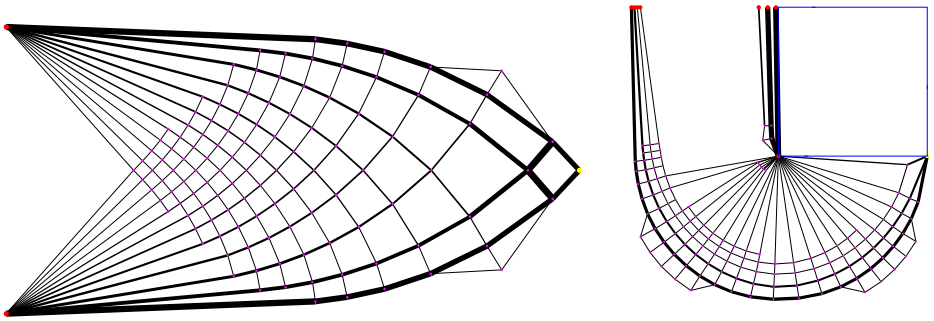

(a) Michell cantilever. (b) L-shaped beam.

Figure 4.13: Frame structures extracted from homogenization-based topology optimization.

5 Multi-scale topology optimization for single scale designs

In this chapter, I will discuss how the theory of the previous chapters can be combined to obtain high-resolution designs at a low computational cost. First, I will discuss methods to improve the performance of the projected designs. Numerical examples from [P1] will be shown, to demonstrate the effectiveness of the approach.

Furthermore, a method to do homogenization-based topology optimization of coated structures, proposed in [P4], will be discussed. Coated structures consist of a solid interface and porous infill material, where it should be noted that these structures can have desirable properties compared to classical density-based designs.

Finally, I will discuss one of the most critical issues in doing multi-scale topology optimization, which is the optimization of the orientation of the microstructure. Both layer widths and orientations need to be smooth throughout domain Ω to allow for a design to be projected on a single scale. Hence, besides an optimal design something extra is required.

5.1 Practical considerations for multi-scale design

All practicalities to perform multi-scale design for a single load case problem in 2D will be discussed in this Section. However, a large part of the discussed methods can also be applied to problems with multiple load cases or problems in 3 dimensions.

5.1.1 Note on discretization and boundary conditions

Consider the Michell cantilever shown in Figure 3.3(a), parameterized using square unit-cells with a rectangular hole. As shown in Table 3.1, the compliance values $\mathcal{J}^c$, are relatively constant for different optimization meshes $\mathcal{T}^c$. This might seem counter intuitive, since a finer mesh allows for more design freedom and the influence of the density filter is reduced. However, the fact that this effect is not represented in the compliance values is purely due to h-refinement. To demonstrate this, the homogenization-based designs are interpolated on a fine mesh $\mathcal{T}^f$ of 1600×800 elements using nearest-neighbor interpolation. The corresponding compliance values $\mathcal{J}^f$, can be found in Table 5.1.

As expected, a finer $\mathcal{T}^c$ allows for better performing structures; however, it should be noted that the designs are smoothly varying. For a coarse mesh of 80×40 elements the total time it takes to do homogenization-based topology optimization is less than 5 minutes. Hence, it can be concluded that a mesh consisting of less than 5000 elements in 2D is sufficient to use as input for the projection approach described in Chapter 4.

Table 5.1: Compliance values $\mathcal{J}^c$ on different optimization meshes, and on a mesh of 1600×800 elements, for the Michell cantilever with a clamped support (see Figure 3.3(a)) and with point supports. $V_{max} = 0.4$, $E_0 = 1$ and $\nu_0 = 0.3$.

		40×20	80×40	120×60	160×80	200×100
Normal supports	$\mathcal{J}^c$	71.92	71.00	70.67	70.69	71.04
Normal supports	$\mathcal{J}^f$	76.27	72.42	71.35	71.07	71.26
Point supports	$\mathcal{J}^c$	90.46	98.91	104.22	108.38	111.90
Point supports	$\mathcal{J}^f$	142.68	140.05	139.59	139.60	139.94

It should be noted that if point supports are used, the mesh convergence is different. To demonstrate this, a similar study as above is performed for the Michell cantilever with point-supports, used in [P2]. The corresponding compliance values $\mathcal{J}^c$ on the coarse mesh at which the optimization is performed, and the values $\mathcal{J}^f$ on the fine mesh are also shown in Table 5.1.

Besides the standard effect of h-refinement, stress concentrations can be observed at the point supports. The smaller the element size, the larger the stress concentration. Hence, a large difference in the performance can be observed when the design is analyzed at a different discretization. It is therefore recommended that point loads and point supports are avoided in the context of multi-scale design. Furthermore, it should be noted that this type of supports does not make sense when practical design examples are considered.

Furthermore, it is recommended to strictly enforce solid material at the Dirichlet and Neumann boundary conditions, as is proposed in [P4] . This reinforces the structure and prevents large load concentrations; furthermore, it prevents a degraded performance for possibly misaligned mapping fields ϕ_i at the supports. Finally, I should mention that except for symmetry conditions, it is not recommended to strongly enforce a roller support at a finite length, since this can result in artificial bending moments. As is proposed in [P4] it is better to apply such a support as a multi-point constraint.

5.1.2 Procedure to restrict large and small widths

In Figures 4.3(a) and (b) it can be seen that in a large part of the domain, extremely thin members occur. These thin members cannot be manufactured, and have to be avoided. Not only to reduce the number of regions where length-scale f_{min} has to be enforced using the approach discussed in Section 4.3.1; but also, to get a clear distinction between regions that consist of a microstructure $\tilde{\Omega}^I$ and regions that are solid and void.

Instead of having thin strips of solid material or void, it is desired that the physical parameters that describe the height and width of the hole $\bar{\tilde{a}}_1$ and $\bar{\tilde{a}}_2$, are either 0, 1, or on the interval $[\eta, 1-\eta]$. In [P1] an interpolation scheme is proposed

that links the density filtered design variables $\tilde{a}_i$ to the physical dimensions $\bar{\tilde{a}}_i$,

$$\bar{\tilde{a}}_i = \tilde{a}_i\big(1 - \bar{H}(\beta, (1-\eta), \tilde{a}_i)\big)\bar{H}(\beta, \eta, \tilde{a}_i) + \left(\frac{\beta - 1}{\beta} + \frac{\tilde{a}_i}{\beta}\right)\bar{H}(\beta, (1-\eta), \tilde{a}_i). \quad (5.1)$$

Where $\bar{H}$ is the well-known smoothed Heaviside function, introduced by Wang et al. [2010],

$$\bar{H}(\beta, \eta, \tilde{a}_i) = \frac{\tanh(\beta\eta) + \tanh(\beta(\tilde{a}_i - \eta))}{\tanh(\beta\eta) + \tanh(\beta(1-\eta))}. \quad (5.2)$$

with parameter β controlling the sharpness of the projection. The interpolation scheme for different values of β and η is shown in Figure 5.1. The order of lines in the legend shows the continuation approach that is taken, with 50 iterations per step. This means that the material interpolation scheme begins close to a linear function, gradually η is increased to enforce the length-scale on solid and void. Finally, β is increased to ensure that the far majority of physical dimensions of the hole are either 0, 1 or in the region $[\eta, 1-\eta]$.

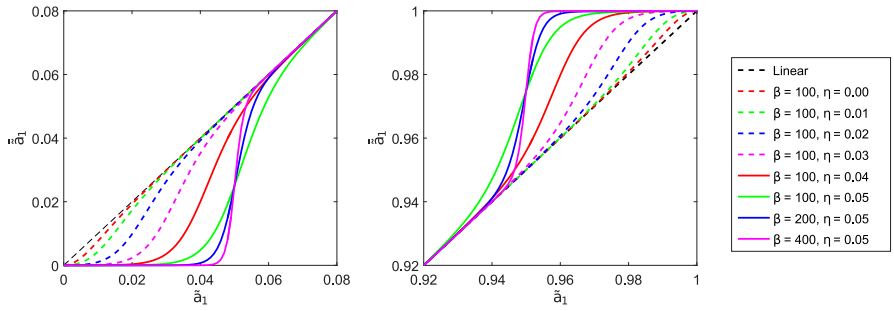

Figure 5.1: Interpolation scheme plotted for the intervals where the behavior is non-linear, for different values of η and β, that follow the order of the continuation approach.

Numerical experiments, have indicated that the effect of this continuation scheme on the performance of the homogenization-based designs is negligible. Furthermore, the width $w_i = (1 - \bar{\tilde{a}}_i)$, can be used to determine whether a region is a microstructure $\tilde{\Omega}_i$, or solid or void. Hence,

$$\boldsymbol{x} \in \tilde{\Omega}_i \quad \text{if} \quad w_i(\boldsymbol{x}) > \eta \text{ and } \rho(\boldsymbol{x}) < (1-\eta). \quad (5.3)$$

Please note that μ_i can be substituted into the Equation when rank-N microstructures are considered as microstructure. Finally, it should be mentioned that a similar method can be used to only restrict small (or large) values of $\bar{\tilde{a}}_i$, such an approach has been proposed in [P2].

5.1.3 Clean up of the projected designs

Designs projected on a fine scale can contain non-load carrying structural members. These can be explained by the interpolation of the widths w_i from $\mathcal{T}^c$ onto $\mathcal{T}^f$. Since

a linear interpolation method is used, structural members that do not carry any loads can arise at high-contrast regions. To remove these members a simple iterative update scheme has been proposed in [P1]. In this scheme a finite element analysis is performed at $\mathcal{T}^f$; afterwards, the solid elements that have a strain energy density $\mathcal{E}$ lower than 0.1% of the mean strain energy density $\bar{\mathcal{E}}$ are set to void. To make sure that the length-scale f_{min} is still satisfied after each iteration, an open-close filter operation [Sigmund, 2007] is applied.

The combination of removal of solid elements with a low strain energy density, followed by the open-close filter operation, generally convergences within 5-10 iterations. Besides a clean and well-connected design, the performance of the design on the fine-scale $\mathcal{J}^f$ is immediately known.

5.1.4 Overview of the multi-scale design approach

All methods presented so far can be combined to obtain high-resolution manufacturable microstructures at a low computational cost. The different steps that have to be taken are shown below:

1. Homogenization-based topology optimization, using the restriction approach presented in Section 5.1.2, on coarse mesh $\mathcal{T}^c$.
2. Consistent alignment of $\boldsymbol{n}_i$ on $\mathcal{T}^c$, using connected component labeling as presented in Section 4.2 on $\mathcal{T}^c$.
3. Calculating mapping functions ϕ_i as shown in Section 4.1, on intermediate mesh $\mathcal{T}^i$.
4. Calculating w_i^* to satisfy feature-size f_{min}, using the method presented in Section 4.3.1, on fine mesh $\mathcal{T}^f$.
5. Projection of the shape using Equation 4.2 or Equation 4.12 on fine mesh $\mathcal{T}^f$.
6. Removal of the non-load carrying materials using the iterative method described in Section 5.1.3 on mesh $\mathcal{T}^f$.

It has to be mentioned that the approach can be applied using different microstructures, *e.g.* square unit-cells using rectangular holes, or rank-3 microstructures. A requirement; however, is that the angle fields obtained from homogenization-based topology optimization are smooth up to 180 degrees, which unfortunately is not a trivial task. A detailed discussion on methods to obtain smooth angle fields and their limitations will be given later in this Chapter.

To demonstrate the effectiveness of the proposed approach, the Michell cantilever from Figure 3.3(a) is once more used. As is discussed in [P1] the topology optimization is performed on a mesh of 80×40 elements using a the square unit-cells with rectangular holes and a volume constraint $V_{max} = 0.5$, resulting in $\mathcal{J}^c = 58.31$. The performance of this homogenization-based design interpolated on $\mathcal{T}^f$ using nearest neighbor interpolation is $\mathcal{J}^f = 61.32$. The volume fraction V^ϕ and compliance $\mathcal{J}^\phi$ of the projected shape for various values ϵ and minimum feature sizes f_{min} are shown in Table 5.2. Furthermore, the required time on the coarse, intermediate, and fine mesh are given by T^c, T^i and T^f, respectively.

It is interesting to see that $\mathcal{J}^\phi$ is lower than $\mathcal{J}^f$; however, the explanation for this is simple. In the projection procedure the properties w_i and θ_i are interpolated using

Table 5.2: Performance and computational cost of the projection method, when the Michell cantilever, optimized using the square unit-cell with rectangular hole, is projected on a fine mesh consisting of 1600×800 elements.

ϵ	f_{min}	V^ϕ	$\mathcal{J}^f$	$\mathcal{J}^\phi$	T^c	T^i	T^f	T^{tot}
20 h^f	2 h^f	0.503	61.32	60.27	199.5 s	10.7 s	145.2 s	355.4 s
20 h^f	3 h^f	0.519	61.32	58.21	199.5 s	10.2 s	260.6 s	470.3 s
20 h^f	4 h^f	0.540	61.32	56.23	199.5 s	10.8 s	266.6 s	476.9 s
30 h^f	2 h^f	0.500	61.32	60.93	199.5 s	10.7 s	150.3 s	360.5 s
30 h^f	3 h^f	0.509	61.32	59.72	199.5 s	11.2 s	233.6 s	444.3 s
30 h^f	4 h^f	0.518	61.32	58.71	199.5 s	10.5 s	285.3 s	495.3 s
40 h^f	2 h^f	0.500	61.32	59.55	199.5 s	10.7 s	115.5 s	325.7 s
40 h^f	3 h^f	0.505	61.32	59.03	199.5 s	10.2 s	145.6 s	355.3 s
40 h^f	4 h^f	0.510	61.32	58.57	199.5 s	10.0 s	148.7 s	358.2 s

linear-interpolation while a nearest-neighbor interpolation is used to evaluate $\mathcal{J}^f$. Furthermore, it can be seen that for reasonable ratios of $\frac{\epsilon}{f_{min}} > 10$, the violation of the volume constraint due to the explicit length-scale enforcement is small. However, if the ratio is small, *e.g.* $\frac{\epsilon}{f_{min}} = 5$ a lot of material is added as can be seen in Figure 5.2(a). From Figure 5.2(b) it can be seen, that the besides a manufacturable shape, a design performing close to the coarse scale compliance is obtained. Hence, using the proposed approach a near-optimal design is obtained using more than a million elements, in less than 10 minutes on a standard PC. Compared to a density-based approach using a continuation scheme, on a similarly fine mesh (see *e.g.* [Sigmund et al., 2016]), a reduction in computational cost by more than 50 times is achieved!

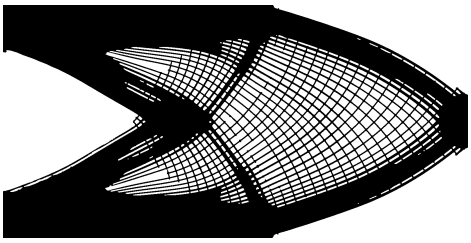

(a) $\epsilon = 20\ h^f$, $f_{min} = 4\ h^f$, $\mathcal{J}^\phi = 56.23$, and $V^\phi = 0.540$.

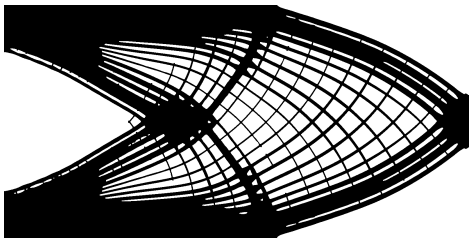

(b) $\epsilon = 40\ h^f$, and $f^{min} = 4\ h_f$, $\mathcal{J}_\phi = 58.57$, and $V^\phi = 0.510$.

Figure 5.2: Michell cantilever problem projected on a fine scale of 1600×800.

5.2 Multi-scale design of coated structures

Coated structures consist of a solid material and a porous infill. This class of structures can benefit from the desired properties of using porous infill material, *e.g.* good energy

absorption, an high thermal and acoustic insulation properties. Compared to their solid counterparts, coated structures can exhibit increased buckling stability [Clausen et al., 2016], and a better performance w.r.t unpredicted loading conditions and material deficiency [Wu et al., 2018].

In the context of density-based topology optimization, Clausen et al. [2015a, 2017] presented a method to optimize a coated structure with a solid isotropic shell and porous isotropic infill material. This approach has been extended by Wu et al. [2017] to allow for a density-based infill material. This means that a more complex and locally optimized infill description can be used; however, at a high computational cost since a fine mesh is required for fine details. To get a locally optimized infill description at a low computational cost, it is possible to represent the spatially varying infill by homogenized microstructures, as is proposed in [P4].

5.2.1 Homogenization-based topology optimization of coated structures

Analogous to Clausen et al. [2015a], we use two fields to distinguish between regions of the domain that consist of coating Ω_c, lattice-like infill Ω_l or void Ω_v. To do so, field φ is used to represent the base structure and field τ to describe the coating, such that,

$$\boldsymbol{x} \in \begin{cases} \Omega_v & \text{if} \quad \varphi(\boldsymbol{x}) = 0 \quad \text{and if } \tau(\boldsymbol{x}) = 0, \\ \Omega_l & \text{if} \quad \varphi(\boldsymbol{x}) = 1 \quad \text{and if } \tau(\boldsymbol{x}) = 0, \\ \Omega_c & \text{if} \quad \tau(\boldsymbol{x}) = 1. \end{cases} \tag{5.4}$$

Successive filter operations are used to obtain φ and τ. The first filter operation that is used is the Helmholtz-type PDE-based density filter [Lazarov and Sigmund, 2011], for which scalar R describes the length-scale imposed by the filter operation. Furthermore, the smoothed Heaviside projection function introduced by Wang et al. [2010] is used (see, Equation 5.2), where scalar $\eta \in [0, 1]$ is the threshold parameter, and β determines the steepness of the projection. The successive smoothing projection and gradient operations are shown in Figure 5.3.

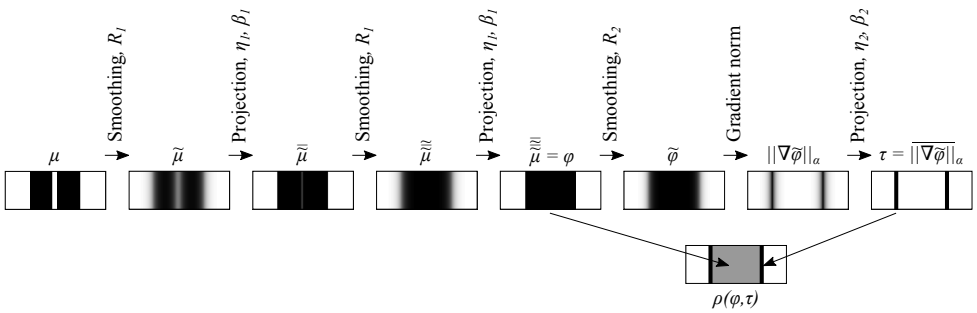

Figure 5.3: Subsequent filtering steps, allowing to separate the base structure φ and the coating τ.

The design field μ is filtered and projected twice using filter radius R_1, and parameters β_1 and η_1, which indirectly control the length-scale of φ. The base structure which is now either 0 or 1, is smoothed again using $R_2 < R_1$, the coating layer can then be defined by taking the Euclidean norm of the spatial gradients of $\tilde{\varphi}$. $\|\nabla\tilde{\varphi}\|$ is then normalized such that the largest possible gradient norm corresponds to 1. For this, a normalization factor α is used that can be related to R_2 as is described in [Clausen et al., 2015a]. The normalized gradient norm, written as $\|\nabla\tilde{\varphi}\|_\alpha$ is subsequently projected using β_2 and η_2 to define the coating field $\tau = \overline{\|\nabla\tilde{\varphi}\|}_\alpha$. In Clausen et al. [2015a] an analytical relation is shown between R_2 and the maximum coating thickness, which is used to determine R_2 for a user-specified coating thickness t_{ref}.

$$R_2 = \frac{\sqrt{3}}{\ln(2)} t_{ref} \approx 2.5 t_{ref}. \tag{5.5}$$

It can be seen that for the design field a double smoothing and projection (DSP) approach as proposed by Christiansen et al. [2015] is used. The reason is that numerical experiments using a single smoothing and projection (SSP) approach showed the possibility that fields φ and τ describing the base structure and coating, did not converge exactly to 0 or 1. More details on the parameter for the chosen filter scheme and the parameter choices are given in [P4]. Furthermore, it should be noted that the use of homogeneous Neumann boundary conditions used in the smoothing operation with the PDE-based filter causes artifacts on the optimized design near the domain boundary. A method to treat this, based on the domain extension approach proposed by Clausen and Andreassen [2017] is given in [P4].

With the description of the coating and the infill, it is possible to interpolate the elasticity tensor $\boldsymbol{E}$, and the density description ρ throughout domain Ω.

$$\rho(\varphi, \tau, a_1, a_2) = \rho^I(a_1, a_2)\varphi + (1 - \rho^I(a_1, a_2)\varphi)\tau. \tag{5.6}$$

Similarly, the local elasticity tensor $\boldsymbol{E}$ can be defined.

$$\boldsymbol{E}(\varphi, \tau, \theta, a_1, a_2) = 10^{-9}\boldsymbol{E}^0 + \Big(\boldsymbol{E}^I(\theta, a_1, a_2) - 10^{-9}\boldsymbol{E}^0\Big)\varphi^p + (\boldsymbol{E}^0 - \boldsymbol{E}^I(\theta, a_1, a_2)\varphi^p)\tau. \tag{5.7}$$

For the infill material, the square unit-cell with rectangular hole is used (see Figure 2.3). The elasticity tensor of the infill $\boldsymbol{E}^I$ is based on the orientation θ, and height a_1 and width of the hole a_2. Furthermore, ρ^I is the local density of the infill material, and $\boldsymbol{E}^0$ the elasticity tensor of the solid coating. Parameter p is a penalization parameter, to penalize intermediate values of φ. More details regarding the implementation, parameter choices and sensitivity analysis are given in [P4]. Finally, I should mention that the above-mentioned procedure works for any class microstructures for the infill material, *e.g.* rank-N laminates.

5.2.2 Numerical examples

To demonstrate the performance of the method, consider the MBB-beam example shown in Figure 5.4. The dotted line represents the extended filter domain, while

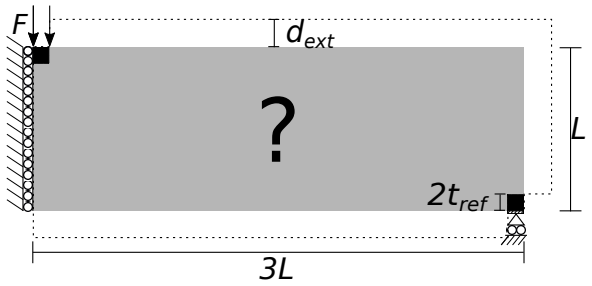

Figure 5.4: Design domain Ω and boundary conditions of the MBB-beam. Ω is indicated using gray material, the extended filter domain is bounded by the dotted line.

the design domain is sown in gray. Furthermore, solid material is prescribed at the boundary conditions, which are applied in a distributed sense.

Different optimization problems can be envisioned with various restrictions on the infill material. Three problem forms are shown, all using a constant infill density ρ^I. The simplest (*Problem 0*) is to use an isotropic infill material as is proposed by Clausen et al. [2015a], with a Young's modulus that satisfies the upper Hashin-Shtrikman bound [Hashin and Shtrikman, 1963]. For *Problem 1* orthotropic infill material using a square hole, *i.e.* $a_1 = a_2$ is considered. For *Problem 2* the shape of the hole is allowed to vary with an upper bound a_u on a_1 and a_2.

For the examples a discretization of 300×100 elements is used; furthermore $V_{max} = 0.4$, $R_1 = 0.15\ L$ and $t_{ref} = 0.03\ L$ is used. The compliance values $\mathcal{J}^c$ corresponding to the three problem types for different infill volume fractions ρ^I are shown in Table 5.3.

Table 5.3: Compliance $\mathcal{J}^c$ for different problem formulations and different infill densities ρ^I.

	$\rho^I = 0.4$	$\rho^I = 0.5$	$\rho^I = 0.6$	$\rho^I = 0.7$	$\rho^I = 0.8$	$\rho^I = 0.9$
Problem 0	362.83	325.94	297.78	279.80	256.68	237.63
Problem 1	318.45	291.14	274.92	266.85	251.38	236.37
Problem 2	267.92	247.52	234.30	227.02	219.67	217.73

As expected a better performance is obtained when more anisotropy is introduced in the microstructures. Furthermore, it is clear that for larger infill densities the structures converge to the results of a three-field SIMP approach (SIMP with smoothing and projection). The MBB-beam optimized using three-field SIMP has a corresponding compliance $\mathcal{J}^c = 213.57$. Finally, I should mention that more types of optimization problems can be envisioned, *e.g.* using a spatially varying infill density ρ^I as is described in [P4].

The optimized coated structures can be projected on a fine mesh of 3000×1000 elements, using Equations 4.2 and 4.4. In Figure 5.5(a) the design using *Problem 1* and $\rho^I = 0.5$ is shown for $\epsilon = 20\ h^f$. The compliance of the projected design

$\mathcal{J}^\phi = 307.93$ is very similar to the compliance of the homogenization-based design on the fine mesh $\mathcal{J}^f = 305.32$.

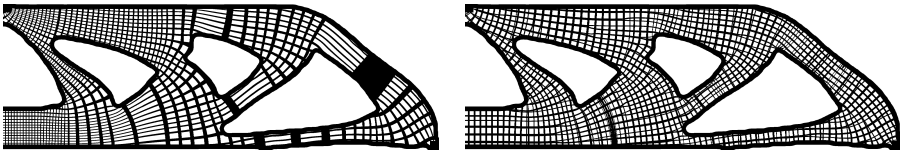

(a) Without adaptive periodicity. (b) With adaptive periodicity.

Figure 5.5: Projected designs for the MBB-example optimized using *Problem 1* and $\rho^I = 0.5$, the designs are projected on a mesh of 3000×1000 elements, using $\epsilon = 20\ h^f$.

Unfortunately however, the local layer spacing λ_i is distorted, resulting in long thin members, which are prone to local buckling. To avoid long thin members, the same design can be projected using the adaptive periodicity approach presented in Section 4.3.2. The projected shape with a similar compliance of $\mathcal{J}^\phi = 307.58$ is shown in Figure 5.5(b).

Finally, the proposed approach to do multi-scale design for coated structures is compared to the method by Wu et al. [2017] where the infill is optimization using a density-based approach. For the approach by Wu et al. [2017] similar settings as for the example with $\rho^I = 0.5$ and *Problem 2* are used; however, the optimization is performed on a resolution of 600×200 element to represent fine details. It should be noted that the optimization procedure took nearly five hours, hence a finer resolution was not considered practical. The performance of this structure, evaluated at a fine mesh of 3000×1000 elements is $\mathcal{J}^f = 281.95$, and the corresponding structure can be seen in Figure 5.6(a).

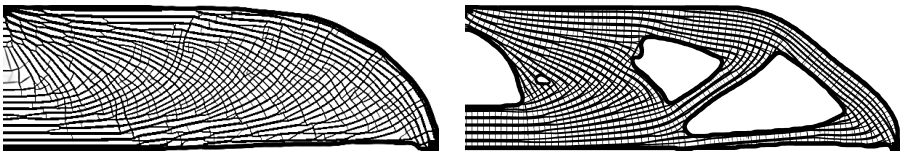

(a) Infill design using SIMP. (b) Proposed multi-scale procedure.

Figure 5.6: Comparison of the MBB-beam example using a SIMP-based approach [Wu et al., 2017], and the proposed multi-scale approach using *Problem 2* and $\rho^I = 0.5$.

The homogenization-based design using $\rho^I = 0.5$ and *Problem 2*, evaluated at a fine mesh of 3000×1000 elements has $\mathcal{J}^f = 256.31$. The corresponding projected design using the adaptive periodicity approach with $\epsilon = 20\ h^f$ can be seen in Figure 5.6(b). Compliance $\mathcal{J}^\phi = 261.96$ is significantly lower than the design with density-based infill, while the multi-scale design procedure took less than 24 minutes. Hence, using a multi-scale design method better performing and more detailed

design can be achieved, with a reduction of at least an order of magnitude in the computational cost, compared to conventional density-based topology optimization.

5.3 Optimizing the microstructure orientation

Besides requiring optimal microstructures, the projection procedure described in the previous chapter, requires the layer widths and orientations to be smoothly varying throughout domain Ω. Hence, it is not possible to interpret a rank-2 laminate on a single scale when the two layers are interchanged locally. In general, it can be observed that if the layer orientations θ_i vary smoothly, the corresponding widths w_i vary smoothly as well. Therefore, I will discuss several methods that can be used to obtain smooth and continuous layer orientations. This is an active research topic in itself, that overlaps with the research field of composite optimization for tape layering machines (see *e.g.* [Peeters et al., 2015]).

5.3.1 Orientation based on the principal directions

As is discussed by Pedersen [1989, 1990], the optimal orientation of an orthotropic composite is aligned with the principal strain directions. It can be shown that for a stationary point, the principal stress and strain directions are the same. A similar result can be derived when the optimization problem is written in terms of stresses [Allaire, 2002] As is discussed by Norris [2005], these results can be extended in 3D. Furthermore, it can be shown that in a similar fashion to [Pedersen, 1989], optimality conditions can be derived for orienting an orthotropic composite s.t. multiple loading conditions [Díaz and Bendsøe, 1992].

Hence, it is possible to obtain optimal microstructure orientations for orthogonal microstructures (*e.g.* rank-2 or the square unit-cell with rectangular hole) based on the principal stresses. This requires an accurate stress calculation in Ω for each design iteration; subsequently, the orientation of the microstructures can be updated to align with these directions. In 2D it is possible to sort the principal stresses such that the two principal values σ_I and σ_{II} and directions are continuous through the domain (*i.e.* smooth up to 180 degrees). In other words, the directions do not interchange if there is multiplicity in the eigenvalues or when the absolute values are similar. To do so, the principal stress values can be calculated from stress tensor $\boldsymbol{\sigma}$ as,

$$\begin{aligned} \sigma_I &= \frac{\sigma_{11}+\sigma_{22}}{2} + \sqrt{(\frac{\sigma_{11}-\sigma_{22}}{2})^2 + \sigma_{12}^2}, \\ \sigma_{II} &= \frac{\sigma_{11}+\sigma_{22}}{2} - \sqrt{(\frac{\sigma_{11}-\sigma_{22}}{2})^2 + \sigma_{12}^2}. \end{aligned} \tag{5.8}$$

The eigenvectors corresponding to σ_I and σ_{II} can subsequently be used to align the microstructures. Where it has to be noted that the above-mentioned sorting has been used in [P1], [P2] and [P4].

Unfortunately, such a smooth parameterization cannot be found in 3D, due to the cubic root that has to be solved for in the eigenvalue problem. By using Cardano's method [Smith, 1961] there is an inherent ordering in the obtained principal stress

values, *i.e.* $\sigma_I \geq \sigma_{II} \geq \sigma_{III}$, this means that the layer directions swap 90 degrees at points where there is multiplicity in the eigenvalues.

Several methods have been tested to determine whether it is possible to identify the surfaces where there is multiplicity of eigenvalues. For example, calculating the discriminant of the cubic equation should give such an indication, *i.e.* when the discriminant goes to zero two or more eigenvalues are identical. Unfortunately, the calculated stress values using tri-linear finite elements are not accurate enough to allow for such a procedure. A more accurate stress description can be obtained by either using higher-order finite elements [Szabó and Babuska, 1991], or using stress recovery techniques [Payen and Bathe, 2012; Sharma et al., 2018; Zienkiewicz and Zhu, 1992] ; however, these methods have not been implemented in this work.

5.3.2 Comparing gradient-based update vs. principal directions

It is also possible to align the microstructure orientation based on the gradients. A downside of such an approach is that extra design variables are required in the gradient-based optimization algorithm. However, the performance of the optimized designs is not affected. To demonstrate this, consider the Michell cantilever example shown in Figure 3.3(a).

A rank-2 laminate is used to parameterize the microstructure, with $E_0 = 1$, $\nu_0 = 0.3$ and $V_{max} = 0.3$. Five different methods are used to test the alignment of the microstructure. Using *Method 1*, the orientation is updated for each design iteration, based on the principal directions. Afterwards, design vectors $\boldsymbol{\mu}_1$ and $\boldsymbol{\mu}_2$ are updated using the new orientation. For *Method 2*, $\boldsymbol{\mu}_1$ and $\boldsymbol{\mu}_2$ are updated based on the old orientation, used to calculate displacement fields of the current iteration. Furthermore, gradient-based optimization for the angles is performed using a uniform starting guess (SG) for the angle field $\boldsymbol{\theta} = 0$ (*Method 3*), and SG of $\boldsymbol{\theta} = \pi/4$ (*Method 4*). Finally, gradient-based optimization is performed with a SG based on the principal directions for a domain consisting of isotropic material (*Method 5*). The corresponding compliance values for all alignment methods and using different discretizations can be seen in 5.4.

Table 5.4: Compliance values $\mathcal{J}^c$ for the Michell cantilever, optimized using different discretizations and different alignment methods.

Method	40×20	80×40	120×60	160×80	200×100
1	89.61	89.37	89.51	89.79	90.19
2	89.63	89.37	89.56	89.78	90.19
3	89.41	89.13	89.29	89.86	91.17
4	89.39	89.04	89.02	89.38	89.48
5	89.40	89.11	89.16	89.24	89.42

It can be seen that the designs obtained with the different alignment methods perform almost identical, where it has to be noted that similar observations can be made for other optimization examples. Especially the order of how the layer widths $\boldsymbol{\mu}_i$ are updated using principal directions, does not seem to have an influence on

the performance. In general, slightly better objective values can be reached using gradient-based alignment for the angles. A possible explanation can be that the gradients are directly obtained w.r.t. the primal fields instead of the stresses, which are less accurate. If gradient-based optimization is performed using a starting guess based on the principal directions, smooth and continuous angle fields can be obtained.

A similar experiment can be performed in 3D, resulting into the same conclusions. However, when the principal stress directions are used for the alignment, layer jumps can occur when two eigenvalues are very close, *i.e.* the corresponding directions interchange during the iterations. Therefore, in 3D examples it is recommended to update both layer widths and orientations based on their gradients.

5.3.3 Methods to regularize orientation

The optimized angles in 3D are only smooth up to 90 degrees, which means that the mapping functions ϕ_i cannot be calculated correctly. Therefore, it is important to look at methods that can restrict/regularize the change in orientation, such that smooth angle fields are ensured.

In this context Greifenstein and Stingl [2016] considered slope constraints on the orientation field. This method works well, and the maximum curvature can be restricted such that smooth angle fields are obtained. However, introducing a large number of additional constraints significantly slows down the optimization process. Furthermore, putting a severe restricting the orientation can result in a reduced optimality, since it is very likely the optimizer gets stuck in worse local minima compared to an unconstrained optimization problem, for which the optimized solution might be smooth.

To overcome the large number of local constraints, and to allow for smooth orientations, Nomura et al. [2014] introduced a vector based angle parameterization. The vector based representation allows for the angle θ to be represented by 2 vector components in x and y-direction in 2D, and three components in 3D [Petrovic et al., 2017]. The angle defined by the vector components is considered twice the angle of the microstructure θ. Hence, the same vector is used to describe a microstructure if it is rotated 180 degrees. Regularization is performed independently on the x and y components of the vector using a PDE-based filter scheme. The filtered components are then projected back to a vector of unit-length. Although the method looks promising, no exact maximum restriction can be ensured since the filter is applied on the unprojected vector components. Furthermore, the numerical examples shown in [Nomura et al., 2014] indicate that the proposed regularization can lead to quite a large reduction of optimality.

In a different approach, Allaire et al. [2018] also use vector to represent the microstructure orientation in 2D. The orientation is regularized by penalizing the Euclidean norm of the curvature, *i.e.* the angle gradient. It should be noted that the starting guess used in the regularization is based on the principal directions. This means that optimized angle field is smooth throughout the domain, while no bad performing local optima are encountered.

Besides, using a vector based parameterization of the orientation, a regularization can be envisioned directly using the orientation angle θ. To do so, consider edge or

face n between two adjacent elements i and j. A penalty function $\mathcal{P}_n \in [0,1]$ can be envisioned, which is based on the square of the inner product between two layer normals,

$$\mathcal{P}_n = \frac{1}{2} - \frac{1}{2}\cos\left\{2\theta(\boldsymbol{x}^i) - 2\theta(\boldsymbol{x}^j)\right\}. \tag{5.9}$$

Here the penalization value is 1 for an angle difference of $\pi/2$, and 0 if the angle difference is $k\pi$ for any integer k. Penalty function $\mathcal{P}_n$ can be used to apply a local curvature constraint between each adjacent pair of elements. However, it is also possible to aggregate the penalty functions for all edges/faces n_f using a factor q, such that a single regularization function $\mathcal{J}_\theta$ can be added to the optimization objective.

$$\mathcal{J}_\theta = \gamma_\theta\Big(\sum_{n=1}^{n_f} \mathcal{P}_n^q\Big)^{1/q}. \tag{5.10}$$

Numerical experiments for various values of γ_θ and q indicate, that it is impossible to get an angle field that is smoothly defined up to 180 degrees, without a severe reduction in compliance $\mathcal{J}$, when a uniform starting guess is used. However, when the principal directions are used in 2D examples as starting guess, smooth orientation fields have been obtained. In general a norm aggregation q of 1 is recommended, since locally it can be required that the angle changes rapidly, *e.g.* close to a boundary condition.

Unfortunately, no good regularization method has been developed to obtain angle fields that are smooth up to π in 3D. However, it should be mentioned that very recently, Geoffroy-Donders et al. [2018] proposed a regularization method that seems to work well for 3D problems s.t. a single loading case.

5.3.4 Multi-scale design for multiple load cases

As is discussed before, there are many different ways to parameterize a microstructure for multiple loading cases. To demonstrate these differences, the two load bridge example shown in Figure 5.7 is considered. It should be noted that the loads and supports are applied in a distributed manner, with equal weights for load cases; furthermore, the problem is solved for $E_0 = 1$, $\nu_0 = 0.3$, $E_{min} = 10^{-4}E_0$ and $V_{max} = 0.2$.

First of all, a parameterization using a density field ρ and four trigonometric moments $\boldsymbol{m}$ is used. A hierarchical optimization problem is solved, since the strain energy can be maximized for each element separately. Although this approach is used by Díaz et al. [1995], it is highly unstable. The local elasticity tensor $\boldsymbol{E}^{RN}$ differs drastically during the design iterations, which means that convergence can only be guaranteed by severe restrictions on the allowed change of the design. Better results are obtained if the local problems concern minimization of the complementary energy (see, *e.g.* [Cherkaev et al., 1998]). Nevertheless, it is still required to have a maximum allowable change of 0.05 on the design variables during the iterations.

The optimization procedure with a moment parameterization is computationally demanding, due to the large number of local sub-problems. Unfortunately, this meant that a design on a coarse mesh of 40×20 elements, was the largest resolution that can

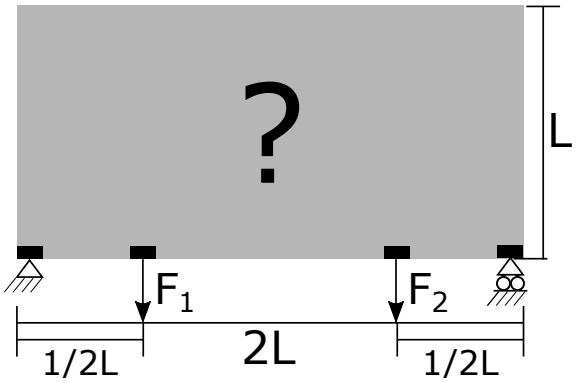

Figure 5.7: Design domain Ω and boundary conditions of the two load bride example. The loads and supports are applied in a distributed manner.

be achieved in less than a day on a standard PC using a single core MATLAB code. To identify if better results can be obtained with other rank-N parameterizations, the relative layer widths μ_i and orientations θ_i of a rank-N design are updated using an optimization problem of Equation 2.27. This approach reduces the computational cost with more than 3 orders of magnitude compared to a moment parametrization, allowing for finer meshes as can be seen in Table 5.5.

Table 5.5: Compliance values $\mathcal{J}$ for the two load bridge example, optimized using different discretizations and different alignment methods.

Method	40×20	80×40	120×60	160×80	200×100
moment form	38.39	-	-	-	-
rank-2	38.41	38.65	38.99	39.42	40.00
rank-3	37.97	38.10	38.23	38.36	38.45
rank-4	37.97	38.08	38.26	38.41	38.62
rank-3 reg	38.53	38.59	38.88	39.08	39.30
rank-$(2n_\sigma)$ (princ.)	39.97	39.19	39.31	39.77	40.62
rank-$(2n_\sigma)$ (princ. as SG)	37.95	38.06	38.18	38.32	38.45

It can be seen that the difference in performance using rank-2 an rank-3 laminates is surprisingly small. Using only 2 layers, a near-optimal design can be achieved. As expected, introducing a rank-4 parameterization does not result in a better performing design compared to an optimal rank-3; however, both perform better than a design with a moment parameterization. Furthermore, the regularization scheme presented above, is used to obtain smooth orientation fields θ_1, θ_2 and θ_3 of the rank-3 design. As can be seen in Table 5.5 the corresponding performance (depending on γ_θ) is slightly worse. However, all orientation fields are smooth and the corresponding design can be projected on a single scale using Equations 4.2 and 4.4, as can be seen in Figure 5.8(a).

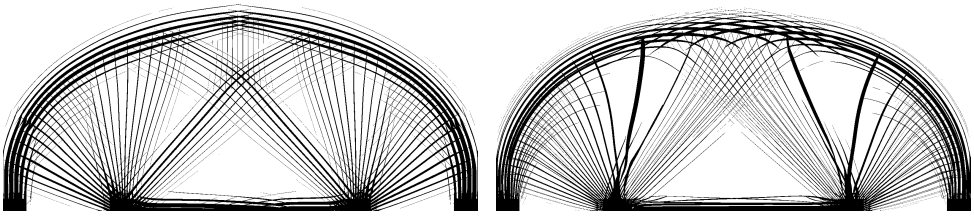

(a) Rank-3, regularized orientation. (b) Rank-4, SG based on principal directions.

Figure 5.8: Two angle parameterizations of the two load bridge example, projected on a fine mesh of 1600×800 elements, using $\epsilon = 20\ h^f$.

Although the fields describing the orientation and layer widths are smooth throughout Ω, it can be seen that the projected shape is not completely well-connected. Structural members, which are projected from the first layer seem to correspond in another part of the domain to the second layer, resulting in a slight mismatch at the transition from one layer to the other. This leads to a worse compliance for the projected design $\mathcal{J}^\phi = 69.71$.

To identify if continuous projected members can be achieved from the load to the supports, the principal stress directions of each individual load case are used as layer directions. Hence, a rank-$(2n_\sigma)$ laminate is used, resulting in 4 layers for the two load bridge example. The resulting compliance when the layer directions are updated using these principal directions can also be seen in Table 5.5. Furthermore, a rank-$(2n_\sigma)$ is used where the orientation is updated in a gradient-based fashion, with a SG based on the principal directions. The corresponding projected design, shown in Figure 5.8(b) consists of overlapping members. Hence, two or more layers have similar orientation and finite width. Unfortunately, an evaluation of the compliance of the projected shape $\mathcal{J}^\phi = 182.49$ reveals that the fine scale design has a significantly reduced performance compared to the homogenization-based design.

To conclude, for multiple load-case problems it is not enough to have smooth and continuous orientation field to achieve well-performing single-scale designs. Something extra is needed, *e.g.* separate layers with the same orientation need to be avoided. Finding a method that can do this, such that the projected designs have similar performance as the homogenization-based designs remains a topic of research. Nevertheless, the projected shapes shown in Figures 5.8 can be obtained in less than 5 minutes, and can give valuable information to engineers on the shape of an optimal design.

6 Concluding remarks

This thesis considered the interpretation of multi-scale designs optimized for maximum stiffness on a single length-scale. By performing homogenization-based topology optimization with optimal or near-optimal microstructures, a multi-scale design can be obtained in less than 10 minutes for 2D problems on a standard PC. Even 3D designs, although not presented in this thesis, can be obtained without requiring parallelized codes.

It is my opinion that this relatively short time allows engineers and designers to quickly gain insight in the optimal material distribution, layer directions, and the lower bound on the performance for compliance minimization problems. Hence, it is somewhat disappointing to see that almost none of the works on multi-scale topology optimization show a comparison with what is theoretically possible if optimal microstructures are used. Especially, since the results in this thesis and attached papers do indicate that it pays off to exploit the existing knowledge on optimal microstructures.

In the context of material design it is shown that when an optimal rank-3 laminate is known, simpler and better performing microstructures can be reached compared to the use of classical starting guesses. Furthermore, a class of simple and manufacturable truss lattice structures has been proposed, which performs close to what is theoretically possible. Not only are these designs highly optimal for anisotropic loading conditions, their simple geometry allows for manufacturing using 3D printing techniques.

Multi-scale designs for 2D problems subject to a single loading case can be efficiently approximated on a single-scale. Several methods are presented to control the corresponding feature size and microstructure spacing. However, for the treatment of singularities and other improvements it can be beneficial to look to the field of geometry processing, since similar types of problems are considered.

Compared to standard density-based topology optimization, the required computational cost can be reduced by more than 50 times! Nevertheless, extensions to multiple load cases and 3D are not trivial, partially due to the non-uniqueness of the optimal microstructures and partially due to the large number of layers involved. Nevertheless, smooth multi-scale designs for multiple load cases can be projected on a single scale, and although not completely well-connected, these projected shapes still provide great insight on the optimal design, at a low computational cost.

More research has to be performed on the development of regularization methods, to allow for well-connected and smoothly varying layers throughout the macroscopic domain. It is my belief that a good method can and will be found, due to the non-uniqueness of the optimal microstructures, which allows for something extra to be optimized. A major challenge when regularization methods are considered is to avoid a large reduction in optimality. A smooth and well-connected shape that is far from optimal is not desired anyway. Hence, the obtained designs should always be compared to what is truly optimal.

Finally, it is important that more complex problems than compliance minimization are considered. E.g. Krog and Olhoff [1997] consider optimization of fundamental frequency for free vibration problems. Different types of physics or non-linear behavior should be considered for multi-scale design problems. A key part of the work here includes finding an optimal or near-optimal class of microstructures that cover the space of desired extremal properties. Doing this might be a Ph.D. project in itself. However, if a well-performing macroscopically smooth parameterization can be found, the potential savings in computational cost can be enormous.

Bibliography

N. Aage, E. Andreassen, and B. S. Lazarov. Topology optimization using PETSc: An easy-to-use, fully parallel, open source topology optimization framework. *Structural and Multidisciplinary Optimization*, 51(3):565–572, 2014. doi:10.1007/s00158-014-1157-0.

N. Aage, E. Andreassen, B. S. Lazarov, and O. Sigmund. Giga-voxel computational morphogenesis for structural design. *Nature*, 550(7674):84–86, oct 2017. doi:10.1038/nature23911.

J. Alexandersen and B. Lazarov. Topology optimisation of manufacturable microstructural details without length scale separation using a spectral coarse basis preconditioner. *Computer Methods in Applied Mechanics and Engineering*, 290: 156–182, 2015. doi:10.1016/j.cma.2015.02.028.

G. Allaire. *Shape Optimization by the Homogenization Method*. Springer-Verlag, New York, 2002.

G. Allaire and S. Aubry. On optimal microstructures for a plane shape optimization problem. *Structural optimization*, 17(2):86–94, 1999. doi:10.1007/BF01195933.

G. Allaire and G. A. Francfort. A numerical algorithm for topology and shape optimization. In *Topology Design of Structures*, pages 239–248. Springer Netherlands, 1993. doi:10.1007/978-94-011-1804-0_16.

G. Allaire and R. Kohn. Optimal-design for minimum weight and compliance in plane-stress using extremal microstructures. *European Journal of Mechanics A-solids*, 12(6):839–878, 1993.

G. Allaire, Z. Belhachmi, and F. Jouve. The homogenization method for topology and shape optimization. single and multiple loads case. *Revue Européenne des Éléments Finis*, 5(5-6):649–672, 1996. doi:10.1080/12506559.1996.10511241.

G. Allaire, E. Bonnetier, G. Francfort, and F. Jouve. Shape optimization by the homogenization method. *Numerische Mathematik*, 76(1):27–68, 1997. doi:10.1007/s002110050253.

G. Allaire, P. Geoffroy-Donders, and O. Pantz. Topology optimization of modulated and oriented periodic microstructures by the homogenization method. *Computers & Mathematics with Applications*, aug 2018. doi:10.1016/j.camwa.2018.08.007.

L. Ambrosio and G. Buttazzo. An optimal design problem with perimeter penalization. *Calculus of Variations and Partial Differential Equations*, 1(1):55–69, mar 1993. doi:10.1007/bf02163264.

E. Andreassen and C. Andreasen. How to determine composite material properties using numerical homogenization. *Computational Materials Science*, 83:488–495, 2014. doi:10.1016/j.commatsci.2013.09.006.

E. Andreassen, A. Clausen, M. Schevenels, B. S. Lazarov, and O. Sigmund. Efficient topology optimization in MATLAB using 88 lines of code. *Structural and Multidisciplinary Optimization*, 43(1):1–16, 2010. doi:10.1007/s00158-010-0594-7.

E. Andreassen, B. S. Lazarov, and O. Sigmund. Design of manufacturable 3d extremal elastic microstructure. *Mechanics of Materials*, 69(1):1–10, 2014. doi:10.1016/j.mechmat.2013.09.018.

E. Andreassen, J. Jensen, O. Sigmund, and J. Thomsen. *Optimal Design of Porous Materials*. PhD thesis, 2015.

M. Avellaneda. Optimal bounds and microgeometries for elastic two-phase composites. *SIAM Journal on Applied Mathematics*, 47(6):1216–1228, 1987. doi:10.1137/0147082.

M. Avellaneda and G. Milton. Bounds on the effective elasticity tensor of composites based on two-point correlations. In *American Society of Mechanical Engineers, Petroleum Division (Publication) PD*, volume 24, pages 89–93. American Society of Mechanical Engineers (ASME), 1988.

C. Barbarosie and A.-M. Toader. Optimization of bodies with locally periodic microstructure. *Mechanics of Advanced Materials and Structures*, 19(4):290–301, 2012. doi:10.1080/15376494.2011.642939.

M. Bendsøe and N. Kikuchi. Generating optimal topologies in structural design using a homogenization method. *Computer Methods in Applied Mechanics and Engineering*, 71(2):197–224, 1988. doi:10.1016/0045-7825(88)90086-2.

M. Bendsøe and O. Sigmund. *Topology optimization-theory, methods, and applications*. Springer, Berlin, 2004.

M. P. Bendsøe. Optimal shape design as a material distribution problem. *Structural Optimization*, 1(4):193–202, 1989. doi:10.1007/bf01650949.

M. P. Bendsøe and R. B. Haber. The michell layout problem as a low volume fraction limit of the perforated plate topology optimization problem: An asymptotic study. *Structural optimization*, 6(4):263–267, 1993. doi:10.1007/BF01743385.

M. P. Bendsøe and O. Sigmund. Material interpolation schemes in topology optimization. *Archive of Applied Mechanics*, 69(9-10):635–654, 1999. doi:10.1007/s004190050248.

M. P. Bendsoe, J. M. Guedes, R. B. Haber, P. Pedersen, and J. E. Taylor. An analytical model to predict optimal material properties in the context of optimal structural design. *Journal of Applied Mechanics*, 61(4):930, 1994. doi:10.1115/1.2901581.

A. Bensoussan, J.-L. Lions, and G. Papanicolaou. *Asymptotic Analysis for Periodic Structures (Studies in mathematics and its applications)*. Elsevier Science Ltd, 1978. ISBN 0444851720.

D. Bommes, H. Zimmer, and L. Kobbelt. Mixed-integer quadrangulation. In *ACM SIGGRAPH 2009 papers on - SIGGRAPH09*. ACM Press, 2009. doi:10.1145/1576246.1531383.

R. T. Bonnecaze, G. J. Rodin, O. Sigmund, and J. S. Jensen. Systematic design of phononic band-gap materials and structures by topology optimization. *Philosophical Transactions of the Royal Society of London. Series A: Mathematical, Physical and Engineering Sciences*, 361(1806):1001–1019, 2003. doi:10.1098/rsta.2003.1177.

B. Bourdin. Filters in topology optimization. *International Journal for Numerical Methods in Engineering*, 50(9):2143–2158, 2001. doi:10.1002/nme.116.

B. Bourdin and R. V. Kohn. Optimization of structural topology in the high-porosity regime. *Journal of the Mechanics and Physics of Solids*, 56(3):1043–1064, 2008. doi:10.1016/j.jmps.2007.06.002.

T. Bruns and D. Tortorelli. Topology optimization of non-linear elastic structures and compliant mechanisms. *Computer Methods in Applied Mechanics and Engineering*, 190(26–27):3443–3459, 2001. doi:10.1016/S0045-7825(00)00278-4.

J. E. Cadman, S. Zhou, Y. Chen, and Q. Li. On design of multi-functional microstructural materials. *Journal of Materials Science*, 48(1):51–66, 2013. doi:10.1007/s10853-012-6643-4.

K.-T. Cheng. On non-smoothness in optimal design of solid, elastic plates. *International Journal of Solids and Structures*, 17(8):795–810, 1981. doi:10.1016/0020-7683(81)90089-5.

K.-T. Cheng and N. Olhoff. An investigation concerning optimal design of solid elastic plates. *International Journal of Solids and Structures*, 17(3):305–323, 1981. doi:10.1016/0020-7683(81)90065-2.

A. Cherkaev. *Variational Methods for Structural Optimization*. Springer-Verlag, New York, 2000.

A. Cherkaev and R. Palais. Optimal design of three-dimensional axisymmetric elastic structures. *Structural Optimization*, 12(1):35–45, 1996. doi:10.1007/bf01270442.

A. Cherkaev, L. Krog, and I. Kucuk. Stable optimal design of two-dimensional elastic structures. *Control and Cybernetics*, 27(2):265–282, 1998.

R. Christensen. Mechanics of low density materials. *Journal of the Mechanics and Physics of Solids*, 34(6):563–578, 1986. doi:10.1016/0022-5096(86)90037-2.

R. Christensen and F. Waals. Effective stiffness of randomly oriented fibre composites. *Journal of Composite Materials*, 6(4):518–532, 1972. doi:10.1177/002199837200600407.

R. E. Christiansen, B. S. Lazarov, J. S. Jensen, and O. Sigmund. Creating geometrically robust designs for highly sensitive problems using topology optimization. *Structural and Multidisciplinary Optimization*, 52(4):737–754, 2015. doi:10.1007/s00158-015-1265-5.

A. Clausen and E. Andreassen. On filter boundary conditions in topology optimization. *Structural and Multidisciplinary Optimization*, 56(5):1147–1155, 2017. doi:10.1007/s00158-017-1709-1.

A. Clausen, N. Aage, and O. Sigmund. Topology optimization of coated structures and material interface problems. *Computer Methods in Applied Mechanics and Engineering*, 290:524–541, 2015a. doi:10.1016/j.cma.2015.02.011.

A. Clausen, F. Wang, J. S. Jensen, O. Sigmund, and J. A. Lewis. Topology optimized architectures with programmable poisson's ratio over large deformations. *Advanced Materials*, 27(37):5523–5527, 2015b. doi:10.1002/adma.201502485.

A. Clausen, N. Aage, and O. Sigmund. Exploiting additive manufacturing infill in topology optimization for improved buckling load. *Engineering*, 2(2):250–257, 2016. doi:10.1016/J.ENG.2016.02.006.

A. Clausen, E. Andreassen, and O. Sigmund. Topology optimization of 3d shell structures with porous infill. *Acta Mechanica Sinica*, 33(4):778–791, 2017. doi:10.1007/s10409-017-0679-2.

P. Coelho, J. Cardoso, P. Fernandes, and H. Rodrigues. Parallel computing techniques applied to the simultaneous design of structure and material. *Advances in Engineering Software*, 42(5):219–227, 2011. doi:10.1016/j.advengsoft.2010.10.003.

P. Coelho, L. Amiano, J. Guedes, and H. Rodrigues. Scale-size effects analysis of optimal periodic material microstructures designed by the inverse homogenization method. *Computers & Structures*, 174:21–32, 2016. doi:10.1016/j.compstruc.2015.10.001.

R. D. Cook, D. S. Malkus, and M. E. Plesha. *Concepts and Applications of Finite Element Analysis*. Wiley, 2001. ISBN 0471356050.

A. D. Cramer, V. J. Challis, and A. P. Roberts. Microstructure interpolation for macroscopic design. *Structural and Multidisciplinary Optimization*, 53(3):489–500, 2015. doi:10.1007/s00158-015-1344-7.

J. D. Deaton and R. V. Grandhi. A survey of structural and multidisciplinary continuum topology optimization: post 2000. *Structural and Multidisciplinary Optimization*, 49(1):1–38, jul 2013. doi:10.1007/s00158-013-0956-z.

A. Díaz and R. Lipton. Optimal material layout for 3d elastic structures. *Structural Optimization*, 13(1):60–64, 1997. doi:10.1007/bf01198376.

A. Díaz and O. Sigmund. Checkerboard patterns in layout optimization. *Structural Optimization*, 10(1):40–45, 1995. doi:10.1007/bf01743693.

A. R. Díaz and M. P. Bendsøe. Shape optimization of structures for multiple loading conditions using a homogenization method. *Structural Optimization*, 4(1):17–22, mar 1992. doi:10.1007/bf01894077.

A. R. Díaz and R. Lipton. Optimal material layout in three-dimensional elastic structures subjected to multiple loads. *Mechanics of Structures and Machines*, 28 (2-3):219–236, 2000. doi:10.1081/sme-100100619.

A. R. Díaz, R. Lipton, and C. A. Soto. A new formulation of the problem of optimum reinforcement of reissner-mindlin plates. *Computer Methods in Applied Mechanics and Engineering*, 123(1):121–139, 1995. ISSN 0045-7825. doi:10.1016/0045-7825(94)00777-K.

C. Fleury. Mathematical programming methods for constrained optimization: dual methods. In P. Kamat, editor, *Structural optimization: status and promise, progress in Astronautics and Aeronautics*, volume 150, chapter 7, pages 123–150. AIAA, 1993.

G. Francfort, F. Murat, and L. Tartar. Fourth-order moments of nonnegative measures on s2 and applications. *Archive for Rational Mechanics and Analysis*, 131(4):305–333, 1995. doi:10.1007/bf00380913.

G. A. Francfort and F. Murat. Homogenization and optimal bounds in linear elasticity. *Archive for Rational Mechanics and Analysis*, 94(4):307–334, 1986. doi:10.1007/BF00280908.

P. Geoffroy-Donders, G. Allaire, and O. Pantz. 3-d topology optimization of modulated and oriented periodic microstructures by the homogenization method. working paper or preprint, 2018.

Y. Grabovsky and R. V. Kohn. Anisotropy of the Vigdergauz microstructure. *Journal of Applied Mechanics*, 62(4):1063–1065, 1995. ISSN 0021-8936. doi:10.1115/1.2896043.

J. Greifenstein and M. Stingl. Simultaneous parametric material and topology optimization with constrained material grading. *Structural and Multidisciplinary Optimization*, pages 1–14, 2016. doi:10.1007/s00158-016-1457-7.

J. Guedes and N. Kikuchi. Preprocessing and postprocessing for materials based on the homogenization method with adaptive finite element methods. *Computer Methods in Applied Mechanics and Engineering*, 83(2):143–198, 1990. doi:10.1016/0045-7825(90)90148-F.

J. M. Guedes, H. C. Rodrigues, and M. P. Bendsøe. A material optimization model to approximate energy bounds for cellular materials under multiload conditions. *Structural and Multidisciplinary Optimization*, 25(5-6):446–452, 2003. doi:10.1007/s00158-003-0305-8.

J. K. Guest and J. H. Prévost. Design of maximum permeability material structures. *Computer Methods in Applied Mechanics and Engineering*, 196(4):1006–1017, 2007. ISSN 0045-7825. doi:10.1016/j.cma.2006.08.006.

J. K. Guest, J. H. Prévost, and T. Belytschko. Achieving minimum length scale in topology optimization using nodal design variables and projection functions. *International Journal for Numerical Methods in Engineering*, 61(2):238–254, aug 2004. doi:10.1002/nme.1064.

G. Gurtner and M. Durand. Stiffest elastic networks. *Proceedings of the Royal Society A: Mathematical, Physical and Engineering Sciences*, 470(2164):20130611–20130611, 2014. doi:10.1098/rspa.2013.0611.

V. Hammer, M. Bendsøe, R. Lipton, and P. Pedersen. Parametrization in laminate design for optimal compliance. *International Journal of Solids and Structures*, 34 (4):415–434, 1997. doi:10.1016/s0020-7683(96)00023-6.

Z. Hashin and S. Shtrikman. A variational approach to the theory of the elastic behaviour of multiphase materials. *Journal of the Mechanics and Physics of Solids*, 11(2):127–140, 1963. doi:10.1016/0022-5096(63)90060-7.

B. Hassani and E. Hinton. A review of homogenization and topology optimization I homogenization theory for media with periodic structure. *Computers & Structures*, 69(6):707–717, 1998a. doi:10.1016/S0045-7949(98)00131-X.

B. Hassani and E. Hinton. A review of homogenization and topology optimization II analytical and numerical solution of homogenization equations. *Computers & Structures*, 69(6):719–738, 1998b. doi:10.1016/S0045-7949(98)00132-1.

B. Hassani and E. Hinton. A review of homogenization and topology optimization III topology optimization using optimality criteria. *Computers & Structures*, 69 (6):739–756, 1998c. doi:10.1016/S0045-7949(98)00133-3.

R. H. W. Hoppe, C. Linsenmann, and S. I. Petrova. Primal-dual newton methods in structural optimization. *Computing and Visualization in Science*, 9(2):71–87, 2006. doi:10.1007/s00791-006-0018-9.

J. Jensen and O. Sigmund. Topology optimization for nano-photonics. *Laser & Photonics Reviews*, 5(2):308–321, 2011. doi:10.1002/lpor.201000014.

T. Jiang, J. Huang, Y. Wang, Y. Tong, and H. Bao. Frame field singularity correctionfor automatic hexahedralization. *IEEE Transactions on Visualization and Computer Graphics*, 20(8):1189–1199, aug 2014. doi:10.1109/tvcg.2013.250.

C. S. Jog, R. B. Haber, and M. P. Bendsøe. Topology design with optimized, self-adaptive materials. *International Journal for Numerical Methods in Engineering*, 37(8):1323–1350, 1994. doi:10.1002/nme.1620370805.

F. Kälberer, M. Nieser, and K. Polthier. Quadcover - surface parameterization using branched coverings. *Computer Graphics Forum*, 26(3):375–384, 2007. doi:10.1111/j.1467-8659.2007.01060.x.

M. Kočvara and S. Mohammed. Primal-dual interior point multigrid method for topology optimization. *SIAM Journal on Scientific Computing*, 38(5):B685–B709, 2016. doi:10.1137/15m1044126.

R. V. Kohn and G. Strang. Optimal design and relaxation of variational problems, i. *Communications on Pure and Applied Mathematics*, 39(1):113–137, jan 1986. doi:10.1002/cpa.3160390107.

M. Krein and A. Nudelman. *The Markov moment problem and extremal problems, Translations of Mathematical Monographs, Vol. 50*. American Mathematical Society, Providence, Rhode Island, 1977.

L. A. Krog and N. Olhoff. Topology and reinforcement layout optimization of disk, plate, and shell structures. In *Topology Optimization in Structural Mechanics*, pages 237–322. Springer Vienna, 1997. doi:10.1007/978-3-7091-2566-3_9.

U. D. Larsen, O. Sigmund, and S. Bouwsta. Design and fabrication of compliant micromechanisms and structures with negative poisson's ratio. *Journal of Microelectromechanical Systems*, 6(2):99–106, 1997. doi:10.1109/84.585787.

R. M. Latture, M. R. Begley, and F. W. Zok. Design and mechanical properties of elastically isotropic trusses. *Journal of Materials Research*, 33(03):249–263, 2018. doi:10.1557/jmr.2018.2.

B. S. Lazarov. Topology optimization using multiscale finite element method for high-contrast media. In *Large-Scale Scientific Computing*, pages 339–346. Springer Berlin Heidelberg, 2014. doi:10.1007/978-3-662-43880-0_38.

B. S. Lazarov and O. Sigmund. Filters in topology optimization based on Helmholtz-type differential equations. *International Journal for Numerical Methods in Engineering*, 86(6):765–781, 2011. doi:10.1002/nme.3072.

B. Lévy, S. Petitjean, N. Ray, and J. Maillot. Least squares conformal maps for automatic texture atlas generation. *ACM Transactions on Graphics*, 21(3), jul 2002. doi:10.1145/566654.566590.

T. Lewiński and G. I. N. Rozvany. Exact analytical solutions for some popular benchmark problems in topology optimization iii: L-shaped domains. *Structural and Multidisciplinary Optimization*, 35(2):165–174, 2008. doi:10.1007/s00158-007-0157-8.

T. Lewiński, M. Zhou, and G. Rozvany. Extended exact solutions for least-weight truss layouts—part i: Cantilever with a horizontal axis of symmetry. *International Journal of Mechanical Sciences*, 36(5):375–398, 1994a. doi:10.1016/0020-7403(94)90043-4.

T. Lewiński, M. Zhou, and G. Rozvany. Extended exact least-weight truss layouts—part ii: Unsymmetric cantilevers. *International Journal of Mechanical Sciences*, 36(5):399–419, 1994b. doi:10.1016/0020-7403(94)90044-2.

R. Lipton. On optimal reinforcement of plates and choice of design parameters. *Control Cybernetics*, 23(3):481–493, 1994a.

R. Lipton. A saddle-point theorem with application to structural optimization. *Journal of Optimization Theory and Applications*, 81(3):549–568, 1994b. doi:10.1007/bf02193100.

K. Liu and A. Tovar. An efficient 3d topology optimization code written in matlab. *Structural and Multidisciplinary Optimization*, 50(6):1175–1196, 2014. doi:10.1007/s00158-014-1107-x.

L. Liu, J. Yan, and G. Cheng. Optimum structure with homogeneous optimum truss-like material. *Computers & Structures*, 86(13):1417–1425, 2008. doi:10.1016/j.compstruc.2007.04.030. Structural Optimization.

K. A. Lurie and A. V. Cherkaev. G-closure of some particular sets of admissible material characteristics for the problem of bending of thin elastic plates. *Journal of Optimization Theory and Applications*, 42(2):305–316, 1984. doi:10.1007/bf00934301.

P. Martínez, P. Martí, and O. M. Querin. Growth method for size, topology, and geometry optimization of truss structures. *Structural and Multidisciplinary Optimization*, 33(1):13–26, 2007. doi:10.1007/s00158-006-0043-9.

M. C. Messner. Optimal lattice-structured materials. *Journal of the Mechanics and Physics of Solids*, 96:162–183, 2016. doi:10.1016/j.jmps.2016.07.010.

A. Michell. LVIII. the limits of economy of material in frame-structures. *The London, Edinburgh, and Dublin Philosophical Magazine and Journal of Science*, 8(47): 589–597, 1904. doi:10.1080/14786440409463229.

G. W. Milton. Modelling the properties of composites by laminates. In J. L. Ericksen, D. Kinderlehrer, R. Kohn, and J.-L. Lions, editors, *Homogenization and Effective Moduli of Materials and Media*, pages 150–174, New York, NY, 1986. Springer New York.

G. W. Milton. *The Theory of Composites*. Cambridge University Press, 2002. doi:10.1017/cbo9780511613357.

M. M. Neves, O. Sigmund, and M. P. Bendsøe. Topology optimization of periodic microstructures with a penalization of highly localized buckling modes. *International Journal for Numerical Methods in Engineering*, 54(6):809–834, 2002. doi:10.1002/nme.449.

M. Nieser, U. Reitebuch, and K. Polthier. CubeCover- parameterization of 3d volumes. *Computer Graphics Forum*, 30(5):1397–1406, aug 2011. doi:10.1111/j.1467-8659.2011.02014.x.

F. Niordson. Optimal design of elastic plates with a constraint on the slope of the thickness function. *International Journal of Solids and Structures*, 19(2):141–151, 1983. doi:10.1016/0020-7683(83)90005-7.

J. Nocedal and S. wright. *Numerical Optimization*. Springer, New York, 2006. doi:10.1007/978-0-387-40065-5.

T. Nomura, E. M. Dede, J. Lee, S. Yamasaki, T. Matsumori, A. Kawamoto, and N. Kikuchi. General topology optimization method with continuous and discrete orientation design using isoparametric projection. *International Journal for Numerical Methods in Engineering*, 101(8):571–605, dec 2014. doi:10.1002/nme.4799.

A. Norris. A differential scheme for the effective moduli of composites. *Mechanics of Materials*, 4(1):1–16, 1985. doi:10.1016/0167-6636(85)90002-x.

A. N. Norris. Optimal orientation of anisotropic solids. *The Quarterly Journal of Mechanics and Applied Mathematics*, 59(1):29–53, nov 2005. doi:10.1093/qjmam/hbi030.

N. Olhoff, K. A. Lurie, A. V. Cherkaev, and A. V. Fedorov. Sliding regimes and anisotropy in optimal design of vibrating axisymmetric plates. *International Journal of Solids and Structures*, 17(10):931–948, 1981. doi:10.1016/0020-7683(81)90032-9.

N. Olhoff, E. Rønholt, and J. Scheel. Topology optimization of three-dimensional structures using optimum microstructures. *Structural Optimization*, 16(1):1–18, 1998. doi:10.1007/bf01213995.

M. Osanov and J. K. Guest. Topology optimization for architected materials design. *Annual Review of Materials Research*, 46(1):211–233, 2016. doi:10.1146/annurev-matsci-070115-031826.

O. Pantz and K. Trabelsi. A post-treatment of the homogenization method for shape optimization. *SIAM Journal on Control and Optimization*, 47(3):1380–1398, 2008. doi:10.1137/070688900.

O. Pantz and K. Trabelsi. Construction of minimization sequences for shape optimization. In *15th International Conference on Methods and Models in Automation and Robotics (MMAR)*, pages 278–283, 2010. doi:10.1109/MMAR.2010.5587222.

B. Paul. Prediction of elastic constants of multiphase materials. *Transaction of the American Institute of Mining and Metallurgical Engineers*, 218(1):36–41, 1960.

D. J. Payen and K.-J. Bathe. A stress improvement procedure. *Computers & Structures*, 112-113:311–326, 2012. doi:10.1016/j.compstruc.2012.07.006.

P. Pedersen. On optimal orientation of orthotropic materials. *Structural optimization*, 1(2):101–106, 1989. doi:10.1007/BF01637666.

P. Pedersen. Bounds on elastic energy in solids of orthotropic materials. *Structural optimization*, 2(1):55–63, 1990. doi:10.1007/BF01743521.

D. M. Peeters, S. Hesse, and M. M. Abdalla. Stacking sequence optimisation of variable stiffness laminates with manufacturing constraints. *Composite Structures*, 125:596–604, jul 2015. doi:10.1016/j.compstruct.2015.02.044.

J. Petersson and O. Sigmund. Slope constrained topology optimization. *International Journal for Numerical Methods in Engineering*, 41(8):1417–1434, apr 1998. doi:10.1002/(sici)1097-0207(19980430)41:8<1417::aid-nme344>3.0.co;2-n.

M. Petrovic, T. Nomura, T. Yamada, K. Izui, and S. Nishiwaki. Orthotropic material orientation optimization method in composite laminates. *Structural and Multidisciplinary Optimization*, 57(2):815–828, aug 2017. doi:10.1007/s00158-017-1777-2.

K. Polthier and E. Preuß. Identifying vector field singularities using a discrete hodge decomposition. In *Mathematics and Visualization*, pages 113–134. Springer Berlin Heidelberg, 2003. doi:10.1007/978-3-662-05105-4_6.

W. Prager and G. Rozvany. OPTIMIZATION OF STRUCTURAL GEOMETRY. In *Dynamical Systems*, pages 265–293. Elsevier, 1977. doi:10.1016/b978-0-12-083750-2.50023-0.

A. Reuss. Berechnung der fließgrenze von mischkristallen auf grund der plastizitätsbedingung für einkristalle . *Zeitschrift für Angewandte Mathematik und Mechanik*, 9(1):49–58, 1929. doi:10.1002/zamm.19290090104.

U. T. Ringertz. On finding the optimal distribution of material properties. *Structural Optimization*, 5(4):265–267, 1993. doi:10.1007/bf01743590.

H. Rodrigues, J. Guedes, and M. Bendsøe. Hierarchical optimization of material and structure. *Structural and Multidisciplinary Optimization*, 24(1):1–10, 2002. doi:10.1007/s00158-002-0209-z.

S. Rojas-Labanda and M. Stolpe. Benchmarking optimization solvers for structural topology optimization. *Structural and Multidisciplinary Optimization*, 52(3):527–547, 2015. doi:10.1007/s00158-015-1250-z.

M. Rossow and J. Taylor. A finite element method for the optimal design of variable thickness sheets. *AIAA Journal*, 11(11):1566–1569, 1973. doi:10.2514/3.50631.

G. I. N. Rozvany. Exact analytical solutions for some popular benchmark problems in topology optimization. *Structural optimization*, 15(1):42–48, 1998. doi:10.1007/BF01197436.

R. Rumpf and J. Pazos. Synthesis of spatially variant lattices. *Optics Express*, 20 (14):15263–15274, 2012. doi:10.1364/OE.20.015263.

F. Schury, M. Stingl, and F. Wein. Efficient two-scale optimization of manufacturable graded structures. *SIAM Journal on Scientific Computing*, 34(6):B711–B733, 2012. doi:10.1137/110850335.

L. G. Shapiro and G. Stockman. *Computer Vision*. Prentice Hall PTR, Upper Saddle River, NJ, USA, 1st edition, 2001.

R. Sharma, J. Zhang, M. Langelaar, F. van Keulen, and A. M. Aragón. An improved stress recovery technique for low-order 3d finite elements. *International Journal for Numerical Methods in Engineering*, 114(1):88–103, jan 2018. doi:10.1002/nme.5734.

O. Sigmund. Materials with prescribed constitutive parameters: An inverse homogenization problem. *International Journal of Solids and Structures*, 31(17): 2313–2329, 1994. doi:10.1016/0020-7683(94)90154-6.

O. Sigmund. On the optimality of bone microstructure. In P. Pedersen and M. P. Bendsøe, editors, *IUTAM Symposium on Synthesis in Bio Solid Mechanics*, pages 221–234, Dordrecht, 1999. Springer Netherlands.

O. Sigmund. A new class of extremal composites. *Journal of the Mechanics and Physics of Solids*, 48(2):397–428, 2000. doi:10.1016/S0022-5096(99)00034-4.

O. Sigmund. A 99 line topology optimization code written in matlab. *Structural and Multidisciplinary Optimization*, 21(2):120–127, 2001. doi:10.1007/s001580050176.

O. Sigmund. Morphology-based black and white filters for topology optimization. *Structural and Multidisciplinary Optimization*, 33(4-5):401–424, 2007. doi:10.1007/s00158-006-0087-x.

O. Sigmund and K. Maute. Topology optimization approaches. *Structural and Multidisciplinary Optimization*, 48(6):1031–1055, 2013. doi:10.1007/s00158-013-0978-6.

O. Sigmund and S. Torquato. Composites with extremal thermal expansion coefficients. *Applied Physics Letters*, 69(21):3203–3205, 1996. doi:10.1063/1.117961.

O. Sigmund and S. Torquato. Design of materials with extreme thermal expansion using a three-phase topology optimization method. *Journal of the Mechanics and Physics of Solids*, 45(6):1037–1067, 1997. ISSN 0022-5096. doi:10.1016/S0022-5096(96)00114-7.

O. Sigmund, N. Aage, and E. Andreassen. On the (non-)optimality of michell structures. *Structural and Multidisciplinary Optimization*, 54(2):361–373, 2016. doi:10.1007/s00158-016-1420-7.

R. Sivapuram, P. D. Dunning, and H. A. Kim. Simultaneous material and structural optimization by multiscale topology optimization. *Structural and Multidisciplinary Optimization*, 54(5):1267–1281, 2016. doi:10.1007/s00158-016-1519-x.

O. K. Smith. Eigenvalues of a symmetric 3x3 matrix. *Communications of the ACM*, 4(4):168, apr 1961. doi:10.1145/355578.366316.

K. Svanberg. The method of moving asymptotes–a new method for structural optimization. *International Journal for Numerical Methods in Engineering*, 24(2): 359–373, 1987. doi:10.1002/nme.1620240207.

B. Szabó and I. Babuska. *Finite Element Analysis*. Wiley-Interscience, 1991. ISBN 9780471502739.

C. R. Thomsen, F. Wang, and O. Sigmund. Buckling strength topology optimization of 2d periodic materials based on linearized bifurcation analysis. *Computer Methods in Applied Mechanics and Engineering*, 339:115–136, 2018. ISSN 0045-7825. doi:10.1016/j.cma.2018.04.031.

S. Torquato, S. Hyun, and A. Donev. Multifunctional composites: Optimizing microstructures for simultaneous transport of heat and electricity. *Phys. Rev. Lett.*, 89:266601, 2002. doi:10.1103/PhysRevLett.89.266601.

S. B. Vigdergauz. Two-dimensional grained composites of extreme rigidity. *Journal of Applied Mechanics*, 61(2):390–394, 1994. ISSN 0021-8936. doi:10.1115/1.2901456.

W. Voigt. *Lehrbuch der Kristallphysik*. Vieweg+Teubner Verlag, 1966. doi:10.1007/978-3-663-15884-4.

F. Wang, B. S. Lazarov, and O. Sigmund. On projection methods, convergence and robust formulations in topology optimization. *Structural and Multidisciplinary Optimization*, 43(6):767–784, dec 2010. doi:10.1007/s00158-010-0602-y.

Y. Wang, F. Chen, and M. Y. Wang. Concurrent design with connectable graded microstructures. *Computer Methods in Applied Mechanics and Engineering*, 317: 84–101, 2017. doi:10.1016/j.cma.2016.12.007.

A. Weldeyesus, M. Stolpe, and E. Lund. *Models and Methods for Free Material Optimization*. PhD thesis, Denmark, 2014.

J. Wu, A. Clausen, and O. Sigmund. Minimum compliance topology optimization of shell-infill composites for additive manufacturing. *Computer Methods in Applied Mechanics and Engineering*, 326:358–375, 2017. ISSN 0045-7825. doi:10.1016/j.cma.2017.08.018.

J. Wu, N. Aage, R. Westermann, and O. Sigmund. Infill optimization for additive manufacturing - approaching bone-like porous structures. *IEEE Transactions on Visualization and Computer Graphics*, 24(2):1127–1140, 2018. doi:10.1109/TVCG.2017.2655523.

L. Xia and P. Breitkopf. Recent advances on topology optimization of multiscale nonlinear structures. *Archives of Computational Methods in Engineering*, 24(2): 227–249, 2017. doi:10.1007/s11831-016-9170-7.

W. Zhang and S. Sun. Scale-related topology optimization of cellular materials and structures. *International Journal for Numerical Methods in Engineering*, 68(9): 993–1011, 2006. doi:10.1002/nme.1743.

K. Zhou and X. Li. Topology optimization for minimum compliance under multiple loads based on continuous distribution of members. *Structural and Multidisciplinary Optimization*, 37(1):49–56, 2008a. doi:10.1007/s00158-007-0214-3.

K. Zhou and X. Li. Topology optimization of truss-like continua with three families of members model under stress constraints. *Structural and Multidisciplinary Optimization*, 43(4):487–493, 2010. doi:10.1007/s00158-010-0584-9.

M. Zhou and G. Rozvany. The (coc) algorithm, part ii: Topological, geometrical and generalized shape optimization. *Computer Methods in Applied Mechanics and Engineering*, 89(1-3):309–336, 1991. doi:10.1016/0045-7825(91)90046-9.

S. Zhou and Q. Li. Design of graded two-phase microstructures for tailored elasticity gradients. *Journal of Materials Science*, 43(15):5157–5167, 2008b. doi:10.1007/s10853-008-2722-y.

O. C. Zienkiewicz and J. Z. Zhu. The superconvergent patch recovery anda posteriori error estimates. part 1: The recovery technique. *International Journal for Numerical Methods in Engineering*, 33(7):1331–1364, may 1992. doi:10.1002/nme.1620330702.

F. W. Zok, R. M. Latture, and M. R. Begley. Periodic truss structures. *Journal of the Mechanics and Physics of Solids*, 96:184–203, 2016. doi:10.1016/j.jmps.2016.07.007.

Publications

Publication [P1]

J.P. Groen and O. Sigmund. Homogenization-based topology optimization for high-resolution manufacturable micro-structures. *International Journal for Numerical Methods in Engineering*, 113(8):1148–1163, 2018 (online, 2017). doi:10.1002/nme.5575

Received: 28 August 2016 | Revised: 17 April 2017 | Accepted: 24 April 2017
DOI: 10.1002/nme.5575

SPECIAL ISSUE ON ADVANCED TOPOLOGY OPTIMIZATION

WILEY

Homogenization-based topology optimization for high-resolution manufacturable microstructures

Jeroen P. Groen | Ole Sigmund

Department of Mechanical Engineering, Solid Mechanics, Technical University of Denmark, Kongens Lyngby, Denmark

Correspondence
Jeroen P. Groen, Department of Mechanical Engineering, Solid Mechanics, Technical University of Denmark, Nils Koppels Allé, Building 404, 2800 Kongens Lyngby, Denmark.
Email: jergro@mek.dtu.dk

Summary

This paper presents a projection method to obtain high-resolution, manufacturable structures from efficient and coarse-scale homogenization-based topology optimization results. The presented approach bridges coarse and fine scale, such that the complex periodic microstructures can be represented by a smooth and continuous lattice on the fine mesh. A heuristic methodology allows control of the projected topology, such that a minimum length scale on both solid and void features is ensured in the final result. Numerical examples show excellent behavior of the method, where performances of the projected designs are almost equal to the homogenization-based solutions. A significant reduction in computational cost is observed compared to conventional topology optimization approaches.

KEYWORDS

high-resolution, homogenization, manufacturing constraints, topology optimization

1 | INTRODUCTION

Nowadays, the wide-spread availability of computational resources has resulted in topology optimization as a mature design method, with numerous applications in industry. Nevertheless, large-scale topology optimization still comes at a high computational cost, dominated by the finite element analysis.[1] Furthermore, to ensure near optimal solutions, continuation approaches have to be used, which increase the number of design iterations and computational time. Theoretically, it is known that the optimal topology consists of periodic composites with infinitesimally small features. In homogenization-based topology optimization, the space of admissible designs is relaxed to allow such composites.[2] In this way, that provided the basis for the original works in topology optimization, optimal solutions could be obtained at a much lower computational cost compared to density-based topology optimization.

Even more than an optimal design, a manufacturable structure is required, which can of course not consist of infinitesimally small features. To get manufacturable designs out of the relaxed solutions, several multiscale techniques have been used. Rodrigues et al proposed a hierarchical optimization scheme that combines free material optimization on the macroscale, with an optimization of the microstructure using inverse homogenization.[3] This approach was later extended to allow for parallel computations,[4] as well as for nonlinear elasticity.[5] To reduce the computational cost, one can also consider to restrict the amount of unique microstructures throughout the domain; however, this comes at a reduction of optimality.[6,7] A limitation of these methods is that the connectivity between neighboring microstructures is not guaranteed. Greifenstein and Stingl approached this problem by constraining the variation of the material.[8] Multiscale techniques such as the aforementioned approaches have received rapid growing interest, in part spurred by the increased availability of additive manufacturing techniques. By far, most of the published work (all of which shall not be listed here) is based on "separation of scales", i.e., it is assumed that microscopic patterns are much smaller than the macroscopic details, in turn allowing for separate modelling of the microscale and

macroscale. In connection with additive manufacturing, one should also mention the treatment of in-fill, i.e., porous structures that, apart from weight saving, also may increase buckling stability of topology optimized structures, see Clausen et al.[9,10]

In a different approach, Lazarov and Alexandersen use the multiscale finite element method to design high-resolution manufacturable structures.[11,12] These works do not assume separation of scales and hence provide better analysis and design of structures with finite periodicity, although the computational cost is high compared to homogenization-based topology optimization.

In a very appealing approach, Pantz and Trabelsi introduced a method to project the microstructures from the relaxed design space to obtain a solid-void design with finite length scale.[13,14] The local structure is oriented along the directions of lamination such that a well-connected design is achieved. This approach paves the way for coarse-scale topology optimization where the projection can be performed on a high-resolution mesh in a postprocessing step, without a need for cumbersome and expensive multiscale formulations. In a related study, Rumpf and Pazos show that any type of (also spatially varying) unit cell, represented by a Fourier series, can be projected on a fine scale mesh.[15,16]

This paper shall be seen as a simplification and improvement of the approach introduced by Pantz and Trabelsi.[13,14] We simplify the projection approach and introduce procedures for controlling the size and shape of the projected design, such that high-resolution (e.g., 1.3 million elements in 2D), near-optimal, and manufacturable lattice designs can be achieved within a few minutes in a single processor MATLAB code on a standard PC. This short time allows a designer to get high-resolution manufacturable designs at speeds, which potentially can make high-resolution topology optimization an integrated part of interactive design processes.[17]

The paper is organized as follows: the methodology of numerical homogenization, and how it can be used in the context of topology optimization is introduced in Section 2. The projection method and its implementation details are presented in Section 3. In Section 4, a method to control the shape of the projected designs is shown. Corresponding numerical examples are shown in Section 5. Finally, the most important conclusions of this study are presented in Section 6.

2 | HOMOGENIZATION-BASED TOPOLOGY OPTIMIZATION

It is well-known that for many topology optimization problems, the optimal solutions can be found in the relaxed design space, ie, the space allowing for microstructural materials that have an infinitely fast variation in solid and void regions.[18-20] At the microscopic scale, these microstructures are assumed to be uniform, hence they can be represented by periodic unit cells. While at the macroscopic scale, geometries and orientations are spatially varying such that optimal structural properties can be obtained. In the original works on topology optimization, microstructures were either described by square cells with rectangular holes[2] or as layered materials.[21] Similar to these works, we apply topology optimization to compliance minimization of linear-elastic plane problems subject to a single load case, where the main focus of this study is on the physical realization of these optimized topologies.

Avellaneda has shown that the optimal solution for minimum compliance problems is in the space of layered materials, the so-called rank-n laminates.[20] Here, rank-2 laminates are optimal for plane problems subject to a single load case, and rank-3 laminates are optimal for plane problems subject to multiple load cases. Unfortunately, rank-n laminates require different length scales, which poses a challenge on their physical realization. Therefore, we restrict ourselves to the suboptimal (but close in performance) square unit cells with rectangular holes, used by Bendsøe and Kikuchi.[2] An illustration of one unit cell, with its local coordinate system (y_1,y_2) and link to the global coordinate system (x_1,x_2), is seen in Figure 1.

2.1 | Numerical homogenization

The macroscopic constitutive properties of the unit cell in its local coordinate system (y_1,y_2) form the homogenized elasticity tensor $\mathbf{C}^H$. These properties, which depend on the parameters describing the height a_1 and width a_2 of the hole*, can be obtained using numerical homogenization. A discussion on the theory of homogenization is outside the scope of this work; instead, the interested readers are referred to previous works,[22-25] in which detailed descriptions of the theory and implementation can be found.

In topology optimization, the parameters a_1 and a_2 are spatially varying and subject to change during each design iteration. Therefore, it is cumbersome to perform numerical homogenization for each variation in a_1 and a_2. Instead, we can calculate $\mathbf{C}^H$ for a large number of combinations of a_1 and a_2 and interpolate between them, as proposed by Bendsøe and Kikuchi.[2] To do so,

*Hence, a_1 determines the stiffness of the unit cell in the y_1-direction, and a_2 determines the stiffness of the unit cell in the y_2-direction

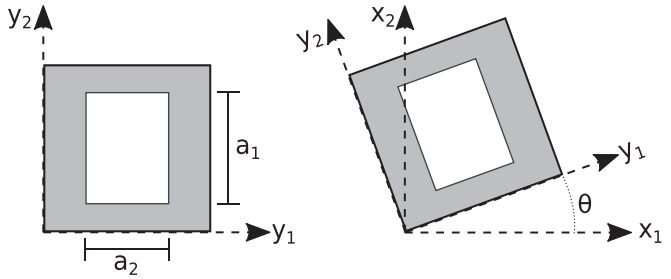

FIGURE 1 Layout of the unit cell with a rectangular hole, in local (y_1,y_2) and global (x_1,x_2) coordinate system

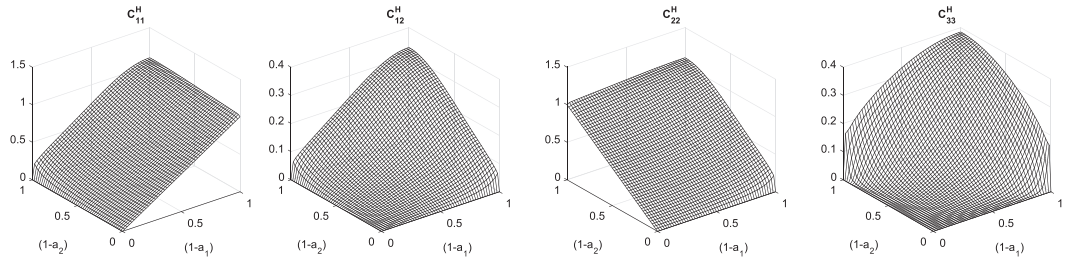

FIGURE 2 The indices of the homogenized elasticity tensor $\mathbf{C}^H$ for different values of a_1 and a_2, where $E_{strong} = 1$ and $\nu = 0.3$

the publicly available and easy-to-use MATLAB code by Andreassen and Andreasen is used.[26] With this code, a mesh consisting of 100×100 bilinear finite elements has been created, on which $\mathbf{C}^H$ has been determined for 51×51 different combinations of a_1 and a_2. The used material properties are $E = 1$ and $\nu = 0.3$, while a very compliant material plays the role of void, ie, $E_{void} = 10^{-9}E$. To avoid discontinuities in elastic properties, we treat the hole as an infinitesimally thin crack when one of the parameters a_i takes the value 0. The resulting curves for the 4 unique indices of the homogenized elasticity coefficients are shown in Figure 2, where linear interpolation is applied to obtain values between the data points.

With these curves known, the macroscopic elasticity tensor in the global reference frame $\mathbf{C}$ can be calculated.

$$\mathbf{C}(a_1, a_2, \theta) = \mathbf{R}^T(\theta)\mathbf{C}^H(a_1, a_2)\mathbf{R}(\theta), \tag{1}$$

where $\mathbf{R}$ is the well-known rotation matrix. Finally, the amount of material in unit cell m can be calculated as

$$m = 1 - a_1 a_2. \tag{2}$$

2.2 | Topology optimization formulation

Topology optimization is a material distribution problem, where the goal is to find an optimized material distribution that minimizes an objective function, subject to a number of constraints.[27] In this study, we will restrict ourselves to minimizing compliance $\mathcal{J}$, for single load-case problems, subject to an upper bound on the volume. The design domain is discretized in elements, in which the shape and orientation of the microstructure are assumed to be uniform. The local design variables a_1, a_2, and θ can thus be combined into design vectors $\mathbf{a}_1$, $\mathbf{a}_2$, and $\boldsymbol{\theta}$.

The topology optimization problem is solved in nested form, by successive minimizations w.r.t. design variables $\mathbf{a}_1$, $\mathbf{a}_2$, and $\boldsymbol{\theta}$; where for each design iteration, the equilibrium equations are satisfied by finite element analysis. As is shown by Pedersen,[28,29] the optimal orientation of an orthotropic composite coincides with the principal stress directions, hence $\boldsymbol{\theta}$ is aligned accordingly for each minimization step. Subsequently, design vectors $\mathbf{a}_1$ and $\mathbf{a}_2$ are updated at each minimization step based on their gradients. The discretized optimization problem can thus be written as

$$\begin{aligned} \min_{\mathbf{a}_1,\mathbf{a}_2,\theta} &: \mathcal{J}(\mathbf{a}_1,\mathbf{a}_2,\theta,\mathbf{U}), \\ \text{s.t.} &: \mathbf{K}(\mathbf{a}_1,\mathbf{a}_2,\theta)\mathbf{U} = \mathbf{F}, \\ &: \mathbf{v}^T\mathbf{m}(\mathbf{a}_1,\mathbf{a}_2) - V_{max} \leqslant 0, \\ &: \mathbf{0} \leqslant \mathbf{a}_1,\mathbf{a}_2 \leqslant \mathbf{1}, \end{aligned} \tag{3}$$

where $\mathbf{m}(\mathbf{a}_1,\mathbf{a}_2)$ describes the amount of material within an element (see Equation 2), $\mathbf{v}$ is the vector containing the element volumes, and V_{max} is the maximum allowed volume of the material in the design domain. Stiffness matrix $\mathbf{K}$ is a function of $\mathbf{a}_1,\mathbf{a}_2$, and θ; $\mathbf{F}$ describes the loads acting on the domain; and $\mathbf{U}$ describes the solution of the equilibrium equation. For the design update of $\mathbf{a}_1$ and $\mathbf{a}_2$, the MATLAB implementation of the method of moving asymptotes is used.[30]

As shown in Díaz and Sigmund,[31] checkerboard patterns can occur since the strain energy density of these patterns is overestimated using bilinear finite elements. To prevent the checkerboarding, the solution space is restricted using a density filter applied to $\mathbf{a}_1$ and $\mathbf{a}_2$ independently.[32,33] A small filter radius r_{min} of 1.5 times the element width h_c is used, since the filter only has to prevent the occurrence of checkerboard patterns and should not impose a length scale on the design. The physical dimensions of the hole $\tilde{\mathbf{a}}_1$ and $\tilde{\mathbf{a}}_2$ are the filtered design variables. These values are used to determine the homogenized elasticity tensor $\mathbf{C}^H$ and to determine the amount of material within a unit cell m.

2.3 | Test problems

In this study, 2 test problems are considered. The first is a cantilever problem, subject to a distributed unit load over 20% of the right boundary, shown in Figure 3A. A volume constraint of 0.5 is set, and a coarse discretization of 80×40 elements is used to solve the homogenization-based topology optimization problem. The second problem is a Michell-type problem with circular support, subject to a distributed unit load over 10% of the right boundary, shown in Figure 3B. For this problem, a volume constraint of 0.25 is set, while a mesh of 80×60 elements is used to perform the topology optimization. For both problems, a solid material with unit stiffness, and a Poisson's ratio of $\nu = 0.3$, is used.

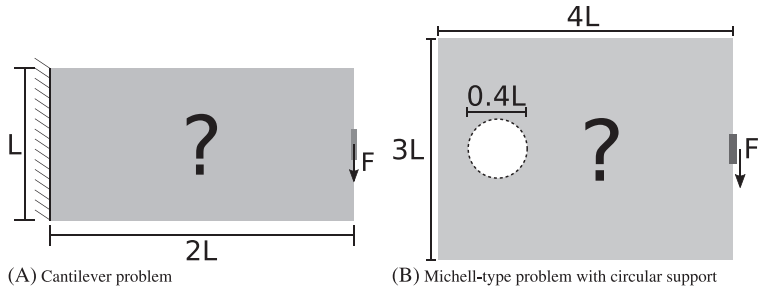

(A) Cantilever problem (B) Michell-type problem with circular support

FIGURE 3 Boundary conditions of the 2 numerical examples considered in this study

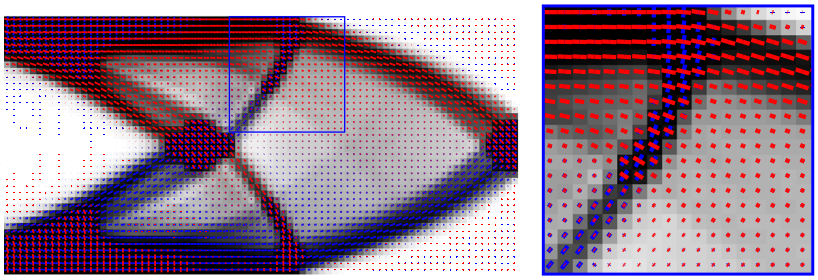

(A) Homogenization-based optimized topology (B) Close-up of the optimized topology

FIGURE 4 Optimized topology for the 2D cantilever problem, using 80×40 elements

To verify the homogenization-based topology optimization algorithm, the cantilever beam problem is solved, which results in a compliance of 58.35. This value is very close to the value of 56.73 obtained using the more optimal rank-2 laminate as microstructure, reported in Sigmund et al.[34] The unit-cell densities of the optimized topology can be seen in Figure 4A. A close-up of this design can be seen in Figure 4B, where the red and blue lines correspond to $1 - a_1$ and $1 - a_2$, respectively. The challenge is now to convert this result to a practically realizable structure with the highest possible precision using the least computational effort.

3 | PROJECTION OF MICROSTRUCTURES ON THE FINE SCALE

Almost any type of periodic microstructure can be represented by a complex exponential Fourier series with spatially varying parameters.[15,16] This allows one to project a complex microstructure on a fine scale, yet maintaining a smooth and continuous lattice.

3.1 | Projecting a uniform microstructure

The unit cell with a rectangular hole, used in the topology optimization problem, is simple enough to be represented by just 2 orthogonal cosine waves.[13,14] The first cosine wave describes the part of the unit cell aligned with y_1, while the second cosine wave describes the part aligned with y_2. Each of these cosine waves can be obtained independently from each other, thus we here restrict ourselves to the derivation of the first cosine wave $\tilde{\rho}_1$. This cosine wave is oriented using unit vector $\mathbf{e}_1$, such that it is constant in the direction of y_1, hence $\mathbf{e}_1$ is orthogonal to y_1.

$$\tilde{\rho}_1(\mathbf{x}) = \frac{1}{2} + \frac{1}{2}\cos(P(\mathbf{e}_1 \cdot \mathbf{x})), \tag{4}$$

where $\mathbf{e}_1$ can be written for the local orientation angle θ as

$$\mathbf{e}_1 = \begin{bmatrix} -\sin(\theta) \\ \cos(\theta) \end{bmatrix}. \tag{5}$$

P is a term that scales the periodicity based on the size of the unit-cell ε:

$$P = \frac{2\pi}{\varepsilon} \tag{6}$$

Homogenization-based topology optimization is based on an infinite periodicity, i.e., $\varepsilon \to 0$; however, this can of course not be realized. Therefore, the microstructures have to be magnified towards a fine but realizable scale on the macroscopic level, using a finite ε. To take into account the height of the void (a_1), and to get a clear solid-void design, a Heaviside step function is used. Here $\tilde{\rho}_1$ is projected to a a physical design ρ_1, where the threshold parameter η_1 is based on a_1.

$$\rho_1(a_1(\mathbf{x})) = H(\tilde{\rho}_1(\mathbf{x}) - \eta_1(a_1(\mathbf{x}))), \tag{7}$$

$$\eta_1(a_1(\mathbf{x})) = \frac{1}{2} + \frac{1}{2}\cos(\pi(1 - a_1(\mathbf{x}))). \tag{8}$$

The shape of the projected unit cell can then be retrieved using

$$\rho(\mathbf{x}) = \min\{\rho_1(\mathbf{x}) + \rho_2(\mathbf{x}), 1\}. \tag{9}$$

where the second cosine wave ρ_2 is oriented using unit vector $\mathbf{e}_2$, which is orthogonal to $\mathbf{e}_1$. The projection procedure of a sequence of uniform rectangular unit cells can be seen in Figure 5. Figure 5A and Figure 5B show cosine waves $\tilde{\rho}_1$ and $\tilde{\rho}_2$ obtained using Equation 4, while the projected shape of the lattice obtained using Equation 9 is seen in Figure 5C. The domain has unit width and height, with $\varepsilon = 0.25$.

3.2 | Projecting a spatially variant microstructure

Equation 4 does not hold when the orientation of the microstructures is spatially varying. A unit cell cannot be square if the spatial variation in angles has to be satisfied. Instead, we use a mapping function ϕ_1, which maps the optimization domain Ω onto a periodic set in $\mathbb{R}^2$ that describes the composite,[13,14] ie, $\phi_1 : \Omega \to \mathbb{R}^2$. Using this mapping function, we can reformulate Equation 4 such that the cosine wave $\tilde{\rho}_1$ can be described by

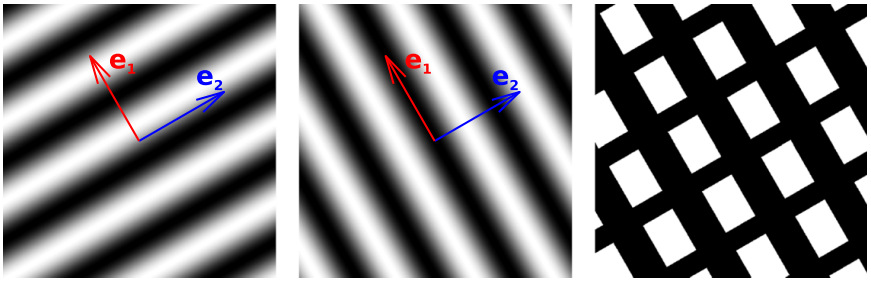

(A) First cosine wave $\tilde{\rho}_1(\mathbf{x})$ (B) Second cosine wave $\tilde{\rho}_2(\mathbf{x})$ (C) Projected structure $\rho(\mathbf{x})$

FIGURE 5 Projection of a uniform microstructure on a fine scale using just 3 parameters, $a_1 = 0.7$, $a_2 = 0.5$, and $\theta = \pi/6$

$$\tilde{\rho}_1(\mathbf{x}) = \frac{1}{2} + \frac{1}{2}\cos(P\phi_1(\mathbf{x})). \tag{10}$$

The challenge is thus to find a suitable parameterization ϕ_1, such that each point in Ω corresponds to the correct composite shape. We can solve for ϕ_1 by minimizing the least-squares error between unit vector $\mathbf{e}_1$ and the gradient of ϕ_1[13,15]:

$$\min_{\phi_1(\mathbf{x})} : \mathcal{I}(\phi_1(\mathbf{x})) = \frac{1}{2}\int_\Omega \|\nabla\phi_1(\mathbf{x}) - \mathbf{e}_1(\mathbf{x})\|^2 \mathrm{d}\Omega. \tag{11}$$

However, this is a best fit that tries to take both the enforcement of the angle and lattice spacing into account simultaneously.[16] We will argue that the projected shape resembles the homogenization-based topology best if the angles are enforced exactly, at the cost of a relaxed lattice spacing. To further enforce that the unit cells are oriented corresponding to the output of the homogenization problem, ϕ_1 has to be constant in the direction of $\mathbf{e}_2$. Equation 11 can thus be reformulated in the following constrained least-squares minimization problem.

$$\begin{aligned} &\min_{\phi_1(\mathbf{x})} : \mathcal{I}(\phi_1(\mathbf{x})) = \frac{1}{2}\int_\Omega \|\nabla\phi_1(\mathbf{x}) - \mathbf{e}_1(\mathbf{x})\|^2 \mathrm{d}\Omega, \\ &\text{s.t.} : \nabla\phi_1(\mathbf{x}) \cdot \mathbf{e}_2(\mathbf{x}) = 0. \end{aligned} \tag{12}$$

Finally, it has to be mentioned that domain Ω can be split up into 3 parts: a void domain Ω_v, a part of the domain that is completely solid Ω_s, and a part that describes a lattice structure Ω_l. These 3 different parts are defined as

$$\mathbf{x} \in \begin{cases} \Omega_v & \text{if} \quad m(\mathbf{x}) = 0, \\ \Omega_s & \text{if} \quad m(\mathbf{x}) = 1, \\ \Omega_l & \text{if} \quad 0 < m(\mathbf{x}) < 1. \end{cases} \tag{13}$$

The mapping ϕ_1 should be just described accurately in Ω_l, hence we can relax the accuracy of ϕ_1 in Ω_s and Ω_v to make sure the best projection is obtained. To do this, we reformulate the constrained least-squares minimization problem into a spatially weighted problem.

$$\begin{aligned} &\min_{\phi_1(\mathbf{x})} : \mathcal{I}(\phi_1(\mathbf{x})) = \frac{1}{2}\int_\Omega \alpha_1(\mathbf{x})\|\nabla\phi_1(\mathbf{x}) - \mathbf{e}_1(\mathbf{x})\|^2 \mathrm{d}\Omega, \\ &\text{s.t.} : \alpha_2(\mathbf{x})\nabla\phi_1(\mathbf{x}) \cdot \mathbf{e}_2(\mathbf{x}) = 0, \end{aligned} \tag{14}$$

where

$$\alpha_1(\mathbf{x}) = \begin{cases} 0.01 & \text{if} \quad \mathbf{x} \in \Omega_v \\ 0.1 & \text{if} \quad \mathbf{x} \in \Omega_s \\ 1 & \text{if} \quad \mathbf{x} \in \Omega_l \end{cases}, \quad \alpha_2(\mathbf{x}) = \begin{cases} 0 & \text{if} \quad \mathbf{x} \in \Omega_v \\ 0 & \text{if} \quad \mathbf{x} \in \Omega_s \\ 1 & \text{if} \quad \mathbf{x} \in \Omega_l \end{cases}. \tag{15}$$

The term α_1 is introduced to relax the projection of ϕ_1 in Ω_v and Ω_s, where the low values still ensure some regularization to the lattice spacing. Furthermore, the term α_2 is used to turn off exact angular enforcement in these regions. If equally weighted, requirements to the enforcement of angles in Ω_v, where orientations may be badly determined, would severely influence the outcome in important higher density regions. Similarly, for Ω_s, the orientation of the unit cell is less important since it will neither affect the constitutive properties nor the projected shape. The Lagrangian corresponding to Equation 14 can thus be written as

$$\mathcal{L}(\phi_1(\mathbf{x}), \lambda(\mathbf{x})) = \int_\Omega \frac{\alpha_1(\mathbf{x})}{2} \|\nabla\phi_1(\mathbf{x}) - \mathbf{e}_1(\mathbf{x})\|^2 - \lambda(\mathbf{x})\alpha_2(\mathbf{x})(\nabla\phi_1(\mathbf{x}) \cdot \mathbf{e}_2(\mathbf{x}))\mathrm{d}\Omega, \tag{16}$$

where λ is the Lagrange multiplier corresponding to the constraint.

3.3 | Projecting a rotationally symmetric spatially variant microstructure

The optimization problem solved in Equation 14 works well for a smoothly varying angle field θ. Unfortunately, the principal stress directions used to calculate θ are rotationally symmetric, hence there may be jumps of size π in the optimized angle field. This rotational symmetry has neither an influence on the shape of the microstructure nor on its constitutive properties. However, it means that Equation 12 cannot be used, unless vectors $\mathbf{e}_1$ and $\mathbf{e}_2$ are oriented in a consistent fashion. To circumvent this problem, Pantz and Trabelsi[13] reformulated the problem and solved for vector fields $\mathbf{v}_1$ and $\mathbf{v}_2$ instead of the scalar fields ϕ_1 and ϕ_2.

We argue that the approach proposed by Pantz and Trabelsi overly complicates the procedure and propose that the vector fields $\mathbf{e}_1$ and $\mathbf{e}_2$ can be oriented consistently in a straightforward fashion, in turn avoiding the computational burden in solving for vector fields $\mathbf{v}_1$ and $\mathbf{v}_2$. To do so, we use a well-known image-processing technique called connected component labeling.[35] The main idea is to divide the image into separate components, where the pixels in each of the components have uniform or near-uniform properties. Using this technique, it is possible to find the components in the design domain where the angle field θ is rotated with π. To identify if voxel i and adjacent voxel j are in the same component, the following 2 conditions should be satisfied.

1. The relative difference between θ_i and θ_j should be smaller than $\pi/2$.
2. Voxels i and j should both be in Ω_v or should both be in $\Omega_s \cup \Omega_l$

The first condition assumes that the principal stress field is smooth and should not rotate more than $\pi/2$ between 2 adjacent elements. The second condition is used to find the boundaries of regions in which there is no material. This is important when considering the Michell-type problem with the circular support. Here, we want the support to be a separate component that does not influence the orientation of angle field θ outside of the support. Connected component labeling is a well-known image-processing task, for which various efficient implementations exist.[35] Furthermore, it has to be noted that the technique works equally well on irregular meshes, provided that the adjacent elements are known.

To demonstrate the procedure, consider the vector field $\mathbf{e}_1$ shown in Figure 6A. We assume a nonvoid domain, i.e., condition 2 is always satisfied, and perform the connected component label algorithm described above. A component label is assigned to each of the elements, and it can be seen in Figure 6B that the edges of the components correspond to the places where angle field θ is rotated by π. The different components can then be oriented consistently by making sure that the difference in θ at these boundaries is close to $k2\pi$, where k is an integer. This aligns the angle field in a consistent fashion, and hence the projection can be performed using Equation 14.

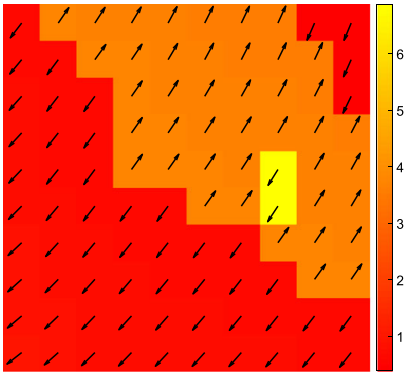

(A) $\mathbf{e}_1$ plotted on top of θ

1	2	2	2	2	2	2	2	4	4
1	1	2	2	2	2	2	2	2	4
1	1	1	2	2	2	2	2	2	4
1	1	1	2	2	2	2	2	2	2
1	1	1	2	2	2	2	3	2	2
1	1	1	1	1	2	2	3	2	2
1	1	1	1	1	1	1	2	2	2
1	1	1	1	1	1	1	1	2	2
1	1	1	1	1	1	1	1	1	1
1	1	1	1	1	1	1	1	1	1

(B) Component label assigned to each element

FIGURE 6 Angle field θ, which exhibits rotational symmetry, and the corresponding connected component labeling

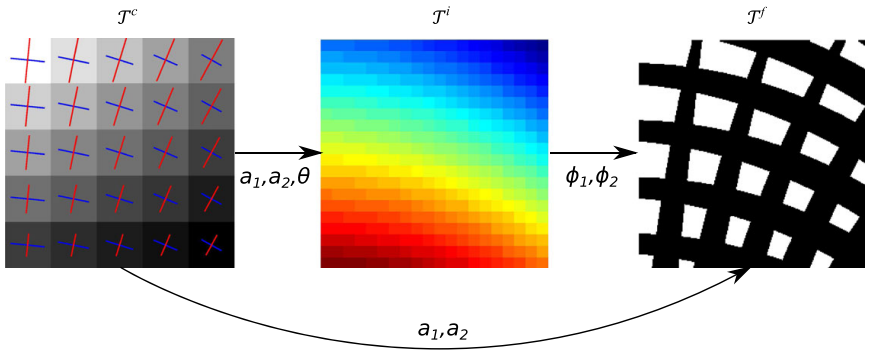

FIGURE 7 The different types of meshes and how they are linked

3.4 | Numerical implementation of the projection method

The solution of the topology optimization problem, obtained on coarse mesh $\mathcal{T}^c$, is projected onto a fine scale mesh $\mathcal{T}^f$, where $h_f < h_c/15$ to obtain a high-resolution design at a low computational cost. The calculation of $\boldsymbol{\phi}_1$ and $\boldsymbol{\phi}_2$ is done on an intermediate mesh $\mathcal{T}^i$, where the mesh-size is a trade-off between the computational cost and the quality of the result; however, a general rule of thumb is that $h_i < h_c/3$.[15] An overview of these 3 different meshes and how they are related can be found in Figure 7; where in the coarse mesh $\mathcal{T}^c$, the red lines correspond to $1 - a_1$, while the blue lines correspond to $1 - a_2$.

Different numerical methods exist to find ϕ_1 and λ. Here, we solve the minimization problem of Equation 14 in finite difference form, where the solution vectors $\boldsymbol{\phi}_1$ and $\boldsymbol{\lambda}$ contain the corresponding unknowns on the intermediate mesh. The resulting discretized Lagrangian can be written as

$$\mathcal{L}(\boldsymbol{\phi}_1, \lambda) = \frac{1}{2}\|\mathbf{A}_1(\mathbf{D}\boldsymbol{\phi}_1 - \mathbf{E})\|^2 - \lambda^T \mathbf{A}_2 \mathbf{B}\mathbf{D}\boldsymbol{\phi}_1, \tag{17}$$

where $\mathbf{D}$ is a finite difference matrix, vector, $\mathbf{E}$ contains the unit vectors $\mathbf{e}_1$ at all discrete points, and matrix $\mathbf{B}$ holds the values of $\mathbf{e}_2$. It has to be noted that $\mathbf{A}_1$ and $\mathbf{A}_2$ are diagonal matrices such that the spatial weighting terms are taken into account, hence $\mathbf{A}_1$ contains values of $\sqrt{\alpha_1}$ at the corresponding discrete points. Using the discretized Lagrangian and constraint, we can solve for $\boldsymbol{\phi}_1$ and $\boldsymbol{\lambda}$ using the following KKT-system:

$$\begin{bmatrix} \mathbf{D}^T\mathbf{A}_1^T\mathbf{A}_1\mathbf{D} & -\mathbf{D}^T\mathbf{B}^T\mathbf{A}_2^T \\ \mathbf{A}_2\mathbf{B}\mathbf{D} & \mathbf{0} \end{bmatrix} \begin{bmatrix} \boldsymbol{\phi}_1 \\ \boldsymbol{\lambda} \end{bmatrix} = \begin{bmatrix} \mathbf{D}^T\mathbf{A}_1^T\mathbf{A}_1\mathbf{E} \\ \mathbf{0} \end{bmatrix}. \tag{18}$$

The solution of ϕ_1 is prone to local high-frequency variations, as can be seen in Figure 8A. These variations can be prevented by solving for ϕ_1 on a finer mesh; however, this increases the cost of the projection. Furthermore, it was observed that smoothing ϕ_1 resolved the issue equally well. To smooth scalar field ϕ_1, a density filter with a radius of $2h_i$ is used in a postprocessing step. The effect of this smoothing operation can be seen in Figure 8B.

3.5 | Scaling the periodicity

The projection procedure ensures that the local microstructure is oriented with θ, at the cost of the lattice spacing. The local lattice spacing is described by $||\nabla\phi_1||$ and $||\nabla\phi_2||$. If the angle is uniform throughout the domain, both values are 1, since $\mathbf{e}_1$ and $\mathbf{e}_2$ are unit vectors. Hence, $||\nabla\phi_i|| > 1$ means that cosine wave i is locally compressed, while $||\nabla\phi_i|| < 1$ means that the cosine wave is locally stretched. To make sure that the average size of the projected unit cell corresponds to ε, we have to find the average lattice spacing $\bar{p}_i$ in the part of the domain that consists of material $(\Omega \setminus \Omega_v)$.

$$\bar{p}_i = \frac{\int_{(\Omega\setminus\Omega_v)} ||\nabla\phi_i(\mathbf{x})|| \mathrm{d}(\Omega \setminus \Omega_v)}{\int_{(\Omega\setminus\Omega_v)} \mathrm{d}(\Omega \setminus \Omega_v)} \tag{19}$$

Hence, $\bar{p}_i > 1$ means that cosine wave i is compressed in the domain of interest. Therefore, the periodicity for the ith cosine wave P_i has to be scaled using

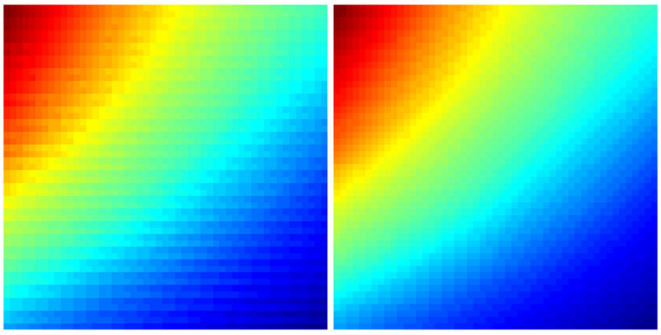

(A) ϕ_1, with high-frequency variations (B) ϕ_1 after smoothing

FIGURE 8 Smoothing of field ϕ_1 using a density filter

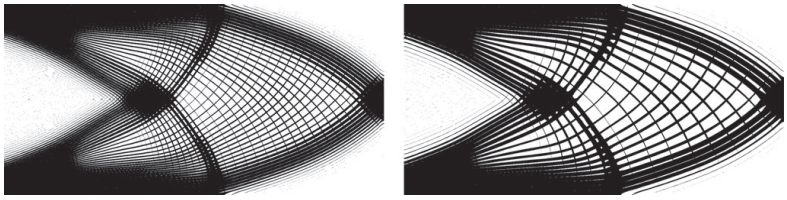

(A) $\varepsilon = 15h_f$, $\mathcal{J}_f = 63.6$ (B) $\varepsilon = 30h_f$, $\mathcal{J}_f = 61.2$

FIGURE 9 Projection of the test problem on a fine scale of 1600×800 elements

$$P_i = \frac{2\pi}{\varepsilon}\frac{1}{\bar{p}_i}. \tag{20}$$

The cantilever beam, for which the homogenization-based topology is shown in Figure 4, is treated as above. Here, $\mathcal{T}^c$ consists of 80×40 elements, $\mathcal{T}^i$ consists of 320×160 elements, and the final shape shown in Figure 9A is obtained on a fine mesh consisting of 1600×800 elements, using $\varepsilon = 15h_f$. The projection resembles the optimized shape well, and the corresponding compliance calculated on the fine mesh $\mathcal{J}_f = 63.6$. Similarly, the test problem has been projected for $\varepsilon = 30h_f$ as shown in Figure 9B, with the corresponding compliance of 61.2. It is interesting to note that in this case, a larger magnification leads to a better performing design. This is because of a larger number of small features being disconnected when $\varepsilon = 15h_f$. How to resolve these small and sometimes disconnected features is the subject of the next section.

4 | CONTROL OF THE SHAPE OF THE PROJECTED MICROSTRUCTURE

The size of the microstructures can be varied using ε. However, this parameter does not provide any control of the feature size of the individual structural members. Furthermore, if we take a closer look at Figure 9A, we can identify structural members that do not seem to carry any load, see close-ups in Figure 10A, as well as structural members that are so thin that they cease to exist, see Figure 10B.

To avoid these undesired features, some control of the projected design is required. Therefore, we present a heuristic method that enforces a minimum feature size f_{min} on both solid and void. First, we propose a continuation scheme that restricts the shape of the microstructures to prevent the occurrence of unit cells with very small structural members. Nevertheless, this approach still results in locations where the feature size of the projected design f is smaller than f_{min}; therefore, material is added at these locations until manufacturability is ensured. Furthermore, we present a method that removes the material in nonload-carrying regions. Finally, we show an overview of all steps that have to be taken to project the homogenization-based structure.

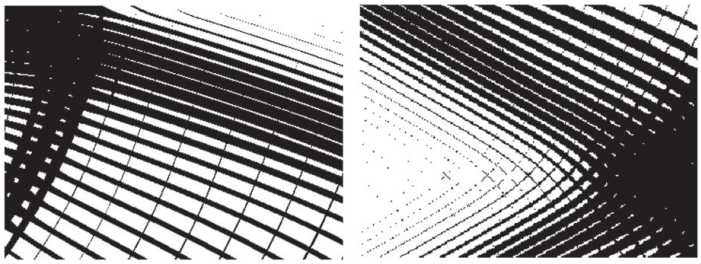

(A) Non-load carrying structural members (B) Thin structural members

FIGURE 10 Close-up of the cantilever beam, projected on a fine scale of 1600×800 elements, with $\epsilon = 15h_f$

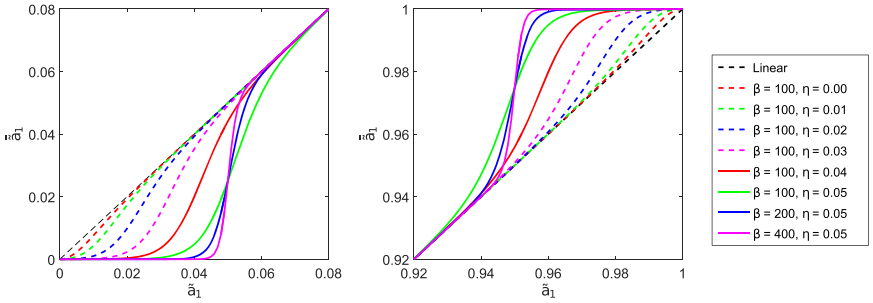

FIGURE 11 Interpolation scheme plotted for the intervals where the behavior is non-linear, for different values of η and β, that follow the order of the continuation approach

4.1 | Restriction of solution space

Microstructures with value of a_1 and a_2 close but not equal to 0 or 1 have to be prevented. These values describe unit cells with very thin strips of solid or void, which cannot be manufactured when the solution is projected on a fine scale. Instead, we want these values to either be 0, 1, or in a region $[\eta, 1-\eta]$, which is bounded by length-scale η on both the solid and void. To get a solution that satisfies these conditions, the following interpolation scheme is used, which links the filtered design variables $\tilde{a}_1$ and $\tilde{a}_2$ to the physical dimensions of the void $\bar{\tilde{a}}_1$ and $\bar{\tilde{a}}_2$.

$$\bar{\tilde{a}}_1 = \tilde{a}_1\big(1 - \widetilde{H}(\beta, (1-\eta), \tilde{a}_1)\big)\widetilde{H}(\beta, \eta, \tilde{a}_1) + \left(\frac{\beta - 1}{\beta} + \frac{\tilde{a}_1}{\beta}\right)\widetilde{H}(\beta, (1-\eta), \tilde{a}_1), \tag{21}$$

where $\widetilde{H}$ is the smoothed Heaviside function,[36]

$$\widetilde{H}(\beta, \eta, \tilde{a}_1) = \frac{\tanh(\beta\eta) + \tanh(\beta(\tilde{a}_1 - \eta))}{\tanh(\beta\eta) + \tanh(\beta(1-\eta))}. \tag{22}$$

β controls the sharpness of the projection, and η controls the threshold value. For a high value of β and $\eta = 0$, we have that $\bar{\tilde{a}}_1 = \tilde{a}_1$. The interpolation function for different values of β and η can be found in Figure 11. The order of lines in the legend shows the continuation approach that is taken, using 50 iterations per step. First, the material interpolation scheme is close to a linear function, but gradually, η is increased to enforce the length scale on solid and void. Finally, β is increased to ensure that the far majority of physical dimensions of the hole are either 0, 1, or in the region $[\eta, 1-\eta]$, such that the small feature sizes are avoided.

The cantilever beam problem has been solved using the continuation approach resulting in a compliance of 58.31 compared to the compliance of 58.35 using only density filtering. The difference between these values is negligible; similar differences have been observed for different mesh-sizes and different optimization problems. This shows that even though the solution space is restricted, equally well performing topologies can be found at different local minima. Hence, based on our experience, the presented approach does not negatively affect the performance of the design for the chosen parameters.

4.2 | Satisfying the local feature-sizes

The presented restriction method greatly reduces the violation of length-scale f_{min} in the projected design. Nevertheless, it does not enforce an explicit length scale on the projected shape. It is possible to identify the projected feature-sizes f_s and f_v, corresponding to the solid and void, respectively, using the local periodicity and a_1 and a_2.

$$f_{s,i}(\mathbf{x}) = \frac{\varepsilon(1 - a_i(\mathbf{x}))}{||\nabla \phi_i(\mathbf{x})||}, \tag{23}$$

$$f_{v,i}(\mathbf{x}) = \frac{\varepsilon a_i(\mathbf{x})}{||\nabla \phi_i(\mathbf{x})||}. \tag{24}$$

If $f_{s,i}(\mathbf{x})$ is smaller than f_{min}, the feature size of the solid is violated. To compensate for this, a new value a_i^* is found such that the length scale is satisfied.

$$a_i^*(\mathbf{x}) = 1 - \frac{f_{min}}{\varepsilon}||\nabla \phi_i(\mathbf{x})|| \tag{25}$$

Similarly, if $f_{v,i} < f_{min}$, the hole is too small. However, we observed that removing material to satisfy the length scale has a significant negative effect on the optimality of the projected shape. Therefore, to make sure that the feature size is satisfied, the hole is closed instead, ie, $a_i^* = 0$. This approach adds material to the structure and thus violates the volume constraint V_{max} used in the optimization problem. Nevertheless, we argue that this violation is small, e.g., 5% of V_{max}, if reasonable values for ε and f_{min} are used. The restriction of the solution space discussed previously makes sure that most of the unit cells in the domain do not have small feature sizes. Furthermore, the nonload carrying structural members shown in Figure 10A still have to be removed, which will reduce the violation of the volume constraint.

4.3 | Removal of material at nonload carrying solids

Nonload carrying structural members, see, e.g., Figure 10A, can partially be explained by using the restriction method presented above, but mostly by the interpolation of a_1 and a_2 from $\mathcal{T}^c$ onto $\mathcal{T}^f$. Since a linear interpolation method is used, isolated structural members can arise at high-contrast regions. To remove these structural members, we use a simple iterative update scheme. In this scheme, a finite element analysis is performed at the fine scale; afterwards, the solid voxels that have a strain energy density c_e lower than 0.1% of the mean strain energy density $\bar{c_e}$ are set to void. To make sure that the length scale f_{min} on both the solid and void is still satisfied after each iteration, we perform an open-close filter operation as is proposed by Sigmund.[37] This operation efficiently eliminates features smaller than the filter size but leaves other details virtually untouched.

The combination of removal of solid voxels with a low strain energy density, followed by the open-close filter operation, is a heuristic method to get smooth and manufacturable microstructures. Nevertheless, we have observed excellent behavior of this method and generally convergence is obtained within 5 to 10 iterations. Alternatively, one could use the projected microstructure as a starting guess for fine-scale topology optimization. However, even when an efficient topology optimization framework is used, e.g. Andreassen,[38] the corresponding optimization will require significantly more time-consuming fine-scale iterations until convergence and probably result in no significant improvement in performance.

4.4 | Overview of the projection procedure

The methods described in the previous sections are combined to obtain high-resolution manufacturable microstructures at low computational cost. The different steps that have to be taken are shown below:

1. Homogenization-based topology optimization for rectangular unit cells using the restriction approach presented in section 4.1, on coarse mesh $\mathcal{T}^c$.
2. Connected component labeling and consistent alignment of $\mathbf{e}_1$ and $\mathbf{e}_2$, using the methodology presented in section 3.3 on $\mathcal{T}^c$.
3. Calculating mapping functions ϕ_1 and ϕ_2 as shown in section 3.4, on intermediate mesh $\mathcal{T}^i$.
4. Satisfying feature-size f, using the method presented in section 4.2, on fine mesh $\mathcal{T}^f$.
5. Projection of the cosine waves using Equations 7 to 10 on fine mesh $\mathcal{T}^f$.
6. Removal of the nonload carrying materials using the iterative method described in section 4.3 on mesh $\mathcal{T}^f$.

5 | NUMERICAL EXAMPLES

The solution of the cantilever beam problem has been projected on a fine mesh consisting of 1600 × 800 elements. The homogenization-based topology optimization took 199.4 seconds, and the subsequent connected component labeling 0.1 seconds. Hence, the total time spent on the coarse mesh $T_c = 199.5$ seconds. The compliance of the optimized homogenization-based topology $\mathcal{J}_c = 58.31$. The projection is performed for various sizes of the unit cell ε, and several values of f_{min}. The corresponding compliance on the fine scale $\mathcal{J}_f$ and volume V_f of the projected structures can be found in Table 1. Furthermore, T_i which is the time it took to calculate ϕ_1 and ϕ_2 on the intermediate mesh is shown, as well as T_f the time it took to satisfy the feature size, project the cosine waves, and remove the nonload carrying members on the fine mesh. Finally, the time for the entire procedure T_{tot} is given in Table 1.

A small unit-cell size combined with a large minimum length-scale leads to a large violation of the volume constraint. This is visualized for $\varepsilon = 20h_f$ and $f_{min} = 4h_f$ in Figure 12A, where most structural members have a width corresponding to f_{min}. However, for reasonable combinations of ε and f_{min}, the volume constraint is hardly violated. A good rule of thumb is that $\frac{f_{min}}{\varepsilon} > 10$ such that the violation of the volume constraint is within 2% of V_{max}. Furthermore, it is very interesting to see that for these projected structures excellent results are achieved, where the compliance is close to the performance of the homogenization-based topology. For $\varepsilon = 40$, and a small feature-size $f_{min} = 2$, we obtain a structure that does not violate the volume constraint, see Figure 12B, while the performance is within 2% of the homogenization-based topology. Using a larger feature size $f_{min} = 4$, slightly increases the volume; however, this results in a topology for which the performance is almost identical to the homogenization-based topology. Furthermore, this larger feature-size ensures manufacturability as can be seen in Figure 13.

The presented procedure for calculating mapping functions ϕ_1 and ϕ_2 is highly efficient resulting in an average time of 10.6seconds. The time it took to project the structure on the fine scale and satisfy the feature size is negligible compared to the cost of removing the nonload-carrying materials. The cost for this iterative procedure depends on the required number of iterations, where an average iteration costs approximately 28 seconds. This means that the total time to optimize and project the design T_{tot} never exceeded 500seconds, where it has to be noted that all experiments have been performed on a standard PC, using a single-core MATLAB code.

TABLE 1 Performance and computational cost of the projection method, when the cantilever beam problem is projected on a fine mesh consisting of 1600 × 800 elements

ε	f_{min}	V_f	$\mathcal{J}_c$	$\mathcal{J}_f$	T_c	T_i	T_f	T_{tot}
$20h_f$	$2h_f$	0.503	58.31	60.27	199.5 s	10.7 s	145.2 s	355.4 s
$20h_f$	$3h_f$	0.519	58.31	58.21	199.5 s	10.2 s	260.6 s	470.3 s
$20h_f$	$4h_f$	0.540	58.31	56.23	199.5 s	10.8 s	266.6 s	476.9 s
$30h_f$	$2h_f$	0.500	58.31	60.93	199.5 s	10.7 s	150.3 s	360.5 s
$30h_f$	$3h_f$	0.509	58.31	59.72	199.5 s	11.2 s	233.6 s	444.3 s
$30h_f$	$4h_f$	0.518	58.31	58.71	199.5 s	10.5 s	285.3 s	495.3 s
$40h_f$	$2h_f$	0.500	58.31	59.55	199.5 s	10.7 s	115.5 s	325.7 s
$40h_f$	$3h_f$	0.505	58.31	59.03	199.5 s	10.2 s	145.6 s	355.3 s
$40h_f$	$4h_f$	0.510	58.31	58.57	199.5 s	10.0 s	148.7 s	358.2 s

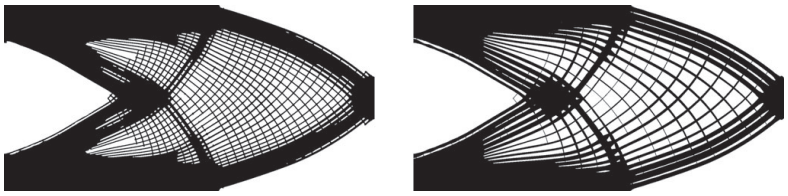

(A) $\varepsilon = 20\ h_f,\ f_{min} = 4\ h_f,\ \mathcal{J}_f = 56.23$, and $V_f = 0.540$.

(B) $\varepsilon = 40\ h_f,\ f_{min} = 2\ h_f,\ \mathcal{J}_f = 59.55$, and $V_f = 0.500$.

FIGURE 12 Cantilever problem projected on a fine scale of 1600 × 800

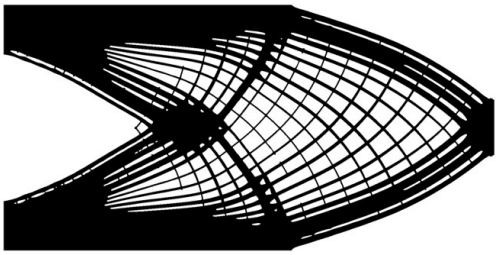

FIGURE 13 Projection of the cantilever problem, on a fine scale of 1600×800 using $\varepsilon = 40h_f$ and $f_{min} = 4h_f$. The compliance $\mathcal{J}_f = 58.57$, while $V_f = 0.510$

TABLE 2 Performance and computational cost of the projection method, when the Michell-type problem with circular support is projected on a fine mesh consisting of 1200×900 elements

ε	f_{min}	V_f	$\mathcal{J}_c$	$\mathcal{J}_f$	T_c	T_i	T_f	T_{tot}
$20h_f$	$2h_f$	0.248	84.31	75.57	225.6 s	16.8 s	109.6 s	352.0 s
$20h_f$	$3h_f$	0.266	84.31	73.44	225.6 s	17.5 s	112.7 s	355.8 s
$20h_f$	$4h_f$	0.297	84.31	62.76	225.6 s	16.1 s	150.4 s	392.1 s
$30h_f$	$2h_f$	0.236	84.31	76.68	225.6 s	17.7 s	174.2 s	417.5 s
$30h_f$	$3h_f$	0.241	84.31	74.72	225.6 s	17.5 s	132.5 s	375.6 s
$30h_f$	$4h_f$	0.252	84.31	71.89	225.6 s	15.7 s	175.3 s	416.6 s
$40h_f$	$2h_f$	0.250	84.31	68.37	225.6 s	16.5 s	111.6 s	353.7 s
$40h_f$	$3h_f$	0.252	84.31	67.83	225.6 s	17.3 s	112.6 s	355.5 s
$40h_f$	$4h_f$	0.256	84.31	66.51	225.6 s	17.7 s	92.9 s	336.2 s

To require the same resolution using a standard density-based topology optimization approach, a minimum of 100 iterations is required, each costing approximately 25 seconds. Furthermore, for a standard topology optimization approach, a continuation strategy is required to get as close to the optimal solution as obtained by the suggested projection approach. Such a continuation approach requires approximately 1000 iterations,[34] which would mean a total optimization time of approximately 25 000 seconds. Because of its optimization at a coarse scale, the presented method is thus able to be reduce the computational cost by more than 50 times.

The proposed scheme is also applied to the Michell-type problem with circular support. The coarse-scale optimization performed on a mesh of 80×60 elements resulted in a compliance of 84.31 obtained within 225.4 seconds. The shape is projected on a fine mesh of 1200×900 elements, for various sizes of the unit cell ε, and several values of f_{min}. The corresponding volume, compliance, and times it took for each part of the procedure are shown in Table 2

It is interesting to see that for $\varepsilon = 30h_f$, the volume of the projected and postprocessed shape is smaller than the volume constraint in the topology optimization problem. The reason for this is that 2 peaks of the cosine waves are located exactly at the boundary of the void domain and are not well connected to the rest of the structure, as can be seen in Figure 14A. Therefore, these waves are nonload carrying and removed by the fine-scale optimization procedure as can be seen in Figure 14B. This unfortunate result is purely a problem of the periodicity P having an unlucky value such that the projected structure at some positions is not well connected. If we use $\varepsilon = 40h_f$, the peaks of the cosine waves are positioned in a better way and excellent results are obtained. The projection using $40h_f$ and $3h_f$ is shown in Figure 15, the violation of the volume constraint is negligible, and the corresponding compliance is 67.83. It is interesting that this value is much lower than the compliance of the homogenization-based topology. This difference can be explained by the enforcement of the circular boundary condition, which is known to have a very strong influence on the resulting compliance for this classical example. If the homogenization-based topology optimization is performed on a finer scale, the boundary is approximated more accurately, and it was observed that the compliance converges to the value obtained using the projection.

From the numerical examples, we can conclude that the presented method is able to provide high-resolution (more than a million elements), near-optimal, manufacturable topologies, at low computational cost. However, the exact locations of the peaks of the cosine waves are difficult to predict; therefore, the projected shape can have some poorly connected structural

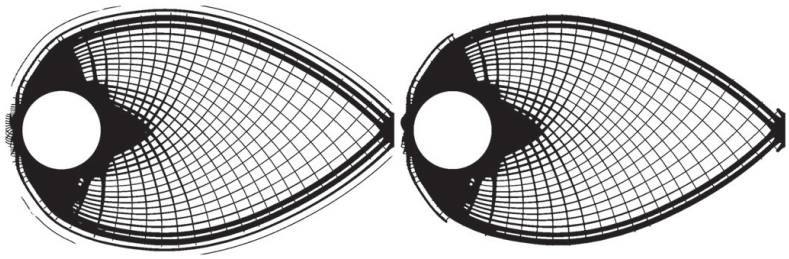

(A) Before removal of non-load carrying material (B) After removal of non-load carrying material

FIGURE 14 The Michell-type problem with circular support projected on a fine mesh consisting of 1200×900 elements. $\epsilon = 30h_f$ and $f_{min} = 3h_f$

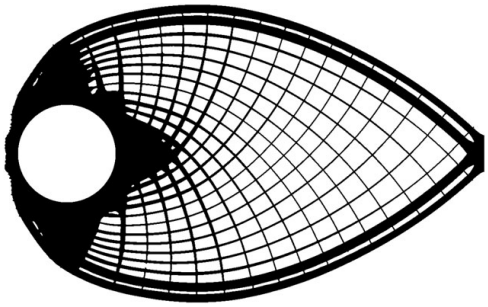

FIGURE 15 The Michell-type problem with circular support projected on a fine mesh consisting of 1200×900 elements. $\epsilon = 40h_f$ and $f_{min} = 3h_f$. The compliance $\mathcal{J}_f = 67.83$, while $V_f = 0.252$

members, as is demonstrated in Figure 14A and Figure 14B. This problem can be circumvented by shifting the cosine waves slightly, or by solving the projection procedure as a true multiscale approach. In such an approach, the topology optimized shape is also the shape that can be projected best.

Finally, a close inspection of Figures 13 and 15 shows that the projected shapes are not perfectly symmetric. The reason for this are angular fluctuations in low density regions. The influence of these regions on the projection is small; nevertheless, it can still result in a slight asymmetry as is best visible around the circular support in Figure 15. This asymmetry can be circumvented by reducing the computational domain at which the projection is performed to the nonvoid regions or by enforcing symmetry in all variable sets. We will leave further improvements in this direction to future works.

6 | CONCLUSION

An efficient approach to obtain near-optimal, high-resolution, manufacturable microstructures from coarse scale optimization studies has been presented. The methodology projects the unit cells of homogenization-based topology optimization on a fine mesh with minimum computational effort, where emphasis has been put on how to treat the rotational symmetry in the optimized angle field. Furthermore, an efficient method to control the shape of the projected design has been presented, such that the final topology satisfies a length-scale on both solid and void regions. Based on numerical experiments, this heuristic method has shown to produce near-optimal designs, at a speed which for the considered 2D examples is 50 times lower than conventional density-based topology optimization methods.

This overall promising performance paves the way for extending the proposed methodology to multiload problems, where more complex unit cells need to be considered. Furthermore, the excellent performance for single load-case minimum compliance problems allows for a natural extension of the methodology to 3D applications, where cubic unit cells with rectangular holes will have to be considered. We are confident that the presented methodology is robust enough to allow these extensions, such that its potential for incorporation in an efficient, interactive design process can be further revealed.

ACKNOWLEDGMENTS

The authors acknowledge the support of the Villum Fonden through the NextTop project. The authors would also like to thank Jens Gravesen and Boyan Lazarov for valuable discussions during the preparation of the work. Finally, the authors wish to thank Krister Svanberg for the MATLAB MMA code.

ORCID

Jeroen P. Groen http://orcid.org/0000-0003-3565-9385
Ole Sigmund http://orcid.org/0000-0003-0344-7249

REFERENCES

1. Aage N, Andreassen E, Lazarov BS. Topology optimization using petsc: an easy-to-use, fully parallel, open source topology optimization framework. *Struct Multidiscip O*. 2015;51(3):565-572. https://doi.org/10.1007/s00158-014-1157-0
2. Bendsøe MP, Kikuchi N. Generating optimal topologies in structural design using a homogenization method. *Comput Method Appl M*. 1988;71(2):197-224. https://doi.org/10.1016/0045-7825(88)90086-2
3. Rodrigues H, Guedes J, Bendsøe MP. Hierarchical optimization of material and structure. *Struct Multidiscip O*. 2002;24(1):1-10. https://doi.org/10.1007/s00158-002-0209-z
4. Coelho PG, Cardoso JB, Fernandes PR, Rodrigues HC. Parallel computing techniques applied to the simultaneous design of structure and material. *Adv Eng Softw*. 2011;42(5):219-227. https://doi.org/10.1016/j.advengsoft.2010.10.003
5. Xia L, Breitkopf P. Recent advances on topology optimization of multiscale nonlinear structures. *Arch Comput Method E*. 2017;24(2):227-249. https://doi.org/10.1007/s11831-016-9170-7
6. Schury F, Stingl M, Wein F. Efficient two-scale optimization of manufacturable graded structures. *SIAM J Sci Comput*. 2012;34(6):B711-B733. https://doi.org/10.1137/110850335
7. Sivapuram R, Dunning PD, Kim HA. Simultaneous material and structural optimization by multiscale topology optimization. *Struct Multidiscip O*. 2016;54(5):1267-1281. https://doi.org/10.1007/s00158-016-1519-x
8. Greifenstein J, Stingl M. Simultaneous parametric material and topology optimization with constrained material grading. *Struct Multidiscip O*. 2016;54(4):985-998. https://doi.org/10.1007/s00158-016-1457-7
9. Clausen A, Aage N, Sigmund O. Topology optimization of coated structures and material interface problems. *Comput Method Appl M*. 2015;290:524-541. https://doi.org/10.1016/j.cma.2015.02.011
10. Clausen A, Aage N, Sigmund O. Exploiting additive manufacturing infill in topology optimization for improved buckling load. *Engineering*. 2016;2:250-257. https://doi.org/10.1016/J.ENG.2016.02.006
11. Lazarov BS. Topology optimization using multiscale finite element method for high-contrast media. In: Lirkov I, Margenov S, Waśniewski J, eds. *Large-Scale Scientific Computing: 9th International Conference, LSSC 2013, Sozopol, Bulgaria, June 3-7, 2013. Revised selected papers*. Berlin, Heidelberg: Springer Berlin Heidelberg; 2014:339-346. https://doi.org/10.1007/978-3-662-43880-038
12. Alexandersen J, Lazarov BS. Topology optimisation of manufacturable microstructural details without length scale separation using a spectral coarse basis preconditioner. *Comput Method Appl M*. 2015;290:156-182. https://doi.org/10.1016/j.cma.2015.02.028
13. Pantz O, Trabelsi K. A post-treatment of the homogenization method for shape optimization. *SIAM J Control Optim*. 2008;47(3):1380-1398. https://doi.org/10.1137/070688900
14. Pantz O, Trabelsi K. Construction of minimization sequences for shape optimization. In: 2010 15th International Conference on Methods and Models in Automation and Robotics (MMAR); Międzyzdroje, Poland; 2010:278-283. https://doi.org/10.1109/MMAR.2010.5587222
15. Rumpf RC, Pazos J. Synthesis of spatially variant lattices. *Opt Express*. 2012;20(14):15263-15274. https://doi.org/10.1364/OE.20.015263
16. Rumpf RC, Pazos J, Digaum JL, Kuebler SM. Spatially variant periodic structures in electromagnetics. *Philos T R Soc A*. 2015;373(2049):1-22. https://doi.org/10.1098/rsta.2014.0359
17. Aage N, Nobel-Jørgensen M, Andreasen CS, Sigmund O. Interactive topology optimization on hand-held devices. *Struct Multidiscip O*. 2013;47(1):1-6. https://doi.org/10.1007/s00158-012-0827-z
18. Cheng K-T, Olhoff N. An investigation concerning optimal design of solid elastic plates. *Int J Solids Struct*. 1981;17(3):305-323. https://doi.org/10.1016/0020-7683(81)90065-2
19. Francfort GA, Murat F. Homogenization and optimal bounds in linear elasticity. *Arch Ration Mech An*. 1986;94(4):307-334. https://doi.org/10.1007/BF00280908
20. Avellaneda M. Optimal bounds and microgeometries for elastic two-phase composites. *SIAM J Appl Math*. 1987;47(6):1216-1228. https://doi.org/10.1137/0147082
21. Bendsøe MP. Optimal shape design as a material distribution problem. *Struct Optimization*. 1989;1(4):193-202. https://doi.org/10.1007/BF01650949
22. Guedes J, Kikuchi N. Preprocessing and postprocessing for materials based on the homogenization method with adaptive finite element methods. *Comput Method Appl M*. 1990;83(2):143-198. https://doi.org/10.1016/0045-7825(90)90148-F
23. Hassani B, Hinton E. A review of homogenization and topology optimization I homogenization theory for media with periodic structure. *Comput Struct*. 1998;69(6):707-717. https://doi.org/10.1016/S0045-7949(98)00131-X

24. Hassani B, Hinton E. A review of homogenization and topology optimization II analytical and numerical solution of homogenization equations. *Comput Struct*. 1998;69(6):719-738. https://doi.org/10.1016/S0045-7949(98)00132-1
25. Hassani B, Hinton E. A review of homogenization and topology optimization III topology optimization using optimality criteria. *Comput Struct*. 1998;69(6):739-756. https://doi.org/10.1016/S0045-7949(98)00133-3
26. Andreassen E, Andreasen CS. How to determine composite material properties using numerical homogenization. *Comput Mater Sci*. 2014;83:488-495. https://doi.org/10.1016/j.commatsci.2013.09.006
27. Sigmund O, Maute K. Topology optimization approaches. *Struct Multidiscip O*. 2013;48(6):1031-1055. https://doi.org/10.1007/s00158-013-0978-6
28. Pedersen P. On optimal orientation of orthotropic materials. *Struct Optim*. 1989;1(2):101-106. https://doi.org/10.1007/BF01637666
29. Pedersen P. Bounds on elastic energy in solids of orthotropic materials. *Struct Optim*. 1990;2(1):55-63. https://doi.org/10.1007/BF01743521
30. Svanberg K. The method of moving asymptotes a new method for structural optimization. *Int J Numer Methods Eng*. 1987;24(2):359-373. https://doi.org/10.1002/nme.1620240207
31. Díaz A, Sigmund O. Checkerboard patterns in layout optimization. *Struct Optim*. 1995;10(1):40-45. https://doi.org/10.1007/BF01743693
32. Bourdin B. Filters in topology optimization. *Int J Numer Methods Eng*. 2001;50(9):2143-2158. https://doi.org/10.1002/nme.116
33. Bruns TE, Tortorelli DA. Topology optimization of non-linear elastic structures and compliant mechanisms. *Comput Method Appl M*. 2001;190(26–27):3443-3459. https://doi.org/10.1016/S0045-7825(00)00278-4
34. Sigmund O, Aage N, Andreassen E. On the (non-)optimality of michell structures. *Struct Multidiscip O*. 2016;54(2):361-373. https://doi.org/10.1007/s00158-016-1420-7
35. Shapiro LG, Stockman G. *Computer Vision*. 1st ed. Upper Saddle River, NJ, USA: Prentice Hall PTR; 2001.
36. Wang F, Lazarov BS, Sigmund O. On projection methods, convergence and robust formulations in topology optimization. *Struct Multidiscip O*. 2011;43(6):767-784. https://doi.org/10.1007/s00158-010-0602-y
37. Sigmund O. Morphology-based black and white filters for topology optimization. *Struct Multidiscip O*. 2007;33(4):401-424. https://doi.org/10.1007/s00158-006-0087-x
38. Andreassen E, Clausen A, Schevenels M, Lazarov BS, Sigmund O. Efficient topology optimization in matlab using 88 lines of code. *Struct Multidiscip O*. 2011;43(1):1-16. https://doi.org/10.1007/s00158-010-0594-7

How to cite this article: Groen JP, Sigmund O. Homogenization-based topology optimization for high-resolution manufacturable micro-structures. *Int J Numer Meth Engng*. 2018;113:1148–1163. https://doi.org/10.1002/nme.5575

Publication [P2]

S.D. Larsen, O. Sigmund and J.P. Groen. Optimal truss and frame design from projected homogenization-based topology optimization. *Structural and Multidisciplinary Optimization*, 57(4):1461–1474, 2018. doi:10.1007/s00158-018-1948-9

Structural and Multidisciplinary Optimization (2018) 57:1461–1474
https://doi.org/10.1007/s00158-018-1948-9

RESEARCH PAPER

Optimal truss and frame design from projected homogenization-based topology optimization

S. D. Larsen[1] · O. Sigmund[1] · J. P. Groen[1]

Received: 17 October 2017 / Revised: 19 January 2018 / Accepted: 11 February 2018 / Published online: 7 March 2018
© Springer-Verlag GmbH Germany, part of Springer Nature 2018

Abstract
In this article, we propose a novel method to obtain a near-optimal frame structure, based on the solution of a homogenization-based topology optimization model. The presented approach exploits the equivalence between Michell's problem of least-weight trusses and a compliance minimization problem using optimal rank-2 laminates in the low volume fraction limit. In a fully automated procedure, a discrete structure is extracted from the homogenization-based continuum model. This near-optimal structure is post-optimized as a frame, where the bending stiffness is continuously decreased, to allow for a final design that resembles a truss structure. Numerical experiments show excellent behavior of the method, where the final designs are close to analytical optima, and obtained in less than 10 minutes, for various levels of detail, on a standard PC.

Keywords Optimal frame design · Optimal truss design · Michell theory · Topology optimization

1 Introduction

A classical topic within structural optimization is to find solutions for Michell's problem of least-weight trusses (Michell 1904). Computational methods to solve these problems of optimal truss design date back to the early sixties, when Dorn et al. (1964) introduced the ground structure approach. This approach requires a fixed set of nodal joints and elements, which make up the ground structure. The cross-sectional areas of these elements are then optimized, classically using linear programming methods. In recent years two easy-to-use implementations have been presented. Sokół T (2011) has published a 99 line code programmed in Mathematica, while Zegard and Paulino (2014) present a frame work for arbitrary 2D domains in MATLAB.

A downside of ground structure approaches is that the location of the nodal joints has a large influence on the performance of the design. To get a near-optimal solution a large set of nodes and potential elements have to be considered. Furthermore, the large number of members and the fact that some of these members are overlapping poses a limit on the manufacturability of these designs.

It is also possible to include the location of the nodes as design variables, i.e. both size and geometry are optimized, as introduced by Dobbs and Felton (1969) and Pedersen (1969). In this case a small set of nodes and elements suffices to get a near-optimal design; however, due to the non-linearity of the combined size and geometry optimization problem the initial position of nodes and connectivity still has a large influence on the result.

To get close to the optimal distribution of nodes and elements, growth methods have been considered (Rule 1994). Martínez et al. (2007) introduce an efficient growth method where sequentially a node and elements are introduced, size and topology optimization are performed, and geometry optimization is applied. The resulting designs are close in performance to analytical solutions for Michell's problem of least-weight trusses and obtained in a relatively short time. However, due to the nature of the heuristics involved in the growth method, it may not always converge to a near-optimal solution as is discussed by He and Gilbert (2015). Another downside of the growth method is that the procedure of finding an appropriate position to

Communicated by: Gregoire Allaire

✉ J. P. Groen
jergro@mek.dtu.dk

[1] Department of Mechanical Engineering, Solid Mechanics, Technical University of Denmark, Nils Koppels Alle, B.404, 2800 Kgs. Lyngby, Denmark

insert a new joint becomes increasingly slow when more members are considered.

In an approach somewhat related to the present, He and Gilbert (2015) make use of an efficient ground structure method, in which not all members are considered initially, but adaptively inserted (Gilbert and Tyas 2003). The position of this set of nodes is then optimized in a subsequent geometry optimization step. Furthermore, crossing elements are treated by inserting new nodes at crossings, leading to near-optimal and manufacturable designs in a short time.

In a different approach Zhou and Li (2008, 2011) use truss-like continua to get a near-optimal distribution of material and orientations. In a semi-automated approach starting points for ray tracing are manually selected, the grid formed by these rays is interpreted as a truss structure, on which subsequent size and geometry optimization is performed. Similar to this approach, Gao et al. (2017) obtain an initial ground structure for size optimization, using principal stress trajectories. These trajectories are obtained when the domain is modeled as an isotropic medium; however, here it should be mentioned that these principal stress lines do not necessarily correspond to the principal directions for an orthotropic truss-like material. In both of the above mentioned approaches the initial member areas are not chosen based on the continuum model, but are found in a subsequent sizing optimization model.

In this article, we propose a novel method to obtain a near-optimal set of nodes and elements, based on the solution of a homogenization-based topology optimization model. The approach is fully automatic and the extracted structure remains close to optimal. In a final step, the nodal positions and element areas are further optimized, and redundant nodes and elements eliminated. An overview of the proposed method can be seen in Fig. 1.

As discussed by Bendsøe and Haber (1993), the compliance minimization problem in the low volume fraction limit, using optimal rank-2 laminates, reduces to Michell's problem of least-weight trusses. In this limit a rank-2 laminate can be represented by a combination of two orthogonal rank-1 laminates acting on the same length-scale (Bourdin and Kohn 2008), similar to the truss-like continua used by Zhou and Li (2008). Such a microstructure can be projected on a fine scale using the method proposed in Pantz and Trabelsi (2008) and Groen and Sigmund (2017). However, we can also use the information of the mapping functions, required to do the projection, to establish nodes and initial connectivity. Furthermore, based on the optimal material distribution of the continuum model, a near-optimal initial starting guess for element areas is obtained.

Although the projected structure is close to the optimal solution, it is not always in the space of statically determinate structures. Hence, when modeled as a truss structure, the stiffness matrix can be singular. To tackle the problem of a singular stiffness matrix in the context of topology optimization several approaches have been proposed. Bruns (2006) uses a pseudo-inverse method, Washizawa et al. (2004) use Krylov subspace methods, and Ramos and Paulino (2016) use a potential energy approach with Tikhonov regulation. However, as a simple and reliable alternative we choose to model the structure as a thin frame structure and gradually decrease the bending contribution

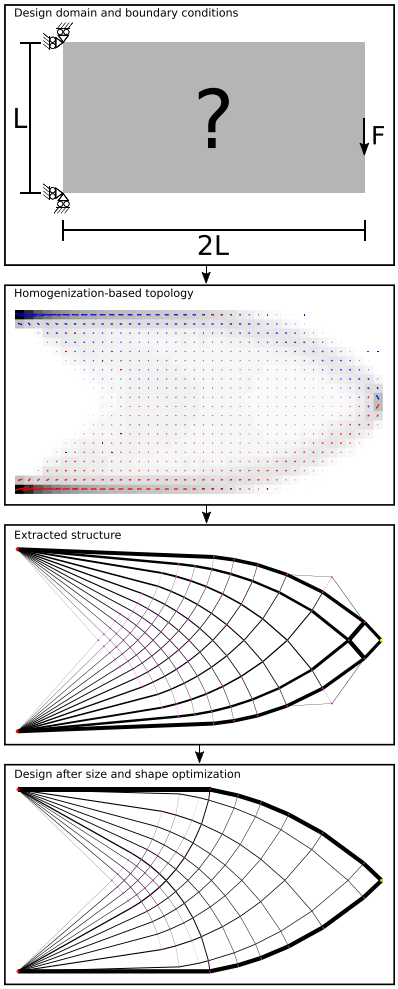

Fig. 1 Proposed procedure to obtain a solution to Michell's problem of least-weight trusses for a Michell cantilever

using a continuation scheme. As an added benefit, our approach allows to study the relation between optimized frame and truss structures.

The combined procedure of obtaining a near-optimal initial structure and post-optimization, for designs with several hundreds of nodes, requires less than 10 minutes, using a single processor MATLAB code on a standard PC. This short time potentially allows designers to use topology optimization as an interactive tool in the design process, Aage et al. (2013). To demonstrate the performance of the proposed approach five examples are considered. The cantilever beam shown in Fig. 1, and the MBB-beam, MBB-beam with void domain, L-shaped domain and Michell cantilever with circular support shown in Fig. 2a–d, respectively. The paper is organized as follows: The methodology of the homogenization-based topology optimization is introduced in Section 2. In Section 3 the theory used to obtain a near-optimal frame structure from projection of the rank-2 laminates is explained. The procedure to do further optimization is introduced in Section 4. The corresponding tests on the performance and efficiency of the developed method are shown in Section 5. Finally, the most important conclusions of this study are summarized in Section 6.

2 Homogenization-based topology optimization

Two orthogonal rank-1 laminates are used as microstructure to perform the homogenization-based topology optimization. The microstructures are defined by μ_1, and μ_2, which are the relative widths of the isotropic material in layer 1 and 2 respectively, and angle θ, which describes the angle between the material frame of reference to the global frame of reference. The corresponding constitutive properties $\mathbf{C}$ in the global coordinate system are written in matrix form using Voigt notation; furthermore, the macroscopic volume fraction m can be calculated as,

$$\begin{aligned}\mathbf{C}(\mu_1,\mu_2,\theta) &= \mathbf{R}^T(\theta)\begin{bmatrix} E\mu_1 & 0 & 0 \\ 0 & E\mu_2 & 0 \\ 0 & 0 & 0 \end{bmatrix}\mathbf{R}(\theta) \\ &\quad + \frac{E_{min}}{1-\nu^2}\begin{bmatrix} 1 & \nu & 0 \\ \nu & 1 & 0 \\ 0 & 0 & \frac{1-\nu}{2} \end{bmatrix} \\ m(\mu_1,\mu_2) &= \mu_1 + \mu_2 \end{aligned} \tag{1}$$

Here E is the Young's modulus of the isotropic material, and $\mathbf{R}$ is the transformation matrix rotating constitutive

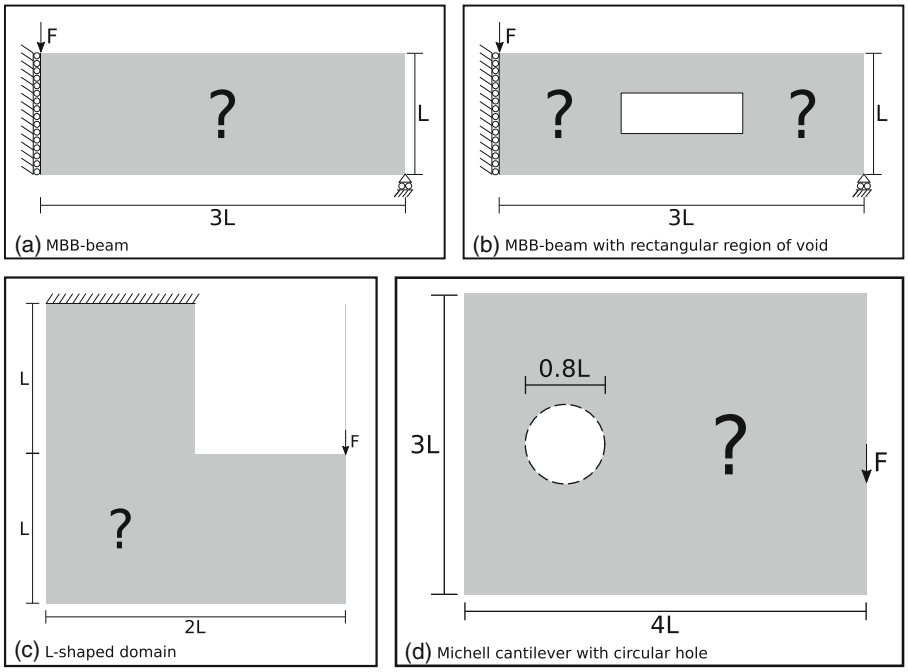

Fig. 2 Design domains and boundary conditions of examples used in this paper

properties from the material frame of reference to the global frame of reference. For stability reasons a small isotropic stiffness ($E_{min} = 0.005E$ and $\nu = 0.3$) is added to the composite constitutive properties.

Design domain Ω is discretized in n_e bi-linear finite elements, each consisting of a uniform microstructure described by local design variables μ_1, μ_2, and θ. The optimization problem, aimed at minimizing compliance $\mathcal{J}$, is solved in a nested-approach, where the design vectors describing the relative widths $\boldsymbol{\mu}_1$, and $\boldsymbol{\mu}_2$ are updated using the Method of Moving Asymptotes (MMA), (Svanberg 1987). As discussed by Pedersen (1989, 1990), the optimal orientation of an orthotropic composite is along the directions of principal stresses, hence at each design iteration the angles $\boldsymbol{\theta}$ are updated accordingly. In Michell's problem of least-weight trusses the relative material distribution has to be found, hence $\boldsymbol{\mu}_1$ and $\boldsymbol{\mu}_2$ are only bounded from below, and the volume constraint can be arbitrarily set to one. The discretized optimization problem can thus be written as,

$$\begin{aligned} \min_{\boldsymbol{\mu}_1,\boldsymbol{\mu}_2,\boldsymbol{\theta}} &: \mathcal{J}(\boldsymbol{\mu}_1, \boldsymbol{\mu}_2, \boldsymbol{\theta}, \mathbf{U}) = \mathbf{F}^T\mathbf{U} \\ \text{s.t.} &: \mathbf{K}(\boldsymbol{\mu}_1, \boldsymbol{\mu}_2, \boldsymbol{\theta})\mathbf{U} = \mathbf{F} \\ &: \mathbf{v}^T\mathbf{m}(\boldsymbol{\mu}_1, \boldsymbol{\mu}_2) - 1\sum_{e=1}^{n_e} v_e \leq 0 \\ &: \mathbf{0} \leq \boldsymbol{\mu}_1, \boldsymbol{\mu}_2 \end{aligned} \tag{2}$$

Where $\mathbf{v}$ is the vector containing the element volumes v_e. Stiffness matrix $\mathbf{K}$ is a function of $\boldsymbol{\mu}_1$, $\boldsymbol{\mu}_2$, and $\boldsymbol{\theta}$, $\mathbf{F}$ is the load vector, and $\mathbf{U}$ describes the displacement field. To avoid checkerboard patterns due to the use of bi-linear finite elements, a standard density filter with a filter radius of 1.5 element widths is applied on both fields μ_1 and μ_2 independently, Bourdin (2001) and Bruns and Tortorelli (2001). Furthermore, small values of μ_1 and μ_2 need to be prevented to make a clear distinction between regions consisting of material and regions which are void, as is proposed in Groen and Sigmund (2017). To do so, the following material interpolation scheme is used,

$$\bar{\tilde{\mu}}_i = \tilde{\mu}_i \frac{\tanh(\beta\eta) + \tanh(\beta(\tilde{\mu}_i - \eta))}{\tanh(\beta\eta) + \tanh(\beta(1-\eta))} \tag{3}$$

Where $\tilde{\mu}_i$ is the filtered width, and $\bar{\tilde{\mu}}_i$ is the physical laminate width used to calculate the constitutive properties. By carefully choosing a continuation scheme for the threshold parameter η, and the sharpness of the projection β, small widths between 0 and η can be banned from the solution space with little effect on the performance of the design. The parameters used for the continuation approach can be found in Fig. 3, where the legend shows the order of the scheme that is taken, using 50 iterations per step. Here the choice for $\eta = 0.05$, means that no microstructures are allowed that contain less than 5% of the average volume.

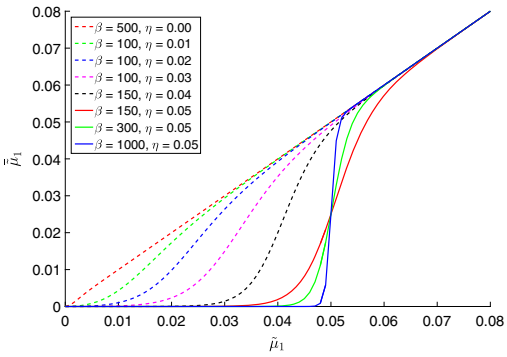

Fig. 3 Interpolation scheme plotted for different values of η and β, the order of the lines follows the continuation approach

3 Mapping microstructures onto frame structure

In recent works homogenization-based topologies have been projected as smooth and continuous lattice structures using two orthogonal layers (Pantz and Trabelsi 2008, 2010; Groen and Sigmund 2017). For each of the two orthogonal layers of the unit cell used in the homogenization-based topology optimization, a mapping function is determined that is locally aligned with the direction of lamination. Using these two mapping functions, ϕ_1 and ϕ_2 respectively, a continuous sequence of unit cells can be projected by means of cosine functions.

In this section, we present an alternative method to create a near-optimal frame structure based on ϕ_1 and ϕ_2, which subsequently can be used for further optimization. The discussion on the derivation of the mapping functions will be kept limited, since this is not the main goal of this work. For a detailed derivation the reader is referred to Groen and Sigmund (2017).

3.1 Mapping a periodic composite shape

Mapping functions ϕ_1 and ϕ_2 can be obtained independently of each other, using a similar approach, therefore we restrict ourselves to the derivation of ϕ_1. A suitable parameterization of ϕ_1 has to fulfill two requirements:

1. ϕ_1 should be constant in the direction of lamination in non-void domains, such that the frame structure can be described as contour lines.

2. The spacing between the contour lines of ϕ_1 in these non-void domains, should be as regular as possible without violating the first requirement.

These requirements are not equally weighted throughout domain Ω. As shown in Fig. 1, a part of the homogenization-based topology does not consist of material, hence the mapping functions do not have to be accurate here. Furthermore, requirement 1 is too strict in regions where the angle field changes rapidly, e.g. at the Dirichlet BC's in the cantilever beam example. Therefore domain Ω is split in three subdomains, a smooth lattice domain Ω_l, a void domain Ω_v, and a domain Ω_θ in which the angle field is rapidly changing. These domains are defined as,

$$\mathbf{x} \in \begin{cases} \Omega_v & \text{if} \quad \tilde{\bar{\mu}}_1(\mathbf{x}), \tilde{\bar{\mu}}_2(\mathbf{x}) < \eta \\ \Omega_\theta & \text{if} \quad \tilde{\bar{\mu}}_1(\mathbf{x}), \tilde{\bar{\mu}}_2(\mathbf{x}) \geq \eta \quad \text{and } \nabla\theta(\mathbf{x}) > \gamma_\theta \\ \Omega_l & \text{if} \quad \tilde{\bar{\mu}}_1(\mathbf{x}), \tilde{\bar{\mu}}_2(\mathbf{x}) \geq \eta \quad \text{and } \nabla\theta(\mathbf{x}) < \gamma_\theta \end{cases} \tag{4}$$

where, γ_θ is a threshold that dictates whether the angular field is rapidly changing or not.

$$\gamma_\theta = \frac{\pi}{4}\frac{1}{h_c} \tag{5}$$

Here h_c is the element length used in the homogenization-based topology optimization. Due to the selected threshold, Ω_θ contains the parts of the domain where the angle field is close to singular. Using these different domains, we can solve for mapping function ϕ_1 by means of a spatially weighted constrained least-squares minimization problem.

$$\begin{aligned} \min_{\phi_1(\mathbf{x})} &: \mathcal{I}(\phi_1(\mathbf{x})) = \frac{1}{2}\int_\Omega \alpha_1(\mathbf{x}) \, \|\nabla\phi_1(\mathbf{x}) - \mathbf{e}_1(\mathbf{x})\|^2 \, \mathrm{d}\Omega \\ \text{s.t.} &: \alpha_2(\mathbf{x})\nabla\phi_1(\mathbf{x}) \cdot \mathbf{e}_2(\mathbf{x}) = 0 \end{aligned} \tag{6}$$

where,

$$\alpha_1(\mathbf{x}) = \begin{cases} 0.01 & \text{if} \quad \mathbf{x} \in \Omega_v \\ 0.1 & \text{if} \quad \mathbf{x} \in \Omega_\theta \\ 1 & \text{if} \quad \mathbf{x} \in \Omega_l \end{cases}, \quad \alpha_2(\mathbf{x}) = \begin{cases} 0 & \text{if} \quad \mathbf{x} \in \Omega_v \\ 0 & \text{if} \quad \mathbf{x} \in \Omega_\theta \\ 1 & \text{if} \quad \mathbf{x} \in \Omega_l \end{cases} \tag{7}$$

Furthermore, unit vectors $\mathbf{e}_1$, $\mathbf{e}_2$ depend on the local directions of lamination θ,

$$\mathbf{e}_1 = \begin{bmatrix} -\sin(\theta) \\ \cos(\theta) \end{bmatrix}, \quad \mathbf{e}_2 = \begin{bmatrix} \cos(\theta) \\ \sin(\theta) \end{bmatrix} \tag{8}$$

It can be seen that the constraint, which dictates exact angular enforcement, is only active in Ω_l, i.e. the part of the domain where the lattice is smooth. Experiments have shown that a high gradient in angle field in combination with angular enforcement results in a severely distorted lattice spacing, hence the calculation of ϕ_1 in Ω_θ is relaxed. Since ϕ_1 does not have to be accurate in Ω_v, its calculation is heavily relaxed to allow for the best approximation in other parts of Ω.

Furthermore, it has to be noted that the principal stress directions used to calculate θ are rotationally symmetric, hence there may be jumps of size π in angle field θ. These

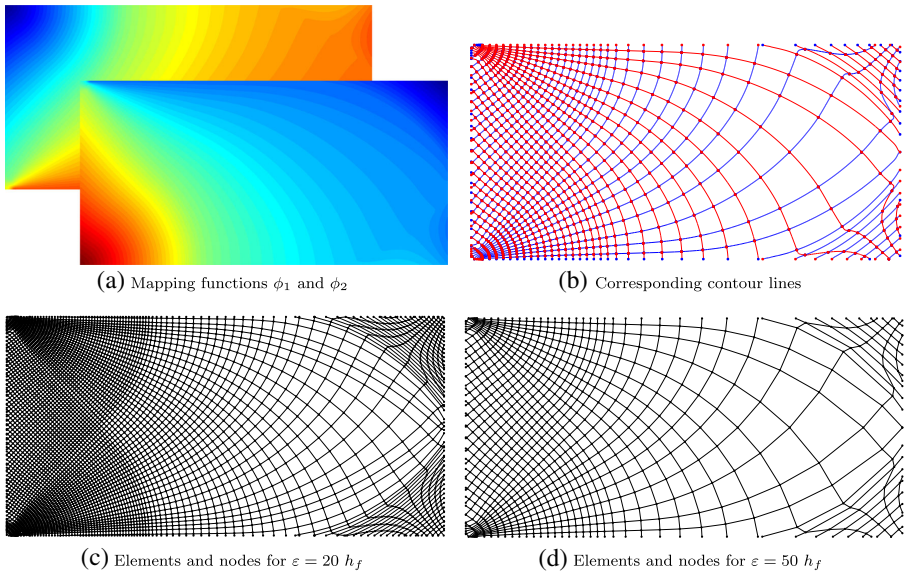

(a) Mapping functions ϕ_1 and ϕ_2

(b) Corresponding contour lines

(c) Elements and nodes for $\varepsilon = 20\ h_f$

(d) Elements and nodes for $\varepsilon = 50\ h_f$

Fig. 4 The nodes and element-connectivity extracted from the mapping functions for the Michell cantilever problem

jumps are identified using connected component labeling and aligned consistently as suggested in Groen and Sigmund (2017), to allow for a smooth projection using (6).

The mapping functions for the Michell cantilever are shown in Fig. 4a. The microstructure is optimized on a coarse mesh of 80×40 elements. Afterwards, mapping functions ϕ_1 and ϕ_2 are calculated on a six times finer mesh of 480×240 elements, This is done to get smooth and accurate values for ϕ_1 and ϕ_2 yet still at low computational cost.

3.2 Extraction of nodes and connectivity

The contour lines of mapping functions ϕ_1 and ϕ_2, shown in Fig. 4b resemble a frame-like structure. Using standard MATLAB functions (e.g. `contour`), these contour lines can be extracted, from which nodal positions and connectivity of the initial frame structure are established. To obtain highly accurate locations of the contour lines, mapping functions ϕ_1 and ϕ_2 are interpolated on a fine mesh of 1600×800 elements, i.e. 20 times finer than the mesh used for homogenization-based topology optimization.

For simplicity, we choose to draw a contour line when mapping function ϕ_i takes a whole value. To influence the number of contour lines, ϕ_i is multiplied with periodicity scaling parameter P_i, which is based on a user-defined average length of a frame member ε.

$$P_i = \frac{1}{\varepsilon} \frac{\int_{(\Omega \setminus \Omega_v)} \mathrm{d}(\Omega \setminus \Omega_v)}{\int_{(\Omega \setminus \Omega_v)} \|\nabla \phi_i(\mathbf{x})\|_2 \, \mathrm{d}(\Omega \setminus \Omega_v)} \tag{9}$$

Where the integrals scale mapping functions ϕ_i w.r.t. their average spacing. It can easily be seen that a large value of ε results in a small number of nodes and elements, while a small value results in a detailed frame structure. Finally, to make sure that a contour line passes through a specific point, e.g. the load-node, functions ϕ_1 and ϕ_2 can be shifted, before the contour-lines are extracted. An overview of the nodes and element connectivity for the Michell cantilever can be seen in Fig. 4, here figures (c) and (d) show the nodes and connectivity for $\varepsilon = 20\, h_f$, and $\varepsilon = 50\, h_f$ respectively.

3.3 Mapping of material distribution to element areas

Relative areas are assigned to the frame elements based on the values of $\bar{\tilde{\mu}}_1$, and $\bar{\tilde{\mu}}_2$ from the homogenization-based topology optimization. To transfer the continuous material distribution to the discrete elements, a polygon is drawn around each element, which describes the area in the continuum domain the element covers. An example of such a polygon can be seen in Fig. 5a. These polygons are

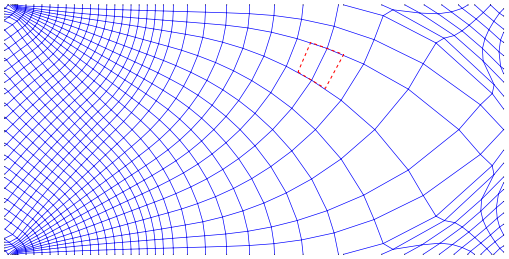

(a) Polygon around element to integrate volume

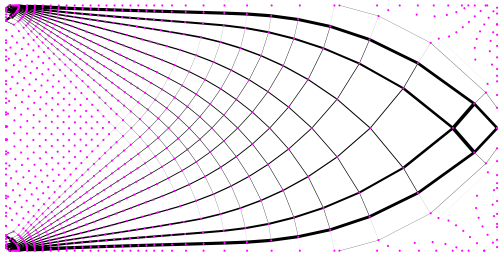

(b) Material mapped to elements

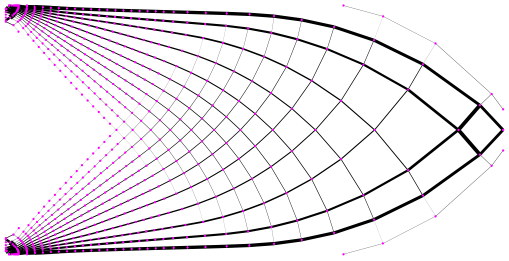

(c) Removal of elements with area smaller than A_η

Fig. 5 Procedure for mapping material from the continuum solution of homogenization-based topology optimization to discrete frame elements

obtained using the spacing of the contour lines, w_i, which can be approximated locally using mapping function ϕ_i.

$$w_i(\mathbf{x}) = \frac{1}{\|\nabla \phi_i(\mathbf{x})\|_2} \tag{10}$$

For each node of an element this spacing is calculated, and by taking a step orthogonal to the element with a stepsize of half the spacing the corresponding polygon can be drawn. By integrating the values of $\bar{\tilde{\mu}}_1$ or $\bar{\tilde{\mu}}_2$ in each of the polygons and dividing by the element length, a near-optimal initial area distribution of the frame structure is obtained based on the continuum solution, see e.g. Fig. 5b. Finally, we can identify the threshold area A_η, which is the area that an

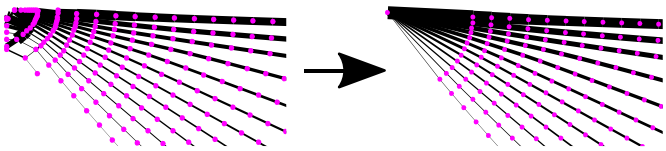

Fig. 6 Operation that pulls in all nodes and elements within $R_{BC} = 100\,h_f$ to generate a *fan-BC*

average sized frame element (*i.e.* with length ε) should have if $\bar{\tilde{\mu}}_i = \eta$.

$$A_\eta = \eta\varepsilon \tag{11}$$

Bars that have an area smaller than this value, occur when a part of the polygon, used for integrating the volume, is within Ω_v. Hence, elements with a mapped area that is smaller than A_η are removed, as can be seen in Fig. 5c.

3.4 Assigning boundary conditions

A distinction is made between how two different types of boundary conditions (BC's) are applied to the frame structure. Most nodes to which a BC needs to be assigned (in this work referred to as *standard-BC's*) can be identified easily, e.g. by finding the intersection with a line along which the BC's have to be applied. However, the analytical solutions for Michell's problem of least-weight trusses (Hemp 1973; Lewiński et al. 1994a, b; Lewiński and Rozvany 2008), also consists of boundary conditions that can be interpreted as source points from which multiple elements originate. These so-called *fan-BC's* can be found for example at the nodal Dirichlet BC's in the analytical solution of the Michell cantilever example (Lewiński et al. 1994b). Careful inspection of the contour lines obtained for this example (Fig. 4b) reveals that multiple contour lines point to the location where these BC's have to be applied. To allow for these *fan-BC's* in the initial structure, all elements and nodes within radius $R_{BC} = 1/8\ L$ of both BC's are pulled exactly into the boundary nodes, as is shown in Fig. 6.

We can automatically identify if a boundary condition needs to be a *standard-BC* or a *fan-BC*. Therefore, we look at orientation field θ, inside radius R_{BC} of the boundary nodes. At locations where a *fan-BC* needs to be inserted, the angular field is rapidly changing, hence we can simply check if points close to a nodal BC are inside Ω_θ.

3.5 Preparation of initial frame structure

To clean up and improve the stability of the initial structure, normal nodes (*i.e.* non-boundary conditions) connected to only one or two elements are removed. In the case of a node connected to a single element, the element cannot carry any load, hence both node and element are removed. Furthermore, connections between two elements are unstable and do not exist in the solution space for Michell's problem of least-weight trusses. Therefore the corresponding elements are merged into a single element, while the node is removed. In some situations this operation will result in crossing elements. If this happens the largest element in a crossing is removed. Finally, it has to be mentioned that all operations that modify the structure, e.g. assigning BC's, are made volume preserving. Hence, the relative material distribution throughout the domain remains as close to the material distribution of the continuum model as possible.

The initial frame structure for the Michell cantilever obtained using the approach described above, for $\varepsilon = 50\,h_f$ can be seen in Fig. 7a. Similarly, the initial structures for the MBB-beam and the Michell cantilever with circular

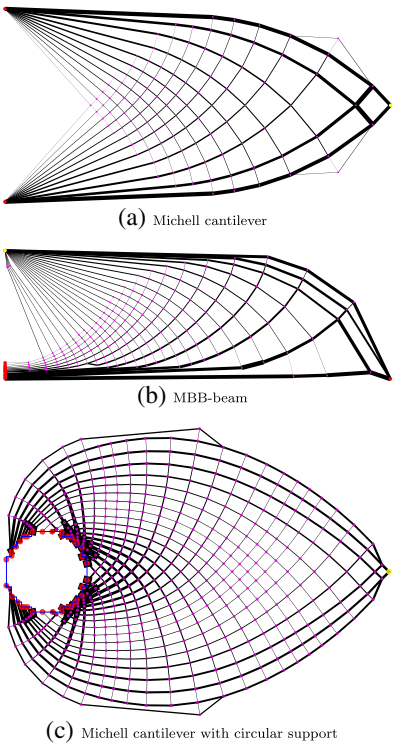

(a) Michell cantilever

(b) MBB-beam

(c) Michell cantilever with circular support

Fig. 7 Initial structures extracted from homogenization-based topology optimization for $\varepsilon = 50\,h_f$

support, both for $\varepsilon = 50\, h_f$, can be seen in Fig. 7b and c respectively.

3.6 Void regions inside design domain

The mapping procedure described above can easily be extended to take specified void regions in the design domain into account. However, special care needs to be taken at the corners of these void regions, since the homogenization based microstructures are either oriented parallel to the void region, or oriented to go exactly through the corner point of a void region. This highly optimal use of the available design space can result in mapped elements that cross the void domain. Furthermore, it should be noted that corners of a void region can also be a source of a *fan* similar to the *fan-BC's*. As discussed by Lewiński and Rozvany (2008) the optimal solution for the L-shaped domain, shown in Fig. 2c, consists of a *fan* at the corner of the void domain.

To accommodate for these *fan* corner nodes, a check is performed for each corner of a specified void domain. If points within R_{BC} of these corners are inside Ω_θ, a *fan* is created in the exact same manner as a *fan-BC*. At a corner of the void domain, which is not a *fan*, and at which an element crosses, a node is inserted and the crossing element is split in two elements.

The projected frame structure for the L-shaped domain can be seen in Fig. 8a, the initial frame structure for the MBB-beam with a rectangular region of void is shown in Fig. 8b, where for both structures $\varepsilon = 50\, h_f$.

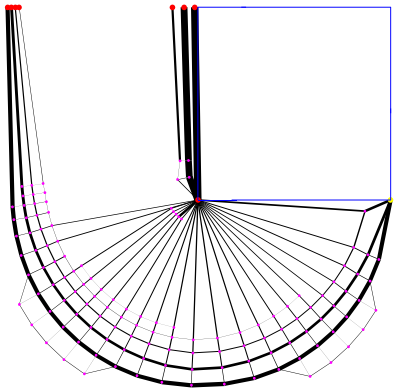

(a) L-shaped domain

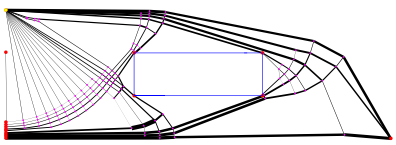

(b) MBB-beam with a rectangular region of void

Fig. 8 Initial structures extracted from homogenization-based topology optimization for $\varepsilon = 50\, h_f$

4 Post size- and geometry-optimization

In this section we propose a frame optimization scheme that ensures solutions close to the solutions of Michell's problems of least-weight trusses, hence with a negligible bending contribution. Furthermore, we propose a strategy to avoid: 1) elements that are very thin, 2) elements that are very short, and 3) elements that are parallel and partially overlap, since each of these three cases result in a singular stiffness matrix when modeled as truss.

4.1 Motivation for frame analysis

It is well-known that solutions of Michell's problem of least-weight trusses are in the space of statically determinate structures, Pedersen (1969). However, it is not possible to use truss elements to assess the performance of the mapped structures. Small misalignments close to boundary conditions, e.g. at the symmetry conditions for the MBB-beam example, may result in indeterminate structures. Nevertheless, a post-optimization scheme is required, such that the projected structures converges towards solutions of Michell's problem of least-weight trusses. To do so, frame elements are used that, contrary to truss elements, not only carry axial loads but also have bending stiffness.

For such an analysis appropriate relations between the domain length L and element areas have to be chosen, such that the bending stiffness does not become dominant. A circular cross-section is chosen for the frame elements, hence for given element i the relation between axial (k_a) and bending (k_b) stiffness is given by,

$$\frac{k_a}{k_b} \propto \frac{l_i^2}{A_i} \tag{12}$$

where l_i is the length of the element and A_i the corresponding area.

The design vector for geometry optimization $\mathbf{x}_n$ holds the coordinates of the nodal positions. To get a well conditioned optimization problem the length of the domain is scaled such that $\mathbf{x}_n \in [0, 10]$. The vector of element areas $\mathbf{A}$ is obtained using the design vector for size optimization $\mathbf{x}_e$, and the maximum allowable element area A_{max}.

$$\mathbf{A}(\mathbf{x}_e) = \mathbf{x}_e A_{max} \forall\, \mathbf{x}_e \in [0, 1[\tag{13}$$

Here $\mathbf{x}_e$ is based on the relative material distribution in the mapped elements. The relative values in $\mathbf{x}_e$ are scaled down far enough such that the upper bound of 1 never becomes active to prevent that $\mathbf{A} > A_{max}$. Therefore, the relation

between bending and axial stiffness is only controlled by choosing an appropriate value for A_{max}. Hence, A_{max} is chosen differently for each optimization example such that the relation between the mean values of $\frac{k_a}{k_b}$ $(i.e.\ \frac{\bar{k}_a}{\bar{k}_b})$ is always exactly the same at the start of the post-optimization scheme, e.g. $\frac{\bar{k}_a}{\bar{k}_b} = 100$.

To converge towards a design that is purely loaded in axial direction, the relative importance of the bending stiffness is slowly decreased using a continuation scheme. In this scheme A_{max} and the volume constraint V^* are lowered by 12.5 % for every 10 iterations. This does not have an effect on the relative distribution of axial loads; however, it does make it uneconomical to have elements that are not purely loaded in axial direction. The continuation scheme start after the first 100 iterations and is continued until A_{max} is less than 2.5% of its initial value. At this point the contribution of the bending stiffness to the strain energy is negligible, as will be discussed in more detail in Section 5. The choice for the steps used in the continuation scheme result from a trade-off between the performance of the design and computational cost. For smaller steps, significantly more iterations are required to optimize the design, resulting in a slightly better objective. Similarly, a larger stepwise reduction in bending stiffness, means that the algorithm converges more quickly; however, resulting in a reduced performance.

4.2 Optimization scheme

The frame optimization problem is solved to minimize compliance $\mathcal{J}_f$, subject to a volume constraint V^*, which is the amount of material in the frame members at the first iteration. The optimization problem is solved in nested form using a gradient-based optimization scheme, where we use the Method of Moving Asymptotes (MMA) to update the design variables (Svanberg 1987). The corresponding optimization problem can be written as,

$$\begin{aligned} \min_{\mathbf{x}_n, \mathbf{x}_e} &: \mathcal{J}_f(\mathbf{x}_n, \mathbf{x}_e, \mathbf{U}) = \mathbf{F}^T\mathbf{U} \\ \text{s.t.} &: \mathbf{K}(\mathbf{x}_n, \mathbf{x}_e)\mathbf{U} = \mathbf{F} \\ &: \frac{\sum_{i=1}^{n_e} l_i(\mathbf{x}_n) A_i(\mathbf{x}_e)}{V^*} - 1 \leq 0 \\ &: \mathbf{x}_{n,l} \leq \mathbf{x}_n \leq \mathbf{x}_{n,u} \\ &: \mathbf{x}_{e,l} \leq \mathbf{x}_e \leq \mathbf{x}_{e,u} \end{aligned} \tag{14}$$

Where $\mathbf{x}_{e,l}$, $\mathbf{x}_{e,u}$, $\mathbf{x}_{n,l}$ and $\mathbf{x}_{n,u}$ are the lower and upper bounds for the size and geometry design vectors respectively. For each design iteration lower and upper bounds on the design variables are adaptively selected. These bounds are chosen such that the design changes gradually, furthermore, the bounds on $\mathbf{x}_n$ make sure that elements will not cross each other, or move into the specified void domains.

4.3 Removal of thin elements

During the optimization, values in $\mathbf{x}_e$ can become close to 0, hence these elements contain almost no material. Typically, these are prevented by using a lower bound on the areas; however, this adds artificial stiffness to the structures, and can also prevent structures from becoming statically determinate. Therefore, elements smaller than a selected threshold will be removed from the solution space. This threshold is based on the value of A_η used in the mapping procedure, but scaled with the same factor used to obtain $\mathbf{x}_e$. Furthermore, the threshold is consistently updated during the continuation scheme.

By removing thin elements from the frame mesh, normal nodes (*i.e* non-BC's) can be connected to only one or two elements, making the structure unstable. To avoid this undesired effect, the exact same procedure is applied as discussed in Section 3.5.

4.4 Merging of close nodes

It is well-known that for some elements the nodes move towards the same point, making the corresponding element length zero. This effect, sometimes referred to as melting nodes (Achtziger 2007), will cause a singularity in the stiffness matrix and is therefore undesired. To take this into account, the nodes of elements shorter than a selected threshold l_{short} will be merged, removing a node from the solution space in an approach similar to He and Gilbert (2015). The value for the threshold l_{short} is selected to be one fifth of the average size of the projected element ε, scaled with the same scaling factor used to obtain $\mathbf{x}_n$.

By merging nodes, it is possible that non-unique elements exist between two nodes. To take this undesired effect into account, one of the corresponding elements is removed, and the volume of both elements is contained by the remaining element.

4.5 Merging of parallel and partially overlapping elements

It is possible that during post-optimization two or more elements, located along boundaries of the design domain are partially overlapping and parallel. This situation can be observed at the lower boundary of the MBB-beam example with a void, shown in Fig. 9. Here, there is an element between node 1 and node 2, an element between node 2 and node 3, and an element between node 1 and node 3.

Although all three elements are unique, it is unphysical that the elements overlap, furthermore, this can have an undesired effect on the condition-number of the stiffness matrix. To remedy this, the longest element is split into two elements. In this case the two smaller elements already exist,

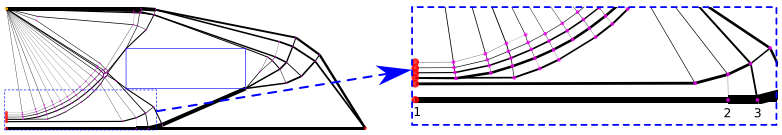

Fig. 9 MBB-beam with a rectangular region of void, to demonstrate that elements can be parallel and partially overlap. There is an element between node 1 and node 2, an element between node 2 and node 3, and an element between node 1 and node 3

and the volume of the longest elements is transferred to the smaller elements consistently.

5 Numerical examples

An overview of all parameters used in this work can be found in Table 1. The horizontal lines are used to show a division in parameters used in: 1) homogenization-based topology optimization, 2) calculation of mapping functions, 3) post-optimization. Please note that we use $\varepsilon = 50\ h_f$, unless otherwise stated. In the following, we demonstrate the suggested procedure on a number of examples and compare with analytical solutions when available.

5.1 Michell cantilever

The near-optimal initial structure for the Michell cantilever, shown in Fig. 7a, has been optimized using the presented post-optimization scheme. The result, shown in Fig. 10, can be modeled as a truss, *i.e.* it is statically determinate.

To assess the performance of the optimized design, one can look at the non-dimensional mass when evaluated as truss $\overline{M}_t$, which for a Michell cantilever can be calculated as Rozvany (1998) and Bendsøe et al. (1994),

$$\overline{M}_t = \frac{\sqrt{ME\mathcal{J}_t}}{FL} \tag{15}$$

Here M is the volume of the final structure, and $\mathcal{J}_t$ the compliance when modeled as a truss structure. The non-dimensional mass for the optimized Michell cantilever is 7.0391, which is close to the optimal value, $\overline{M}_{opt} = 7.0247$, found in a table in Graczykowski and Lewiński (2010). This means that the non-dimensional mass of the optimized structure is just 0.204% higher than the analytical optimum. Furthermore, the compliance when the structure is modeled as a truss $\mathcal{J}_t$, is almost identical to the compliance modeled as a frame structure $\mathcal{J}_f = 7.0390$, used in the post-optimization scheme. It is possible to identify a measure (f_b) of the total contribution of the bending stiffness on $\mathcal{J}_f$.

$$f_b = \frac{\mathcal{J}_f - \mathbf{U}_t^T \mathbf{F}_t}{\mathcal{J}_f} \times 100\% \tag{16}$$

Here $\mathbf{U}_t$ and $\mathbf{F}_t$ correspond to the displacement indices of the solution and load vector respectively, *i.e.* excluding indices corresponding to rotation. The bending contribution for the optimized Michell cantilever is 0.00045%. A plot of this contribution for each iteration of the post-optimization scheme can be seen in Fig. 11.

Due to the continuation scheme, the bending contribution is lowered every 10 iterations after the 100^{th} iteration. However, it is more interesting to see that the bending contribution is drastically reduced in the first few iterations. The reason is that tiny misalignments of nodal positions close to the boundary conditions severely deteriorate the

Table 1 Parameters used in the numerical experiments

Parameter	Definition	Value
E	Young's modulus of material in continuum model	1
E_{min}	Young's modulus of background material	0.005 E
ν	Poisson's ratio for isotropic background material	0.3
r_{min}	Filter radius used in continuum topology optimization	1.5 h_c
η	Minimum feature size per layer in the microstructure	0.05
γ_θ	Threshold value that determines whether angular field is rapidly changing	$\frac{\pi}{4}\frac{1}{h_c}$
α_1	Spatially variant parameter to relax the objective of projection	[0.01, 0.1 , 1]
α_2	Spatially variant parameter to relax the constraint of projection	[0, 1]
ε	average length of the frame member	50 h_f
R_{BC}	Radius to search for a $fan\text{-}BC$, and to pull in all nodes to BC	1/8 L
l_{short}	Short element length which dictates when two nodes are merged	0.2 ε
$\frac{k_a}{k_b}$	Starting relation between the mean axial and bending stiffness	100
$\frac{A_{max,end}}{A_{max,start}}$	Measure for reduction in bending stiffness	0.025

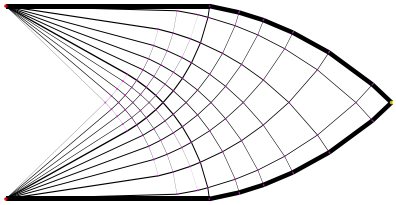

Fig. 10 Optimized structure for the Michell cantilever, using initial structure for $\varepsilon = 50\, h_f$

performance of the structure (e.g. singular matrix when modeled as truss). When modeled as a frame structure, the initial bending stiffness provides stability; however, the performance is improved when these nodes are better aligned, hence the contribution of the bending to the compliance is reduced.

The optimization is performed for the Michell cantilever using three different levels of detail of the initial structure, *i.e.* $\varepsilon = 20\, h_f$, $\varepsilon = 50\, h_f$, and $\varepsilon = 100\, h_f$. The optimized structures for $\varepsilon = 20\, h_f$, and $\varepsilon = 100\, h_f$ can be seen in Fig. 12a and b respectively.

The corresponding size of the fine mesh on which the nodes and elements are obtained, the number of nodes N_n, number of elements N_e, the performance measured in non-dimensional masses ($\overline{M}_f$ and $\overline{M}_{opt}$), the error ξ between $\overline{M}_f$ and the analytical solution $\overline{M}_{opt}$ and the contribution of the bending stiffness f_b can be found in Table 2. As expected, a finer initial structure results in a better performing design. Furthermore, the time to do the homogenization-based topology optimization on the coarse mesh T_c, the time to obtain the initial structure T_ϕ, the time to do the post-optimization T_f, and the total time T_{tot} are shown. Here it has to be noted that all experiments are performed using a single processor MATLAB code on a standard PC. Hence, large potential for further time reduction exists.

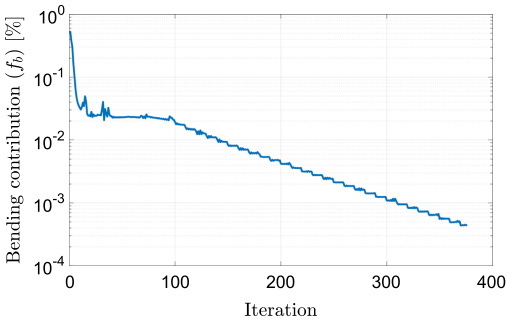

Fig. 11 Contribution of the bending stiffness to the overall compliance for the Michell cantilever

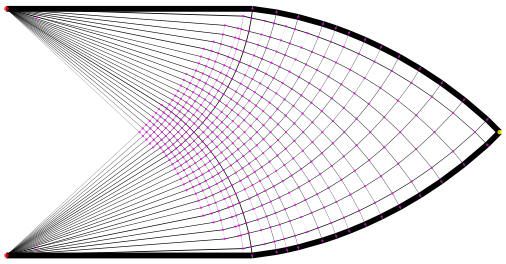

(a) $\varepsilon = 20\, h_f$

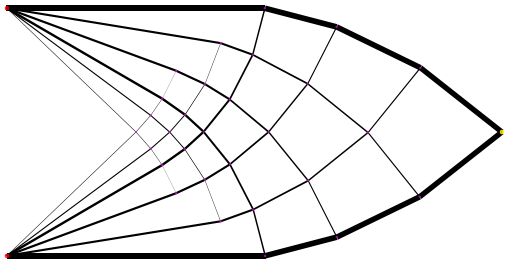

(b) $\varepsilon = 100\, h_f$

Fig. 12 Optimized structures for the Michell cantilever

It can be seen that a more detailed structure comes at a larger computational cost, which is dominated by the sensitivity analysis for the post-optimization scheme. Furthermore, the increased level of detail means an increase in computational cost to obtain the initial mesh, since more contour lines of mapping function ϕ_1 and ϕ_2 need to be considered. Nevertheless, the increase in computational cost is significantly smaller compared to growth methods, where the time to insert a new member scales exponentially.

5.2 Stability of optimized results

The far majority of the optimized structures for the other examples is unstable when modeled as a truss. To explain this we can take another look at Fig. 9, where the bottom of the MBB-beam with a rectangular void is shown. In this example, a condition for stability when modeled as truss, is that node 1 and node 2, should have the exact same value for their y-coordinate. Even the slightest misalignment (e.g. 10^{-6}) will result in an unstable structure since node 1, is only supported in the x-direction.

When modeled as frame, even the smallest bending contribution, will prevent such an instability. Hence, for the post-optimized MBB-beam shown in Fig. 13, the element that is connected to the middle node of the symmetry boundary is nearly horizontal; however not exactly.

Table 2 Performance and computational cost of the near optimal truss and frame structures

Ex.	Proj. mesh	ε	N_n	N_e	$\overline{M}_f$	$\overline{M}_{opt}$	ξ	f_b	T_c	T_ϕ	T_f	T_{tot}
1	1600×800	$20\,h_f$	453	900	7.0327	7.0247	0.114%	0.00032%	96.0 s	104.2 s	339.9 s	540.0 s
1	1600×800	$50\,h_f$	103	202	7.0392	7.0247	0.206%	0.00045%	96.0 s	22.9 s	67.5 s	186.4 s
1	1600×800	$100\,h_f$	32	60	7.0545	7.0247	0.422%	0.00059%	96.0 s	18.4 s	29.3 s	143.7 s
2	1600×1200	$50\,h_f$	380	710	2.1248	2.1401	−0.720%	0.0173%	136.3 s	47.0 s	288.4 s	487.5 s
2	1600×1200	$100\,h_f$	122	212	2.1474	2.1401	0.340%	0.0021%	136.3 s	30.5 s	72.7 s	255.3 s
3	2520×840	$50\,h_f$	106	208	14.1878	14.0937	0.663%	0.0055%	152.1 s	45.1 s	94.8 s	292.0 s
3	2520×840	$100\,h_f$	40	74	14.2675	14.0937	1.218%	0.0085%	152.1 s	32.6 s	43.8 s	228.4 s
4	2520×840	$50\,h_f$	40	67	14.5616	–	–	0.0029%	146.6 s	48.5 s	65.8 s	260.9 s
4	2520×840	$100\,h_f$	19	28	14.6425	–	–	0.0031%	146.6 s	43.3 s	37.8 s	227.7 s
5	1600×1600	$50\,h_f$	26	46	9.3004	9.283	0.187%	0.0074%	178.4 s	53.3 s	58.2 s	289.8 s
5	1600×1600	$100\,h_f$	15	24	9.3284	9.283	0.487%	0.0044%	178.4 s	45.8 s	37.0 s	261.2 s

Where example 1) is the Michell cantilever, 2) the Michell cantilever with circular support, 3) the MBB-beam, 4) the MBB-beam with void, and 5) the L-shaped domain

Unfortunately, this statical indeterminacy means that we cannot assess the performance as a truss, and hence an exact comparison between the optimal value for the non-dimensional mass, $\overline{M}_{opt} = 14.0937$ and $\overline{M}_t$ is not possible. Nevertheless, we argue that the bending contribution is sufficiently small, $f_b = 0.0055\%$ to allow for a comparison between $\overline{M}_{opt}$ and the non-dimensional weight calculated with the compliance from the frame model, $\overline{M}_f = 14.1878$.

To demonstrate this we decrease A_{max} by different orders of magnitude, such that the bending stiffness of the node at the symmetry boundary is reduced. As can be seen in Table 3, this will lead to an increase in non-dimensional mass of the frame model ($\overline{M}_f$). However, the contribution of the purely axial stiffness $\overline{M}(\mathbf{U}_t^T \mathbf{F}_t)$ remains almost perfectly intact. The reason for this is that the node at the symmetry boundary is the only node that causes an instability. Only this node is affected by a decrease in bending stiffness, hence the increase in strain energy in the system is purely due to the near horizontal element being stretched. This increase in energy has a negligible effect on the energy in the rest of the system, even for low values of A_{max}, and therefore we argue that $\overline{M}_f$ can be used to compare with the optimal solution $\overline{M}_{opt}$.

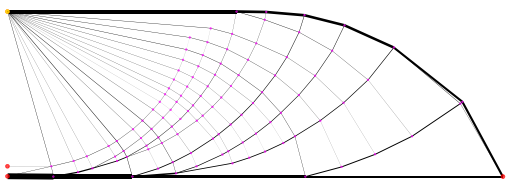

Fig. 13 Optimized structure for the MBB-beam, using initial structure for $\varepsilon = 50\,h_f$

5.3 Discussion of results

The post-optimized structures for the MBB-beam, Michell cantilever with circular support, MBB-beam with rectangular void and L-shaped domain, all for $\varepsilon = 50\,h_f$ can be seen in Fig. 13, Fig. 14a, b and c respectively. While the corresponding performance and the different times can be seen in Table 2. It is interesting to see that the optimized structures perform very close to the optimal solution, at a negligible bending contribution. However, the performance of the MBB-beam with rectangular void cannot be compared to an analytical solution, since this solution is not known.

Furthermore, it is interesting to see that the non-dimensional mass for the Michell cantilever with circular support is lower than the analytical optimum. This does not come from the fact that it is modeled as a frame, nor does it come from the analytical solution being wrong. The simple reason is that the boundary of the extracted structure is not perfectly circular as can be seen in Fig. 14a. This jagged boundary has its origin in the coarse-scale homogenization-based topology optimization model, where the circular

Table 3 Non-dimensional mass of the frame structure $\overline{M}_f$, and purely axial contribution of the non-dimensional mass $\overline{M}(\mathbf{U}_t^T \mathbf{F}_t)$ when the area is scaled down

Area scaling	$\overline{M}_f$	$\overline{M}(\mathbf{U}_t^T \mathbf{F}_t)$	f_b
A_{max}	14.1878	14.1870	0.0055%
$10^{-1}\,A_{max}$	14.1890	14.1890	0.0050%
$10^{-2}\,A_{max}$	14.1940	14.1890	0.0340%
$10^{-3}\,A_{max}$	14.2370	14.1890	0.3360%
$10^{-4}\,A_{max}$	14.6600	14.1890	3.2120%
$10^{-5}\,A_{max}$	18.3610	14.1900	22.7140%
$10^{-6}\,A_{max}$	39.4440	14.3250	63.6830%

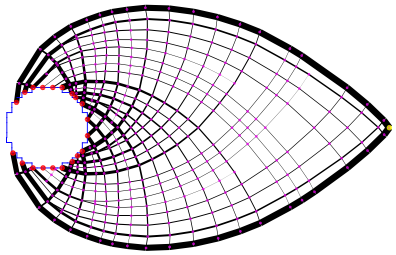

(a) Michell cantilever with circular support

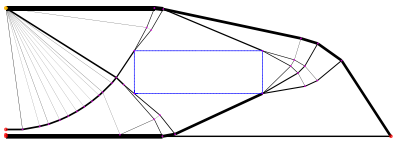

(b) MBB-beam with rectangular void

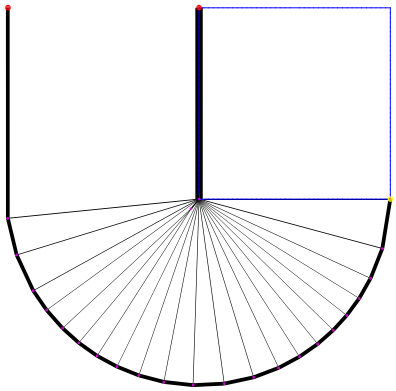

(c) L-shaped domain

Fig. 14 Optimized structures extracted from homogenization-based topology optimization for $\varepsilon = 50\, h_f$

boundary is approximated by coarse square elements. In our algorithm, this is the boundary that is transferred down from the coarse-scale topology optimization model to the frame model, hence the difference with the analytical optimum.

Besides the fact that the final structures perform well, it has to mentioned that the total procedure comes at a relatively low computational cost, i.e. all examples have been obtained within 10 minutes using a single processor MATLAB code on a standard PC. The homogenization-based topology optimization can be done in a couple of minutes, where the difference in time between the examples comes from different mesh sizes. E.g. the Michell cantilever is optimized on a mesh of 80×40 elements, while the L-shaped domain is optimized on a mesh consisting of 80×80 elements. The extraction time for the initial structure does increase when the average spacing ε is decreased. However, this increase in computational cost is more or less quadratically related to $1/\varepsilon$, which is a significant advantage over growth methods that scale exponentially when fine designs are considered.

6 Conclusion

An approach to obtain near-optimal frame structures has been presented, where the discrete structures are based on the solution of a homogenization-based topology optimization model. The coarse-scale homogenization-based continuum solution is used to create a close to optimal initial structure, which is obtained by solving for two mapping functions and using their corresponding contour lines. Furthermore, accurate integration of the continuum solution allows for a good starting guess for the element areas. Afterwards, these initial structures are optimized using a frame optimization code, to avoid the problem of a singular matrix when modeled as truss. To make sure that the final structures are close to the known solutions of Michell's problem of least–weight trusses, we gradually reduce the bending stiffness such that the final structures are only loaded in axial direction.

Based on numerical experiments, we can conclude that the presented approach produces near-optimal frame structures at a relatively low computational cost. This promising performance paves the way for extending the methodology to multiple load problems. In these problems, the optimal continuum solution is in the space of rank-3 microstructures, compared to the orthogonal microstructures used in the current approach. The extension to 3-dimensions is also possible, based on orthogonal projection of (sub-optimal) truss-like microstructures.

Acknowledgements The authors acknowledge the support of the Villum Fonden through the Villum investigator project InnoTop. The authors would also like to thank Andreas Bærentzen and Niels Aage for valuable discussions during the preparation of the work. Finally, the authors wish to thank Krister Svanberg for providing the MATLAB MMA code.

References

Aage N, Nobel-jørgensen M, Andreasen CS, Sigmund O (2013) Interactive topology optimization on hand-held devices. Struct Multidiscip Optim 47(1):1–6. https://doi.org/10.1007/s00158-012-0827-z

Achtziger W (2007) On simultaneous optimization of truss geometry and topology. Struct Multidiscip Optim 33(4):285–304. https://doi.org/10.1007/s00158-006-0092-0

Bendsøe MP, Haber RB (1993) The michell layout problem as a low volume fraction limit of the perforated plate topology optimization

problem: an asymptotic study. Structural optimization 6(4):263–267. https://doi.org/10.1007/BF01743385
Bendsøe MP, Ben-Tal A, Zowe J (1994) Optimization methods for truss geometry and topology design. Structural optimization 7(3):141–159. https://doi.org/10.1007/BF01742459
Bourdin B (2001) Filters in topology optimization. Int J Numer Methods Eng 50(9):2143–2158. https://doi.org/10.1002/nme.116
Bourdin B, Kohn R (2008) Optimization of structural topology in the high-porosity regime. J Mech Phys Solids 56(3):1043–1064. https://doi.org/10.1016/j.jmps.2007.06.002
Bruns T (2006) Zero density lower bounds in topology optimization. Comput Methods Appl Mech Eng 196(1):566–578. https://doi.org/10.1016/j.cma.2006.06.007
Bruns T, Tortorelli D (2001) Topology optimization of non-linear elastic structures and compliant mechanisms. Comput Methods Appl Mech Eng 190(26–27):3443–3459. https://doi.org/10.1016/S0045-7825(00)00278-4
Dobbs MW, Felton LP (1969) Optimization of truss geometry. J Struct Div 95(10):2105–2118
Dorn WS, Gomory RE, Greenberg HJ (1964) Automatic design of optimal structures. Journal de Mecanique 3:25–52
Gao G, yu Liu Z, bin Li Y, feng Qiao Y (2017) A new method to generate the ground structure in truss topology optimization. Eng Optim 49(2):235–251. https://doi.org/10.1080/0305215X.2016.1169050
Gilbert M, Tyas A (2003) Layout optimization of large-scale pin-jointed frames. Eng Comput 20(8):1044–1064. https://doi.org/10.1108/02644400310503017
Graczykowski C, Lewiński T (2010) Michell cantilevers constructed within a half strip. tabulation of selected benchmark results. Struct Multidiscip Optim 42(6):869–877. https://doi.org/10.1007/s00158-010-0525-7
Groen JP, Sigmund O (2017) Homogenization-based topology optimization for high-resolution manufacturable micro-structures. Int J Numer Methods Eng :1–18. https://doi.org/10.1002/nme.5575
He L, Gilbert M (2015) Rationalization of trusses generated via layout optimization. Struct Multidiscip Optim 52(4):677–694. https://doi.org/10.1007/s00158-015-1260-x
Hemp WS (1973) Optimum structures. Clarendon Press, Oxford
Lewiński T, Rozvany GIN (2008) Exact analytical solutions for some popular benchmark problems in topology optimization iii: L-shaped domains. Struct Multidiscip Optim 35(2):165–174. https://doi.org/10.1007/s00158-007-0157-8
Lewiński T, Zhou M, Rozvany G (1994a) Extended exact least-weight truss layouts—part ii: Unsymmetric cantilevers. Int J Mech Sci 36(5):399–419. https://doi.org/10.1016/0020-7403(94)90044-2
Lewiński T, Zhou M, Rozvany G (1994b) Extended exact solutions for least-weight truss layouts—part i: Cantilever with a horizontal axis of symmetry. Int J Mech Sci 36(5):375–398. https://doi.org/10.1016/0020-7403(94)90043-4
Martínez P, Martí P, Querin OM (2007) Growth method for size, topology, and geometry optimization of truss structures. Struct Multidiscip Optim 33(1):13–26. https://doi.org/10.1007/s00158-006-0043-9
Michell A (1904) The limits of economy of material in frame-structures. Phil Mag 8(47):589–597. https://doi.org/10.1080/14786440409463229
Pantz O, Trabelsi K (2008) A post-treatment of the homogenization method for shape optimization. SIAM J Control Optim 47(3):1380–1398. https://doi.org/10.1137/070688900
Pantz O, Trabelsi K (2010) Construction of minimization sequences for shape optimization. In: 15th international conference on methods and models in automation and robotics (MMAR), pp 278–283. https://doi.org/10.1109/MMAR.2010.5587222
Pedersen P (1969) On the minimum mass layout of trusses. In: AGARD conference proceedings no 36, symposium on structural optimization, pp 36–70
Pedersen P (1989) On optimal orientation of orthotropic materials. Structural optimization 1(2):101–106. https://doi.org/10.1007/BF01637666
Pedersen P (1990) Bounds on elastic energy in solids of orthotropic materials. Structural optimization 2(1):55–63. https://doi.org/10.1007/BF01743521
Ramos JrAS, Paulino GH (2016) Filtering structures out of ground structures – a discrete filtering tool for structural design optimization. Struct Multidiscip Optim 54(1):95–116. https://doi.1007/s00158-015-1390-1
Rozvany GIN (1998) Exact analytical solutions for some popular benchmark problems in topology optimization. Structural optimization 15(1):42–48. https://doi.org/10.1007/BF01197436
Rule WK (1994) Automatic truss design by optimized growth. J Struct Eng 120(10):3063–3070
Sokół T (2011) A 99 line code for discretized michell truss optimization written in mathematica. Struct Multidiscip Optim 43(2):181–190. https://doi.org/10.1007/s00158-010-0557-z
Svanberg K (1987) The method of moving asymptotes—a new method for structural optimization. Int J Numer Methods Eng 24(2):359–373. https://doi.org/10.1002/nme.1620240207
Washizawa T, Asai A, Yoshikawa N (2004) A new approach for solving singular systems in topology optimization using krylov subspace methods. Struct Multidiscip Optim 28(5):330–339. https://doi.org/10.1007/s00158-004-0439-3
Zegard T, Paulino GH (2014) Grand - ground structure based topology optimization for arbitrary 2d domains using matlab. Struct Multidiscip Optim 50(5):861–882. https://doi.org/10.1007/s00158-014-1085-z
Zhou K, Li X (2008) Topology optimization for minimum compliance under multiple loads based on continuous distribution of members. Struct Multidiscip Optim 37(1):49–56. https://doi.org/10.1007/s00158-007-0214-3
Zhou K, Li X (2011) Topology optimization of truss-like continua with three families of members model under stress constraints. Struct Multidiscip Optim 43(4):487–493. https://doi.org/10.1007/s00158-010-0584-9

Publication [P3]

E. Träff, O. Sigmund and J.P. Groen. Simple single-scale microstructures based on optimal rank-3 laminates. *Structural and Multidisciplinary Optimization*, 1-11, 2019. doi:10.1007/s00158-018-2180-3

Structural and Multidisciplinary Optimization
https://doi.org/10.1007/s00158-018-2180-3

RESEARCH PAPER

Simple single-scale microstructures based on optimal rank-3 laminates

E. Träff[1] · O. Sigmund[1] · J. P. Groen[1]

Received: 11 September 2018 / Revised: 4 December 2018 / Accepted: 11 December 2018
© Springer-Verlag GmbH Germany, part of Springer Nature 2019

Abstract
With the goal of identifying optimal elastic single-scale microstructures for multiple loading situations, the paper shows that qualified starting guesses, based on knowledge of optimal rank-3 laminates, significantly improves chances of convergence to near optimal designs. Rank-3 laminates, optimal for a given set of anisotropic loading conditions, are approximated on a single scale using a simple mapping approach. We demonstrate that these mapped microstructures perform relatively close to theoretical energy bounds. Microstructures with a performance even closer to the bounds can be obtained by using the approximated rank-3 structures in a further step as starting guesses for inverse homogenization problems. Due to the nonconvex nature of inverse homogenization problems, the starting guesses based on rank-3 laminates outperform classical starting guesses with homogeneous or random material distributions. Furthermore, the obtained single-scale microstructures are relatively simple, which enhances manufacturability. Results, obtained for a wide range of loading cases, indicate that microstructures with performance within 5–8% of the theoretical optima can be guarantied, as long as feature sizes are not limited by minimium size constraints.

Keywords Inverse homogenization · Optimal microstructures · Starting guess

1 Introduction

For many engineering applications, it is of interest to design periodic materials with tailored or extremal properties. The use of topology optimization to such design problems was introduced by Sigmund (1994) and is generally referred to as inverse homogenization. Since its introduction, the approach has been applied to many design problems, such as materials with negative Poisson's ratio (Larsen et al. 1997; Andreassen et al. 2014; Clausen et al. 2015), materials with maximum shear and bulk moduli (Sigmund and Bendsøe 1999; Sigmund 2000), or materials with increased buckling strength (Neves et al. 2002; Thomsen et al. 2018). Besides elasticity problems, the method has been successfully applied to design materials, e.g., thermal, fluid, and wave guiding problems, as well as a large number of other applications. A detailed discussion and overview of the field of material design is given in the recent review paper by Osanov and Guest (2016).

In the context of elasticity, several researchers have looked into multiscale or so-called hierarchical designs. Here, the topology optimization problem is divided into a global material distribution problem and local composite material design problems at the microscale. The composite microstructures are tailored for maximum strain energy, subject to the local stresses or strains (Rodrigues and Guedes 2002; Coelho et al. 2011; Xia and Breitkopf 2017). Hence, at each local point, an inverse homogenization problem is solved to optimize the microstructures for one or more loading cases. To reduce the computational cost associated with the large number of inverse homogenization problems or to ensure less complex manufacturing, one can restrict the amount of unique microstructures; however, this comes with a loss of optimality (Liu et al. 2008; Schury et al. 2012; Sivapuram et al. 2016). Anyway, when assuming separation of scales, multiscale design approaches require repeated and pointwise optimization of local microstructures, subjected to one or more load cases.

It is well-known that composite microstructures, assembled from two isotropic materials (possibly one of them being void), satisfying the optimal bound on complementary energy (i.e., maximal strain energy) can be realized

Responsible Editor: Gregoire Allaire

✉ J. P. Groen
jergro@mek.dtu.dk

[1] Department of Mechanical Engineering, Solid Mechanics, Technical University of Denmark, Nils Koppels Alle, B.404, 2800 Kgs. Lyngby, Denmark

Published online: 03 January 2019

as so-called rank-3 laminates (Lurie and Cherkaev 1984; Francfort and Murat 1986; Milton 1986; Avellaneda 1987), for plane problems under the assumption of linear elasticity. For extensive details on rank-N laminates and homogenization-based topology optimization, the reader is referred the monographs by Cherkaev (2000), Allaire (2002), and Bendsøe and Sigmund (2004). In fact, Guedes et al. (2003) compared the performance of microstructures optimized using inverse homogenization with the energy bounds that can be reached using optimal rank-3 laminates. Interestingly, however, this has never lead to a detailed study that aims at using knowledge of the optimal rank-3 laminates for the design of single-scale microstructures using inverse homogenization.

Apart from rank-N laminates, single-scale, so-called Vigdergauz microstructures have been conceived and analyzed by analytical means (Vigdergauz 1994a, b; Grabovsky and Kohn 1995; Liu et al. 2007), or have come out as result of many topology optimization approaches, e.g., (Sigmund and Bendsøe 1999; Sigmund 2000). Vigdergauz structures may achieve the maximum bulk modulus bound (i.e., are optimal for hydrostatic loading), but cannot achieve the maximum shear modulus bound simultaneously (i.e., a single-scale structure cannot produce the theoretically maximal isotropic Young's modulus). A proof that more length scales are required to reach the theoretical bounds is given by Allaire and Aubry (1999). Hence, it is clear that imposing a single-scale constraint on microstructure design inherently will put a limit on achievable performance, but on the other hand, this optimality gap may be acceptable considering that the microstructures become manufacturable. For other works and discussions on single-scale microstructures with respect to theoretical bounds, the readers are referred to Bourdin and Kohn (2008), Sigmund et al. (2016), and Berger et al. (2017).

In this work, we propose a systematic approach for creating near-optimal single-scale microstructures, based on the layer directions and relative widths of optimal rank-3 laminates (see, e.g., Fig. 1). We demonstrate that this approximation of the microstructures already performs relatively close, e.g., 5–15%, to the optimal energy bounds. Furthermore, we demonstrate that this performance can be further improved by using these single-scale microstructures as starting guess for an inverse homogenization problem. In general, the nonconvex nature of the inverse homogenization problem results in convergence to inferior or very complex microstructures when using traditional starting guesses, such as uniform or random material distributions. It is shown that the proposed starting guesses from rank-3 laminates perform overall better than conventional starting guesses, especially when lower volume fractions are considered. Besides this better performance, the optimized microstructures using rank-3 inspired starting guesses are geometrically much simpler, in turn facilitating a simpler manufacturing process.

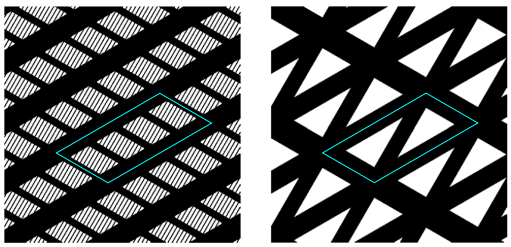

Fig. 1 Left: rank-3 microstructure with indicated hierarchy; right: approximated single-scale microstructure. Illustrations are based on a rank-3 laminate with $\rho = 0.7$, $\theta_1 = \pi/3$, $p_1 = 2/7$, $\theta_2 = -\pi/6$, $p_2 = 2/7$, $\theta_3 = \pi/6$, and $p_3 = 3/7$

2 Interpreting optimal microstructures on a single scale

The theory to obtain optimal rank-N laminates is well-established, as mentioned before, and only included here for completeness. In this work, we parameterize the optimal rank-3 laminate in terms of four trigonometric moments as introduced by Avellaneda and Milton (1988). Afterwards, we use the method of Lipton (1994) to reconstruct a rank-3 laminate from the optimal moments. Finally, we propose a novel method to approximate the rank-3 microstructure by a single-scale microstructure.

2.1 Optimal microstructures by the moment formulation

We seek to minimize the complementary work $\mathcal{C}$ on a periodic microstructure subjected to n_s stress cases.

$$\mathcal{C} = \frac{1}{2}\sum_{j}^{n_s} w_j \boldsymbol{\sigma}_j : \boldsymbol{C}^H : \boldsymbol{\sigma}_j, \tag{1}$$

where, $\boldsymbol{\sigma}_j$ is the stress tensor corresponding to the jth load case, w_j is the relative weighting such that $\sum_{j=1}^{n_s} w_j = 1$, and $\boldsymbol{C}^H$ describes the effective material compliance tensor of the considered microstructure. For a finite-rank microstructure, the effective compliance tensor can be written as follows:

$$\boldsymbol{C}^H = \boldsymbol{C}^+ - (1-f) \left(\left(\boldsymbol{C}^+ - \boldsymbol{C}^-\right)^{-1} - f\boldsymbol{E}^+ \sum_{n=1}^{N} p_n (\boldsymbol{t}_n \otimes \boldsymbol{t}_n) \otimes (\boldsymbol{t}_n \otimes \boldsymbol{t}_n) \right)^{-1}, \tag{2}$$

with $\boldsymbol{C}^+$ and $\boldsymbol{C}^-$ being the properties of the stiff (+) and compliant (-) material respectively, f is the volume fraction

of the stiff material, while E^+ is its corresponding Young's modulus. Furthermore, $\boldsymbol{t}_n$ represents the tangent vector of layer n, while $p_n \geq 0$ describes the relative contribution of the nth layer, s.t. $\sum_{n=1}^{N} p_n = 1$. Finally, $\otimes$ indicates the dyadic product.

For convenience, we can rewrite the fourth-rank tensor using the following orthogonal basis of second-rank tensors as follows:

$$\boldsymbol{\xi}_1 = \frac{1}{\sqrt{2}}\begin{bmatrix} 1 & 0 \\ 0 & -1 \end{bmatrix}, \quad \boldsymbol{\xi}_2 = \frac{1}{\sqrt{2}}\begin{bmatrix} 0 & 1 \\ 1 & 0 \end{bmatrix}, \quad \boldsymbol{\xi}_3 = \frac{1}{\sqrt{2}}\begin{bmatrix} 1 & 0 \\ 0 & 1 \end{bmatrix}. \tag{3}$$

Furthermore, we can reduce the number of variables describing the effective laminate properties using the following four moments as follows:

$$\begin{aligned} m_1 &= \sum_{n=1}^{N} p_n \cos(2\theta_n), \quad m_2 = \sum_{n=1}^{N} p_n \sin(2\theta_n), \\ m_3 &= \sum_{n=1}^{N} p_n \cos(4\theta_n), \quad m_4 = \sum_{n=1}^{N} p_n \sin(4\theta_n). \end{aligned} \tag{4}$$

Hence, we can write as follows:

$$\begin{aligned} &\boldsymbol{\xi} : \left(\sum_{n=1}^{N} p_n (\boldsymbol{t}_n \otimes \boldsymbol{t}_n) \otimes (\boldsymbol{t}_n \otimes \boldsymbol{t}_n) \right) : \boldsymbol{\xi} = \boldsymbol{M}, \\ &\boldsymbol{M} = \frac{1}{4}\begin{bmatrix} 1+m_3 & m_4 & -2m_1 \\ & 1-m_3 & -2m_2 \\ & & 2 \end{bmatrix}. \end{aligned} \tag{5}$$

As described by Krein and Nudelman (1977), the feasible set of moments $\mathcal{M}$ can be described as follows:

$$\begin{aligned} \mathcal{M} &= \boldsymbol{m} \in \mathbb{R}^4, \\ s.t. &\begin{cases} m_1^2 + m_2^2 \leq 1, \\ -1 \leq m_3 \leq 1, \\ \frac{2m_1^2}{1+m_3} + \frac{2m_2^2}{1-m_3} + \frac{m_4^2}{1-m_3^2} - \frac{4m_1 m_2 m_4}{1-m_3^2} \leq 1. \end{cases} \end{aligned} \tag{6}$$

Hence, for a given set of loadings conditions, and material properties f, E^+ and $E^- = 10^{-9}E^+$, we can find the optimal set of moments, minimizing $\mathcal{C}$, to find the optimal effective compliance tensor. As discussed by Lipton (1994), this is a convex problem with respect to the moments. This problem is solved using the built-in version of the interior-point method in MATLAB. We specify the gradients of the objective and constraints, while the Hessian is approximated using a finite-difference scheme. Furthermore, Lipton (1994) proposed a procedure to reconstruct the relative layer contributions p_n and orientations θ_n of some of the rank-3 laminates corresponding to the optimal moments, which is for convenience repeated in the Appendix.

2.2 Approximation of a rank-3 laminate on a single scale

We abandon the separation of length scales specific to rank-3 laminates and try to approximate the third-layered composite on a single scale. To do so, we need (1) to create a periodic unit-cell respecting the original layer orientations and (2) to make sure that the relative contributions of the different layer widths are preserved on the single scale.

To transform a rank-3 layered composite into a single-scale periodic lattice structure (see, illustration in Fig. 1), the spacing of each layer λ_n has to be adapted, such that the unit-cell can be described using a parallelogram (as shown in Fig. 2).

In this work, layer 3 is set to be the base layer, with a layer spacing $\lambda_3 = 1$. Using standard geometric relations, the other two layer spacings can be calculated as follows:

$$\begin{aligned} \lambda_1 &= |\sin(\theta_1 - \theta_3)| \left| \frac{\lambda_3}{\tan(\theta_2 - \theta_3)} - \frac{\lambda_3}{\tan(\theta_1 - \theta_3)} \right|, \\ \lambda_2 &= |\sin(\theta_2 - \theta_3)| \left| \frac{\lambda_3}{\tan(\theta_2 - \theta_3)} - \frac{\lambda_3}{\tan(\theta_1 - \theta_3)} \right|. \end{aligned} \tag{7}$$

The area A of the parallelogram is described as follows:

$$A = \left| \frac{\lambda_3^2}{\tan(\theta_2 - \theta_3)} - \frac{\lambda_3^2}{\tan(\theta_1 - \theta_3)} \right|. \tag{8}$$

To make the unit-cell have unit-area, the corresponding layer spacings are normalized to the following:

$$\tilde{\lambda}_1 = \frac{\lambda_1}{\sqrt{A}}, \quad \tilde{\lambda}_2 = \frac{\lambda_2}{\sqrt{A}}, \quad \tilde{\lambda}_3 = \frac{\lambda_3}{\sqrt{A}}. \tag{9}$$

For the case that the reconstructed laminate is only a rank-2 laminate, we set the corresponding layer spacings equal, while maintaining a unit-area.

For the layer widths, we make use of the parameters that describe the relative contribution of each layer, i.e., p_n for

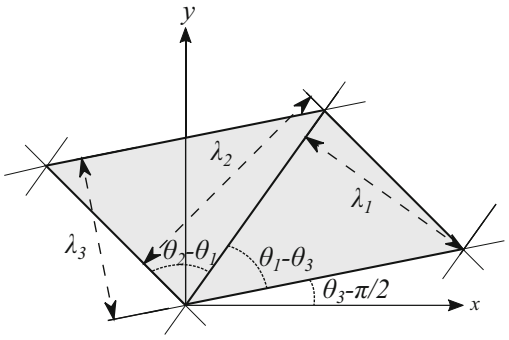

Fig. 2 Parallelogram used as unit-cell and corresponding dimensions

$n = 1, 2, 3$. The width of each layer used on the single scale, w_n, is then obtained as follows:

$$w_n = \psi p_n, \quad n = 1, 2, 3. \tag{10}$$

Here, ψ is a scaling parameter found using a bi-section algorithm, such that the projected microstructure has the same volume fraction f as the stiff material in the rank-3 laminate.

With the layer widths and relative spacings known, we can project the periodic microstructure. For this, we use an approach similar to the recently proposed projection approaches presented in Pantz and Trabelsi (2008), Groen and Sigmund (2017), and Allaire et al. (2018). A periodic sequence of layer n on a single scale has a material distribution $\tilde{\rho}_n$ which can be described as follows:

$$\tilde{\rho}_n(\boldsymbol{x}) = H\left(\cos\left(\frac{2\pi(\boldsymbol{n}_n \cdot \boldsymbol{x})}{\tilde{\lambda}_n}\right) - \cos(\pi w_n)\right). \tag{11}$$

Here, $\boldsymbol{x}$ describes the spatial location, $\boldsymbol{n}_n$ describes the layer normal of layer n, and H is the Heaviside function. Finally, the individual layer contributions can be combined in the total density distribution of the microstructure as follows:

$$\rho(\boldsymbol{x}) = \min\{\tilde{\rho}_1(\boldsymbol{x}) + \tilde{\rho}_2(\boldsymbol{x}) + \tilde{\rho}_3(\boldsymbol{x}), 1\}. \tag{12}$$

Figure 1 shows an example of a resulting single-scale microstructure.

3 Optimization for single-scale microstructures

The unit-cell description given above can be used to parameterize the unit-cell using a discrete number of elements, such that density-based topology optimization can be performed. The unit-cell description of (12) is used to form design vector, $\boldsymbol{\rho}$. Subsequently, the vector containing the physical densities, $\hat{\tilde{\boldsymbol{\rho}}}$, can be obtained based on the design vector, $\boldsymbol{\rho}$, using a smoothing and projection step, as will be discussed below in more detail. To tailor the microstructure properties such that the weighted complementary energy $\mathcal{C}$ is minimized an inverse homogenization approach is used. The topology optimization problem is solved in nested form, i.e., for each design iteration and given material distribution, the homogenized constitutive properties, as well as the objective function and its corresponding derivatives are calculated. Afterwards, the material distribution is updated based on the gradients. The discretized optimization problem can thus be written as,

$$\begin{aligned} \min_{\boldsymbol{\rho}} &: \mathcal{C}(\boldsymbol{\rho}) = \frac{1}{2}\sum_{j}^{n_s} w_j \boldsymbol{\sigma}_j : \boldsymbol{C}^H(\hat{\tilde{\boldsymbol{\rho}}}(\boldsymbol{\rho})) : \boldsymbol{\sigma}_j, \\ \text{s.t.} &: \boldsymbol{v}^T \hat{\tilde{\boldsymbol{\rho}}}(\boldsymbol{\rho}) - f \leq 0, \\ &: \boldsymbol{0} \leq \boldsymbol{\rho} \leq \boldsymbol{1}. \end{aligned} \tag{13}$$

Here, $\boldsymbol{v}$ is a vector containing the volumes of each density element, and $\boldsymbol{C}^H(\hat{\tilde{\boldsymbol{\rho}}}(\boldsymbol{\rho}))$ is the homogenized compliance tensor. To obtain this tensor we make use of the publicly available MATLAB code of Andreassen and Andreasen (2014), which is modified to return the sensitivities of the objective w.r.t. design variables. More details regarding the sensitivity analysis for inverse homogenization problems can be found in Sigmund (1994), Guedes et al. (2003), and Bendsøe and Sigmund (2004). Furthermore, we use the MATLAB implementation of the Method of Moving Asymptotes (MMA) introduced by Svanberg (1987) to update the design varilables.

To ensure a well-posed problem, control of the minimum feature size of solid regions, as well as discreteness of optimized designs, the physical densities $\hat{\tilde{\boldsymbol{\rho}}}$, are related to design variables $\boldsymbol{\rho}$ using the Heaviside projection scheme introduced by Guest et al. (2004). This scheme employs a standard density filter using filter radius R, which is slightly modified to take the periodicity of the unit-cell into account. The filtered design variables $\bar{\boldsymbol{\rho}}$ are subsequently projected to the physical densities $\hat{\tilde{\boldsymbol{\rho}}}$ using a smoothed Heaviside function. Here parameter β controls the steepness of this projection step. At the start of the iteration scheme β is chosen as 0.01 to allow $\hat{\tilde{\boldsymbol{\rho}}}$ to have intermediate values. After 15 iterations, β is increased to 1. Afterwards, β is doubled every 15–100 iterations until $\beta = 32$. The exact number of iterations before β is doubled depends on whether the maximum change in the design variables is less than 0.01. When $\beta = 32$ at least 100 iterations are required before the optimization scheme is terminated, which happens when the maximum change in the design variables is less than 0.01.

4 Numerical examples

In all examples, three different starting guesses are used; for the design vector, $\boldsymbol{\rho}$ was used in the inverse homogenization problems. The reason we use the starting guess for $\boldsymbol{\rho}$ instead of $\hat{\tilde{\boldsymbol{\rho}}}$ is that we would like the physical densities to have intermediate values in the beginning of the iteration scheme. A pure binary (0-1) starting guess usually converges or sticks to bad local minima.

First of all, the rank-3 laminate mapped on a single scale is used (*Mapped SG*). The performance of the optimized design is compared to a design obtained with a starting guess containing a random density field (*Random SG*), as well as a starting guess using a homogeneous density field (*Homog. SG*). Furthermore, we directly evaluate the performance of the rank-3 microstructure approximated on the single scale (*Mapped Rank-3*) obtained using (12). Finally, we compare all results to the energy bound given by the optimal rank-3 laminate (*Rank-3*).

The *Random SG* is obtained by generating a random sequence of numbers on the interval $[0, 2f]$ using the random number generator in MATLAB, restarted using a seed value of 1. These random numbers are subsequently scaled between 0 and $\min(1, 2f)$. This means that the volume of the starting guess cannot be larger than 0.5. Obviously, however, larger values of f can be obtained during the subsequent topology optimization procedure. Finally, a density filter is applied to the random densities to ensure some continuity in the initial guess. The *Homog. SG* is not truly homogeneous; otherwise, numerical problems will arise from having identical sensitivity values for all elements. Instead, all elements are set to the value of f, except for the elements within a filter radius R of the unit-cell center, which are set to 0. In this manner, the starting guess is perturbed independently of mesh refinement.

Both the *Random SG* and the *Homog. SG* are optimized in a unit-cell of dimensions 1×1. To make comparisons with the rank-3-inspired parallelogram unit-cell starting guesses more fair, we also tried to include the angle between the axes as an additional design variable. However, this increased design freedom did in general not lead to better designs; hence, we stick to a square unit-cell for the *Random SG* and *Homog. SG* in the following.

4.1 Example 1: Small filter radius

This first three examples are based on four stress cases, which are weighted using parameter $\chi \in [0, 1]$ as proposed by Guedes et al. (2003). The four cases, with their respective weight are shown in Fig. 3, and can be written out as follows:

$$w_1\sigma_1 = \frac{\chi}{2}\begin{bmatrix} -1 & 0 \\ 0 & 1 \end{bmatrix}, \quad w_2\sigma_2 = \frac{\chi}{2}\begin{bmatrix} 0 & 1 \\ 1 & 0 \end{bmatrix},$$

$$w_3\sigma_3 = \frac{1-\chi}{2}\begin{bmatrix} 1 & 0 \\ 0 & 0 \end{bmatrix}, \quad w_4\sigma_4 = \frac{1-\chi}{2}\begin{bmatrix} 0 & 0 \\ 0 & 1 \end{bmatrix}. \quad (14)$$

The enforced length scale in this example is $2R = 0.05$, corresponding to 5% of the side length in a square unit-cell. This small feature size allows for quite fine structural members. Furthermore, a volume fraction of $f = 0.5$ is used, and the unit-cells are discretized using 200×200 elements.

The found objective values $\mathcal{C}$ for different starting guesses and 11 equally spaced values of χ are shown in the top of Fig. 4. These results are in agreement with the results obtained by Guedes et al. (2003). In the normalized plot shown in the bottom of Fig. 4, starting guesses are compared based on their relative performance, i.e., the results are normalized using the energy bound of the rank-3 microstructure.

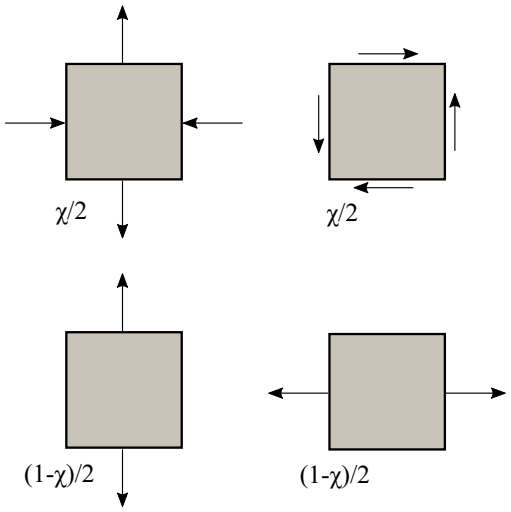

Fig. 3 Illustration of the four stress cases and their respective weights used in examples 1, 2, and 3

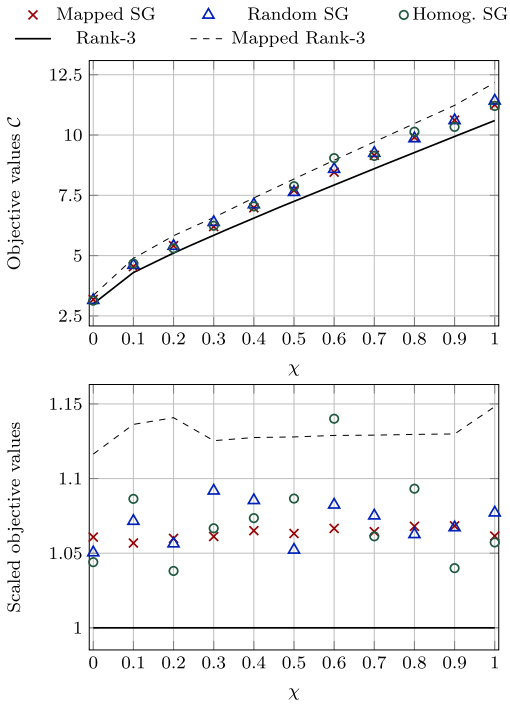

Fig. 4 Top: resulting complimentary energy $\mathcal{C}$ for different values of χ, $f = 0.5$, and a length scale of 0.05. Bottom: values normalized using the rank-3 energy bound

From the objective values observed in this example, it is not yet clear that the proposed starting guess has much benefit. Only when $\chi = 0.1$, $\chi = 0.3$, $\chi = 0.4$, and $\chi = 0.6$, the *Mapped SG* outperforms the other two starting guesses. The single-scale microstructures corresponding to $\chi = 0.7$ are shown in Fig. 5. It is clear from Fig. 5c that using *Random SG* results in somewhat chaotic looking optimized microstructures, which, although well-performing, may become problematic in terms of manufacturability. Therefore, we focus in the remainder on a comparison between the use of *Mapped SG* and *Homog. SG*

Furthermore, it can be observed that the structures generated with *Homog. SG* are more complex and consist of many members at the smallest allowable feature size. On the other hand, the microstructures generated with *Mapped SG* have few large design features, while being only marginally worse in terms of performance. These fewer and larger design features may be desirable from a manufacturing viewpoint.

An interesting observation is made from comparing the optimized designs using *Mapped SG* and *Homog. SG* obtained for $\chi = 0$, shown in Fig. 6a, b. Here, the *Mapped SG* got stuck in the slightly suboptimal single length-scale design dictated by the starting guess, whereas the *Homog. SG* design resulted in a split bar structure, somewhat mimicking the special class of extremal composites proposed by Sigmund (2000). Actually, the "true optimal" single-scale microstructure will probably be one where the width and number of the split bars are exactly determined by the imposed minimum length scale. This can be mimicked by modifying the *Mapped SG* starting guess to accommodate for these extremal composites. In practice, this is done by splitting thick members of the mapped design into members that are close to the minimum feature size as seen in Fig. 6c. As expected, the relative performance of the improved mapping, which is 1.10 is lower than the value of 1.12 for the *Mapped Rank-3*. The corresponding optimized design, shown in Fig. 6d resembles the extremal Sigmund composite, and its normalized performance of 1.03 outperforms the microstructure obtained using the *Homog. SG*, which has a relative performance of 1.04. Nevertheless, we abandon this more advanced starting guess in the following, in favor of producing simpler and easier to manufacture designs.

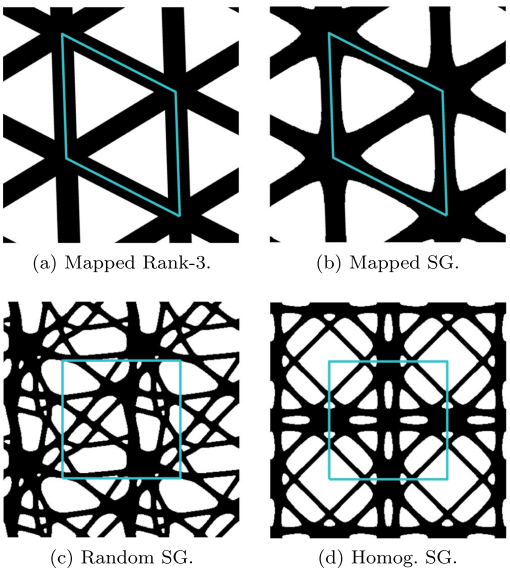

(a) Mapped Rank-3. (b) Mapped SG. (c) Random SG. (d) Homog. SG.

Fig. 5 Resulting structures shown in a domain of size 2×2 with the unit-cell highlighted, for $\chi = 0.7$, $f = 0.5$, and a length scale of 0.05

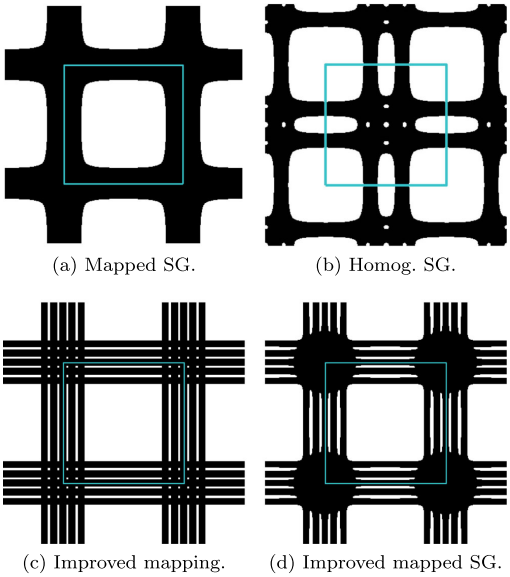

(a) Mapped SG. (b) Homog. SG. (c) Improved mapping. (d) Improved mapped SG.

Fig. 6 Resulting structures shown in a domain of size 2×2 with the unit-cell highlighted, for $\chi = 0.0$, $f = 0.5$, and a length-scale of 0.05

4.2 Example 2: large filter

This example uses the same load case and volume fraction as example 1, but imposes a larger minimal length scale of 0.15, corresponding to 15% of the square domain. Hence, the microstructures optimized using *Random SG's* and *Homog. SG's* are forced to find structures with thicker features, closer to the feature sizes of the *Mapped SG*.

The relative objective function values are shown in Fig. 7. It is clear that designs optimized using *Mapped SG* now

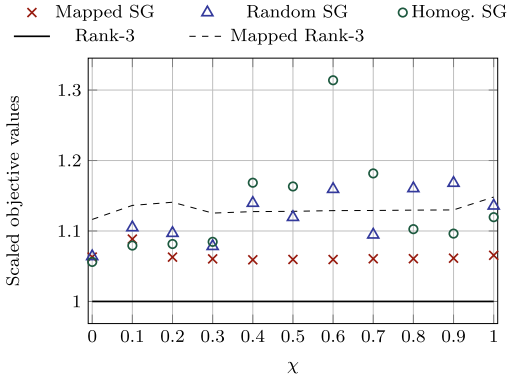

Fig. 7 $\mathcal{C}$ normalized using the rank-3 energy bound, for different values of χ, $f = 0.5$, and a length scale of 0.15

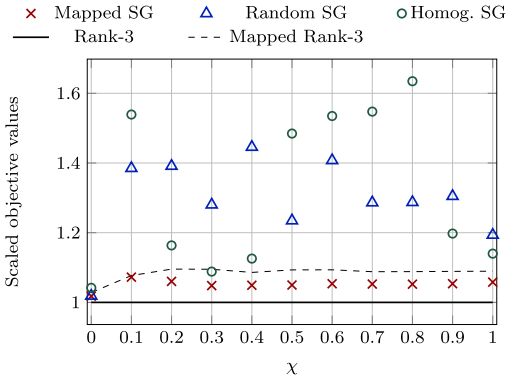

Fig. 9 $\mathcal{C}$ normalized using the rank-3 energy bound, for different values of χ, $f = 0.2$, and a length scale of 0.05

outperform the microstructures using *Random SG's* and *Homog. SG's* in terms of objective function value. Some optimized designs using *Random SG's* and *Homog. SG's* are even outperformed by the *Mapped Rank-3*, which is obtained using purely geometrical means. Finally, it can be seen from Figs. 4 and 7 that both the mapped structures and subsequently optimized microstructures have a very stable relative objective function value across the load cases, compared to the other starting guesses.

When comparing, the resulting structures for $\chi = 0.3$ (shown in Fig. 8), it can be seen that the structure obtained by the *Mapped SG* is still very simple compared to the one obtained by the *Homog. SG*, as the latter contains smaller holes.

4.3 Example 3: low volume fraction

The same load cases are used as for the previous two examples; however, in this example, a lower volume fraction of $f = 0.2$ is used in combination with a minimum feature size of 0.05. The resulting performance values are shown in Fig. 9. It can be seen that the results using the *Mapped SG* clearly outperform the other starting guesses, except for the case with $\chi = 0$, where all methods perform equally well.

When inspecting the resulting structures shown for $\chi = 0.1$ in Fig. 10 and for $\chi = 0.8$ in Fig. 11, it can again be seen that the designs based on the *Mapped SG* are simple triangle structures. However, it can also be seen that the diagonal bar crossing the center of the unit-cell in Fig. 10b has exactly the imposed minimum length scale as feature width. Interestingly, this bar is thicker than the bar following directly from *Mapped Rank-3*, as shown in Fig. 10a. Hence, the imposed feature size limits the optimality of the optimized microstructure. This effect can also be seen in Fig. 9 where the relative compliance value is slightly higher for $\chi = 0.1$ than for all other values of χ. A similar effect can be observed for $\chi = 0.1$ in Fig. 7.

4.4 Example 4: rotating uni-axial stresses

For this final example, we introduce a new loading case with three uni-axial stresses, independently applied in different directions as illustrated in Fig. 12. The angle parameter χ

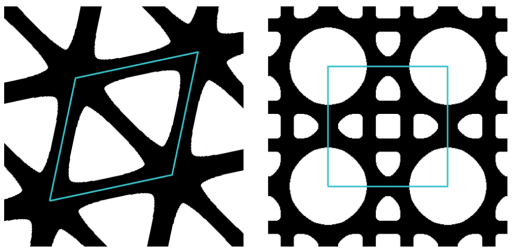

(a) Mapped SG. (b) Homog. SG.

Fig. 8 Resulting structures shown in a domain of size 2×2 with the unit-cell highlighted, for $\chi = 0.3$, $f = 0.5$, and a length scale of 0.15

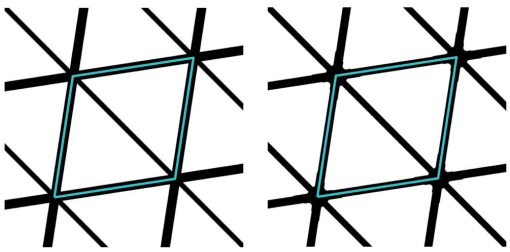

(a) Mapped Rank-3. (b) Mapped SG.

Fig. 10 Resulting structures shown in a domain of size 2×2 with the unit-cell highlighted, for $\chi = 0.1$, $f = 0.2$, and a length scale of 0.05

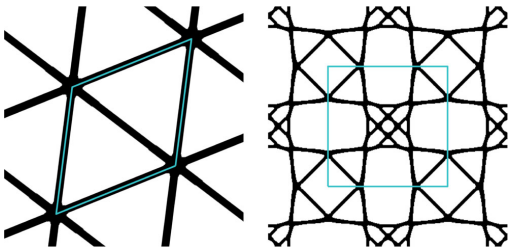

(a) Mapped SG. (b) Homog. SG.

Fig. 11 Resulting structures shown in a domain of size 2×2 with the unit-cell highlighted, for $\chi = 0.8$, $f = 0.2$, and a length scale of 0.15

is increased in steps of 5° from 0 to 60°, resulting in a load case varying from a single load to three uni-axial loads with 60° symmetry. The example is performed with a volume fraction of $f = 0.25$, using a minimum feature length of 0.05.

The resulting normalized objective function values are shown in Fig. 13, where it can be seen that using the *Mapped SG* results in much better objective function values for all cases. Another important observation is that the *Mapped Rank-3* outperforms the optimized structure for values of $\chi = 5°, 10°, 15°, 20°, 25°, 30°$. This is, as discussed before, due to the minimum length scale not being enforced in the reconstruction of the rank-3 laminate, as is shown in Fig. 14. After the topology optimization procedure, the concerned members have either the imposed length scale or are removed completely.

5 Discussion and conclusions

When comparing the various starting guesses as applied here, it is important to note that two different unit-cell parameterizations are used. Due to the parallelogram element shapes, features will have different jaggedness in the solid-void interface depending on orientation. To avoid negative effects caused by this difference, the optimization problems have been resolved using a sufficiently fine mesh such that the minimum feature size is at least ten finite elements wide in all examples.

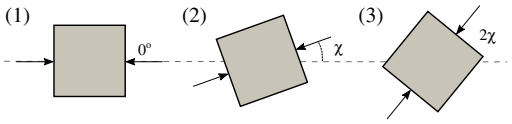

Fig. 12 Illustration of three uni-axial loads, with angles 0, χ, and 2χ

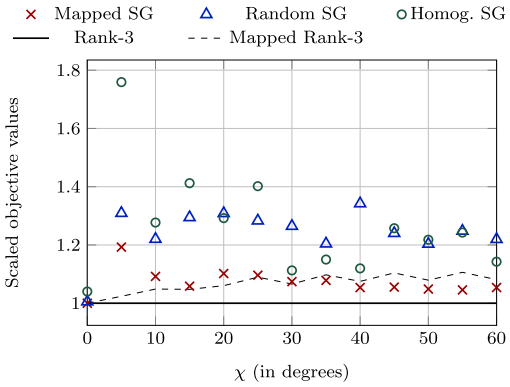

Fig. 13 $\mathcal{C}$ normalized using the rank-3 energy bound, for different values of χ corresponding to example 4, $f = 0.25$, and a length scale of 0.05

To demonstrate the effect of the element size, we calculated the complementary energy of the four structures shown in Fig. 14, for different mesh sizes. We used nearest-neighbor interpolation to make sure the interpolations are volume preserving; the corresponding energies for different element sizes, h, can be found in Fig. 15. The difference in complementary energy is small, even when the mesh is

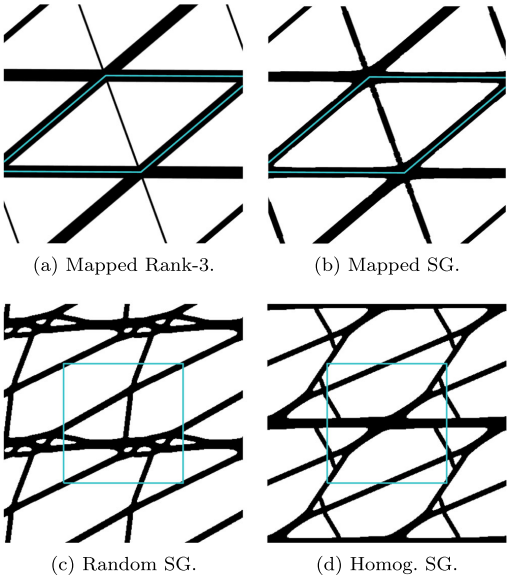

(a) Mapped Rank-3. (b) Mapped SG.

(c) Random SG. (d) Homog. SG.

Fig. 14 Resulting structures shown in a domain of size 2×2 with the unit-cell highlighted, for $\chi = 20°$, $f = 0.25$, and a length scale of 0.05

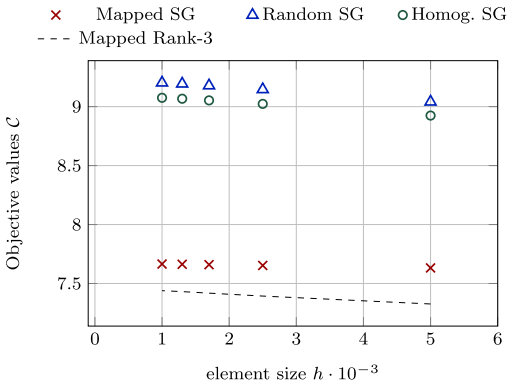

Fig. 15 The designs shown in Fig. 14 interpolated on different meshes uses nearest-neighbor interpolation to demonstrate the small discretization error

refined to 1000 × 1000 elements; furthermore, the relative differences between the different designs remain the same. This means that the chosen discretization of 200 × 200 elements is sufficient.

Furthermore, the skewness of the parallelogram used in the *Mapped SG* makes it impossible to recreate the same structure in a square domain, as they are repeated differently through space. The choice of using a square unit-cell for the other two starting guesses was made since this resulted in the best performing microstructures.

The objective values obtained using the *Mapped SG* display a constant excellent performance, where the results are always around 5–8% from the energy bound. Only when the imposed feature size is larger than a member needs to be, this closeness to theoretical optimality is violated. Furthermore, the optimized microstructures using *Mapped SG* are much simpler than their counterparts optimized using *Random SG* or *Homog. SG*. This simplicity in the microstructures possibly allows for a more robust behavior towards manufacturing uncertainties, and for a simpler manufacturing process in general.

Only in example 1, it was shown that the use of the *Homog. SG* could lead to a slightly better performance. The reason for this, is that this starting guess does not suppress the occurrence of thin features, as happens using *Mapped SG*. Hence, the optimized microstructures based on *Homog. SG* seem to converge better towards the type of extremal composites proposed by Sigmund (2000). However, we also demonstrated that the *Mapped SG* could be improved when the minimum allowed feature size allows for a representation close to Sigmund's class of extremal materials. Nevertheless, we did not pursue this approach further in this work, since we believe that the simplicity of the microstructures using the *Mapped SG* are an important feature. Furthermore, it is noteworthy that for examples 2, 3, and 4, large differences are observed between performance of *Mapped SG* and the other two starting guesses. Hence, it really pays off to use a "smart" starting guess as suggested here. Especially, since the cost of obtaining the approximated rank-3 microstructure on the single scale is negligible compared to the cost of performing inverse homogenization.

The approximated rank-3 laminates directly analyzed and without optimization (*Mapped Rank-3*), already perform within 5–15% of the energy bound posed by the rank-3 laminate. This promising result justifies the recent interest into projection methods that postprocess homogenization-based topologies on a single scale (Pantz and Trabelsi 2008; Groen and Sigmund 2017; Allaire et al. 2018). This result also indicates that similar performance close to theoretical optima can be obtained when multiple load cases are considered. Furthermore, it is notable that the main difference between the *Mapped Rank-3* and the microstructures optimized from the *Mapped SG* are rounded corners at the intersection of connecting bars. This indicates that some more or less heuristic postprocessing scheme may be postulated, that is applied directly on the *Mapped Rank-3*, potentially eliminating the need for inverse homogenization for this type of problems entirely.

Acknowledgements The authors acknowledge the support of the Villum Fonden through the Villum investigator project InnoTop. The authors would also like to thank Krister Svanberg for providing the MATLAB MMA code.

Appendix: Reconstructing a rank-3 laminate from moments

In this section, we discuss the method proposed by Lipton (1994) to reconstruct the relative layer contributions p_n and orientations θ_n of a rank-3 laminate from the optimal moments. Our discussion is similar to the practical implementation given by Díaz et al. (1995), and included for completeness.

We can reduce the set of optimal moments from four to three, by rotating the set of moments (m_1, m_2, m_3, m_4) to $(\tilde{m}_1, \tilde{m}_2, \tilde{m}_3, 0)$ using a change of reference frame and rotation angle γ such that $\tilde{\theta}_n = \theta_n + \gamma$ and the following:

$$\begin{aligned} \tilde{m}_1 &= \sum_{n=1}^{N} p_n \cos(2\tilde{\theta}_n), \quad \tilde{m}_2 = \sum_{n=1}^{N} p_n \sin(2\tilde{\theta}_n), \\ \tilde{m}_3 &= \sum_{n=1}^{N} p_n \cos(4\tilde{\theta}_n), \quad \tilde{m}_4 = \sum_{n=1}^{N} p_n \sin(4\tilde{\theta}_n). \end{aligned} \tag{15}$$

By using the rotated reference frame for the specification of the layer tangents $\boldsymbol{t}_n$, used in (5), the following relations can be found as follows:

$$\begin{aligned}
\tilde{m}_1 &= m_1\cos(2\gamma) - m_2\sin(2\gamma),\\
\tilde{m}_2 &= m_1\sin(2\gamma) + m_2\cos(2\gamma),\\
\tilde{m}_3 &= m_3\cos(4\gamma) - m_4\sin(4\gamma),\\
\tilde{m}_4 &= m_3\sin(4\gamma) + m_4\cos(4\gamma).
\end{aligned} \tag{16}$$

Hence, we can find γ that ensures $\tilde{m}_4 = 0$ using the following:

$$\gamma = \frac{1}{4}\arctan\left(\frac{-m_4}{m_3}\right). \tag{17}$$

From (17), it can be seen that γ is periodic every $\pi/4$. This means that there are at least four rotated sets $\tilde{\boldsymbol{m}}$ to describe the microstructure. Furthermore, the feasible rotated set of moments $\tilde{\mathcal{M}}$ is bounded by the same constraints as in (18).

$$\tilde{\mathcal{M}} = \tilde{\boldsymbol{m}} \in \mathbb{R}^3, s.t. \begin{cases} \tilde{m}_1^2 + \tilde{m}_2^2 \le 1, \\ -1 \le \tilde{m}_3 \le 1, \\ \frac{2\tilde{m}_1^2}{1+\tilde{m}_3} + \frac{2\tilde{m}_2^2}{1-\tilde{m}_3} \le 1. \end{cases} \tag{18}$$

Feasible set $\tilde{\mathcal{M}}$ is a convex set as can be seen in Fig. 16.

The boundary of this convex set $\partial\tilde{\mathcal{M}}$ satisfies the following:

$$\frac{2\tilde{m}_1^2}{1+\tilde{m}_3} + \frac{2\tilde{m}_2^2}{1-\tilde{m}_3} = 1, \tag{19}$$

while the four corner points also satisfy the following:

$$\tilde{m}_1^2 + \tilde{m}_2^2 = 1. \tag{20}$$

It can easily be verified using (15) that the four corner points $\tilde{\boldsymbol{m}} = \{1, 0, 1\}, \{-1, 0, 1\}, \{0, 1, -1\}$ and $\{0, -1, -1\}$ correspond to rank-1 laminates, with the corresponding layer directions $\tilde{\theta}_1 = 0, \pi/2, \pi/4$, and $-\pi/4$ respectively. Hence, if both (19) and (20) are satisfied, the microstructure is a rank-1 microstructure. Depending on the choice of γ, the unique layer orientation θ_1 can be obtained; furthermore, corresponding $p_1 = 1$.

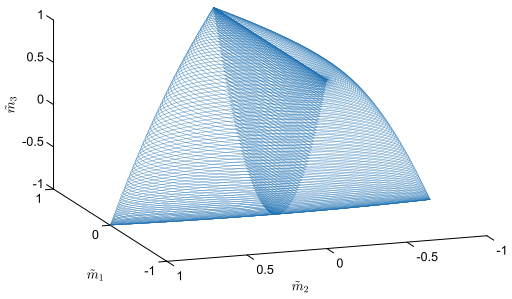

Fig. 16 Convex set $\tilde{\mathcal{M}}$

Since $\tilde{\mathcal{M}}$ is a convex set, each point $\tilde{\boldsymbol{m}}$ can be described as a combination of a corner point $\tilde{\boldsymbol{a}}$ and a point $\tilde{\boldsymbol{b}}$ on $\partial\tilde{\mathcal{M}}$ as follows:

$$\tilde{\boldsymbol{m}} = \alpha\tilde{\boldsymbol{a}} + (1-\alpha)\tilde{\boldsymbol{b}}. \tag{21}$$

Since $\tilde{\boldsymbol{a}}$ corresponds to a rank-1 laminate, point $\tilde{\boldsymbol{b}}$ on boundary $\partial\tilde{\mathcal{M}}$ has to correspond to a rank-2 laminate. Hence,

$$\frac{2\tilde{b}_1^2}{1+\tilde{b}_3} + \frac{2\tilde{b}_2^2}{1-\tilde{b}_3} = 1. \tag{22}$$

Furthermore, we have the following:

$$\alpha = \frac{\tilde{m}_1 - \tilde{b}_1}{\tilde{a}_1 - \tilde{b}_1} = \frac{\tilde{m}_2 - \tilde{b}_2}{\tilde{a}_2 - \tilde{b}_2} = \frac{\tilde{m}_3 - \tilde{b}_3}{\tilde{a}_3 - \tilde{b}_3}. \tag{23}$$

If we take one of the corner points, e.g., $\tilde{\boldsymbol{a}} = \{1, 0, 1\}$, we can solve for $\tilde{\boldsymbol{b}}$ and α, using the Equations above. We know that the rank-2 laminate can be described using two relative layer contributions $p_1^{\tilde{b}}$ and $p_2^{\tilde{b}}$, and two angles $\theta_1^{\tilde{b}}$ and $\theta_2^{\tilde{b}}$, such as the following:

$$\begin{aligned}
p_1^{\tilde{b}} + p_2^{\tilde{b}} &= 1,\\
\tilde{b}_1 &= p_1^{\tilde{b}}\cos(2\theta_1^{\tilde{b}}) + p_2^{\tilde{b}}\cos(2\theta_2^{\tilde{b}}),\\
\tilde{b}_2 &= p_1^{\tilde{b}}\sin(2\theta_1^{\tilde{b}}) + p_2^{\tilde{b}}\sin(2\theta_2^{\tilde{b}}),\\
\tilde{b}_3 &= p_1^{\tilde{b}}\cos(4\theta_1^{\tilde{b}}) + p_2^{\tilde{b}}\cos(4\theta_2^{\tilde{b}}).
\end{aligned} \tag{24}$$

This is system of four equations can be solved for the four unknowns. To do so, one can describe $\tilde{\boldsymbol{b}}$ in terms of two angles, $0 \le t \le 2\pi$ and $0 \le \beta \le \pi/2$ (Lipton 1994).

$$\left\{\tilde{b}_1, \tilde{b}_2, \tilde{b}_3\right\} = \{\cos(\beta)\cos(t), \sin(\beta)\sin(t), \cos(2\beta)\}. \tag{25}$$

The corresponding solution for the rank-2 laminate can then be written as follows:

$$\begin{aligned}
s &= \cos^2(2\beta) - 2\cos(2\beta)\cos(2t) + 1,\\
\delta &= \arctan\left(\frac{\sqrt{s}}{1-\cos^2(2\beta)}\right),\\
p_1^{\tilde{b}} &= \frac{1}{2}\left(1 + \frac{2\cos(2\beta)\sin(2t)}{\sqrt{s}}\right),\\
p_2^{\tilde{b}} &= 1 - p_1^{\tilde{b}},\\
\theta_1^{\tilde{b}} &= \arctan\left(\frac{p_2^{\tilde{b}}\sin(2\delta) - \sin(\beta)\sin(t)}{-(p_1^{\tilde{b}} + p_2^{\tilde{b}}\cos(2\delta) + \cos(\beta)\cos(t))}\right),\\
\theta_2^{\tilde{b}} &= \theta_1^{\tilde{b}} + \delta.
\end{aligned} \tag{26}$$

The corresponding rank-3 laminate in global frame of reference can thus be written as follows:

$$\begin{aligned} p_1 &= \alpha, \quad \theta_1 = -\gamma, \\ p_2 &= (1-\alpha)p_1^{\tilde{b}}, \quad \theta_2 = \theta_1^{\tilde{b}} - \gamma, \\ p_3 &= (1-\alpha)p_2^{\tilde{b}}, \quad \theta_3 = \theta_2^{\tilde{b}} - \gamma. \end{aligned} \tag{27}$$

Publisher's note Springer Nature remains neutral with regard to jurisdictional claims in published maps and institutional affiliations.

References

Allaire G (2002) Shape optimization by the homogenization method. Springer, New York

Allaire G, Aubry S (1999) On optimal microstructures for a plane shape optimization problem. Structural Optimization 17(2):86–94

Allaire G, Geoffroy-Donders P, Pantz O (2018) Topology optimization of modulated and oriented periodic microstructures by the homogenization method, working paper or preprint. Computer & Mathematics with Applications

Andreassen E, Andreasen C (2014) How to determine composite material properties using numerical homogenization. Commun Math Sci 83:488–495

Andreassen E, Lazarov BS, Sigmund O (2014) Design of manufacturable 3D extremal elastic microstructure. Mech Mater 69(1):1–10

Avellaneda M (1987) Optimal bounds and microgeometries for elastic two-phase composites. SIAM J Appl Math 47(6):1216–1228

Avellaneda M, Milton G (1988) Bounds on the effective elasticity tensor of composites based on two-point correlations. In: American society of mechanical engineers, Petroleum division (Publication) PD. vol 24. American Society of Mechanical Engineers (ASME), pp 89–93

Bendsøe M, Sigmund O (2004) Topology optimization-theory, methods and applications. Springer, Berlin

Berger J, Wadley H, McMeeking R (2017) Mechanical metamaterials at the theoretical limit of isotropic elastic stiffness. Nature 543(7646):533–537

Bourdin B, Kohn RV (2008) Optimization of structural topology in the high-porosity regime. J Mech Phys Solids 56(3):1043–1064

Cherkaev A (2000) Variational methods for structural optimization. Springer, New York

Clausen A, Wang F, Jensen JS, Sigmund O, Lewis JA (2015) Topology optimized architectures with programmable Poisson's ratio over large deformations. Adv Mater 27(37):5523–5527

Coelho P, Cardoso J, Fernandes P, Rodrigues H (2011) Parallel computing techniques applied to the simultaneous design of structure and material. Adv Eng Softw 42(5):219–227

Díaz AR, Lipton R, Soto CA (1995) A new formulation of the problem of optimum reinforcement of Reissner-Mindlin plates. Comput Methods Appl Mech Eng 123(1):121–139

Francfort GA, Murat F (1986) Homogenization and optimal bounds in linear elasticity. Arch Ration Mech Anal 94(4):307–334

Grabovsky Y, Kohn RV (1995) Anisotropy of the Vigdergauz microstructure. J Appl Mech 62(4):1063–1065

Groen JP, Sigmund O (2017) Homogenization-based topology optimization for high-resolution manufacturable micro-structures. Int J Numer Methods Eng 113(8):1148–1163

Guedes J, Rodrigues H, Bendsøe MP (2003) A material optimization model to approximate energy bounds for cellular materials under multiload conditions. Struct Multidiscip Optim 25(5-6):446–452

Guest J, Prévost J, Belytschko T (2004) Achieving minimum length scale in topology optimization using nodal design variables and projection functions. Int J Numer Methods Eng 61(2):238–254

Krein M, Nudelman A (1977) The Markov moment problem and extremal problems, Translations of mathematical monographs, vol 50. American Mathematical Society, Providence, Rhode Island

Larsen UD, Sigmund O, Bouwsta S (1997) Design and fabrication of compliant micromechanisms and structures with negative Poisson's ratio. J Microelectromech Syst 6(2):99–106

Lipton R (1994) On optimal reinforcement of plates and choice of design parameters. Control Cybern 23(3):481–493

Liu L, James R, Leo P (2007) Periodic inclusion–matrix microstructures with constant field inclusions. Metall and Mater Trans A 38(4):781–787

Liu L, Yan J, Cheng G (2008) Optimum structure with homogeneous optimum truss-like material. Computers & Structures 86(13):1417–1425. structural Optimization

Lurie KA, Cherkaev AV (1984) G-closure of a set of anisotropically conducting media in the two-dimensional case. J Optim Theory Appl 42(2):283–304

Milton GW (1986) Modelling the properties of composites by laminates. In: Ericksen JL, Kinderlehrer D, Kohn R, Lions J (eds) Homogenization and effective moduli of materials and media. Springer, New York, pp 150-174

Neves MM, Sigmund O, Bendsøe MP (2002) Topology optimization of periodic microstructures with a penalization of highly localized buckling modes. Int J Numer Methods Eng 54(6):809–834

Osanov M, Guest JK (2016) Topology optimization for architected materials design. Annu Rev Mater Res 46(1):211–233

Pantz O, Trabelsi K (2008) A post-treatment of the homogenization method for shape optimization. SIAM J Control Optim 47(3):1380–1398

Rodrigues H, Guedes J (2002) Hierarchical optimization of material and structure. Struct Multidiscip Optim 24(1):1–10

Schury F, Stingl M, Wein F (2012) Efficient two-scale optimization of manufacturable graded structures. SIAM J Sci Comput 34(6):B711–B733

Sigmund O (1994) Materials with prescribed constitutive parameters: an inverse homogenization problem. Int J Solids Struct 31(17):2313–2329

Sigmund O, Bendsøe MP (1999) On the optimality of bone microstructure. In: Pedersen P (ed) IUTAM symposium on synthesis in bio solid mechanics. Springer, Netherlands, pp 221–234

Sigmund O (2000) A new class of extremal composites. J Mech Phys Solids 48(2):397–428

Sigmund O, Aage N, Andreassen E (2016) On the (non-)optimality of Michell structures. Struct Multidiscip Optim 54:361–372

Sivapuram R, Dunning PD, Kim HA (2016) Simultaneous material and structural optimization by multiscale topology optimization. Struct Multidiscip Optim 54(5):1267–1281

Svanberg K (1987) The method of moving asymptotes—a new method for structural optimization. Int J Numer Methods Eng 24(2):359–373

Thomsen CR, Wang F, Sigmund O (2018) Buckling strength topology optimization of 2D periodic materials based on linearized bifurcation analysis. Comput Methods Appl Mech Eng 339:115–136

Vigdergauz SB (1994a) Three-dimensional grained composites of extreme thermal properties. J Mech Phys Solids 42(5):729–740

Vigdergauz SB (1994b) Two-dimensional grained composites of extreme rigidity. J Appl Mech 61(2):390–394

Xia L, Breitkopf P (2017) Recent advances on topology optimization of multiscale nonlinear structures. Arch Comput Meth Eng 24(2):227–249

Publication [P4]

J.P. Groen, J. Wu and O. Sigmund. Homogenization-based stiffness optimization and projection of 2D coated structures with orthotropic infill. *Computer Methods in Applied Mechanics and Engineering*, 349(1):772–742, 2019. doi:10.1016/j.cma.2019.02.031

Available online at www.sciencedirect.com
ScienceDirect
Comput. Methods Appl. Mech. Engrg. 349 (2019) 722–742
Computer methods in applied mechanics and engineering
www.elsevier.com/locate/cma

Homogenization-based stiffness optimization and projection of 2D coated structures with orthotropic infill

Jeroen P. Groen[a,*], Jun Wu[b], Ole Sigmund[a]

[a] *Department of Mechanical Engineering, Solid Mechanics, Technical University of Denmark, Denmark*
[b] *Department of Design Engineering, Delft University of Technology, Netherlands*

Received 14 August 2018; received in revised form 20 February 2019; accepted 20 February 2019
Available online 1 March 2019

Highlights

- Homogenization-based topology optimization of coated structures is performed using orthotropic infill material.
- Near-optimal designs can be obtained on a relatively coarse mesh.
- The designs are subsequently projected on a fine but realizable scale.
- The infill is kept as regular as possible using a novel scheme that adaptively refines the periodicity.
- The projected designs perform excellent in terms of compliance.
- A reduction in computational cost of at least one order of magnitude is achieved compared to density-based optimization of coating and infill.

Abstract

This paper concerns compliance minimization and projection of coated structures with orthotropic infill material in 2D. The purpose of the work is two-fold. First, we introduce an efficient homogenization-based approach to perform topology optimization of coated structures with orthotropic infill material. The design space is relaxed to allow for a composite material description, which means that designs with complex microstructures can be obtained on relatively coarse meshes. Second, a method is presented to project the homogenization-based designs on a fine but realizable scale. A novel method to adaptively refine the lattice structure is presented to allow for a regular spacing of the infill. Numerical experiments show excellent behavior of the projected designs, with structural performance almost identical to the homogenization-based designs. Furthermore, a reduction in computational cost of at least an order of magnitude is achieved, compared to a related approach in which the infill is optimized using a density-based approach.
© 2019 Elsevier B.V. All rights reserved.

Keywords: Topology optimization; Coated structures; Homogenization; High-resolution; Infill

1. Introduction

Topology optimization is recognized as an important design method, with numerous applications in industry and academia. Furthermore, the flexibility offered by additive manufacturing (AM) methods makes topology

* Correspondence to: Department of Mechanical Engineering, Solid Mechanics, Technical University of Denmark, Nils Koppels Allé, Building 404, 2800 kgs. Lyngby, Denmark.
E-mail address: jergro@mek.dtu.dk (J.P. Groen).

https://doi.org/10.1016/j.cma.2019.02.031
0045-7825/© 2019 Elsevier B.V. All rights reserved.

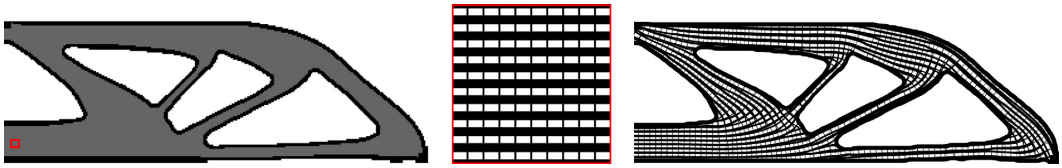

(a) Homogenization-based topology optimization, resolution: 300 × 100 elements.

(b) Microstructure

(c) Projection of composite design on a fine mesh, resolution: 3000 × 1000 elements.

Fig. 1. Overview of the proposed methodology to obtain high-resolution coated designs, with composite orthotropic infill.

optimization the ideal design method for this rapidly growing field. In recent years a large number of works have considered incorporation of constraints posed by the AM process directly into the optimization framework. Examples are geometric constraints to restrict the overhang angle [1–4], and methods to restrict the length-scale of the design as well as to make them robust against manufacturing variations, see [5] for a detailed review of such methods. For a global overview on the state of the art and future trends in topology optimization for additive manufacturing, the reader is referred to [6].

Most additive manufacturing processes, such as Fused Deposition Modeling (FDM) work with a solid shell to represent the surface, reinforced by porous infill. The reason these so-called coated structures are considered instead of solid structures are high strength-to-weight ratio, good energy absorption characteristics, and high thermal and acoustic insulation properties [7]. Furthermore, porous structures can alleviate thermal hot-spots that are prone to cause large stresses in printed designs [8,9]. Compared to their solid counterparts, coated structures with porous infill can obtain significantly increased buckling stability [10], as well as a better performance w.r.t. unpredicted loading conditions and material deficiency [11], at the cost of slightly increased compliance. We do; however, remind the reader that truss or lattice-like infill is inferior to close-walled cell structures when only considering stiffness, as e.g. discussed in [12]. On the other hand, here we consider the 2D-case where the differentiation between open- and closed-walled structures does not directly apply.

Traditionally, the porous infill in coated structures consists of repetitive infill patterns (e.g., triangles and hexagons). However, Wu et al. [11] proposed a density-based method to design bone-inspired microstructures as porous infill. In another approach Clausen et al. [13,14] presented a method to optimize a coated structure, using a solid shell and an isotropic base material that can be interpreted as a uniform porous infill. There, density-based optimization was applied and using successive filtering operations a clear distinction between coating and infill material could be made. In a natural subsequent step these methods have been combined to concurrently design both the coating and the infill [15]. Similar to density-based methods, level-set methods have been used to design for material interface properties [16,17]. This approach was recently extended to first design a coating layer, and subsequently an infill [18]. Besides the computational mechanics community, the computer graphics community has recently proposed many works on the optimization of porous structures, e.g. [19–21].

In this work we extend the method of Clausen et al. [13] to design coated structures with a macroscopically varying orthotropic infill material. The design space is relaxed to allow for a composite material description, which means that designs with complex microstructures can be obtained on relatively coarse meshes, e.g. 300 × 100 elements as is shown in Fig. 1(a). To describe the periodic infill composite we make use of the well-known square unit-cell with a rectangular hole [22], shown in Fig. 1(b). Recent studies [23,24] inspired by Pantz and Trabelsi [25,26] have shown that microstructures with a rectangular hole can be projected on a much finer mesh to obtain manufacturable designs, thereby avoiding the need for separation of scales. Our work is continuing on the projection procedure presented in [23,27], where an explicit constraint is used to align the projected microstructure with the directions of lamination. To keep the unit-cell spacing as regular as possible we also introduce a novel scheme that adaptively refines the periodicity as can be seen in Fig. 1(c), where a resolution of 3000 × 1000 elements is used.

The paper is organized in two parts. The first part encompasses homogenization-based topology optimization for coated structures. The theory is introduced in Section 2, while numerical experiments regarding performance of the optimized results and comparisons to the use of isotropic infill material are discussed in Section 3. The second part of this article deals with the projection method to obtain high-resolution manufacturable structures on a fine mesh. The theory and implementation will be discussed in Section 4, while numerical experiments on the performance

and numerical efficiency of the projected structures are discussed in Section 5. Finally, Section 6 contains the most important conclusions of this study.

2. Homogenization-based topology optimization for coated structures

A coated structure consists of two material phases, a coating and an infill as can be seen in Fig. 1(a). Clausen et al. [13] introduced an elegant method to obtain a coated structure using only a single field as design variable. Successive filter and projection operations allowed for a clear distinction between coating, isotropic infill and void. The use of composite infill material, introduced in this work, will add extra design variables. Nevertheless, the method to distinguish between infill and coating remains almost the same.

2.1. Successive filter operations

The procedure to distinguish between coating and infill makes use of two well-established filter methods in topology optimization. The first is a smoothing operation using the density filter. The second is a projection step to force the smoothed values on the interval [0, 1] towards either 0 or 1.

2.1.1. Smoothing

As basis for subsequent projection we use the Helmholtz-type PDE-based density filter [28],

$$-\left(\frac{R}{2\sqrt{3}}\right)^2\nabla^2\tilde{\phi}+\tilde{\phi}=\phi. \tag{1}$$

Here scalar R corresponds to the length-scale imposed by the filter operation. ϕ is the unfiltered field, while $\tilde{\phi}$ is the filtered field. Homogeneous Neumann boundary conditions are applied at the boundary of the filter domain. A discussion on undesired boundary effects of standard filter methods will be given later in this section.

2.1.2. Projection

Projection methods have been successfully applied in topology optimization to obtain black-and-white designs [29,30]. Here we use the formulation for the smoothed Heaviside projection proposed by Wang et al. [31],

$$\bar{\tilde{\phi}}=\frac{\tanh(\beta\eta)+\tanh(\beta(\tilde{\phi}-\eta))}{\tanh(\beta\eta)+\tanh(\beta(1-\eta))}. \tag{2}$$

Here $\bar{\tilde{\phi}}$ is the projected field. β determines the steepness of the projection, *i.e.* when $\beta\to\infty$ a sharp step is modeled. In general, a continuation approach is used for β, *i.e.* a low value is used during the first iterations, after which β is gradually increased. Furthermore, $\eta\in[0,1]$ is the threshold parameter where $\eta>0.5$ corresponds to an erosion operation, while $\eta<0.5$ corresponds to a dilation operation.

2.1.3. Combining the filters to obtain a coated structure

Analogous to Clausen et al. [13] we use successive filter operations to obtain field φ describing the base structure and field τ describing the coating. Additional variables, which will be introduced in Section 2.2, are used to describe the shape of the infill. However, these variables do not affect the distinction between coating Ω_c, infill Ω_l or void Ω_v regions.

$$\mathbf{x}\in\begin{cases}\Omega_v & \text{if} \quad \varphi(\mathbf{x})=0 \quad \text{and if } \tau(\mathbf{x})=0,\\ \Omega_l & \text{if} \quad \varphi(\mathbf{x})=1 \quad \text{and if } \tau(\mathbf{x})=0,\\ \Omega_c & \text{if} \quad \tau(\mathbf{x})=1.\end{cases} \tag{3}$$

The successive smoothing projection and gradient operations used in this work can be seen in Fig. 2.

The design field is filtered and projected twice using filter radius R_1, and projection parameters β_1 and η_1, which indirectly control the length-scale of φ. The base structure which is now either 0 or 1, is smoothed again using $R_2<R_1$, such that the resulting field $\tilde{\varphi}$ has smooth boundaries. The coating layer can then be defined by taking

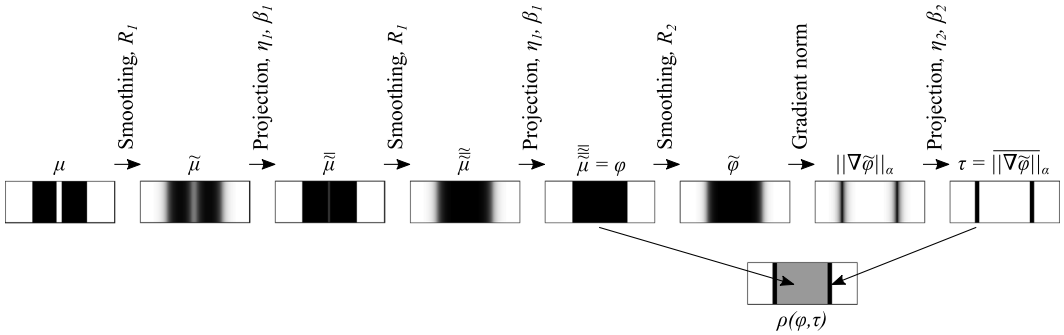

Fig. 2. Subsequent filtering steps, allowing to separate the base structure φ and the coating τ.

the Euclidean norm of the spatial gradients of $\tilde{\varphi}$. $\|\nabla\tilde{\varphi}\|$ is then normalized such that the largest possible gradient norm corresponds to 1. For this we use a normalization factor α, which is related to R_2 using [13],

$$\alpha = \frac{R_2}{\sqrt{3}}. \tag{4}$$

The choice of notation for this normalized gradient norm $\|\nabla\tilde{\varphi}\|_\alpha$ might seem odd; however, it is used to be consistent with the work of Clausen et al. [13] and Wu et al. [15]. Hence, the term shall be read as the Euclidean norm of $\nabla\tilde{\varphi}$ divided by scalar α, rather than as the usual definition, which would be the L^α- norm of $\nabla\tilde{\varphi}$.

The normalized gradient norm $\|\nabla\tilde{\varphi}\|_\alpha$ is subsequently projected using β_2 and η_2 to define the coating field $\tau = \overline{\|\nabla\tilde{\varphi}\|_\alpha}$. In [13] an analytical relation is shown between R_2 and the maximum coating thickness. This is used to select R_2 for a user-specified coating thickness t_{ref} as,

$$R_2 = \frac{\sqrt{3}}{\ln(2)} t_{ref} \approx 2.5 t_{ref}. \tag{5}$$

The motivation for using a double smoothing and projection (DSP) approach for the design field is that numerical experiments using a single smoothing and projection (SSP) approach showed the possibility that fields φ and τ describing the base structure and coating, did not converge exactly to 0 or 1. A similar observation can be made from Fig. 13 in [13], where it is difficult to distinguish between infill and void. To circumvent this undesired effect we use the DSP approach as proposed by [32]. More details on the effect of this DSP approach versus the SSP approach used in [13] will be given in Section 3.

2.1.4. Note on the filter boundary conditions

It is well-known that the use of homogeneous Neumann boundary conditions used in the smoothing operation of Eq. (1) causes artifacts on the optimized design near the domain boundary. To circumvent this undesired effect, we make use of the domain extension approach proposed by Clausen and Andreassen [33]. In this approach the physical domain is padded using void elements ($\mu = 0$), except at boundaries at which the displacement field is constrained. The extension distance $d_{ext} > R_1$ is chosen large enough, such that the homogeneous Neumann filter boundary conditions do not affect the final design. All filtering operations, finite element analysis and objective and constraint calculations are performed on this extended domain. An overview of the design domain Ω and boundary conditions for the MBB-beam example including the extended domain can be seen in Fig. 3.

Solid blocks of material are used at the two boundary conditions. This guarantees a minimum feature size of twice the coating thickness, e.g. $2t_{ref}$, and reinforces the structure thus preventing load concentrations. Furthermore, the load is applied in a distributed fashion over the complete top of the solid block, while the displacement constraint is applied in an average sense over the bottom of the lower block. This is done to prevent load concentrations when the optimized structure is mapped on a finer mesh, as will be discussed later on.

The domain extension approach works well for robust topology optimization problems or three-field SIMP optimization problems (density filtering, followed by projection), using $\eta = 0.5$. However, in the context of coated

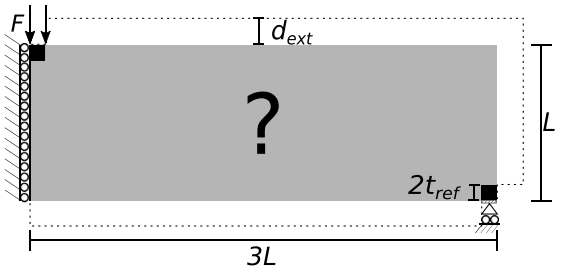

Fig. 3. Design domain Ω and boundary conditions of the MBB-beam example. Ω is indicated using gray material, while the extended filter domain is bounded by the dotted line.

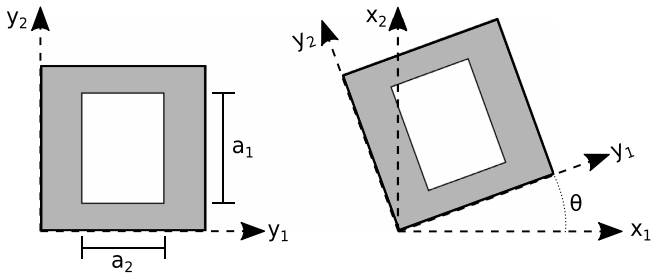

Fig. 4. Layout of the unit-cell with a rectangular hole, in local (y_1, y_2), and global (x_1, x_2) coordinate system.

structures, it is possible that half of the coating ($t_{ref}/2$) can exceed the design domain. To make sure that the optimized structure is within the bounds of Ω, the elasticity tensor in the padded domain is multiplied by penalization parameter $q < 1$, while $q = 1 \in \Omega$. Numerical experiments have shown that the use of $q = 0.2$ effectively restricts optimized structures to Ω.

2.2. Interpolation of elastic properties and density

For the numerical examples we restrict ourselves to coating and infill made from the same material, with Young's modulus $E^0 = 1$, Poisson's ratio $\nu^0 = 0.3$, and mass density $m^0 = 1$; however, extension to different coating and infill material is trivial. As infill we use the square unit-cell with rectangular hole introduced by Bendsøe and Kikuchi [22], shown in Fig. 4.

The constitutive properties which are close in performance to the optimal rank-2 laminate are obtained using numerical homogenization. A database of the constitutive properties in the local frame for a large number of different combinations for the height a_1 and width a_2 of the hole has been created. Afterwards, we can interpolate the effective properties $\mathbf{E}^H$ and sensitivities for any combination of a_1 and a_2. The corresponding elasticity tensor of the infill in the global frame of reference $\mathbf{E}^I$ can be calculated as,

$$\mathbf{E}^I(\theta, a_1, a_2) = \mathbf{R}(\theta)\mathbf{E}^H(a_1, a_2)\mathbf{R}(\theta)^T, \tag{6}$$

with $\mathbf{R}$ being the well-known frame rotation matrix using angle θ describing the angle between material and global frame of reference. The mass fraction of the microstructure m^I is given as,

$$m^I = 1 - a_1 a_2. \tag{7}$$

With the properties of the coating and infill known, we can define the interpolation of the density ρ and elasticity tensor $\mathbf{E}$ throughout the design domain. To this end, we use material indicator φ and coating indicator τ, such that,

$$\rho(\varphi, \tau, a_1, a_2) = m^I(a_1, a_2)\varphi + (1 - m^I(a_1, a_2)\varphi)\tau. \tag{8}$$

Similarly, the local elasticity tensor $\mathbf{E}$ can be defined.

$$\mathbf{E}(\varphi, \tau, \theta, a_1, a_2) = 10^{-9}\mathbf{E}^0 + q\Big(\mathbf{E}^I(\theta, a_1, a_2) - 10^{-9}\mathbf{E}^0\Big)\varphi^{p_1} + q(\mathbf{E}^0 - \mathbf{E}^I(\theta, a_1, a_2)\varphi^{p_1})\tau^{p_2}, \tag{9}$$

where, $\mathbf{E}^0$ is the elasticity tensor for the isotropic coating material, and p_1 and p_2 are penalty parameters to penalize intermediate values of φ and τ. Please note that the model using isotropic infill from Clausen et al. [13] can easily be recovered from Eqs. (8) and (9).

2.3. Problem formulation

We focus on the minimization of a compliance functional $\mathcal{J}$ for plane stress, single load-case problems under the assumption of linear elasticity. We discretize the design domain by bi-linear finite elements, and the material properties are assumed to be element-wise constant. The microstructures of the infill are described by design vectors $\mathbf{a}_1$, $\mathbf{a}_2$, $\boldsymbol{\theta}$ which determine the width and height of the hole as well as the unit-cell orientation, while the coating and base structure are defined by $\boldsymbol{\mu}$.

The topology optimization problem is solved in nested form. For each design iteration the equilibrium equations are satisfied by FE-analysis. As shown by Pedersen [34,35], the optimal orientation of an orthotropic composite coincides with the principal stress directions, hence the unit-cell orientation $\boldsymbol{\theta}$ is updated in each minimization step after the displacement and corresponding stress calculation. Subsequently, design vectors $\boldsymbol{\mu}$, $\mathbf{a}_1$ and $\mathbf{a}_2$ are updated based on their gradients using the updated microstructure orientation. The discretized optimization problem can thus be written as,

$$\begin{aligned} \min_{\boldsymbol{\mu},\mathbf{a}_1,\mathbf{a}_2,\boldsymbol{\theta}} &: \mathcal{J}(\boldsymbol{\mu}, \mathbf{a}_1, \mathbf{a}_2, \boldsymbol{\theta}, \mathbf{U}), \\ \text{s.t.} &: \mathbf{K}(\boldsymbol{\mu}, \mathbf{a}_1, \mathbf{a}_2, \boldsymbol{\theta})\mathbf{U} = \mathbf{F}, \\ &: \mathbf{v}^T\boldsymbol{\rho}(\boldsymbol{\mu}, \mathbf{a}_1, \mathbf{a}_2) - V_{max}A \leq 0, \\ &: \mathbf{a}_l \leq \mathbf{a}_1, \mathbf{a}_2 \leq \mathbf{a}_u, \\ &: \mathbf{0} \leq \boldsymbol{\mu} \leq \mathbf{1}, \end{aligned} \tag{10}$$

where $\mathbf{v}$ is the vector containing the element volumes, and V_{max} is the maximum allowed volume fraction of the material in the design domain, while A is the area of Ω. Stiffness matrix $\mathbf{K}$ is a function of $\boldsymbol{\mu}$, $\mathbf{a}_1$, $\mathbf{a}_2$, and $\boldsymbol{\theta}$. $\mathbf{F}$ describes the loads acting on the domain, and $\mathbf{U}$ describes the solution of the equilibrium equation. The vectors $\mathbf{a}_l$ and $\mathbf{a}_u$ on interval $[0, 1]$ describe the lower and upper bound on the hole size of the microstructure, subject to $\mathbf{a}_u > \mathbf{a}_l$. For the design update of $\boldsymbol{\mu}$, $\mathbf{a}_1$ and $\mathbf{a}_2$ the MATLAB implementation of the Method of Moving Asymptotes (MMA) introduced by Svanberg [36] is used.

The formulation above is the most general formulation. We allow full freedom for the microstructures, within bounds $\mathbf{a}_l$ and $\mathbf{a}_u$. To avoid fully void or solid infill material we use $\mathbf{a}_l \geq 0.1$ and $\mathbf{a}_u \leq 0.9$, where the exact values are problem dependent. In some optimization examples we do not want to exploit the full design freedom of the microstructures. Therefore, we present in total 4 different problem formulations that will be used throughout this work; however, note that more problem formulations can be envisioned.

Problem 0: Fixed microstructure density, isotropic microstructure

This is the original coating approach as proposed in [13]. We specify an infill mass fraction m^I, and choose a stiffness for the isotropic microstructure E^I that satisfies the upper bound of the Hashin–Shtrikman bounds [37],

$$E^I = \frac{m^I}{3 - 2m^I}. \tag{11}$$

Problem 1: Fixed microstructure density, equal widths of hole

This is the simplest problem using the orthotropic microstructure. The infill has a user-defined mass fraction m^I, and both widths are set equal such that,

$$a_i = \sqrt{1 - m^I}, \quad i = 1, 2. \tag{12}$$

Problem 2: Fixed microstructure density, variable widths of hole

Again we have a user-defined mass fraction m^I. However, a_1 and a_2 are allowed to vary such that m^I is always satisfied. Hence, we need one design variable to describe the shape of the rectangular hole. For this we use variable a_1, such that

$$a_2 = \frac{1 - m^I}{a_1}, \tag{13}$$

Furthermore, we can set box-constraints $\mathbf{a}_l$ and $\mathbf{a}_u$ on $\mathbf{a}_1$ to restrict the set of allowed microstructures. Here we always use an upper bound of $\mathbf{a}_u = 0.9$, after which we calculate $\mathbf{a}_l$ which will be larger than 0.1.

Problem 3: Variable microstructure density, variable widths of hole

This is the most general optimization problem, which is the problem shown in Eq. (10), with variables $\boldsymbol{\mu}$, $\mathbf{a}_1$ and $\mathbf{a}_2$ updated using the MMA. This means that contrary to the previous problems, the microstructure density can vary. To avoid artificially stiff checkerboard-like patterns of infill material, we here need to regularize design vectors $\mathbf{a}_1$ and $\mathbf{a}_2$ into $\tilde{\mathbf{a}}_1$ and $\tilde{\mathbf{a}}_2$ describing the physical size of the hole using a density filter with a filter radius just larger than the finite element size.

2.4. Sensitivity analysis

The sensitivity of the self-adjoint objective function $\mathcal{J}$ with respect to any design variable x can be derived as,

$$\frac{\partial \mathcal{J}}{\partial x} = -\mathbf{U}^T \frac{\partial \mathbf{K}}{\partial x}\mathbf{U} = -\sum_j \mathbf{u}_j^T \int_{\Omega_j} \mathbf{B}^T \frac{\partial \mathbf{E}_j}{\partial x}\mathbf{B}\mathrm{d}\Omega_j \mathbf{u}_j, \tag{14}$$

where j indicates the set of elements for which the elasticity tensor $\mathbf{E}_j$ is influenced by x due to filter operations.

2.4.1. Sensitivities w.r.t. μ

The sensitivity of compliance $\mathcal{J}$ w.r.t the variable determining the base structure of element e (φ_e)is,

$$\frac{\partial \mathcal{J}}{\partial \varphi_e} = -\mathbf{u}_e^T \int_{\Omega_e} \mathbf{B}^T \frac{\mathrm{d}\mathbf{E}_e}{\mathrm{d}\varphi_e}\mathbf{B}\mathrm{d}\Omega_e \mathbf{u}_e - \sum_k \mathbf{u}_k^T \int_{\Omega_k} \mathbf{B}^T \frac{\mathrm{d}\mathbf{E}_k}{\mathrm{d}\tau}\frac{d\tau}{d\varphi_e}\mathbf{B}\mathrm{d}\Omega_k \mathbf{u}_k. \tag{15}$$

Here k indicates the set of elements for which the elasticity tensor $\mathbf{E}_k$ is influenced by φ_e due to filter operations. Furthermore,

$$\frac{\mathrm{d}\mathbf{E}_e}{\mathrm{d}\varphi_e} = qp_1\Big(\mathbf{E}^I(\theta, a_1, a_2) - 10^{-9}\mathbf{E}^c\Big)\varphi_e^{p_1-1} - qp_1\mathbf{E}^I(\theta, a_1, a_2)\varphi_e^{p_1-1}\tau^{p_2}, \tag{16}$$

$$\frac{\mathrm{d}\mathbf{E}_k}{\mathrm{d}\tau} = qp_2(\mathbf{E}^c - \mathbf{E}^I(\theta, a_1, a_2)\varphi^{p_1})\tau^{p_2-1}, \tag{17}$$

The derivative of coating field τ w.r.t the element base structure φ_e is omitted here, but can be found in [13]. With the derivatives of the objective w.r.t φ known, it is easy to get the derivatives w.r.t design field μ. These are standard chain rule modifications for the two smoothing and two projection steps. These expressions are well-known and can be found in [28] and [31].

2.4.2. Sensitivities w.r.t. a_i

For an optimization problem of type 3 (full freedom), where both a_1 and a_2 are design variables, we can write the sensitivity of the elasticity tensor w.r.t the filtered variable determining the size of the hole of element e as,

$$\frac{\partial \mathbf{E}_e}{\partial \tilde{a}_{e,1}} = q\mathbf{R}_e \frac{\partial \mathbf{E}_e^H}{\partial \tilde{a}_{e,1}}\mathbf{R}_e^T \varphi_e^{p_1} - q\mathbf{R}_e \frac{\partial \mathbf{E}_e^H}{\partial \tilde{a}_{e,1}}\mathbf{R}_e^T \varphi_e^{p_1}\tau^{p_2}. \tag{18}$$

The derivative of the homogenized elasticity tensor w.r.t. the parameter describing the height of the hole $\tilde{a}_{e,1}$ is obtained by taking the derivative of the interpolation basis, used for the interpolation of the homogenized elasticity tensor. The standard chain rule modification to get the derivative w.r.t the design variable a_1 is again trivial.

Table 1
The parameters that are used in all numerical examples in this work.

p_1	3	Stiffness penalization of base structure φ
p_2	1	Stiffness penalization of coating indicator τ
η_1	0.5	Threshold parameter used to obtain φ
η_2	0.5	Threshold parameter used to obtain τ
β_{start}	2	Starting steepness parameter for the projection
β_{end}	128	Final steepness parameter for the projection
q	0.2	Penalization of elasticity tensor in padded domain

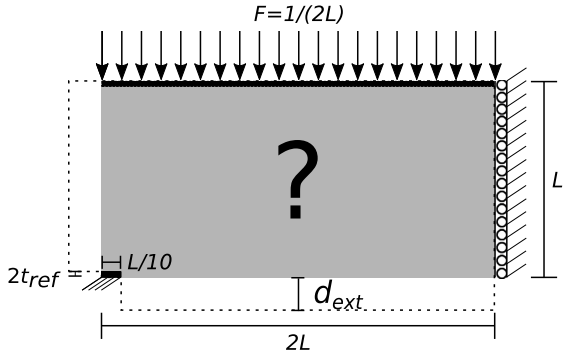

Fig. 5. Design domain Ω and boundary conditions of the bridge example. Ω is indicated using gray material, while the extended filter domain is bounded by the dotted line.

For an optimization problem of type 2, where we only have one variable per element to describe the shape of the hole a_1 we can write,

$$\frac{\partial \mathbf{E}_e}{\partial a_{e,1}} = q\mathbf{R}_e\Big(\frac{\partial \mathbf{E}_e^H}{\partial a_{e,1}} - \frac{1-m^I}{a_{e,1}^2}\frac{\partial \mathbf{E}_e^H}{\partial a_{e,2}}\Big)\mathbf{R}_e^T\varphi_e^{p_1} - q\mathbf{R}_e\Big(\frac{\partial \mathbf{E}_e^H}{\partial a_{e,1}} - \frac{1-m^I}{a_{e,1}^2}\frac{\partial \mathbf{E}_e^H}{\partial a_{e,2}}\Big)\mathbf{R}_e^T\varphi_e^{p_1}\tau^{p_2}. \tag{19}$$

2.5. Parameters to control the optimization problem

An overview of all parameters that are kept the same in all numerical examples in this work can be seen in Table 1.

These parameter choices have been extensively motivated using numerical experiments. For example, the choice for not penalizing the coating ($p_2 = 1$) might seem counter-intuitive at first sight; however, numerical examples using $p_2 > 1$ yielded solutions that more easily ended up in worse local minima. For the steepness parameter of the projection operation we use $\beta_1 = \beta_2$, which we start at β_{start} and double every $30 - 100$ iterations until β_{end}. The exact number if iterations before β is doubled depends on whether the maximum change in each design variable becomes less than 0.01.

3. Numerical examples for topology optimization of coated structures

For the numerical experiments in this paper we focus on the MBB-beam example shown in Fig. 3. Furthermore, we use the bridge example for which the loads and boundary conditions, including padded domain are shown in Fig. 5.

3.1. Experiments on the MBB-beam example

For the experiments on the MBB-beam example we use a discretization of 300×100 finite elements. A volume constraint of $V_{max} = 0.4$, $R_1 = 0.15\ L$ and $t_{ref} = 0.03\ L$ is used. The problem formulations with the fixed

Table 2
Compliance $\mathcal{J}^c$ for different problem formulations and different infill densities m^I. Label DSP indicates a double smoothing and projection approach is used to obtain φ, while label SSP indicates that a single smoothing and projection step is used.

		$m^I = 0.4$	$m^I = 0.5$	$m^I = 0.6$	$m^I = 0.7$	$m^I = 0.8$	$m^I = 0.9$	$m^I = 1.0$
Problem form 0	DSP	362.83	325.94	297.78	279.80	256.68	237.63	215.53
Problem form 1	DSP	318.45	291.14	274.92	266.85	251.38	236.37	215.53
Problem form 2	DSP	267.92	247.52	234.30	227.02	219.67	217.73	215.53
Problem form 0	SSP	360.45	325.75	291.49	273.20	254.35	236.55	213.57
Problem form 1	SSP	315.42	292.41	274.16	258.53	245.42	235.16	213.57
Problem form 2	SSP	266.02	246.83	231.44	224.44	220.19	217.84	213.57

(a) Problem form 0. (b) Problem form 1. (c) Problem form 2.

Fig. 6. Density distributions for the MBB-beam example using $m^I = 0.5$ and optimized for different problem formulations using the double smoothing and projection (DSP) approach.

(a) Problem form 1, DSP, $m^I = 0.7$. (b) Problem form 1, DSP, $m^I = 0.9$. (c) Three-field SIMP (SSP) $m^I = 1$.

Fig. 7. Density distributions for the MBB-beam example optimized for different infill volume fractions m^I.

microstructure density (problems 0–2), have been used to optimize the structure for various infill volume fractions ($m^I = 0.4$, $m^I = 0.5$, $m^I = 0.6$, $m^I = 0.7$, $m^I = 0.8$ and $m^I = 0.9$). The corresponding compliance values on the coarse optimization mesh $\mathcal{J}^c$ can be seen in Table 2.

It can be seen that the compliances $\mathcal{J}^c$ become lower as more freedom is introduced in the microstructures, *i.e.* going from problem 0 to 2. The corresponding density distributions for optimized results using $m^I = 0.5$ are shown in Fig. 6.

From Table 2 it is clear that for larger infill densities the structures converge to the results of a three-field SIMP approach (SIMP with smoothing and projection). This can also be seen in Fig. 7(a) and (b). The MBB-beam optimized using three-field SIMP with these filter settings has a corresponding compliance $\mathcal{J}^c = 213.57$, and can be seen in Fig. 7(c).

The structures using a single smoothing and projection (SSP) approach seem to have a slightly better compliance. However, this is at the cost of undetermined coating and infill, as seen in Fig. 8(a) and (b), where small features of void can be observed, that are not bounded by coating. The reason for vanishing coating can be seen in Fig. 8(c) and (d). At locations where the coating is vanishing the field describing the base structure φ has non-binary values. Since there is no sharp transition from 0 to 1, the corresponding normalized gradient norm $\|\nabla\tilde{\varphi}\|_\alpha$ is smaller than threshold η_2, resulting in a void region without coating. The DSP approach greatly reduces the possibility of φ being non-binary.

We cannot guarantee that a double smoothing and projection (DSP) approach will result in binary features in base structure and coating fields φ and τ. However, numerical experiments have shown a reduction of around 90% in the occurrence of vanishing coating compared to the SSP approach. The rare cases where a void region is not bounded by coating is when there is a thin feature of $\varphi = 0$. These thin features result in $\tilde{\varphi}$ not going to zero in the middle of this void feature, and consequently the corresponding normalized gradient norm $\|\nabla\tilde{\varphi}\|_\alpha$ is smaller than threshold η_2. A large number of numerical experiments have been performed to test the effects of threshold

(a) Problem form 1, $m^I = 0.5$. (b) Problem form 1, $m^I = 0.6$.

(c) φ corresponding to $m^I = 0.6$. (d) $||\nabla\tilde{\varphi}||_\alpha$ corresponding to $m^I = 0.6$.

Fig. 8. Density distributions for the MBB-beam example optimized using a single smoothing and projection (SSP) step.

(a) $R_1 = 0.30\ L$, $R_2 = 0.15\ L$, $\mathcal{J}^c = 262.44$. (b) $R_1 = 0.15\ L$, $R_2 = 0.15\ L$, $\mathcal{J}^c = 241.60$

Fig. 9. Density distributions for the MBB-beam example optimized using problem form 1, a DSP approach and $m^I = 0.5$ for a coating thickness of $t_{ref} = 0.06\ L$, and different filter radii R_1.

Table 3
Compliance $\mathcal{J}^c$ for problem formulations 3 using the DSP and SSP approach for various bounds on the shape of the microstructure.

a_l	0.2	0.2	0.3	0.3	0.4	0.4	0.5	0.5	0.6	0.6
a_u	0.8	0.9	0.8	0.9	0.8	0.9	0.8	0.9	0.8	0.9
DSP	222.81	207.12	228.70	212.42	236.29	219.35	245.61	229.48	259.57	245.15
SSP	226.91	207.09	231.91	212.32	238.04	219.38	248.50	229.34	261.96	244.97

parameters η_1, η_2 and filter radii R_1 and R_2. Unfortunately, changing thresholds η_1 and η_2 only results in reduced performance.

To show the effect of changing coating thickness t_{ref} and filter radius R_1, the density distribution using problem form 1, a DSP approach and $m^I = 0.5$ can be seen in Fig. 9(a) and (b) for a thicker coating $t_{ref} = 0.06\ L$, and 2 values of R_1. As can be seen, increasing t_{ref} results in more coating compared to the amount of infill material, which defies the goal of the present work (to design coated structures). In general, the coating thickness is uniform; however, in case of a small feature it can be seen that the coating thickness reduces. Especially in combination with a low value of R_1, there is an increased possibility of a vanishing coating. Hence, it is recommended to have $R_1 > R_2$.

A possible remedy to avoid the problem of vanishing coatings completely can be to apply image processing after homogenization-based optimization and explicitly enforce coating if required. An alternative approach could be to strongly enforce the length-scale of the coating using the method of Zhou et al. [38]. Testing both these ideas will be the topic of future work.

Finally, when we use the optimization problem with full freedom (problem 3), an even better performing structure than using standard three-field SIMP can be obtained. In Table 3 one can find the compliance values corresponding to several lower a_l and upper a_u bounds on the parameters that describe the shape of the hole.

(a) Problem form 3, DSP, $a_l = 0.2$ and $a_u = 0.9$. (b) Problem form 3, DSP, $a_l = 0.3$ and $a_u = 0.8$.

Fig. 10. Density distribution for the MBB-beam example optimized with DSP approach for the most general optimization problem, shown for various bounds on the shape of the microstructure.

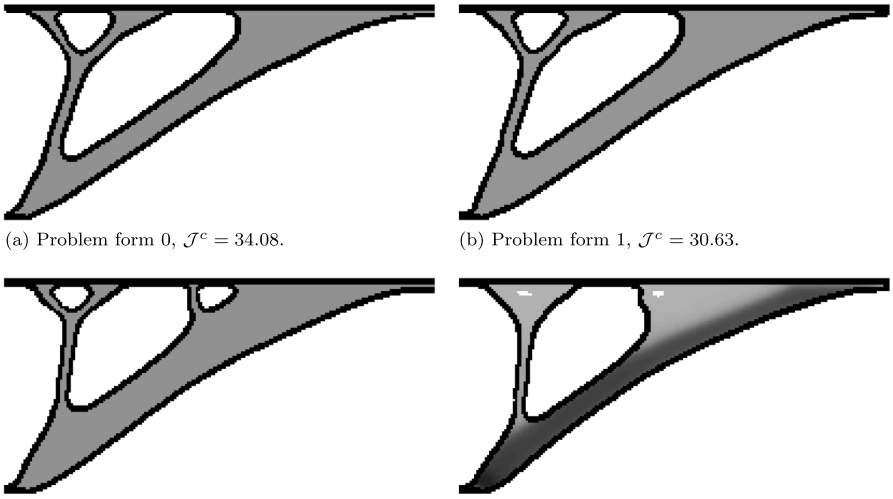

(a) Problem form 0, $\mathcal{J}^c = 34.08$. (b) Problem form 1, $\mathcal{J}^c = 30.63$.

(c) Problem form 2, $\mathcal{J}^c = 27.26$. (d) Problem form 3, $\mathcal{J}^c = 26.13$.

Fig. 11. Density distribution for the bridge design example, for all 4 types of optimization problems.

It can be seen that the lowest compliance can be reached when there is the largest freedom for parameters a_i to vary. To illustrate this, consider the density distribution shown in Fig. 10(a). Here the microstructures are allowed to be nearly solid $a_l = 0.2$ and also get close to void $a_u = 0.9$. Hence, there is no need to create holes. However, if the bounds are set a bit tighter, e.g. $a_l = 0.3$ and $a_u = 0.8$ holes will originate in the optimized structure, as can be seen in Fig. 10(b).

3.2. Bridge design example

The second optimization example considered is the bridge design example, shown in Fig. 5. The optimization is performed on a coarse mesh of 200 × 100 elements. A volume constraint of $V_{max} = 0.2$, $R_1 = 0.15\ L$ and $t_{ref} = 0.03\ L$ are used. The optimized designs and their compliance values, for $m^I = 0.5$, and for problem forms 0–2 are shown in Fig. 11(a)–(c). The design optimized for problem form 3, using $a_l = 0.2$ and $a_u = 0.8$ is shown in Fig. 11(d). Finally, it is noted that this example also has been solved using a three-field SIMP approach, the corresponding compliance of such a design is 24.50.

It is interesting to note that the two small void areas in the top of Fig. 11(d) are not bounded by coating material. This is a rare case where even the DSP approach cannot guarantee coating everywhere. Although this does not happen in many cases, it is still an undesired effect.

4. Projecting coated structures with microstructures as infill

To project the infill as a smooth and continuous lattice structure, two mapping functions ϕ_1 and ϕ_2 have to be determined, representing the two orthogonal layers of the sequence of unit-cells [23,25,26]. These mapping functions are then later used to project the composite shape of the microstructures on a fine mesh. We will not go into full detail on the derivation of the mapping functions; instead we focus on changes and improvements compared to the approach presented in [23].

4.1. Projecting a periodic composite shape

Contrary to previous approaches we do not solve for the mapping function in the void part of Ω, i.e. we create a conformal, albeit regular mesh on $\Omega_m = \Omega_c \bigcup \Omega_l$. Both mapping functions ϕ_1 and ϕ_2 can be obtained independently of each other; therefore, we restrict ourselves to the derivation of ϕ_1. A suitable parameterization of ϕ_1 has to fulfill:

1. ϕ_1 should be constant in the direction perpendicular to the layer normal $\mathbf{n}_1$.
2. The spacing between the contour lines of ϕ_1, should be as regular as possible without violating the first requirement.

To solve for ϕ_1 we use the following minimization problem,

$$\begin{aligned} &\min_{\phi_1(\mathbf{x})} : \mathcal{I}(\phi_1(\mathbf{x})) = \frac{1}{2}\int_{\Omega_m} \|\nabla\phi_1(\mathbf{x}) - \mathbf{n}_1(\mathbf{x})\|^2 \,\mathrm{d}\Omega_m, \\ &\text{s.t.} : \nabla\phi_1(\mathbf{x}) \cdot \mathbf{t}_1(\mathbf{x}) = 0. \end{aligned} \tag{20}$$

Here $\mathbf{t}_1$ is tangential to normal vector $\mathbf{n}_1$, hence both depend on the local directions of lamination θ,

$$\mathbf{n}_1(\mathbf{x}) = \mathbf{t}_2(\mathbf{x}) = \begin{bmatrix} -\sin(\theta(\mathbf{x})) \\ \cos(\theta(\mathbf{x})) \end{bmatrix}, \quad \mathbf{n}_2(\mathbf{x}) = \mathbf{t}_1(\mathbf{x}) = \begin{bmatrix} \cos(\theta(\mathbf{x})) \\ \sin(\theta(\mathbf{x})) \end{bmatrix}. \tag{21}$$

It has to be noted that the parameter describing the direction of lamination θ is rotationally symmetric, hence there may be jumps of size π in the angle field θ. These jumps are identified using connected component labeling and aligned consistently as suggested in [23], to allow for a smooth projection using Eq. (20).

The mapping functions can then be used to project the optimized shape. As opposed to Groen and Sigmund [23] that used a cosine we here use a triangle wave function $\mathcal{S}$ using the `sawtooth` function in MATLAB.

$$\tilde{\rho}_1(\mathbf{x}) = \frac{1}{2} + \frac{1}{2}\mathcal{S}(P_1\phi_1(\mathbf{x})), \tag{22}$$

where P_1 is a periodicity scaling parameter. The exact widths of the microstructure are then projected using Heaviside function H,

$$\rho_1(\mathbf{x}) = H\big(\tilde{\rho}_1(\mathbf{x}) - (1 - a_1(\mathbf{x}))\big). \tag{23}$$

After solving for the densities of both layers independently, they can be combined to obtain the density field ρ,

$$\rho(\mathbf{x}) = \max(\rho_1(\mathbf{x}) + \rho_2(\mathbf{x}) + \tau, 1). \tag{24}$$

The mapping problem is solved using bi-linear finite elements on an intermediate mesh using element size $h^i = h^c/2$, on which angle field θ (after consistent alignment) is interpolated using linear interpolation. The constraint is not enforced explicitly; but in penalty form using penalty parameter γ. For large values of γ the constraint enforces mapping functions ϕ_1 and ϕ_2 to be aligned with θ, at the cost of relaxed periodicity.

Locally we can identify the spacing of the mapping by making use of the Euclidean norm of the derivatives of the mapping functions $\|\nabla\phi_i\|$. If the value of $\|\nabla\phi_i\| > 1$, then the corresponding layer distance is locally compressed, similarly if $\|\nabla\phi_i\| < 1$ the corresponding layer distance is locally stretched. In general we would like to impose an average layer distance ε. To do that we can determine periodicity scaling parameter P_i as,

$$P_i = \frac{2\pi \int_{\Omega_m} \mathrm{d}\Omega_m}{\varepsilon \int_{\Omega_m} \|\nabla\phi_i(\mathbf{x})\| \mathrm{d}\Omega_m}. \tag{25}$$

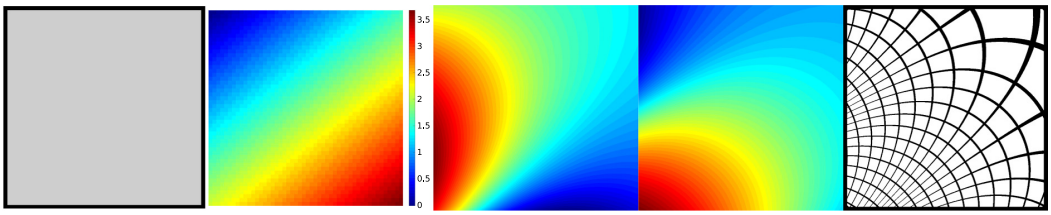

(a) ρ on $\mathcal{T}^c$. (b) θ on $\mathcal{T}^c$. (c) ϕ_1 on $\mathcal{T}^i$. (d) ϕ_2 on $\mathcal{T}^i$. (e) Projected ρ on $\mathcal{T}^f$.

Fig. 12. Example of the mapping procedure, using $\varepsilon = 80\ h^f$. To demonstrate the use of a coarse $\mathcal{T}^c$, intermediate $\mathcal{T}^i$ and fine mesh $\mathcal{T}^f$.

After scaling, the mapping functions are interpolated on a fine mesh where $h^f \leq h^c/10$, and the microstructure can be projected using Eqs. (22)–(24). The normalized gradient norm $\|\nabla\tilde{\varphi}\|_\alpha$ is interpolated using linear interpolation from coarse to fine mesh, afterwards the projection to obtain a clear coating $\tau = \overline{\|\nabla\tilde{\varphi}\|_\alpha}$ is performed.

To demonstrate the mapping procedure consider the simple test case shown in Fig. 12(a). Here we have a coated structure on coarse mesh $\mathcal{T}^c$ consisting of 50×50 coarse elements, where the coating layer is exactly 1 element wide. The square microstructure has $a_1 = a_2 = 0.9$ and the corresponding angle field is shown in Fig. 12(b). The mapping is performed on $\mathcal{T}^i$ using 100×100 elements, where ϕ_1 and ϕ_2 are shown in Fig. 12(c) and (d). The corresponding projection on $\mathcal{T}^f$ consisting of 1000×1000 elements is shown in Fig. 12(e).

4.2. Method to adaptively refine the periodicity

Fig. 12(d) shows a large variation in the layer spacing throughout the domain. However, for performance, and manufacturability of 3D printed structures, a regular spacing is desired. A possible solution to obtain a more regular spacing is to relax the angle constraint by using a small value for γ; however, this results in a decreased performance. Close inspection of optimization results from Wu et al. [15] (where the infill is freely optimized using SIMP) shows that structural members tend to split in two to counter increasing spacing between structural members. This observation leads to the idea of locally adapting the periodicity, to have a layer spacing as close to ε as possible.

Instead of using Eq. (22) we use a function such that the periodicity is adapted using discrete periodicity scaling parameter λ_i, corresponding to the ith mapping function, to obtain

$$\tilde{\rho}_i(\mathbf{x}, \lambda_i(\mathbf{x})) = \frac{1}{2} + \frac{1}{2}\mathcal{S}(2^{(\lambda_i(\mathbf{x})+1)}\pi\phi_i(\mathbf{x}) + \lambda_i(\mathbf{x})\pi). \tag{26}$$

When $\lambda_i = 0$, we have the same function as Eq. (22) with $\varepsilon = 1$. However, when $\lambda_i = 1$, we have the same function as when $\varepsilon = 0.5$. Hence, the periodicity is doubled. To get the periodicity in Eq. (26) as close to ε as possible we choose λ_i as,

$$\lambda_i(\mathbf{x}) = \text{round}\Big(\log\big(\frac{1}{\varepsilon\|\nabla\phi_i(\mathbf{x})\|}\big)\frac{1}{\log(2)}\Big). \tag{27}$$

A plot of λ_1 corresponding to ϕ_1 in Fig. 12(c) can be seen in Fig. 13(a); similarly, λ_2 can be seen in Fig. 13(b). The corresponding projection using Eq. (26) can be seen in Fig. 13(c), where it can be seen that the effective lattice spacing is now bounded to the interval $[\varepsilon 2^{-1/2}, \varepsilon 2^{1/2}]$.

Unfortunately however, the projected structure in Fig. 13(c) is now discontinuous. To reconnect the bars a transition zone $\Omega_{T,i}$ is needed. To this end, we use a convolution operation to obtain $\tilde{\lambda}_i$, shown in Fig. 13(d), using a linearly decaying convolution kernel with radius R^*. Using $\tilde{\lambda}_i$, we can determine splitting parameter ψ_i, which is used to identify if we are in the transition zone between two discrete values of λ_i.

$$\psi_i(\mathbf{x}) = \text{modulo}(\tilde{\lambda}_i(\mathbf{x}), 1). \tag{28}$$

If $\psi_i = 0$, then we are outside $\Omega_{T,i}$ and we can use Eq. (26), as shown in Fig. 13(e) and (f), while inside $\Omega_{T,i}$ the value of ψ_i is shown.

In $\Omega_{T,i}$ a structural member splits from a low periodicity (floor($\tilde{\lambda}_i$)) to a higher periodicity (ceil($\tilde{\lambda}_i$)), where both corresponding functions $\tilde{\rho}_i$ are shown in Fig. 14(a). To model this splitting of members inside $\Omega_{T,i}$, we create

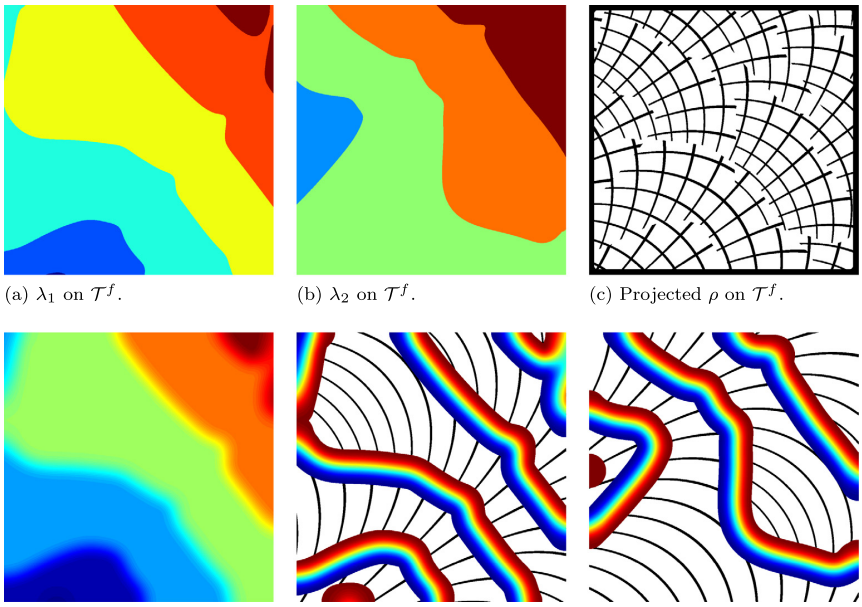

(a) λ_1 on $\mathcal{T}^f$. (b) λ_2 on $\mathcal{T}^f$. (c) Projected ρ on $\mathcal{T}^f$.

(d) $\tilde{\lambda}_1$ on $\mathcal{T}^f$. (e) Projected ρ_1 and ψ_1 on $\mathcal{T}^f$. (f) Projected ρ_2 and ψ_2 on $\mathcal{T}^f$.

Fig. 13. Visual explanation of adaptive periodicity and required transition zone, to split the structural members for $R^* = 0.8\varepsilon$.

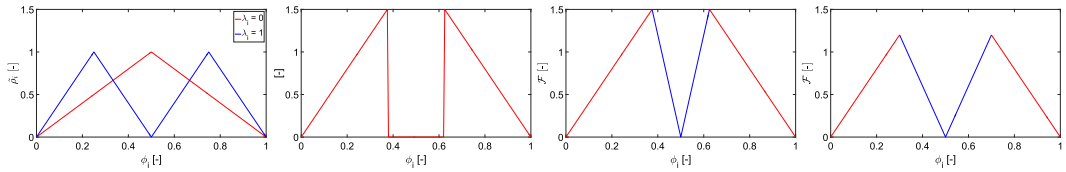

(a) $\tilde{\rho}_i$ for $\lambda_i = 0$ and $\lambda_i = 1$. (b) Base minus $1/2\psi_i$. (c) $\mathcal{F}_i$ for $\psi_i = 0.5$. (d) $\mathcal{F}_i$ for $\psi_i = 0.8$.

Fig. 14. Functions used in the transition zone to let a structural member split up into two members.

function $\mathcal{F}_i$, which is a function of ϕ_i, $\tilde{\lambda}_i$, and ψ_i. $\mathcal{F}_i$ consists of a base wave, on the interval $[0, 2]$. This base wave is defined as $\tilde{\rho}_i$ for a low periodicity (*i.e.* floor($\tilde{\lambda}_i$)) multiplied by 2, from which a part of width $1/2\psi_i$ is subtracted as is shown for $\psi_i = 0.5$ in Fig. 14(b). Afterwards, another sawtooth-like wave is added to create $\mathcal{F}_i$. The distance between the peaks in $\mathcal{F}_i$ linearly increases with ψ_i, as can be seen in Fig. 14(c)–(d).

It has to be mentioned that Eq. (23) cannot be used to impose the exact widths on $\mathcal{F}_i$ to obtain ρ_i. The reason is that, due to the choice of base wave, the peak of $\mathcal{F}_i$ is close to 2 for $\psi \to 0$. Hence, we need to numerically determine the threshold for the Heaviside function that we use to obtain ρ_i from $\mathcal{F}_i$, for a given combination of a_i and ψ_i. To do so, a bi-section scheme is used. The projection of the structure from Fig. 12 using adaptive periodicity scaling can be seen for different values of R^* in Fig. 15(a)–(c). Here it can be observed that increasing R^* leads to a smoother transition for splitting of structural members. Numerical experiments have shown that the compliance of projected designs is the lowest when the transition goes as smooth as possible. Hence, $R^* = 1.6\varepsilon$ has been found to give the best results.

Finally, it has to be mentioned that using the adaptive periodicity projection approach the local unit-cell spacing is restricted to the interval $[\varepsilon^{-1/2}, \varepsilon^{1/2}]$, except in the transition zone where this can be in the range $[\varepsilon^{-3/2}, \varepsilon^{1/2}]$. The corresponding feature size of a member is thus bounded by $[(1 - a_u)\varepsilon^{-3/2}, (1 - a_l)\varepsilon^{1/2}]$. Such a bound cannot be derived explicitly for the original mapping approach.

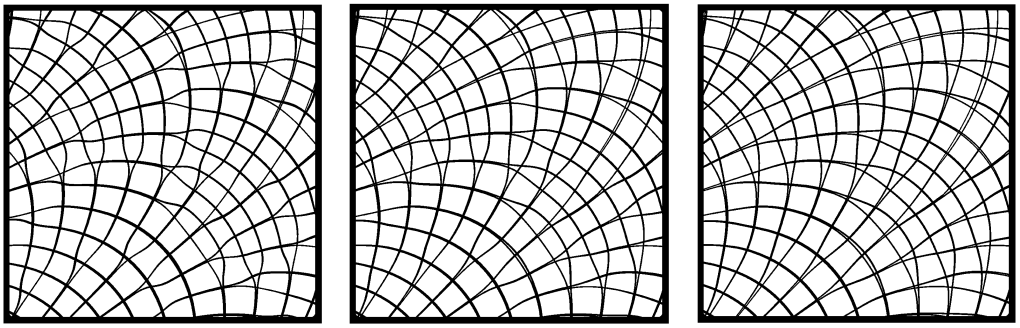

(a) $R^* = 0.8\varepsilon$. (b) $R^* = 1.2\varepsilon$. (c) $R^* = 1.6\varepsilon$.

Fig. 15. Projection on a fine mesh $\mathcal{T}^f$ using various radii for the convolution kernel R^*, using $\varepsilon = 80\ h^f$.

Table 4
Compliance on coarse $\mathcal{J}^c$, and on fine mesh $\mathcal{J}^f$, for the MBB-beam example using the same settings as in Table 2, optimized with problem form 1, for several infill densities m^I. Different interpolation methods for the coating are used.

	Interpolation	$m^I = 0.4$	$m^I = 0.5$	$m^I = 0.6$	$m^I = 0.7$	$m^I = 0.8$	$m^I = 0.9$
$\mathcal{J}^c$	–	318.45	291.14	274.92	266.85	251.38	236.37
$\mathcal{J}^f$	Nearest-neighbor	320.17	295.52	279.40	270.27	256.75	239.82
$\mathcal{J}^f$	Linear	328.34	305.32	286.30	273.18	258.39	239.09

5. Numerical examples for projection of coated structures

The presented projection approach allows the coarse-scale optimized structure to be interpreted on a much finer mesh $\mathcal{T}^f$. We will demonstrate the performance of the projected designs $\mathcal{J}^\phi$, and compare these results to the compliance of the homogenization-based designs on the coarse mesh $\mathcal{J}^c$. Three different sources are identified that can lead to a difference between $\mathcal{J}^\phi$ and $\mathcal{J}^c$: the effect of h-refinement, the interpolation of the coating from $\mathcal{T}^c$ onto $\mathcal{T}^f$, and the projection procedure. First, the effect of the former two will be discussed. Afterwards, various numerical examples will be used to demonstrate the potential of the projection approach in terms of both performance and computational cost.

5.1. Effect of mesh refinement and interpolation of coating

To test the effect of h-refinement, we interpolate the designs optimized with problem form 1 from Table 2 on a fine mesh (3000 × 1000 elements) using nearest-neighbor interpolation. The compliance values of the homogenization-based design on the coarse mesh $\mathcal{J}^c$ will be compared to the compliance values of the homogenization-based design on the fine mesh $\mathcal{J}^f$. Corresponding results are shown in Table 4.

As expected $\mathcal{J}^f$ is larger than $\mathcal{J}^c$ due to more accurate displacement calculation. Furthermore, the effect of the nearest-neighbor interpolation can be seen in Fig. 16(a), where the jagged edges of the coating correspond to 10 elements. To avoid these jagged-edges we use a linear interpolation to map the normalized gradient norm $\|\nabla\tilde{\varphi}\|_\alpha$ onto the fine mesh. The corresponding values of $\mathcal{J}^f$ demonstrating the effect of this interpolation are shown in Table 2 as well.

It can be observed that interpolation of $\|\nabla\tilde{\varphi}\|_\alpha$ using nearest-neighbor interpolation leads to a better performance than linear interpolation. This seems rather counter-intuitive, since the latter method results in a smooth coating without jagged edges as can be seen in 16(b). However, it can be seen that the use of linear interpolation causes somewhat strange jumps close to the bottom right boundary condition, which is assumed to be the cause of the increased error between $\mathcal{J}^c$ and $\mathcal{J}^f$.

Despite a slightly increased compliance, linear interpolation is used for the mapping of $\|\nabla\tilde{\varphi}\|_\alpha$ onto $\mathcal{T}^f$. The reason is that the reference coating thickness is more uniform using this interpolation method. A future remedy can

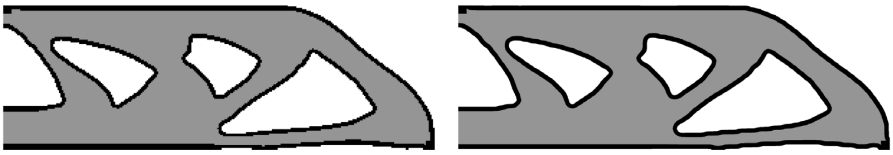

(a) nearest-neighbor, $\mathcal{J}^f = 295.52$. (b) linear, $\mathcal{J}^f = 305.32$.

Fig. 16. Density distribution for the MBB-beam example interpolated on a fine mesh of 3000 × 1000 elements, using different interpolation methods for $\|\nabla\tilde{\rho}\|_\alpha$. The structure optimized using problem form 1, with $m^I = 0.5$.

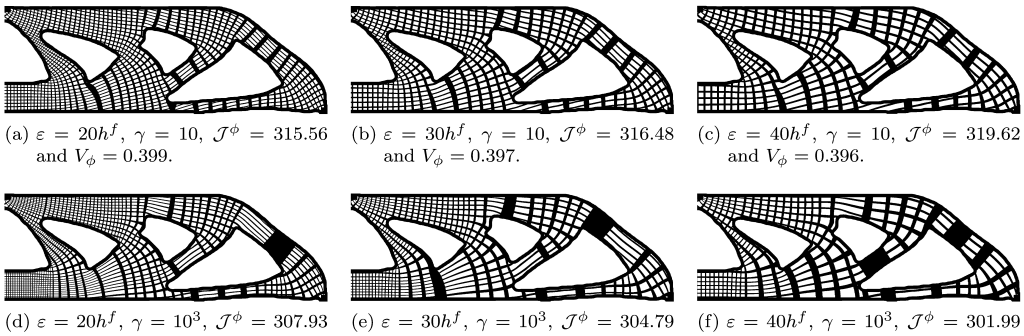

(a) $\varepsilon = 20h^f$, $\gamma = 10$, $\mathcal{J}^\phi = 315.56$ and $V_\phi = 0.399$.
(b) $\varepsilon = 30h^f$, $\gamma = 10$, $\mathcal{J}^\phi = 316.48$ and $V_\phi = 0.397$.
(c) $\varepsilon = 40h^f$, $\gamma = 10$, $\mathcal{J}^\phi = 319.62$ and $V_\phi = 0.396$.
(d) $\varepsilon = 20h^f$, $\gamma = 10^3$, $\mathcal{J}^\phi = 307.93$ and $V_\phi = 0.397$.
(e) $\varepsilon = 30h^f$, $\gamma = 10^3$, $\mathcal{J}^\phi = 304.79$ and $V_\phi = 0.400$.
(f) $\varepsilon = 40h^f$, $\gamma = 10^3$, $\mathcal{J}^\phi = 301.99$ and $V_\phi = 0.411$.

Fig. 17. Projection of the MBB-beam example for a problem of type 1, using $m^I = 0.5$, on a fine mesh of 3000 × 1000 elements, where $\mathcal{J}^f = 305.32$. No adaptive periodicity is used, results are shown for various values of angle constraint importance γ and ε.

be to define the coating and interface on a much finer mesh than the coarse analysis mesh using a multi-resolution approach, e.g. [39,40].

5.2. Effect of the different projection procedures

To demonstrate the performance of the projection method, we consider the MBB-beam example optimized using problem form 1, for $m^I = 0.5$. The structure is projected on a fine mesh (3000 × 1000 elements), without the adaptive periodicity approach. We perform the projection for two different values of γ, $\gamma = 10$ and $\gamma = 10^3$ to demonstrate the effect of the angle constraint enforcement. Furthermore, we project the structure for 3 different average unit-cell sizes ε. The corresponding projected structures, the compliance $\mathcal{J}^\phi$ and the volume of the projected structures V_ϕ are shown in Fig. 17.

From the bottom row it can be observed that a strong constraint enforcement ($\gamma = 10^3$) leads to structures performing very close to $\mathcal{J}^f$, *i.e.* within 1%! Unfortunately however, we can identify a locally very distorted periodicity. These stretched unit-cells can lead to V_ϕ exceeding imposed volume constraint V_{max}, and do not ensure a uniform infill. Lowering the angle constraint enforcement to $\gamma = 10$, as is shown in the top row, yields much more regular infill patterns; however, at the cost of a slightly reduced performance.

A distorted periodicity can also lead to long thin members as can be seen in Fig. 17(d). As was shown by [10] coated structures have an increased critical buckling load; however, thin unsupported infill members will reduce this desired effect by being prone to local buckling. Hence, regular projected unit-cells are required to retain a regular infill.

To use the best of both worlds, (exact angle enforcement, and regular unit-cells), we apply the adaptive periodicity projection approach as proposed in the previous section. The projected structures for $\gamma = 10^3$ and different spacings can be seen in Fig. 18(a)–(c).

It can be seen that values for $\mathcal{J}^\phi$ are again within 1% of $\mathcal{J}^f$, while a more uniform infill is maintained. Unfortunately, the proposed adaptive periodicity mapping procedure does not work perfectly yet when $\tilde{\lambda}_i$ is rapidly

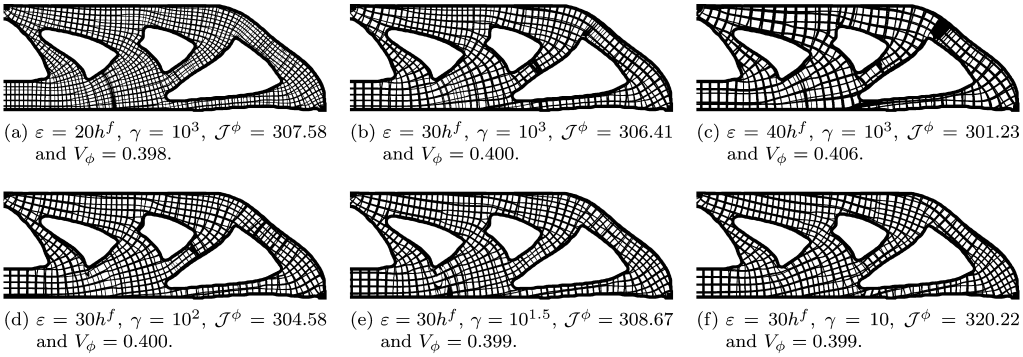

(a) $\varepsilon = 20h^f$, $\gamma = 10^3$, $\mathcal{J}^\phi = 307.58$ and $V_\phi = 0.398$.
(b) $\varepsilon = 30h^f$, $\gamma = 10^3$, $\mathcal{J}^\phi = 306.41$ and $V_\phi = 0.400$.
(c) $\varepsilon = 40h^f$, $\gamma = 10^3$, $\mathcal{J}^\phi = 301.23$ and $V_\phi = 0.406$.
(d) $\varepsilon = 30h^f$, $\gamma = 10^2$, $\mathcal{J}^\phi = 304.58$ and $V_\phi = 0.400$.
(e) $\varepsilon = 30h^f$, $\gamma = 10^{1.5}$, $\mathcal{J}^\phi = 308.67$ and $V_\phi = 0.399$.
(f) $\varepsilon = 30h^f$, $\gamma = 10$, $\mathcal{J}^\phi = 320.22$ and $V_\phi = 0.399$.

Fig. 18. Projection of the MBB-beam example for a problem of type 1, using $m^I = 0.5$, on a fine mesh of 3000 × 1000 elements, where $\mathcal{J}^f = 305.32$. Adaptive periodicity projection is used, results are shown for various values of angle constraint importance γ and ε.

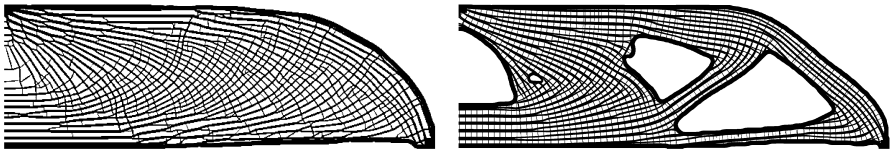

(a) Infill design using SIMP.
(b) Proposed projection procedure.

Fig. 19. Comparison of the MBB-beam example using a SIMP-based approach [15], and the proposed projection based approach for the infill. Uniform infill density with $m^I = 0.5$ is used while the microstructure is allowed to vary (problem form 2).

changing. This can be best seen in the top right of the MBB-beam shown in Fig. 18(c), where the periodicity is locally undergoing a large change, such that there is no space to form nice and clear branches between different periodicities.

To prevent large jumps in periodicity the angle enforcement can be relaxed; therefore, the projection using $\varepsilon = 30h^f$ is shown for various values of γ in Fig. 18(d)–(f). Here it can be seen that $\gamma = 10$, is the only value that completely prevents any of these local effects. Despite being slightly misaligned with the optimal orientation, the effect on the performance is small and the projected structures still perform within 5% of the homogenization-based designs.

To conclude, the proposed adaptive periodicity projection approach in combination with using $\gamma = 10^3$ shows a clear potential. The structures perform almost identically to the homogenization-based designs; while the projected structures consist of near-regular infill. In future work, different formulations for adapting the periodicity in regions with large changes in periodicity will be further investigated, to improve this new and promising method even more.

5.3. Comparison with coated structures optimized using SIMP

To further demonstrate the performance of the approach proposed in this work, we compare it to the work of Wu et al. [15]. In this approach a coated structure is created, where the infill is optimized using a density-based approach as can be seen for the MBB-beam example in Fig. 19(a). Here, a discretization of 600 × 200 elements is used, with $R_1 = 0.15\ L$ and $t_{ref} = 0.03\ L$; furthermore, $V_{max} = 0.4$, $m^I = 0.5$.

The method produces coated structures, where the infill has a locally uniform density, with no restriction on the freedom of the microstructure (close to an optimization problem of form 2). The optimization required a total time $T_{tot} = 292$ min using 600 design iterations. Hence, a more detailed design on a finer mesh is deemed computationally too expensive. The proposed projection procedure does not have a strong restriction on the level of detail of the projected shape, since the topology optimization can be performed on a relatively coarse mesh. The

Table 5
Compliance values for optimization mesh $\mathcal{J}^c$ and for fine mesh $\mathcal{J}^f$, as well as volume fraction V and optimization time T_{opt} (shown in [hh:mm:ss]), for the MBB-beam example using the approach by Wu et al. [15].

m^I	$\mathcal{J}^c$	$\mathcal{J}^f$	V	T_{tot}
0.5	270.21	281.95	0.394	04:52:00
0.6	241.36	247.54	0.400	04:58:00
0.7	227.84	231.94	0.400	05:00:00

Table 6
Compliance values for optimization mesh $\mathcal{J}^c$, fine mesh $\mathcal{J}^f$ and projected design $\mathcal{J}^\phi$, as well as volume fraction V_ϕ and time breakdown (shown in [hh:mm:ss]), for the MBB-beam example optimized using problem form 2 and projected using adaptive periodicity.

m^I	ε	$\mathcal{J}^c$	$\mathcal{J}^f$	$\mathcal{J}^\phi$	V_ϕ	T_{opt}	T_ϕ	T_{tot}
0.5	$20h^f$	247.52	256.31	261.96	0.397	00:23:00	00:00:20	00:23:20
0.5	$30h^f$	247.52	256.31	260.68	0.401	00:23:00	00:00:25	00:23:25
0.5	$40h^f$	247.52	256.31	257.61	0.409	00:23:00	00:00:30	00:23:30
0.6	$20h^f$	234.30	242.53	242.03	0.400	00:21:19	00:00:20	00:21:39
0.6	$30h^f$	234.30	242.53	239.29	0.402	00:21:19	00:00:25	00:21:44
0.6	$40h^f$	234.30	242.53	239.21	0.404	00:21:19	00:00:30	00:21:49
0.7	$20h^f$	227.02	230.83	233.92	0.400	00:21:11	00:00:19	00:21:30
0.7	$30h^f$	227.02	230.83	231.26	0.404	00:21:11	00:00:24	00:21:35
0.7	$40h^f$	227.02	230.83	230.26	0.405	00:21:11	00:00:29	00:21:40

design optimized for problem form 2, with $m^I = 0.5$ and $a_u = 0.9$ is projected on a fine mesh of 3000×1000 elements, using $\gamma = 10^3$, $\varepsilon = 20h^f$ and the adaptive periodicity projection approach as can be seen in Fig. 19(b).

For a fair comparison the structure optimized using the approach of Wu et al. [15] is mapped on a fine mesh of 3000×1000 elements using nearest-neighbor interpolation. The compliance values for both approaches, for various infill densities m^I are shown in Tables 5 and 6. Furthermore, a breakdown of the computational cost in optimization time T_{opt}, mapping time T_ϕ as well as the total time T_{tot} is shown. It has to be noted that all simulations are done using a single processor MATLAB code on a standard PC running Windows 7.

It can be seen that the compliance values of the structures optimized using the mapping approach are in general lower than the compliance values obtained using the approach of Wu et al. [15]. The larger m^I, the smaller the difference between the compliances obtained using both methods. Furthermore, it can be observed that a larger value of ε results in a slightly larger volume of the projected structures, which results in a lower compliance. Another benefit of the projection approach is the clear solid and void structures, in contrast to elements with intermediate density from the infill optimized with SIMP [15].

However, the most important result is the computational efficiency of the proposed mapping method. Coated designs of high resolution (3 million elements!) can be obtained in less than half an hour, thanks to the proposed coarse scale homogenization-based optimization. While, the method by Wu et al. [15] already requires close to 5 h on a relatively coarse mesh of (600×200) elements. A reduction in computational cost of at least an order of magnitude can thus be obtained by the proposed approach, which allows for topology optimization as a more integrated part of the structural design process.

5.4. Room for improvement

As discussed in the previous section, the adaptive periodicity projection approach will restrict the local unit-cell spacing to the interval $[\varepsilon 2^{-1/2}, \varepsilon 2^{1/2}]$, except in the transition zone. When the angle changes slowly the microstructure is spaced in a very regular manner, as can be seen in the main load carrying member of Fig. 20(a).

In the top left of the bridge-example the angle field is rapidly changing. Hence, there is no room for a smooth transition through all the periodicities and the spacing is slightly less regular as in the rest of the domain. A more worrying effect can be seen in the projected figure optimized for problem form 3, shown in 20(b). Here there is a singularity in the angle field below the void in the top left corner. Although the angle constraint ensures that

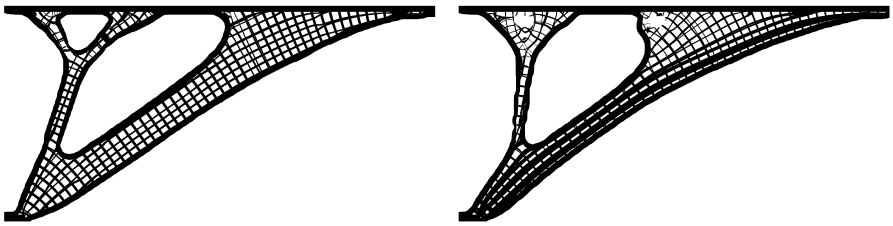

(a) Problem form 1, $\mathcal{J}^f = 31.0874$, $\mathcal{J}^\phi = 31.7504$ and $V_\phi = 0.196$.

(b) Problem form 3, $\mathcal{J}^f = 26.4330$, $\mathcal{J}^\phi = 26.8968$ and $V_\phi = 0.198$.

Fig. 20. Projected structures of the bridge example on a fine mesh of 2000 × 1000, elements using the adaptive periodicity approach, $\varepsilon = 20h^f$ and $\gamma = 10^3$.

most bars are well aligned with θ, and the performance is within 2% of the homogenization-based performance, it can be seen that there is a jump in orientation of mapping functions ϕ_i. We note that the observed singular points have low or negligible stresses, making the appearance less critical in terms of objective value. However, to avoid large changes in orientation and prevent the occurrence of singularities the angle field can possibly be regularized, e.g. using the approach presented by Allaire et al. [24]. We are confident that such a regularization will get $\mathcal{J}^\phi$ even closer to $\mathcal{J}^f$ and result in even more regular mapped designs.

6. Concluding remarks

An efficient approach to perform topology optimization of coated structures with orthotropic infill has been presented. Performing homogenization-based topology optimization allows for the modeling of designs with complex microstructures on a relatively coarse mesh, thus resulting in low computational cost. Furthermore, the double smoothing and projection (DSP) approach ensures in almost all cases a clear distinction between coating, infill and void.

In the second part of the work, a projection approach is presented to map the coated designs from the assumption of infinite periodicity on a fine but realizable scale. A novel method to adaptively refine the periodicity is presented to allow for a regular spacing of the infill. Numerical experiments demonstrate that the projected designs, despite a lack of separation of scales, are very close (within 1%–2%) to the homogenization-based performance. Furthermore, a comparison with [15] where the infill is optimized using a density-based method, shows that the projection procedure yields similar or even better performing designs at a finer resolution and at a computational cost which is at least 10 times lower, and potentially more in a case of mutual refinement.

This overall promising approach allows for extension of the method to 3D or to more complex loading situations. The main challenge here will lie in finding a parameterization that allows for smoothly varying microstructures through the domain. We are confident that such a parameterization can and will be found.

Acknowledgments

The authors acknowledge the financial support from the Villum Foundation (InnoTop VILLUM investigator project) and DTU Mechanical Engineering. Furthermore, the authors would like to express their gratitude to Anders Clausen for sharing his code on the optimization of coated structures. Finally, the authors wish to thank Krister Svanberg for the Matlab MMA code.

References

[1] M. Langelaar, An additive manufacturing filter for topology optimization of print-ready designs, Struct. Multidiscip. Optim. 55 (2017) 871–883, http://dx.doi.org/10.1007/s00158-016-1522-2.

[2] X. Qian, Undercut and overhang angle control in topology optimization: A density gradient based integral approach, Internat. J. Numer. Methods Engrg. 111 (2017) 247–272, http://dx.doi.org/10.1002/nme.5461.

[3] A.T. Gaynor, J.K. Guest, Topology optimization considering overhang constraints: Eliminating sacrificial support material in additive manufacturing through design, Struct. Multidiscip. Optim. 54 (2016) 1157–1172, http://dx.doi.org/10.1007/s00158-016-1551-x.

[4] G. Allaire, C. Dapogny, R. Estevez, A. Faure, G. Michailidis, Structural optimization under overhang constraints imposed by additive manufacturing technologies, J. Comput. Phys. 351 (2017) 295–328, http://dx.doi.org/10.1016/j.jcp.2017.09.041.
[5] B.S. Lazarov, F. Wang, O. Sigmund, Length scale and manufacturability in density-based topology optimization, Arch. Appl. Mech. 86 (2016) 189–218, http://dx.doi.org/10.1007/s00419-015-1106-4, http://dx.doi.org/10.1007/s00419-015-1106-4.
[6] J. Liu, A.T. Gaynor, S. Chen, Z. Kang, K. Suresh, A. Takezawa, L. Li, J. Kato, J. Tang, C.C.L. Wang, L. Cheng, X. Liang, A.C. To, Current and future trends in topology optimization for additive manufacturing, Struct. Multidiscip. Optim. 57 (2018) 2457–2483, http://dx.doi.org/10.1007/s00158-018-1994-3.
[7] L.J. Gibson, M.F. Ashby, Cellular Solids: Structure and Properties, Cambridge university press, 1999.
[8] G. Allaire, L. Jakabčin, Taking into account thermal residual stresses in topology optimization of structures built by additive manufacturing, Math. Models Methods Appl. Sci. 28 (2018) 2313–2366, http://dx.doi.org/10.1142/S0218202518500501.
[9] R. Ranjan, Y. Yang, C. Ayas, M. Langelaar, F. Van Keulen, Controlling local overheating in topology optimization for additive manufacturing, in: Proceedings of Euspen Special Interest Group Meeting: Additive Manufacturing, Belgium Google Scholar, Leuven, 2017.
[10] A. Clausen, N. Aage, O. Sigmund, Exploiting additive manufacturing infill in topology optimization for improved buckling load, Engineering 2 (2016) 250–257, http://dx.doi.org/10.1016/J.ENG.2016.02.006.
[11] J. Wu, N. Aage, R. Westermann, O. Sigmund, Infill optimization for additive manufacturing - approaching bone-like porous structures, IEEE Trans. Vis. Comput. Graphics 24 (2018) 1127–1140, http://dx.doi.org/10.1109/TVCG.2017.2655523.
[12] O. Sigmund, N. Aage, E. Andreassen, On the (non-)optimality of Michell structures, Struct. Multidiscip. Optim. 54 (2016) 361–373, http://dx.doi.org/10.1007/s00158-016-1420-7.
[13] A. Clausen, N. Aage, O. Sigmund, Topology optimization of coated structures and material interface problems, Comput. Methods Appl. Mech. Engrg. 290 (2015) 524–541, http://dx.doi.org/10.1016/j.cma.2015.02.011.
[14] A. Clausen, E. Andreassen, O. Sigmund, Topology optimization of 3D shell structures with porous infill, Acta Mech. Sinica 33 (2017) 778–791, http://dx.doi.org/10.1007/s10409-017-0679-2.
[15] J. Wu, A. Clausen, O. Sigmund, Minimum compliance topology optimization of shell-infill composites for additive manufacturing, Comput. Methods Appl. Mech. Engrg. (ISSN: 0045-7825) 326 (2017) 358–375, http://dx.doi.org/10.1016/j.cma.2017.08.018.
[16] N. Vermaak, G. Michailidis, G. Parry, R. Estevez, G. Allaire, Y. Bréchet, Material interface effects on the topology optimization of multi-phase structures using a level set method, Struct. Multidiscip. Optim. 50 (2014) 623–644, http://dx.doi.org/10.1007/s00158-014-1074-2.
[17] Y. Wang, Z. Kang, A level set method for shape and topology optimization of coated structures, Comput. Methods Appl. Mech. Engrg. 329 (2018) 553–574, http://dx.doi.org/10.1016/j.cma.2017.09.017.
[18] C. Dapogny, R. Estevez, A. Faure, G. Michailidis, Shape and topology optimization considering anisotropic features induced by additive manufacturing processes, Comput. Methods Appl. Mech. Engrg. 344 (2019) 626–665, http://dx.doi.org/10.1016/j.cma.2018.09.036.
[19] L. Lu, A. Sharf, H. Zhao, Y. Wei, Q. Fan, X. Chen, Y. Savoye, C. Tu, D. Cohen-Or, B. Chen, Build-to-last: Strength to weight 3D printed objects, ACM Trans. Graph. 33 (2014) 97:1–97:10, http://dx.doi.org/10.1145/2601097.2601168.
[20] J. Martínez, J. Dumas, S. Lefebvre, Procedural Voronoi foams for additive manufacturing, ACM Trans. Graph. 35 (2016) 44:1–44:12, http://dx.doi.org/10.1145/2897824.2925922.
[21] J. Wu, C.C. Wang, X. Zhang, R. Westermann, Self-supporting rhombic infill structures for additive manufacturing, Comput. Aided Des. (ISSN: 0010-4485) 80 (2016) 32–42, http://dx.doi.org/10.1016/j.cad.2016.07.006.
[22] M. Bendsøe, N. Kikuchi, Generating optimal topologies in structural design using a homogenization method, Comput. Methods Appl. Mech. Engrg. 71 (1988) 197–224, http://dx.doi.org/10.1016/0045-7825(88)90086-2.
[23] J.P. Groen, O. Sigmund, Homogenization-based topology optimization for high-resolution manufacturable micro-structures, Int. J. Numer. Methods Eng. 113 (2018) 1148–1163, http://dx.doi.org/10.1002/nme.5575.
[24] G. Allaire, P. Geoffroy-Donders, O. Pantz, Topology optimization of modulated and oriented periodic microstructures by the homogenization method, Comput. Math. Appl. (2018) http://dx.doi.org/10.1016/j.camwa.2018.08.007.
[25] O. Pantz, K. Trabelsi, A post-treatment of the homogenization method for shape optimization, SIAM J. Control Optim. 47 (2008) 1380–1398, http://dx.doi.org/10.1137/070688900.
[26] O. Pantz, K. Trabelsi, Construction of minimization sequences for shape optimization, in: 15th International Conference on Methods and Models in Automation and Robotics, MMAR, 2010, pp. 278–283, http://dx.doi.org/10.1109/MMAR.2010.5587222.
[27] S.D. Larsen, O. Sigmund, J.P. Groen, Optimal truss and frame design from projected homogenization-based topology optimization, Struct. Multidiscip. Optim. 57 (2018) 1461–1474, http://dx.doi.org/10.1007/s00158-018-1948-9.
[28] B.S. Lazarov, O. Sigmund, Filters in topology optimization based on Helmholtz-type differential equations, Internat. J. Numer. Methods Engrg. 86 (2011) 765–781, http://dx.doi.org/10.1002/nme.3072.
[29] J. Guest, J. Prévost, T. Belytschko, Achieving minimum length scale in topology optimization using nodal design variables and projection functions, Internat. J. Numer. Methods Engrg. 61 (2004) 238–254, http://dx.doi.org/10.1002/nme.1064.
[30] O. Sigmund, Morphology-based black and white filters for topology optimization, Struct. Multidiscip. Optim. 33 (2007) 401–424, http://dx.doi.org/10.1007/s00158-006-0087-x.
[31] F. Wang, B. Lazarov, O. Sigmund, On projection methods, convergence and robust formulations in topology optimization, Struct. Multidiscip. Optim. 43 (2011) 767–784, http://dx.doi.org/10.1007/s00158-010-0602-y.
[32] R.E. Christiansen, B.S. Lazarov, J.S. Jensen, O. Sigmund, Creating geometrically robust designs for highly sensitive problems using topology optimization, Struct. Multidiscip. Optim. 52 (2015) 737–754, http://dx.doi.org/10.1007/s00158-015-1265-5.
[33] A. Clausen, E. Andreassen, On filter boundary conditions in topology optimization, Struct. Multidiscip. Optim. 56 (2017) 1147–1155, http://dx.doi.org/10.1007/s00158-017-1709-1.

[34] P. Pedersen, On optimal orientation of orthotropic materials, Struct. Optim. 1 (1989) 101–106, http://dx.doi.org/10.1007/BF01637666.
[35] P. Pedersen, Bounds on elastic energy in solids of orthotropic materials, Struct. Optim. 2 (1990) 55–63, http://dx.doi.org/10.1007/BF01743521.
[36] K. Svanberg, The method of moving asymptotes–a new method for structural optimization, Internat. J. Numer. Methods Engrg. 24 (1987) 359–373, http://dx.doi.org/10.1002/nme.1620240207.
[37] Z. Hashin, S. Shtrikman, A variational approach to the theory of the elastic behaviour of multiphase materials, J. Mech. Phys. Solids 11 (1963) 127–140, http://dx.doi.org/10.1016/0022-5096(63)90060-7.
[38] M. Zhou, B.S. Lazarov, F. Wang, O. Sigmund, Minimum length scale in topology optimization by geometric constraints, Comput. Methods Appl. Mech. Engrg. 293 (2015) 266–282, http://dx.doi.org/10.1016/j.cma.2015.05.003.
[39] T. Nguyen, G. Paulino, J. Song, C. Le, A computational paradigm for multiresolution topology optimization (MTOP), Struct. Multidiscip. Optim. 41 (2010) 525–539, http://dx.doi.org/10.1007/s00158-009-0443-8.
[40] J.P. Groen, M. Langelaar, O. Sigmund, M. Ruess, Higher-order multi-resolution topology optimization using the finite cell method, Internat. J. Numer. Methods Engrg. 110 (2017) 903–920, http://dx.doi.org/10.1002/nme.5432.

Publication [P5]

Y. Wang, J.P. Groen and O. Sigmund. Simple optimal lattice structures for arbitrary loadings. *Extreme Mechanics Letters*, (accepted), 2019.

Simple optimal lattice structures for arbitrary loadings

Yiqiang Wang*, Jeroen P. Groen, Ole Sigmund

Department of Mechanical Engineering, Solid Mechanics, Technical University of Denmark, Building 404, 2800 Kongens Lyngby, Denmark

Abstract

This paper identifies four categories of optimal truss lattice structures (TLSs) that together provide ultimate stiffness for arbitrary multi-loading scenarios in the low volume fraction limit. Each category consists of 7 periodic sets of straight bars, forming periodic parallelepiped unit cells. Compared to other optimal TLSs, the identified TLSs most probably have the simplest possible geometries with the least number of bar sets. Macroscopic properties of a TLS are estimated using a superposition model, and an optimization problem is solved to determine the exact geometries of the optimal TLSs. Systematic optimization results, run for thousands of random multi-loading conditions, are compared to (postulated) theoretical bounds for both truss and plate lattice structures. The results clearly demonstrate near-optimality of the identified TLSs (relative difference mostly within machine precision except in few cases up to 0.1%) for any loading scenarios in linear elasticity. At the same time, the optimal anisotropic TLSs always have inferior stiffness to the corresponding optimal plate lattice structures and this inferiority is bounded between 1 (single uniaxial load) and a factor of 3 (optimal isotropy).

Keywords: Truss lattice structure, maximum stiffness, anisotropic lattice structure, multiple loading, energy bound

1. Introduction

Microstructures are called optimal if their effective properties attain the theoretical bounds. Specifically in elasticity, optimal microstructures with ultimate stiffness can be recognized by examining Hashin-Shtrikman energy bounds [1, 2]. To date, various groups of optimal elastic microstructures have been proposed. For instance, isotropic sphere assemblages [3] and Vigdergauz-type constructions [4, 5, 6] can achieve the maximum bulk modulus bound but they cannot attain the maximum shear modulus bound simultaneously. Independently, [7, 8, 9] suggested so-called rank-n laminates for attaining the optimal stiffness in both isotropy and anisotropy, where the laminates are made by sequential layerings at n length scales. Moreover in [10, 11], the authors proved that at most $n=3$ and $n=6$ are needed to construct optimal 2D and 3D rank laminates, respectively. This type of composite was further improved to cover all the theoretically allowable elastic properties by using infinitely rigid and compliant constituents [12]. Another class of optimal microstructures achieving the stiffness bounds was proposed by Sigmund [13], formed by a combination of solid material regions and rank-n laminates ($n = 1$ in 2D and $n = 3$ in 3D). One should

*Corresponding author: ywang@mek.dtu.dk

note that the optimal stiffness can be attained only by closed-walled plate lattice structures (PLSs). Nowadays, persistent efforts are made to look for other types of optimal microstructures, especially when considering their manufacturability [14, 15].

Despite possessing sub-optimal stiffness, truss lattice structures (TLSs) may have superior strength and buckling performance [16]. Also, additive manufacturing technology, like powder-based Selective Laser Melting, may hinder realization of plate-like optimal composites. Therefore, it remains of great importance to look for optimal TLSs with maximum stiffness. Most studies in this area have focused on identification of optimal isotropic TLSs, especially in the low volume fraction limit (i.e. volume fraction going to zero). In that case, the maximum Young's modulus is analytically calculated [17] and the optimal TLSs can be explicitly represented using single-scale bars. In 2D, triangular-type TLSs have long been recognized as optimal [18]; and in 3D a class of optimal isotropic TLSs was formed by combining two or three elementary TLSs [19, 20, 21], where the compound TLSs can be named following the system developed in [22]. If a moderate density is concerned, either rounded corners [23] or multi-scale features are demanded to improve the stiffness. Beyond isotropy, Deshpande et al. [24] proposed an octet-type TLS, whose stiffness and strength scale almost linearly up to moderate densities; and it was later fabricated using advanced 3D printing technique at sub-micrometer length scales [25]. However, there still remain big gaps, first to recognize 3D optimal anisotropic TLSs with ultimate stiffness for any prescribed loading scenarios, and second, to quantitatively study stiffness inferiority of the optimal TLSs compared to the corresponding optimal PLSs.

This paper identifies four categories of optimal TLSs for attaining maximum stiffness for any anisotropic loading conditions in the low volume fraction limit. Each category is built from 7 periodic sets of straight bars, forming periodic parallelepiped unit cells. Compared to other optimal TLSs with more bar sets or non-extending bars, the identified TLSs have most probably the simplest geometries achievable and are hence preferable in practical applications. In the low volume fraction limit, the elastic properties of a TLS are efficiently estimated using a superposition model. An optimization problem is then solved to determine the cell shapes and bar areas for representing the optimal TLSs. Near-optimality of the identified TLSs are verified through thousands of numerical tests with multiple loading cases, including the special case of optimal stiffness with isotropy. Furthermore, we quantitatively investigate the inferior stiffness of the optimal TLSs to their counterpart PLSs and conclude that the stiffness inferiority of any optimal TLSs is bounded between 1 and 3, referring to single uniaxial stress cases and optimal isotropy, respectively.

In the following, we first formulate an optimization problem to obtain optimal TLSs subject to any prescribed loading conditions. Secondly, a postulated energy bound is established for identifying optimal anisotropic TLSs. Thirdly, we identify four categories of optimal TLSs and discuss their geometrical advantages and mechanical performance. Finally, stiffness optimality of the identified TLSs and stiffness inferiority of the optimal TLSs are verified by numerical experiments.

2. Method

2.1. Design model

This study concerns TLSs formed by m distinct sets of continuous bars, each individual set involving infinite number of parallel equidistant bars, as illustrated in Fig. 1. In the low volume fraction limit, nodal geometries and locations have marginal effects on the macroscopic properties of the TLS [26]. In this regard, the elastic stiffness matrix $\boldsymbol{D}$ of a TLS can be estimated by directly

adding up stiffness matrices of each individual bar set [17, 18]

$$\boldsymbol{D} = \sum_{i=1}^{m} a_i \boldsymbol{T}_i^{\mathrm{T}} \boldsymbol{D}_0 \boldsymbol{T}_i \tag{1}$$

where $\boldsymbol{T}_i = \boldsymbol{T}(\boldsymbol{p}_i)$ is the 3D rotation matrix; $\boldsymbol{p}_i$ and a_i indicate the normalized pointing direction and relative cross-sectional area of the ith bar set, respectively; and $\boldsymbol{D}_0$ is the stiffness matrix for a single uniaxial bar set.

The optimization problem for identifying optimal TLSs with maximum stiffness is formulated by

$$\begin{aligned} \underset{\boldsymbol{\chi}}{\text{Minimize}} \quad & J = \sum_{k=1}^{N_\sigma} w_k \boldsymbol{\sigma}_k^{\mathrm{T}} \boldsymbol{C}(\boldsymbol{\chi}) \boldsymbol{\sigma}_k - \gamma \|\boldsymbol{a}\| \\ \text{Subject to} \quad & \rho \le \overline{\rho} \\ & \underline{\boldsymbol{\chi}} \le \boldsymbol{\chi} \le \overline{\boldsymbol{\chi}} \end{aligned} \tag{2}$$

Here, J is the weighted complementary energy subject to N_σ prescribed stresses $\boldsymbol{\sigma}_k$, w_k the weighting factor and $\boldsymbol{C} = \boldsymbol{D}^{-1}$ the effective compliance tensor. The regularization term $\gamma\|\boldsymbol{a}\|$ penalizes duplicated bars in the final design with $\gamma \ge 0$ being the regularization factor and $\|\cdot\|$ denoting the $L2$-norm of the area vector $\boldsymbol{a} = \{a_i\}$. The design variable vector $\boldsymbol{\chi}$ indicates geometric parameters representing the TLSs, constrained by $[\underline{\boldsymbol{\chi}}, \overline{\boldsymbol{\chi}}]$ (their exact definitions for specific design problems are given in Section 2.4). A volume fraction constraint is imposed to evaluate optimized energies from different candidates at the same volume fraction level $\overline{\rho}$. Because a_i actually reveals the relative volume fraction of each bar set, the total volume fraction ρ of a TLS can be obtained by summing up each a_i, i.e.

$$\rho = \sum_{i=1}^{m} a_i \tag{3}$$

2.2. Energy bound for anisotropic TLSs

To our best knowledge, no tight theoretical formulation has been set up for identifying optimal anisotropic TLSs. Therefore, a postulated reference bound is used in this study. Analogously to rank-n laminate cases [10, 18], the postulated bound can be established as the optimal energies obtained by optimizations of TLSs involving finite sets of straight bars. For single loading cases, the optimal stiffness is attained by orientating three bar sets in the principal strain (or stress) directions [27]; and for multi-loading cases, the orientations and areas of at least 6 bar sets are freely optimized by running optimization (2). In order to ensure convergence to true optima, we performed optimizations by varying bar numbers from 6 to 10 and chose the minimum value among all the solutions as the reference energy. It is worth noting that the obtained TLSs using this free optimization strategy could typically encounter connectivity issues. Hence, the obtained energy values only make theoretical sense for evaluating the performance of our identified TLSs.

2.3. Identified optimal TLSs

The key contribution of our study is to identify four categories of optimal TLSs with simple connected geometries that are able to attain maximum stiffness subject to any loading conditions. These TLSs can be represented by periodic *parallelepiped* unit cells, and they are built by joining cell vertices to form edge, face and body bars in various combinations. All the bars are continuously

extended when periodically repeating the unit cell over space. Note that multiple parallel bars belong to an identical bar set, and thus from a macroscopic view, each TLS is comprised of only 7 periodic sets of bars. The identified TLSs in cubic unit cells are illustrated in Fig. 1(a) (labelled $L7{-}I$ to $L7{-}IV$).

The reasons to use 7 sets of well-connected bars are twofold. On one hand, at least 7 sets of bars are needed to produce optimal isotropic TLSs (using 3 edge and 4 body bar sets) [19, 21]; and on the other hand, making use of 7 sets of bars turn out to provide near-optimal stiffness based on extensive numerical experiments. There must exist other optimal TLSs with more bar sets, such as the intuitive TLS with 13 sets of bars shown in Fig. 1(b) (labelled $L13$)[1]. However, the TLSs consisting of 7 bar sets are preferable as they have the simplest geometries with the least number of necessary bar sets and can provide the same maximum stiffness as the $L13$.

Because of their distinct geometries, the four $L7$ TLSs cover different mechancial properties. Here, $L7{-}I$ and $L7{-}II$ may behave rigidly in different directions due to their triangular-type rigid frames on various crossed planes, and therefore they may produce optimal rigid TLSs. Conversely, the other two TLSs may be preferred to produce rigidity only in certain directions but may be compliant in other directions. Numerical results (see Section 3.1) show that the suggested four $L7$ TLSs together are able to attain near-optimal stiffness subject to any loading conditions, although there exist many other $L7$ TLSs formed by various combinations of bar sets.

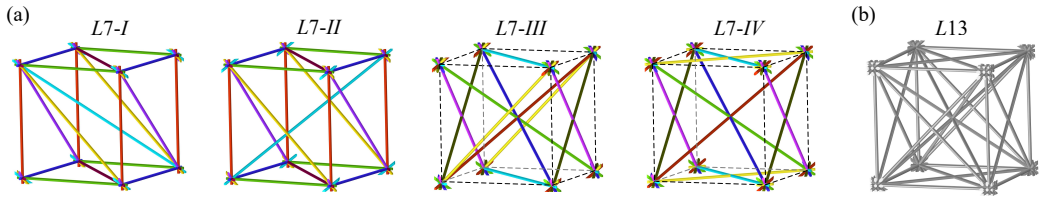

Fig. 1: Identified TLSs in periodic cubic unit cells, including (a) four $L7$ TLSs with 7 bar sets and (b) a $L13$ TLS with 13 bar sets, where different colors in (a) indicate the 7 distinct sets of bars.

2.4. Numerical implementation

Geometries of the optimal TLSs are determined by optimizing three groups of design variables (see Fig. 2). The first group is referring to the relative areas of the bar sets and has $m = 7$ variables for the $L7$ TLSs. The other two groups of variables are used to determine the shapes of the parallelepiped unit cells, referring to the orientation angles θ_j and the length ratios s_k of the cell edges. As the orientation of each cell edge is characterized by two angles, the optimization totally demands six θ_j. Moreover, two s_k are used to indicate length ratios of three edges. Orientations of all the other bar sets with the predefined connections can be calculated in terms of θ_j and s_k. Using these variables, the properties of the TLS are estimated by Eq. (1). To this end, the design variable vector in Eq. (2) is written as

$$\boldsymbol{\chi} = \{a_i,\ \theta_j,\ s_k\} \quad (i = 1, 2, ..., m;\ j = 1, 2, ..., 6;\ k = 1, 2) \tag{4}$$

restricted by $0 \leq a_i \leq \overline{\rho}$, $-2\pi \leq \theta_j \leq 2\pi$ and $0.1 \leq s_k \leq 3$.

[1]The $L13$ TLS involves 3 sets of edge bars, 6 sets of face bars and 4 sets of body bars [21].

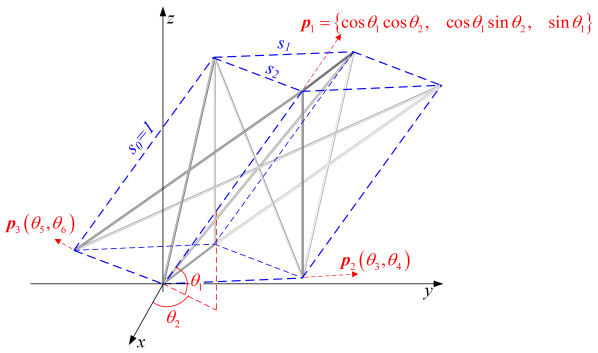

Fig. 2: Angle variables θ_j and length ratio variables s_k representing a parallelepiped unit cell of $L7-III$.

To solve the optimization problems, we first employ a gradient-based interior-point algorithm to get close-to-optimal solutions and then use a global pattern search algorithm to further descrease the optimized energy values[2]. All the optimized TLSs satisfy the optimality conditions, i. e. the sum of the strain energy density in each bar set over all loading cases is equal to a constant. Also, the gradients with respect to the angle and length ratio variables are zeros. Due to symmetries both in the topologies and in the loadings, we provide additional observations regarding optimal strain, stress and strain energy densities on each bar set for the optimal isotropic TLSs in Appendix A.

3. Results and discussions

3.1. Stiffness optimality

Near-optimality of the identified TLSs is verified by optimization for thousands of random loading conditions, where the number of stress cases N_σ is varied from 2 to 7. For each N_σ, 500 loading conditions are randomly generated[3] with $w_k = 1/N_\sigma$. For each loading condition, the four identified $L7$ TLSs are tested using a fixed $\gamma \in [0, 0.01]$, and for each TLS, hundreds of random initial guesses are used to ensure the best solutions. The procedure is terminated if maximum changes in both objective functions and design variables are smaller than 10^{-15}.

The optimization results are shown in Fig. 3. For a specific loading condition, the performance of the optimized TLS is measured by the relative energy difference $d = (J - J_r)/J_r$, where J and J_r are the optimized energy of the best-performing TLS among four $L7$ TLSs and the reference energy by the free design strategy in Section 2.2, respectively. In each group of N_σ, the worst case among 500 solutions has the difference $d^{\max}$, as stated in Table 1. In addition, the minimum eigenvalue $e_{\min}$ of $\boldsymbol{D}/\rho$ is used to examine if an optimal TLS behaves rigidly only in specific directions or in all directions. This measure is normalized by the minimum eigenvalue for the optimal isotropic TLS,

[2]The two optimizers are available by the "*fmincon*" and "*patternsearch*" functions embedded in the Matlab optimization toolbox.

[3]Each stress case in a loading condition is generated by prescribing three random principal stresses on interval [-1 1], which are then rotated by three random angles on interval [-π π].

which is $e_{\min}^{\text{iso}} = 1/15$ (obtained by Eq. (A1) in Appendix), and the normalized eigenvalue is denoted by $\overline{e}_{\min} = e_{\min}/e_{\min}^{\text{iso}}$.

From Fig. 3, it is seen that the optimal TLSs can be divided into compliant TLSs (left part) and rigid TLSs (right part). Compliant TLSs can be observed for $N_\sigma \leq 5$, and have close-to-zero $\overline{e}_{\min}$. They offer stiffness only in specific directions and perform compliant in other directions. For $N_\sigma = 2$ and 3, the maximum stiffness can be obtained by using any one of the four $L7$ TLSs. The small but non-zero numerical errors of 10^{-6} and 10^{-7} arise from the fact that the compliant TLSs are highly sensitive to small misalignments of geometric parameters. For $N_\sigma = 4$, the optimal TLSs offer more complex directional stiffness as required by the increased number of stress cases, hence the optimal performance is more challenging to achieve and a bigger $d^{\max}$ is found. This error comes from the fixed configurations of the identified TLSs and the strong restriction implicitly introduced by periodicity. In that case, $L7{-}III$ and $L7{-}IV$ dominate the best solutions as they can behave more compliant than the two other TLSs. Nevertheless, the claimed $d^{\max}$ is below 0.1% for all these cases, which is fully acceptable for practical means.

In the right part of Fig. 3, the optimal TLSs show rigidity with moderate $\overline{e}_{\min}$, which are found in parts of the results for $N_\sigma = 5$ and in all the results for $N_\sigma = 6$ and 7. Here, $L7{-}I$ and $L7{-}II$ are preferred to attain maximum stiffness with negligible $d^{\max}$ (machine precision). Particularly, $L7{-}I$ itself provides maximum stiffness in almost all the tests for $\overline{e}_{\min} > 0.2$. This is mainly attributed to its configuration fully formed by tetrahedron frames. Furthermore, the identified $L7$ TLSs can together obtain stiffness as close to those using $L13$ (see Table 1).

As a special but important subcase, optimal isotropic TLSs (see the red solid triangle in Fig. 3) are obtained by applying a specific multi-loading condition (see Eq. (A3) or (A4) in Appendix). Besides being able to reproduce the stiffest TLSs proposed in [19], the optimization also yields many other optimal isotropic TLSs. Two examples are presented in Appendix (see Fig. A.1), which are formed by a number of rigid triangular frames and have the maximum Young's modulus matching the theoretical value. To our knowledge, these two TLSs have not appeared in the literature before.

Table 1 Maximum relative difference among 500 solutions in each group of stress case number.

	Compliant TLSs				Rigid TLSs		
N_σ	2	3	4	5	5	6	7
$d_{L7}^{\max}$	2.51×10^{-6}	3.99×10^{-7}	1.09×10^{-3}	6.71×10^{-4}	7.59×10^{-14}	2.34×10^{-14}	2.54×10^{-14}
$d_{L13}^{\max}$	1.82×10^{-6}	4.80×10^{-7}	1.09×10^{-3}	6.71×10^{-4}	5.49×10^{-14}	3.45×10^{-14}	5.04×10^{-14}

3.2. Stiffness inferiority

The stiffness inferiority of optimal TLSs compared to known optimal PLSs can be evaluated by studying their energy ratios $R = J^{\text{TLS}}/J^{\text{PLS}}$. Here, J^{PLS} is obtained by using rank-6 laminates (in the low volume fraction limit) [1] and J^{TLS} corresponds to the postulated energy from the free optimization strategy. The results for single stress cases are also taken into account. In addition, we use an index $M = |\boldsymbol{e}|/\|\boldsymbol{e}\| - 1$ to measure the degree of anisotropy of each optimal TLS, $|\boldsymbol{e}|$ and $\|\boldsymbol{e}\|$ for $L1$- and $L2$-norms of eigenvalue vector $\boldsymbol{e}$, indicating averaged and total stiffness, respectively [28]. It can be checked that M is bounded on the interval [0, 1], where $M = 1$ corresponds to an optimal isotropic TLS and $M = 0$ stands for a single bar member. Note that M is invariant to orientations of TLSs. Also note that M can have various values for a specific loading condition since

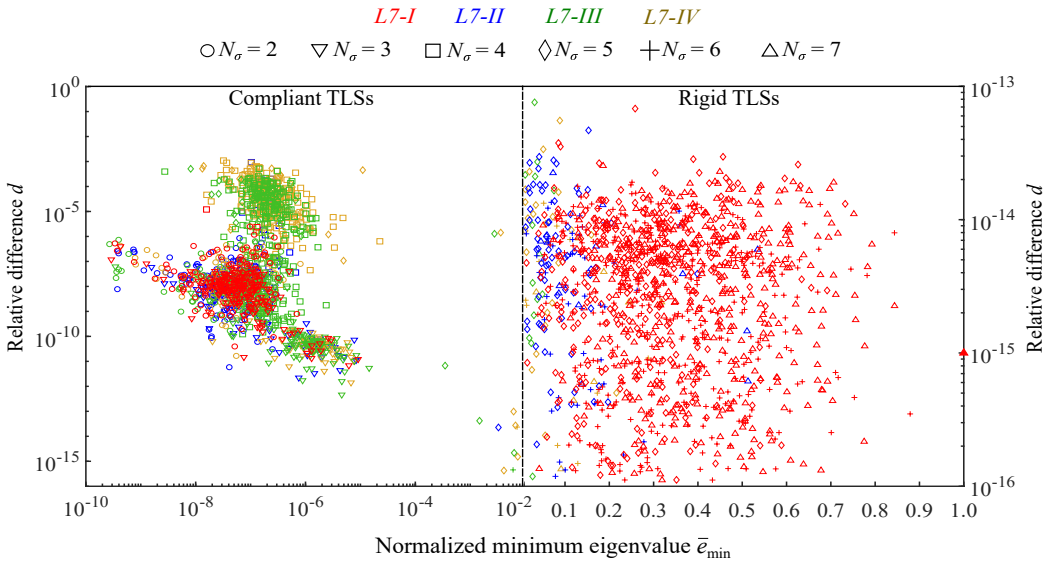

Fig. 3: Relative difference of the best-performing $L7$ TLSs for 6×500 testing problems. Different colors distinguish various $L7$ TLSs; different symbols distinguish different load numbers N_σ; and different scale factors and ranges are separately used for the optimized results of compliant TLSs (left part) and rigid TLSs (right part).

different TLSs might yield the same energy. For the comparisons, the base material has assumed Poisson's ratio of $\nu_0 = 1/3$, but conclusions do not change for other Poission's ratios.

The obtained $M - R$ chart is plotted in Fig. 4. The results clearly verify that the optimal TLSs always have lower stiffness than the optimal PLSs. More importantly, one can observe that the stiffness inferiority of any optimal anisotropic TLS is well bounded. Therein, minimum $R = 1$ appears for a single uniaxial stress, where the two microstructures have a single bar and plate set in the loading direction, indicating no stiffness reduction by using TLSs; and maximum $R = 3$ (function of ν_0 as seen in Appendix) is reached if all the plates in the PLSs are fully loaded, e.g. for a single loading case with three equal principal stresses, where the TLSs will have the maximum stiffness inferiority. The values of $1 < R < 3$ (see colored dots) means that the TLSs can have intermediate inferior stiffness, if there exist plates in the PLSs not fully loaded. Especially, for single stress cases, R can be (analytically) evaluated by using three orthonormal bar and plate sets (see grey regions in Fig. 4 and discussions in Supplementary Material). Note that the optimal isotropic TLSs have the maximum inferior stiffness, with only 1/3 Young's modulus of the optimal isotropic rank-6 laminates, which matches the theoretical estimation in [17] (also see Appendix). Finally, increasing the number of random stress cases will make optimal TLSs behave more isotropically.

4. Summary

We have identified four optimal TLS categories with simple geometries attaining maximum stiffness for arbitrary loading scenarios. Their near-optimal stiffness (below 0.1% of bounds) are verified through thousands of tests with various number of stress cases. In addition, we conclude

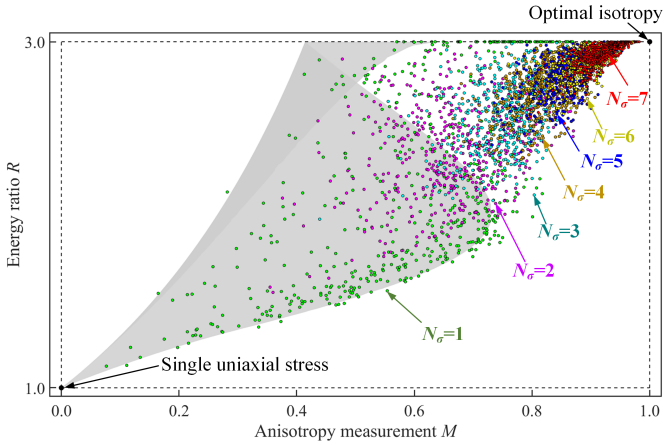

Fig. 4: Energy ratios between optimal TLSs and PLSs, grey regions for single stress cases with 3 bar and plate sets and colored dots for various groups of stress case numbers.

that the optimal TLSs always have inferior stiffness within the range of 1 and 3 compared to PLSs. At this stage, one can readily use these optimal TLSs in stiffness-preferred multi-scale design problems [29].

Acknowledgment

Support from the European Union's Horizon 2020 research and innovation programme under the Marie Sklodowska-Curie grant agreement no. 713683 (COFUNDfellowsDTU) for Y. W. and from the Villum Investigator Project InnoTop for J. G. and O. S.

Appendix A. Optimal isotropy

Analytical properties

In the low volume fraction, Christensen [17] analytically studied the elastic properties of optimal isotropic microstructures. For optimal TLSs, it has

$$\frac{E^*}{\rho} = \frac{1}{6}, \quad \nu^* = \frac{1}{4} \tag{A1}$$

with E^* and ν^* the relative Young's modulus and effective Poisson's ratio of the optimal TLSs, respectively.

For optimal PLSs, it has

$$\frac{E^*}{\rho} = \frac{2(7-5\nu_0)}{3(1-\nu_0)(9+5\nu_0)}, \quad \nu^* = \frac{1+5\nu_0}{9+5\nu_0} \tag{A2}$$

with ν_0 denoting the Poisson's ratio of the base material. The stiffness and compliance matrices can be calculated accordingly.

Loading conditions

Among many others, two loading conditions are used to obtain isotropic TLSs. The first condition applies 6 uniaxial stress cases, whose loading directions (denoted by $\boldsymbol{n}$) match the normal directions of 6 ranks in the optimal isotropic rank-6 laminates [11], stated by

$$\boldsymbol{n}_1 = \{0, 0, 1\}, \quad \boldsymbol{n}_k = \{\sin 2\beta \cos 2k\alpha,\ \sin 2\beta \sin 2k\alpha,\ \cos 2\beta\} \quad (k = 2, ..., 6) \tag{A3}$$

with $\alpha = \pi/5$ and $\cos 2\beta = 1/\sqrt{5}$. The weighting factors are set by $w_k = 1/6$ for $k = 1, 2, ..., 6$.

The second condition involves 7 uniaxial stress cases, whose loading directions are

$$\boldsymbol{n} = \begin{bmatrix} 1 & 0 & 0 & q & -q & q & q \\ 0 & 1 & 0 & q & q & -q & q \\ 0 & 0 & 1 & q & q & q & -q \end{bmatrix}^{\mathrm{T}}, \quad \frac{w_i}{w_j} = \frac{8}{9} \quad (i = 1, 2, 3;\ j = 4, 5, 6, 7) \tag{A4}$$

with $q = \sqrt{3}/3$.

The components of each stress case can then be calculated by rotating a uniaxial stress vector $\boldsymbol{\sigma}_0 = [1, 0, 0, 0, 0, 0]^{\mathrm{T}}$ to the above directions through $\boldsymbol{\sigma}_i = \boldsymbol{R}_i^{\mathrm{T}} \boldsymbol{\sigma}_0 \boldsymbol{R}_i$, with $\boldsymbol{R}_i = \boldsymbol{R}(\boldsymbol{n}_i)$ being the rotation matrix.

Optimal isotropic TLSs

Two new optimal isotropic TLSs are presented in Fig. A.1, together with the corresponding geometric parameters. Both the obtained TLSs have only two different bar areas. Although running optimization (2) can yield other optimal isotropic TLSs, they may have complex geometries with more than two different bar areas. Specifically note that the optimal isotropic TLSs have unit axial strains for all the involved bar sets, i. e. $\epsilon_i = \sum_{k=1}^{N_\sigma} w_k \boldsymbol{p}_i^{\mathrm{T}} (\boldsymbol{C}\boldsymbol{\sigma}_k) \boldsymbol{p}_i = 1$. Furthermore, because of the same constituent material, the bar sets also have a constant axial stress, and therefore, they have an equal strain energy density, hence meeting the optimality conditions.

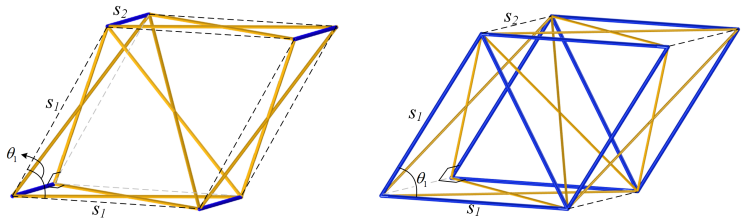

Fig. A.1: Two optimal isotropic TLSs with maximum Young's modulus. The left TLS has 7 bar sets satisfying $s_1/s_2 = 2$, $\theta_1 = \pi/3$ and $a_i/a_j = 1.2$; and the right TLS has 9 bar sets satisfying $s_1/s_2 \approx 0.8165$, $\theta_1 = \pi/3$ and $a_i/a_j = 1.6$, with i and j for blue and yellow bar sets, respectively.

[1] G. Allaire, Shape optimization by the homogenization method, Springer Science & Business Media, 2002.

[2] A. Cherkaev, Variational methods for structural optimization, Vol. 140, Springer Science & Business Media, 2002.

[3] Z. Hashin, The elastic moduli of heterogeneous materials, J. Appl. Mech., 29 (1962) pp.143–150.

[4] S. Vigdergauz, Two-dimensional grained composites of extreme rigidity, J. Appl. Mech., 61 (1994) pp.390–394.
[5] O. Sigmund, On the optimality of bone microstructure, in: IUTAM Symposium on Synthesis in Bio Solid Mechanics,, Springer, 1999, pp. pp.221–234.
[6] L. Liu, R. D. James, P. H. Leo, Periodic inclusion—matrix microstructures with constant field inclusions, Metall. Mater. Trans. A 38 (2007) pp.781–787.
[7] G. A. Francfort, F. Murat, Homogenization and optimal bounds in linear elasticity, Arch. Ration. Mech. Anal., 94 (1986) pp.307–334.
[8] K. A. Lurie, A. V. Cherkaev, Exact estimates of the conductivity of a binary mixture of isotropic materials, Proceedings of the Royal Society of Edinburgh Section A: Mathematics, 104 (1986) pp.21–38.
[9] G. Milton, Modelling the properties of composites by laminates, in: Homogenization and effective moduli of materials and media, Springer, 1986, pp. pp.150–174.
[10] M. Avellaneda, Optimal bounds and microgeometries for elastic two-phase composites, SIAM J. Appl. Math., 47 (1987) pp.1216–1228.
[11] G. Francfort, F. Murat, L. Tartar, Fourth-order moments of nonnegative measures on s2 and applications, Arch. Ration. Mech. Anal., 131 (1995) pp.305–333.
[12] G. W. Milton, A. V. Cherkaev, Which elasticity tensors are realizable?, J. Eng. Mater. Technol., 117 (1995) pp.483–493.
[13] O. Sigmund, A new class of extremal composites, J. Mech. Phys. Solids, 48 (2000) pp.397–428.
[14] J. Berger, H. Wadley, R. McMeeking, Mechanical metamaterials at the theoretical limit of isotropic elastic stiffness, Nature, 543 (2017) pp.533–537.
[15] G. Milton, M. Briane, D. Harutyunyan, On the possible effective elasticity tensors of 2-dimensional and 3-dimensional printed materials, Mathematics and Mechanics of Complex Systems, 5 (2017) pp.41–94.
[16] L. R. Meza, S. Das, J. R. Greer, Strong, lightweight, and recoverable three-dimensional ceramic nanolattices, Science, 345 (2014) pp.1322–1326.
[17] R. Christensen, Mechanics of low density materials, J. Mech. Phys. Solids, 34 (1986) pp.563–578.
[18] B. Bourdin, R. V. Kohn, Optimization of structural topology in the high-porosity regime, J. Mech. Phys. Solids, 56 (2008) pp.1043–1064.
[19] G. Gurtner, M. Durand, Stiffest elastic networks, Proceedings of the Royal Society A: Mathematical, Physical and Engineering Sciences, 470 (2014) pp.20130611.
[20] M. C. Messner, Optimal lattice-structured materials, J. Mech. Phys. Solids, 96 (2016) pp.162–183.
[21] R. M. Latture, M. R. Begley, F. W. Zok, Design and mechanical properties of elastically isotropic trusses, J. Mater. Res., 33 (2018) pp.249–263.
[22] F. W. Zok, R. M. Latture, M. R. Begley, Periodic truss structures, J. Mech. Phys. Solids, 96 (2016) pp.184–203.
[23] E. Traff, J. P. Groen, O. Sigmund, Simple single-scale microstructures based on optimal rank-3 laminates, Struct. Multidiscip. Optim., submitted.
[24] V. S. Deshpande, N. A. Fleck, M. F. Ashby, Effective properties of the octet-truss lattice material, J. Mech. Phys. Solids, 49 (2001) pp.1747–1769.
[25] X. Zheng, H. Lee, T. H. Weisgraber, et al., Ultralight, ultrastiff mechanical metamaterials, Science, 344 (2014) pp.1373–1377.
[26] C. M. Portela, J. R. Greer, D. M. Kochmann, Impact of node geometry on the effective stiffness of non-slender three-dimensional truss lattice architectures, Extreme Mech. Lett., 22 (2018) pp.138–148.
[27] P. Pedersen, On optimal orientation of orthotropic materials, Structural optimization, 1 (1989) pp.101–106.
[28] K. Kowalczyk-Gajewska, J. Ostrowska-Maciejewska, Review on spectral decomposition of hooke's tensor for all symmetry groups of linear elastic material, Engng. Trans., 57 (2009) pp.145–183.
[29] J. P. Groen, O. Sigmund, Homogenization-based topology optimization for high-resolution manufacturable microstructures, Int. J. Numer. Methods Eng., 113 (2018) pp.1148–1163.

Supplementary: Energy ratios for single stress cases

For single stress cases, the maximum stiffness can be attained by orientating three orthonormal sets of bars (for open TLSs) or plates (for PLSs) in the directions of principal stresses [27]. The prescribed stress condition can then be characterized by the three principal stresses σ_i, stated by

$$\boldsymbol{\sigma} = [\sigma_{11}, \sigma_{22}, \sigma_{33}, \sigma_{23}, \sigma_{13}, \sigma_{12}]^{\mathrm{T}} = [\sigma_1, \sigma_2, \sigma_3, 0, 0, 0]^{\mathrm{T}} \tag{S1}$$

with σ_{ij} the stress components in Cartesian-index notation and $-1 \leq \sigma_i \leq 1$. Any rotations of the stress vector will not change the achievable maximum stiffness. Moreover, adding extra bar or plate sets is not able to further improve the maximum stiffness since the three σ_i are orthonormal.

The relative areas of three bar sets in the optimal TLSs can be analytically calculated by

$$\frac{a_i}{a_j} = \frac{|\sigma_i|}{|\sigma_j|} \quad (i, j = 1, 2, 3; i \neq j) \tag{S2}$$

with $|\cdot|$ the absolute number. Referred to the optimal PLSs, the thickness of each plate set should be determined by running optimizations, except for special loading conditions.

The obtained $M - R$ chart is presented in Fig. S.1. The special left-bottom corner is observed with $R = 1$ for a single uniaxial stress. Besides, the results can be classified into two groups, obtained by either (I) all positive principal stresses with $\sigma_i \geq 0$ (see the red-shaded region) or (II) two positive and one negative principal stresses with $\sigma_{i,j} \geq 0$ and $\sigma_k \leq 0$ (see the blue-shaded region). Note that changing the signs of all σ_i simultaneously will retain the energy ratios.

In the group (I) results, the following two situations can be examined.

(1) For prescribed stress cases satisfying

$$\sigma_i + \sigma_j - \sigma_k \geq 0 \quad (i, j, k = 1, 2, 3; i \neq j, i \neq k, j \neq k) \tag{S3}$$

In these cases, all the plate sets in the PLSs are fully loaded and optimal thicknesses t_i can be analytically calculated by

$$\frac{t_i + t_j}{t_j + t_k} = \frac{\sigma_k}{\sigma_i} \quad (i, j, k = 1, 2, 3; i \neq j, i \neq k, j \neq k) \tag{S4}$$

Therefore, the optimal TLSs would have the maximum inferior stiffness, i.e. $R = 3$, as seen by the red solid line on the top edge of the chart. Particularly, the two ends of the line correspond to the results obtained by using two (and one zero) and three equal σ_i.

(2) In other stress cases with Eq. (S3) not satisfied, the plates are not fully loaded. Therefore, the optimal TLSs have lower inferior stiffness with $R < 3$. Particularly, if there exist one zero principal stress like $\sigma_i = 0$, $\sigma_{j,k} \neq 0$, the two optimal microstructures have two bar and one plate sets, respectively, and the results form the left-side boundary of the red-shaded region. On the other side, the results subject to stress cases of $\sigma_i = \sigma_j$ and $2\sigma_i \leq \sigma_k$ form the right-side boundary of the region. Interestingly, these results are found to involve only two plate sets with normal directions along i and j.

In the group (II) results, condition (S3) cannot be met, and thus it has $R < 3$. The right-side boundary of the blue-shaded region is formed by the results subject to stress cases with two equal principal stresses ($\sigma_i = \sigma_j$). Especially, the result point from $\sigma_i = \sigma_j = -\sigma_k$ further partitions the boundary into two parts, where the lower and upper lines are obtained from stress cases of $|\sigma_i| < |\sigma_k|$ and $|\sigma_i| > |\sigma_k|$, respectively. Otherwise, the internal points can be achieved with $\sigma_i \neq \sigma_j$.

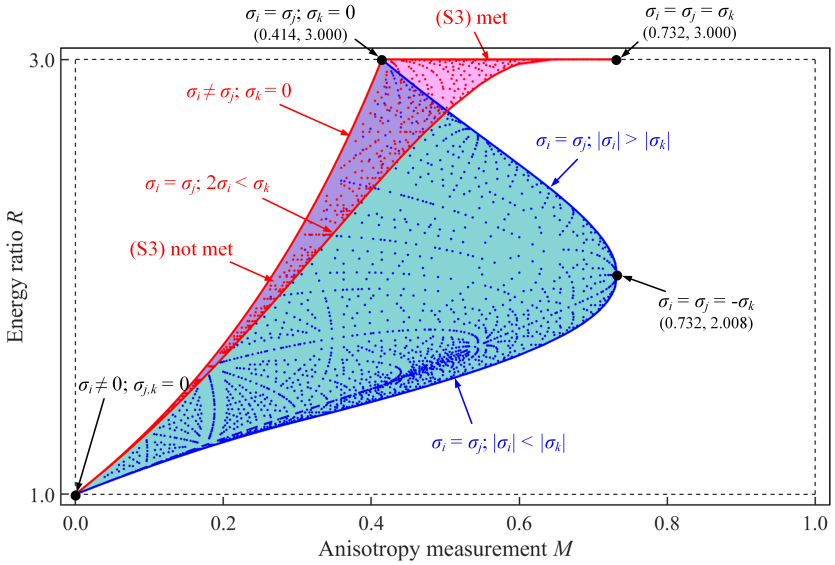

Fig. S.1: Energy ratios between optimal TLSs and PLSs using three bar and plate sets for single loading cases. The red and blue regions and dots indicate the results from group (I) with $\sigma_i \geq 0$ and group (II) with $\sigma_{1,2} \geq 0$ and $\sigma_3 \leq 0$, respectively.